Machine Learning-Enhanced Throughflow Method for the Improved Performance Prediction of Radial Impellers

Durch maschinelles Lernen gestützte Throughflow-Methode zur verbesserten Vorhersage der Leistungsdaten von radialen Laufrädern

Von der Fakultät für Maschinenwesen der
Rheinisch-Westfälischen Technischen Hochschule Aachen
zur Erlangung des akademischen Grades einer
Doktorin der Ingenieurwissenschaften genehmigte Dissertation

vorgelegt von

Sandra Labat Casajust

Berichter: Univ.-Prof. Dr.-Ing. Peter Jeschke
Hon.-Prof. Dr.-Ing. Hannes Benetschik

Tag der mündlichen Prüfung: 14.11.2025

Abstract

In aerospace applications which include a hybrid compressor consisting of multiple axial stages and one final radial stage, challenges arise in the preliminary design phase in matching the efficiencies of the axial and radial stages across a broad operating range. Low-level calculation tools, such as two-dimensional (2D) throughflow methods, require empirical correlations and usually fail to accurately predict the performance of the radial compressor, especially beyond the design point. The complex flow profile hinders the viability of the empirical correlations. For this reason, the preliminary design of radial compressors is often based on three-dimensional (3D) Computational Fluid Dynamics (CFD) simulations instead. However, CFD simulations are time-consuming, and for routine preliminary design, a rapid—and yet accurate—calculation tool would be advantageous. The present dissertation aims to improve the design and off-design predictive accuracy of throughflow methods for radial compressors, specifically for the radial impeller. A methodology is proposed which calibrates 2D calculations to benchmark CFD results by means of machine learning methods.

Relevant performance metrics which are traditionally prescribed through correlations in a throughflow method for radial impellers are the slip factor, the loss coefficient, and the aerodynamic blockage. As a first step, the proposed approach included baseline throughflow calculations by combining established empirical correlations for these three metrics. Subsequently, the baseline values of the metrics were calibrated against reference values from CFD simulations, for which a neural network regression model was used. Applied to two representative test cases, the new throughflow calculations with the calibrated metrics yielded substantially improved predictions of both total-total pressure ratio and isentropic efficiency compared with the initial baseline throughflow results using empirical correlations. The proposed methodology aligned the predicted speed lines for pressure ratio and efficiency with the CFD benchmarks for the majority of operating points considered. The method was also capable of replicating the curvature of the reference speed lines near choke conditions. Still, the most significant disparities in prediction were observed at the limits of the operating range, i.e., in the vicinity of choke and near surge. Between these two limit operating conditions, the relative prediction errors in pressure ratio remained within -2.0% and 0.5%. Across all speed lines, the relative errors in efficiency prediction ranged between -1.0% and 0.5%.

To summarize, the proposed machine learning-enhanced 2D throughflow method appears to be sufficiently accurate for a wide range of operating conditions and thus offers a viable alternative to CFD simulations in the preliminary design of radial impellers. Despite the relatively limited number of test cases considered, this approach shows promise for broader generalization and future integration of additional geometries and operating conditions.

Kurzfassung

Für Turbotriebwerke der Luftfahrt mit kombinierten Axial-Radialverdichtern stellt sich in der Vorauslegung die Herausforderung, die Wirkungsgrade der axialen und radialen Stufen über einen breiten Off-Design-Betriebsbereich abzustimmen. Einfache Berechnungsverfahren, wie beispielsweise zweidimensionale (2D) Throughflow-Methoden, benötigen empirischen Korrelationen und sind in der Regel nicht in der Lage, die Leistungsdaten des Radialverdichters präzise insbesondere außerhalb des Auslegungspunktes vorherzusagen. Die Komplexität der Strömung beeinträchtigt die Anwendbarkeit empirischer Korrelationen. Aus diesem Grund basiert die Vorauslegung von Radialverdichtern häufig auf zeitaufwendigen dreidimensionalen (3D) CFD-Simulationen (engl. Computational Fluid Dynamics). Die vorliegende Arbeit leistet daher einen Beitrag zur Verbesserung der Vorhersagegenauigkeit von Throughflow-Methoden für Radialverdichter, insbesondere für das Laufrad beim Auslegungspunkt und unter Off-Design-Bedingungen. Es wird eine durch maschinelles Lernen gestützte Methodik zur Kalibrierung von 2D-Methoden gegen 3D-Ergebnissen vorgestellt.

Traditionell werden in einer 2D-Berechnung für Laufräder Korrelationen für die Bewertungsgrößen Slip-Faktor, Verlustkoeffizient und aerodynamische Blockage angewendet. Im Rahmen dieser Arbeit wurde zunächst eine 2D-Baseline-Berechnung durch die Kombination etablierter Korrelationen aufgebaut. Im Anschluss erfolgte eine Kalibrierung der Basiswerte der Bewertungsgrößen anhand einer Regression mit neuronalen Netzen gegen Referenzwerte aus CFD-Simulationen. Bei der Anwendung auf zwei Testfälle ergab die 2D-Berechnung mit den kalibrierten Werten eine signifikant verbesserte Vorhersage des Totaldruckverhältnisses und des isentropen Wirkungsgrads im Vergleich zu den ursprünglichen 2D-Baseline-Ergebnissen mit den empirischen Korrelationen. Die Methodik konnte die Kennlinien für das Druckverhältnis und den Wirkungsgrad für die Mehrheit der betrachteten Betriebspunkte mit den CFD-Benchmarkdaten angleichen. Außerdem wurde die Krümmung der Referenz-Drehzahllinien in der Nähe der Sperrgrenze nachgebildet. Die signifikantesten Diskrepanzen in der Vorhersage konnten für die Grenzen des Arbeitsbereichs beobachtet werden, d.h. nahe der Sperr- und Pumpgrenze. Zwischen diesen beiden Betriebsbedingungen blieben die relativen Fehler im Druckverhältnis zwischen $-2{,}0\%$ und $0{,}5\%$. Über alle Kennlinien hinweg lagen die relativen Fehler bei der Vorhersage des Wirkungsgrads zwischen $-1{,}0\%$ und $0{,}5\%$.

Zusammenfassend weist die durch maschinelles Lernen gestützte 2D-Throughflow-Methode gegenüber traditionellen 2D-Methoden eine deutlich verbesserte Präzision für einen breiten Betriebsbereich auf. Sie stellt somit eine praktikable Alternative zu CFD-Methoden für die Vorauslegung von radialen Laufrädern dar. Trotz der relativ begrenzten Anzahl der betrachteten Testfälle ist der vorgeschlagene Ansatz vielversprechend für die zukünftige Integration weiterer Geometrien und Betriebsbedingungen.

Contents

1 Introduction

Climate impact from aviation remains a major environmental concern. In the medium term, lower CO_2 emissions are expected through efficiency improvements to aircraft engines that lower fuel consumption. One effective approach involves increasing the air bypass ratio, which is the ratio between the mass flow rate of the bypass stream and the mass flow rate entering the core. Within the scope of civil aviation, a higher bypass ratio typically reduces the fuel consumption for a given thrust, which in turn results in smaller core sizes. In small turbofans, more compact core sizes can be achieved with a hybrid compressor consisting of multiple axial stages and one final radial stage. This setup enables higher pressure ratios than those achievable with an equivalent number of purely axial stages, exhibiting moderate to high efficiencies. However, hybrid compressors introduce design challenges, particularly in matching the efficiencies of the axial and radial parts across a broad operating range, especially under off-design conditions. In the preliminary design phase, this design complexity demands a predictive calculation tool that adapts easily and quickly to changing performance requirements and specific geometry configurations.

To estimate the performance quickly during preliminary design, engineers rely on simplified analytical models that approximate the complex three-dimensional (3D) flow of axial and radial compressors. Quasi-3D (Q3D) models exist, which assume that the variation of one velocity component is less important than the variations of the other two. In present approaches, this corresponds to the assumption of axisymmetric flow, where the variations in the circumferential direction are neglected such that the governing equations are simplified considerably. With this approximation, the steady relative flow in a turbomachine can be described as a combination of two families of intersecting two-dimensional (2D) stream surfaces: the blade-to-blade (S_1) surfaces and the hub-to-shroud (S_2) surfaces. The flow solution on one family of surfaces provides the boundary conditions for the calculation on the other family of surfaces, which makes Q3D methods iterative in nature. The coupling between the S_1 and S_2 flow solutions is recognized to be a highly unstable process. For this reason, historical Q3D methods are nowadays replaced by full 3D Computational Fluid Dynamics (CFD) methods. Nevertheless, the uncoupled solutions on each of the surfaces are still of great use in the preliminary design of turbomachines. For the S_2 plane, the most representative surface is the mean S_2 (S_{2m}) surface. The solution on this surface is referred to as the throughflow calculation, which provides the distribution of the flow quantities along the hub-to-shroud direction. The individual solution on the S_1 surfaces serves to design the blade geometry in detail.

The flow on the S_{2m} surface is generally considered to be a true circumferential average between the blades. The process of averaging the axisymmetric governing equations yields additional interaction terms that possess a similar structure to the turbulent

Reynolds stresses, but they originate from the nonaxisymmetry of the real flow within a bladed passage. In principle, these interaction terms should be calculated using an S_1 solution, which means that the throughflow methodology is not fully uncoupled. In axial compressors, this issue is usually addressed by implementing a duct throughflow method that only includes calculating stations at the leading and trailing edges of the blade. Without internal calculating stations, the interaction terms in the equations can be ignored. However, for radial compressors with strongly curved geometries, intra-blade calculating stations are required to account for the curvature effects on the flow. In this case, the interaction terms cannot be ignored.

If a throughflow method is to be used as a standalone prediction tool for radial compressors, empirical correlations can be used to replace the calculation of the interaction terms. These correlations are generally employed to ensure that the real outflow conditions of the bladed passage are correctly described. This includes the direction of the relative velocity vector with respect to an ideal, blade-guided flow and the reduction of effective flow area after a blade due to the effect of the boundary layers. The metrics that describe these effects are the slip factor and the outlet aerodynamic blockage, respectively. Additionally, an empirical loss coefficient is incorporated to account for the entropy generation within the blade, making the throughflow calculation a viscous one.

It is generally difficult to correlate these three effects in a 2D plane of a radial compressor. For this reason, the throughflow method in this case typically includes one-dimensional (1D) meanline correlations and, subsequently, appropriate 2D distributions are defined. These empirical correlations are generally based on a limited number of parameters and work fairly well close to the design point of the compressor. However, they become less accurate at off-design operating conditions due to the increasing complexity of the radial compressor flow profile. Consequently, for convenience, 3D CFD simulations are used instead directly after 1D meanline calculations in the preliminary design of a radial compressor, but at the expense of increased computing time. Nevertheless, in hybrid compressor configurations where the preceding axial part is extensively analyzed via throughflow methods, an improved 2D calculation for the final radial compressor becomes essential.

Existing research efforts to extend the predictive capabilities of a standalone throughflow calculation have followed three research lines. The first one consisted in coupling a throughflow method with models representing the blade nonaxisymmetries, i.e., circumferential perturbations to the mean flow, viscous calculations with blade force models, boundary layer calculations, spanwise mixing models, and secondary flow models. The second research line included the definition of aerodynamic loading parameters that captured the flow nonaxisymmetry and could be used to derive guidelines in the preliminary design phase. As for the last research approach, it consisted in calibrating the coefficients of the empirical correlations for the slip factor, the loss coefficient, and the aerodynamic blockage to match reference data of specific compressors with data-driven methods. Among the three research lines, better predictive accuracies were achieved through the calibration of the empirical correlations. However, the resulting calibrated coefficients were typically specific to the respective machines, and the approach did not

allow for the extension of the initial empirical models to account for effects that were not modeled in the correlations.

This dissertation addresses these limitations and aims to enhance the predictive accuracy of throughflow calculations for radial compressors, specifically for the radial impeller. A machine learning-based calibration methodology is proposed, which pursues the reduction in the performance prediction gap between 2D and 3D calculations across a broad range of operating conditions. The objective is to eventually propose a viable alternative to the use of 3D CFD methods in the preliminary design of radial impellers. To achieve this goal, the first step consists in the analysis and recommendation of a robust set of established correlations for the metrics of slip factor, loss coefficient, and aerodynamic blockage. Instead of calibrating the coefficients of the empirical correlations, additional correction models are multiplied to the baseline equations. These models are expressed as offsets between the baseline metrics and CFD benchmark values and are defined as functions of aerodynamic loading parameters. These parameters are intended to capture the effects of 3D flow, particularly of the boundary layer fluid accumulation near the impeller exit, across the performance map. The correction equations are calibrated with an artificial neural network (ANN) regression model because of its ability to approximate complex nonlinear relationships within the given data. The design of the ANN model and the algorithms that train and use it is also part of the research. The proposed methodology is applied to two representative test cases of similar nominal characteristics, which both have an unshrouded impeller and a vaneless diffuser. The data from both test cases are combined in a unified database for the calibration. The central research question is to what extent the proposed calibration methodology allows throughflow calculations of the considered radial impellers to align with benchmark 3D reference results. If successful, this approach could represent a viable alternative to the use of 3D CFD methods in the preliminary design of radial impellers, subject to further generalization to additional test cases.

Chapter 2 provides an overview of the fundamental principles of radial impeller aerodynamics, the quasi-3D approximation of radial compressor flow fields, and machine learning methods for metamodeling. In Chapter 3, a critical review of the prior work on the topic of accuracy enhancement of throughflow calculations is carried out to motivate the proposed approach in this dissertation. The numerical setups of the methods, i.e., 3D CFD, 2D throughflow, and ANN regression, are outlined in Chapter 4. Chapter 5 focuses on the baseline throughflow results with empirical correlations from the literature. Finally, the calibrated throughflow results are presented in Chapter 6. Chapter 7 gives a summary of the thesis and a discussion on the degree of achievement of the originally defined objectives. Suggestions for future research are also outlined.

2 Theoretical Background

In this chapter, the fundamental concepts relevant to this dissertation are described. An initial overview of the flow within the impeller under a one-dimensional control volume approach is presented. Subsequently, three-dimensional flow features in the impeller passage are described. The focus is then shifted to the analytical approximation of the three-dimensional flow field by the quasi-three-dimensional method. Finally, the fundamental concepts of machine learning for metamodeling purposes are also presented.

2.1 Elementary Flow Analysis of a Radial Impeller

A radial compressor consists essentially of a rotating impeller to increase the energy level of the fluid, a diffuser to transform some of the fluid kinetic energy into static pressure, and a volute to collect the fluid and deliver it into a pipe (see Figure 2.1a). The energy transfer in the impeller passage is the result of the input shaft power, which is transmitted to the blade as torque $\vec{T}$ (see Figure 2.1b). As a consequence, the moving

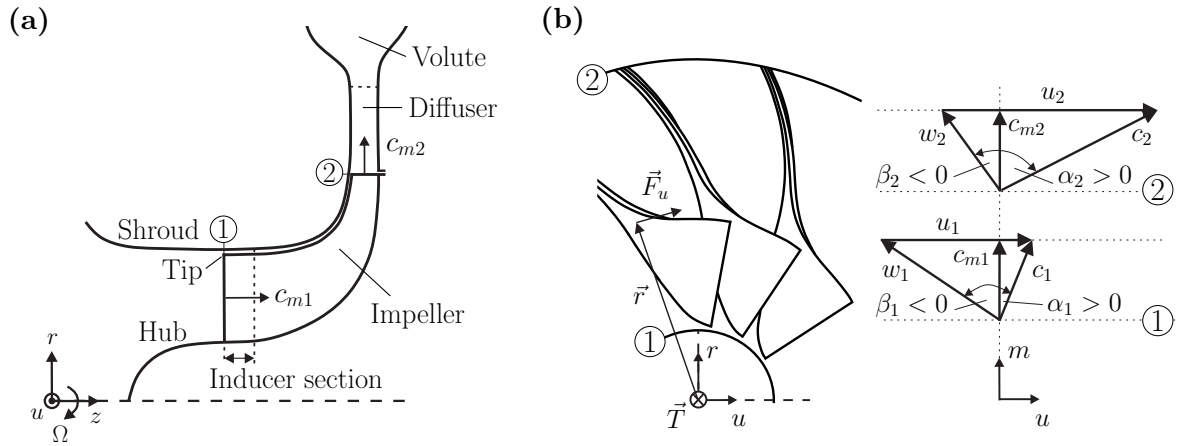

Figure 2.1: **(a)** Meridional view of a radial compressor. The inducer section in the impeller is also highlighted, which starts at impeller inlet ① and ends at the point where the flow begins to move towards the radial direction. The flow at impeller inlet has components in the axial and tangential directions only, giving $c_{m1} = \sqrt{c_{z1}^2 + c_{r1}^2} = c_{z1}$, and at outlet, ②, in the radial and tangential directions, i.e., $c_{m2} = c_{r2}$. **(b)** Velocity triangles for the flow entering and leaving the impeller—the velocities and angles in the stationary frame of reference are denoted by c and α, respectively, and in the relative or rotating frame, by w and β. The angle convention from the meridional direction is chosen. In both subfigures, the cylindrical coordinate system (r, u, z) is used.

blade exerts a tangential force $\vec{F}_u$ on the fluid. By means of Newton's second law of motion, this resulting external force from the entire blade can be related to the change of momentum of the fluid from inlet to outlet as $F_u = \frac{d}{dt}(mc_u) = \dot{m}(c_{u2} - c_{u1})$, where it has been assumed that the fluid enters and leaves the impeller steadily at uniform velocity. Employing Newton's second law in terms of moments of forces, i.e., angular momentum, gives, for the torque $\vec{T} = \vec{r} \times \vec{F}_u$ in scalar form

$$T = \dot{m}(r_2 c_{u2} - r_1 c_{u1}). \tag{2.1}$$

With $c_{u2} > c_{u1}$ from (2.1) and assuming $c_{m2} \approx c_{m1}$ (see Figure 2.1b), the velocity triangle expression $c^2 = c_m^2 + c_u^2$ confirms that there is an increase in kinetic energy ($c^2/2$) in the impeller. The impeller passage is also designed to diffuse the flow, i.e., increase the static enthalpy. This can be demonstrated from the first law of thermodynamics

$$\frac{DE_t}{Dt} = \frac{DQ}{Dt} - \frac{DW}{Dt}, \tag{2.2}$$

which is taken as a rate equation, because the rate of change of the flow quantities is of interest. In (2.2), DE_t/Dt is the change in total energy of the system; DQ/Dt is the rate of energy transfer from the surroundings to the system as heat—which for the case of adiabatic flow is equal to zero—; and DW/Dt, or $\dot{W}$, is the rate of work done by the system. For steady flow in a fixed control volume with no body forces and negligible shear stress work, the work contributions are the shaft work—which for compressors, i.e., work absorbing machines, is negative—and the work done by the fluid within the system on the environment, $(p_2 A_2)c_2 dt - (p_1 A_1)c_1 dt$. With that, (2.2) becomes

$$\begin{aligned} \left(e_2 + \frac{1}{2}c_2^2 + \frac{p_2}{\rho_2}\right)\rho_2 A_2 c_2 - \left(e_1 + \frac{1}{2}c_1^2 + \frac{p_1}{\rho_1}\right)\rho_1 A_1 c_1 &= \dot{W} \\ \dot{m}\left[(h_2 - h_1) + \frac{1}{2}(c_2^2 - c_1^2)\right] &= \dot{W}, \end{aligned} \tag{2.3}$$

where $h = e + p/\rho$ and $\dot{m} = \rho A c$. Incorporating $h_t = h + \frac{1}{2}c^2$ into (2.3) yields

$$\dot{W} = \dot{m}(h_{t2} - h_{t1}). \tag{2.4}$$

The rate of work $\dot{W}$, i.e., power, can also be expressed as the product of the angular speed by the torque, $\dot{W} = \Omega T$. Therefore, with (2.1), the power is

$$\dot{W} = \dot{m}\Omega(r_2 c_{u2} - r_1 c_{u1}) = \dot{m}(u_2 c_{u2} - u_1 c_{u1}), \tag{2.5}$$

where $u = \Omega r$. (2.5) constitutes Euler's turbine equation. Equating (2.4) to (2.5) then yields the first law of thermodynamics applied to the impeller

$$h_{t2} - h_{t1} = u_2 c_{u2} - u_1 c_{u1}, \tag{2.6}$$

from which a nondimensional work coefficient can be defined as

$$\lambda = \frac{\Delta h_{t12}}{u_2^2} = \frac{h_{t2} - h_{t1}}{u_2^2} = \frac{u_2 c_{u2} - u_1 c_{u1}}{u_2^2}. \tag{2.7}$$

To proceed with the derivation of an expression for the increase in static enthalpy (Δh) in the impeller, (2.6) is expanded with the definition of the stagnation enthalpy as

$$h_2 + \frac{1}{2}c_2^2 - u_2 c_{u2} = h_1 + \frac{1}{2}c_1^2 - u_1 c_{u1}. \tag{2.8}$$

On each side of (2.8), $h + \frac{1}{2}c^2 - uc_u$ corresponds to the definition of the rothalpy, I. Therefore, (2.8) can be rewritten as $I_2 = I_1$, meaning that the rothalpy remains constant in the impeller under this one-dimensional control volume approach for steady flow in the rotating frame[1]. The expression $I = h + \frac{1}{2}c^2 - uc_u$ can be modified by including $c^2 = c_m^2 + c_u^2$ and adding and substracting the term $u^2/2$, leading to

$$I = h + \frac{1}{2}c^2 - uc_u = h + \frac{1}{2}\underbrace{(u^2 - 2uc_u + c_u^2)}_{(u-c_u)^2} + \frac{1}{2}(c_m^2 - u^2). \tag{2.9}$$

Incorporating $w_u = u - c_u$ and $w^2 = c_m^2 + w_u^2$ into (2.9) gives

$$I = h + \frac{1}{2}w^2 - \frac{1}{2}u^2 = h_{t,rel} - \frac{1}{2}u^2 = \text{const.}, \tag{2.10}$$

where $h_{t,rel} = h + \frac{1}{2}w^2$ is the relative stagnation enthalpy[2]. Expressing (2.8) in terms of (2.10) yields

$$h_2 + \frac{1}{2}w_2^2 - \frac{1}{2}u_2^2 = h_1 + \frac{1}{2}w_1^2 - \frac{1}{2}u_1^2, \tag{2.11}$$

which rearranged becomes

$$\Delta h = h_2 - h_1 = \frac{1}{2}(u_2^2 - u_1^2) + \frac{1}{2}(w_1^2 - w_2^2). \tag{2.12}$$

(2.12) explains the increase in static enthalpy in the impeller. The first term is the contribution from the centrifugal forces caused by the change in radius, and the second term is the contribution from the deceleration of the relative velocity. (2.12) provides the reason why the static enthalpy rise—pressure rise in incompressible flow—in an impeller is so large compared with an axial rotor, where there is no change in radius and therefore $u_2 = u_1$.

In summary, the mechanical work from the shaft is converted into a rise in angular momentum (see (2.1)), a rise in stagnation enthalpy (see (2.4)), and a rise in static enthalpy (see (2.12)) in the impeller. The efficiency of this energy conversion process is assessed by means of

$$\eta_{12} = \frac{w_{12,rev}}{w_{12}} < 1, \tag{2.13}$$

[1] In fact, the conservation of the rothalpy can only be assumed for steady laminar boundary layers and Prandtl numbers of unity (*Bosman and Jadayel*, 1996), where the kinetic energy loss and the heat production are almost in equilibrium, so that the rothalpy does not change significantly in the direction of the flow. A generalization is only an approximation. Refer to *Lyman* (1992).

[2] From (2.10), since the rothalpy I is constant through the blading but the impeller blade speed u is not ($u_2 \neq u_1$), the relative stagnation enthalpy is therefore also not constant ($h_{t,rel,2} \neq h_{t,rel,1}$). The same applies to $p_{t,rel}$ and $\rho_{t,rel}$.

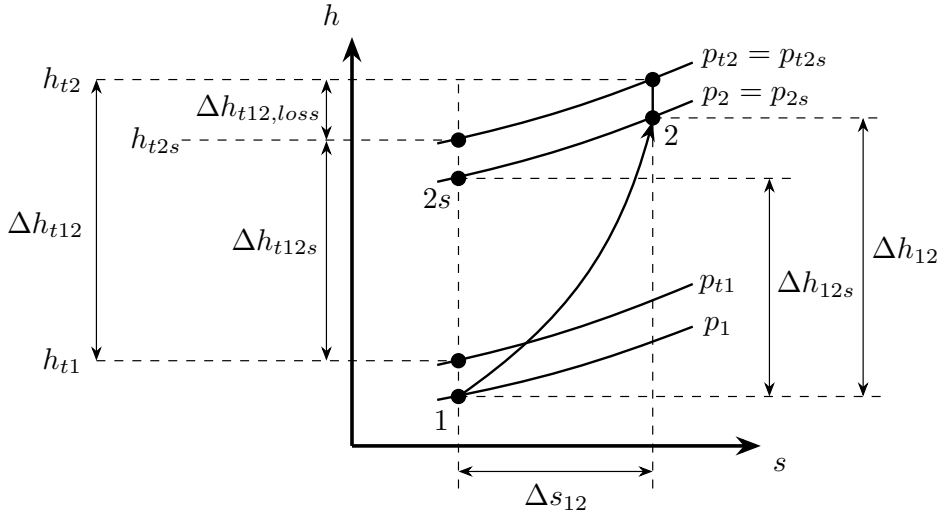

Figure 2.2: h,s diagram showing both the isentropic reversible adiabatic compression $1 \rightarrow 2s$ and the irreversible adiabatic compression $1 \rightarrow 2$. The stagnation enthalpy losses $\Delta h_{t12,loss}$ characterize the difference between the two processes in terms of enthalpy.

where $w_{12,rev}$ is the ideal reversible steady work or minimum work required to compress the flow between pressure levels 1 and 2, and w_{12} is the actual work done to achieve this pressure rise, which will always be greater than $w_{12,rev}$. In general, the reversible process can be defined as either isentropic or polytropic. Isentropic means that the compression takes place at constant entropy from 1 to $2s$, following Figure 2.2, and that the compression path is fully defined by these two states. Contrarily, in a polytropic process, the actual compression path $1 \rightarrow 2$ is generally not known and approximations are required.

If an isentropic reversible process is assumed, (2.13) can also be expressed in the form of either a total-total or a total-static efficiency. Total-total means that the internal losses are taken into account, whereas total-static considers the internal losses plus the wasted kinetic energy. If the compression process is assessed for an intermediate station in the machine, e.g., impeller outlet, the total-total efficiency is generally chosen because the outlet kinetic energy can still be used in the downstream component, i.e., the diffuser. In this case, the useful end state is given by the total conditions at impeller outlet. Accordingly, the impeller total-total isentropic efficiency is defined, from (2.13) and Figure 2.2, as

$$\eta_{s,12}^{tt} = \frac{\int_1^{2s}(vdp)_s + \int_1^{2s}(cdc)_s}{\int_{t1}^{t2} dh_t} = \frac{\int_1^{2s} dh_s + \frac{1}{2}(c_{2s}^2 - c_1^2)}{\int_{t1}^{t2} dh_t} = \frac{\int_{t1}^{t2s} dh_{ts}}{\int_{t1}^{t2} dh_t} = \frac{h_{t2s} - h_{t1}}{h_{t2} - h_{t1}}. \quad (2.14)$$

For a perfect gas ($c_p = \text{const.}$), $h_t = c_p T_t$ holds, so that (2.14) becomes

$$\eta_{s,12}^{tt} = \frac{T_{t2s} - T_{t1}}{T_{t2} - T_{t1}}. \quad (2.15)$$

After some rearranging with the isentropic relations, (2.15) reads

$$\eta_{s,12}^{tt} = \frac{T_{t2s} - T_{t1}}{T_{t2} - T_{t1}} = \frac{\frac{T_{t2s}}{T_{t1}} - 1}{\frac{T_{t2}}{T_{t1}} - 1} = \frac{\left(\frac{p_{t2s}}{p_{t1}}\right)^{\frac{\kappa-1}{\kappa}} - 1}{\frac{T_{t2}}{T_{t1}} - 1} = \frac{\left(\frac{p_{t2}}{p_{t1}}\right)^{\frac{\kappa-1}{\kappa}} - 1}{\frac{T_{t2}}{T_{t1}} - 1}, \tag{2.16}$$

where $\frac{p_{t2}}{p_{t1}} = \pi^{tt}$ is the total-total pressure ratio in the impeller and κ is the ratio of specific heats, $\kappa = c_p/c_v$.

The difference between w_{12} and $w_{12,rev}$ is viewed as the energy lost to do useful work, and is always positive because it relates to the entropy production in the real process, i.e., $\Delta s_{12} \geq 0$ as depicted in Figure 2.2. This entropy increase corresponds, in terms of enthalpy in Figure 2.2, to $\Delta h_{t12,loss} = \Delta h_{t12} - \Delta h_{t12s}$, which helps rewrite the isentropic efficiency (2.14) as

$$\eta_{s,12}^{tt} = \frac{h_{t2s} - h_{t1}}{h_{t2} - h_{t1}} = \frac{\Delta h_{t12s}}{\Delta h_{t12}} = \frac{\Delta h_{t12s}}{\Delta h_{t12s} + \Delta h_{t12,loss}}. \tag{2.17}$$

Performance can only be improved by minimizing the irreversibilities $\Delta h_{t12,loss}$. Accordingly, performance prediction methods for radial impellers have established the loss coefficient

$$\Delta q_{12} = \frac{\Delta h_{t12,loss}}{u_2^2}. \tag{2.18}$$

Depending on the purpose, it can be useful to work with an entropy-based loss coefficient, $(\Delta s/R)_{12}$, instead. For an ideal gas and steady adiabatic flow, it can be calculated as

$$\left.\frac{\Delta s}{R}\right|_{12} = \frac{\kappa}{\kappa - 1} \ln\left(\frac{T_2}{T_1}\right) - \ln\left(\frac{p_2}{p_1}\right). \tag{2.19}$$

The losses $\Delta h_{t12,loss}$ from (2.18) are then included in (2.19) via the static pressure ratio $\frac{p_2}{p_1}$. For an isentropic process, i.e., $ds = 0$, the Gibbs equation $Tds = dh - vdp$ becomes $dh = vdp$. The volume v can be substituted via the relationship $pv^\kappa = p_1 v_1^\kappa$ for an ideal gas and an adiabatic process, leading to

$$dh = \left(\frac{p_1}{p} v_1^\kappa\right)^{\frac{1}{\kappa}}. \tag{2.20}$$

Integration of (2.20) along the isentropic path $1 \rightarrow 2s$ gives, after some manipulation

$$\Delta h_{12s} = \int_1^{2s} dh = p_1^{\frac{1}{k}} v_1 \int_1^{2s} \left(\frac{1}{p}\right)^{\frac{1}{k}} dp = c_p T_1 \left[\left(\frac{p_{2s}}{p_1}\right)^{\frac{\kappa-1}{\kappa}} - 1\right], \tag{2.21}$$

which rearranged provides an expression for the pressure ratio

$$\frac{p_{2s}}{p_1} = \left(1 + \frac{\Delta h_{12s}}{c_p T_1}\right)^{\frac{\kappa}{\kappa-1}}. \tag{2.22}$$

Substituting Δh_{12s} in (2.22) with

$$\Delta h_{12s} = \Delta h_{t12s} - \frac{1}{2}\left(c_2^2 - c_1^2\right) = \left(\Delta h_{t12} - \Delta h_{t12,loss}\right) - \frac{1}{2}\left(c_2^2 - c_1^2\right) \tag{2.23}$$

yields the final expression for the pressure ratio in (2.19)

$$\frac{p_2}{p_1} = \frac{p_{2s}}{p_1} = \left(1 + \frac{\Delta h_{t12} - \Delta h_{t12,loss} - \frac{1}{2}(c_2^2 - c_1^2)}{c_p T_1}\right)^{\frac{\kappa}{\kappa-1}}, \tag{2.24}$$

which allows to obtain $(\Delta s/R)_{12}$ from (2.19) given a loss coefficient Δq_{12}.

2.2 Analysis of Three-Dimensional Impeller Flow

In this section, the phenomena leading to the three-dimensional flow profile in general curved passages and in radial impellers are introduced.

2.2.1 Generation of Secondary Flow in Curved Passages

For a general three-dimensional (3D) flow, the effect of shear forces on the fluid particles translates not only on the movement between fluid layers but also on the rotation of the fluid particles around their own axis caused by the torque applied on the sides of each particle. This rotation of the fluid particles around their own axis is given by the local vorticity $\vec{\omega} = \nabla \times \vec{c}$. However, for the description of the flow field as a whole, the concept of vortex lines is used instead. These are lines everywhere tangent to the local vorticity vector. In a 3D flow, where different parts of a vortex line move with the local fluid particles at different convection rates, the vorticity vector will change in both orientation and magnitude. The alteration of the components of vorticity leads to cross-flow velocity components, or *secondary flow*.

Consider the bottom of the bend in Figure 2.3a, where the initial velocity profile $\vec{c}_1$ has a boundary layer of width δ, and the vortex line AB of vorticity $\vec{\omega}_1$ lies perpendicular to the velocity. This vortex line AB will be convected through the bend by the irrotational primary flow outside of the boundary layer and will end up oriented as $A'B'$. To explain how this transition takes place, a generic flow pattern is now analyzed in which the streamlines are concentric circles, i.e., a plane circular vortex. Figure 2.3b shows a small element in such a reference plane bounded by two streamlines and two radii. The velocities, positive anti-clockwise, are c and $c + \delta c$ along the streamlines, so there is no velocity component perpendicular to the streamlines. The circulation Γ is defined as the line integral of the velocity around a curve enclosing an area A, i.e., $\Gamma = \oint c ds$. Accordingly, in Figure 2.3b, the circulation round the small element is

$$(c + \delta c)\,(R + \delta R)\delta\theta - cR\delta\theta = (c\delta R + R\delta c)\delta\theta, \tag{2.25}$$

where the product of small terms has been neglected and R is the radius of curvature of the streamlines. The vertical vorticity $\omega_\perp$ at a point is defined as the limiting value of the circulation $\delta\Gamma$ divided by the area δA, as δA becomes vanishingly small, giving

$$\omega_\perp = \frac{(c\delta R + R\delta c)\delta\theta}{R\delta\theta\delta R} = \frac{c}{R} + \frac{\delta c}{\delta R} = \frac{c}{R} + \frac{\partial c}{\partial R} \quad \text{as } \delta R \to 0. \tag{2.26}$$

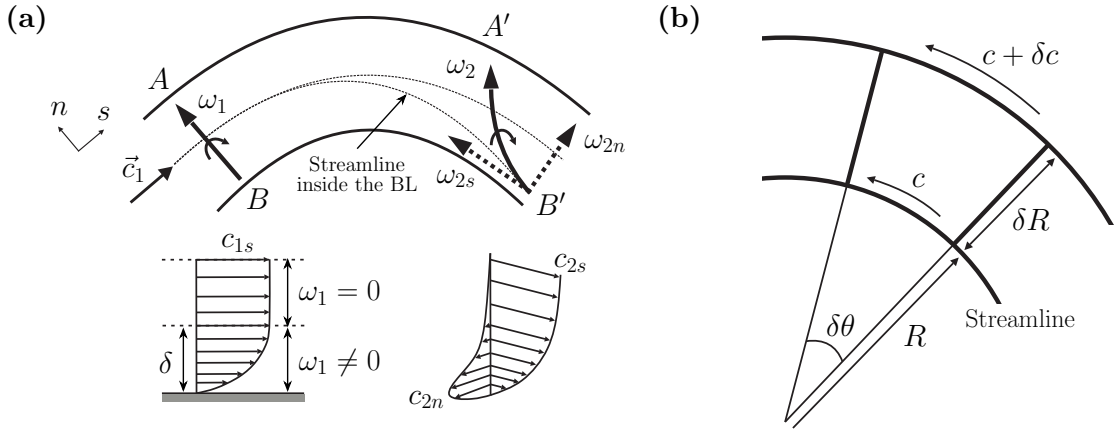

Figure 2.3: **(a)** Schematic showing the generation of streamwise vorticity ω_{2s} and cross-flow velocity c_{2n} when an initial vortex line AB is convected through a bend. The inlet velocity profile has a vorticity ω_1 along the boundary layer (BL) width δ. After the bend, the velocity profile is of three-dimensional nature because of the newly generated velocity component c_{2n} in spanwise direction. Based on *Greitzer et al.* (2004, p. 114, Figure 3.10). **(b)** Plane circular vortex. Based on *Massey and Ward-Smith* (2006, p. 376, Figure 9.17) and *Greitzer et al.* (2004, p. 447, Figure 9.1).

In this case of concentric streamlines, the cross-sectional area remains constant, and, by virtue of continuity, the velocity must also remain constant along each streamline. This means that the velocity varies only with R, so that the partial derivative $\partial c/\partial R$ in (2.26) is equal to the substantial derivative dc/dR. Gravity forces produce a vertical pressure gradient which needs to be balanced at all times to ensure radial equilibrium, and so it will be the same at all depths of the flow profile. If it is assumed that the boundary layer occupies only a small part of the total depth, then the main flow fixes the pressure gradient in the boundary layer. Since for an irrotational main flow $\omega_\perp = 0$ holds, (2.26) leads to the following condition

$$\frac{dc}{dR} = -\frac{c}{R} \quad \rightarrow \quad cR = \text{const.} \tag{2.27}$$

(2.27) states that the fluid particles on the inside radius will have a higher velocity than the particles on the outside radius. Therefore, for the bend in Figure 2.3a, the higher velocity toward the inner radius will cause the lower part of the vortex line AB to travel faster than the upper part, tipping it into the streamwise direction, and resulting in $A'B'$. The new orientation of the vortex line results in a streamwise vorticity component, ω_{2s}, which is in turn associated with a cross-flow velocity component c_{2n} perpendicular to the streamwise direction of c_{2s}. This resulting spanwise velocity c_{2n} is referred to as secondary flow and forms the three-dimensional flow profile.

Instead of an explanation based on vorticity concepts, it is also customary to describe the formation of secondary flow in terms of pressure fields and fluid accelerations. Equilibrium must also be ensured along the normal direction, perpendicular to the streamline. The normal pressure gradient

$$\frac{1}{\rho}\frac{dp}{dn} = \frac{c^2}{R} \tag{2.28}$$

must be balanced at all times between the main flow and the boundary layer. Since the velocities are lower in the boundary layer than in the main flow, (2.28) forces the boundary layer flow to be swept towards the inner radius of the bend. This creates a cross-flow velocity component in the boundary layer, i.e., secondary flow.

2.2.2 Curvature and Rotation Effects on Impeller Flow

As seen in Sec. 2.2.1, secondary flow is generated whenever the flow is nonuniform in the direction perpendicular to the surface and undergoes curvature in the plane of the surface. This occurs on the casing and hub of a radial impeller due to the flow turning from the axial to the radial direction, as well as on the blades due to strong meridional curvature. There are other mechanisms that generate secondary flow, as summarized in *Lakshminarayana* (1996, p. 261), which are mostly inviscid: (1) spanwise density gradients due to compressibility; (2) spanwise variation in blade thickness and 3D blade geometry; (3) rotation, which can affect the behavior of the boundary layers by suppressing or augmenting turbulence production; (4) spanwise variation in work input or output; (5) leakage flow due to tip clearance, which interacts with the endwall flow and the passage flow and generates local vorticity; and (6) mixed-flow regions of subsonic, supersonic, and transonic flow; to name but a few. The resulting flow phenomena in the impeller passage are illustrated in Figure 2.4. Despite the clear distinction of flow phenomena in the figure, in practice it is difficult to separate the individual features. The narrow channels from hub to shroud induce more of a fully-developed turbulent flow instead of a free-stream flow with hub and shroud boundary layers. Also, with the long flow length from inlet to outlet, relatively thick boundary layers are developed, leading to significant secondary flows (*Cumpsty*, 2004, p. 356; *Johnston*, 1974, p. 214).

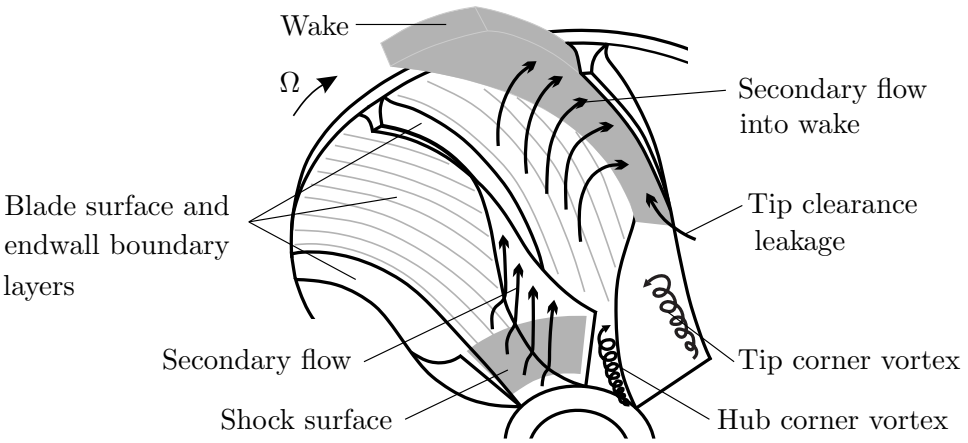

Figure 2.4: Overview of the flow phenomena in a backswept radial impeller. Based on *Lakshminarayana* (1996, p. 12, Figure 1.16).

The analysis of secondary flow has historically been treated inviscidly. The equations for the generation of streamwise vorticity ω_s in stationary passages were derived by *Hawthorne* (1951) and, for rotating systems, by *Smith* (1957). For complex geometries

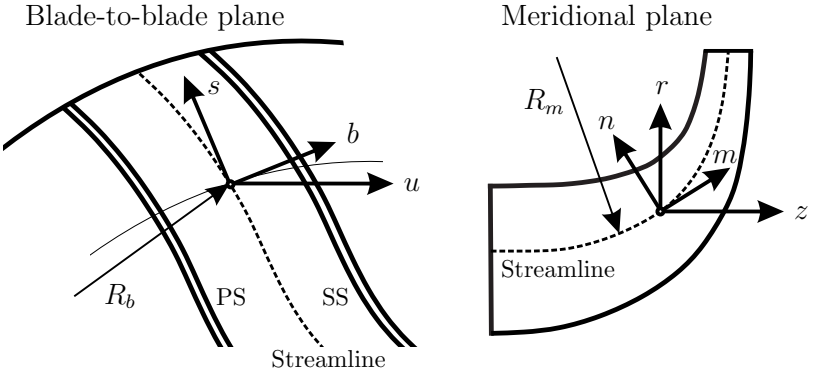

Figure 2.5: Curvilinear metric dimensions (b, s, n) in the directions of a body-fitted coordinate system for a fluid particle on a relative streamline. The cylindrical coordinate system (r, φ, z) is also depicted. Based on *Hehn* (2018, p. 17, Figure 2.8).

such as a radial impeller, however, these equations cannot be solved analytically and serve a predominantly qualitative purpose. The analysis is carried out in the relative frame and secondary circulation is measured by the *absolute* vorticity[3]. The detailed derivation of the equation for the streamwise vorticity generation along a general relative streamline is given in Appendix A.1. The final expression for the s direction reads

$$\frac{\partial}{\partial s}\left(\frac{\omega_s}{w}\right) = \frac{2}{\rho w^2}\Big[\underbrace{\frac{1}{R}\nabla p^*}_{\text{curvature}} + \underbrace{\frac{\Omega}{w}\nabla p^*}_{\text{rotation}}\Big], \tag{2.29}$$

where $p^* = p + \frac{1}{2}\rho w^2 - \frac{1}{2}\rho u^2$ is the rotary stagnation pressure, which is conserved along a relative streamline in an inviscid flow. The first term on the right-hand side of (2.29) corresponds to the curvature effect on secondary flow, and the second one, to the rotation effect. For a radial impeller, the s-components of the gradients in (2.29) are projected into the coordinate system from Figure 2.5, yielding

$$\frac{\partial}{\partial s}\left(\frac{\omega_s}{w}\right) = \frac{2}{\rho w^2}\Big[\underbrace{\frac{1}{R_m}\frac{\partial p^*}{\partial b}}_{\substack{\text{Blade surface}\\ \text{vortex}}} + \underbrace{\frac{1}{R_b}\frac{\partial p^*}{\partial n}}_{\substack{\text{Passage}\\ \text{vortex}}} + \underbrace{\frac{\Omega}{w}\frac{\partial p^*}{\partial z}}_{\substack{\text{Coriolis}\\ \text{vortex}}}\Big], \tag{2.30}$$

where R_m is the radius of curvature of the streamline in the meridional plane; R_b is the radius of curvature in blade-to-blade plane; and z corresponds to the axis of rotation.

From (2.30), it is demonstrated that the growth of the streamwise component of the vorticity is related to the gradients of rotary stagnation pressure. The first term on the right-hand side of (2.30) corresponds to the *blade surface vortex*, which will develop in the axial-to-radial bend of the impeller due to the meridional curvature. The second vortex contribution in (2.30) is called *passage vortex* and will be higher for low blade curvatures. The third term in (2.30) is the *Coriolis vortex*, which will become stronger

[3]It is the absolute vorticity, and not the relative one, that is convected by the relative flow. This is demonstrated by introducing $\vec{\omega} = \vec{\omega}_{rel} + 2\vec{\Omega}$ into the relative vorticity equation $\vec{w} \cdot \nabla\vec{\omega}_{rel} = ([\vec{\omega}_{rel} + 2\vec{\Omega}] \cdot \nabla)\vec{w}$, which yields $\vec{w} \cdot \nabla\vec{\omega} = \vec{\omega} \cdot \nabla\vec{w}$ (*Greitzer et al.*, 2004, p. 472, 473).

towards the exit due to increasing radius. The overall effect of these three types of vortices is the accumulation of low-energy fluid from the hub-pressure side corner to the shroud-suction side corner of the impeller, contributing to the magnitude of the wake (see Figure 2.4). In unshrouded impellers, this flow structure is modified to some extent by the presence of tip leakage flow, which produces a *tip leakage vortex* in the opposite direction from that of the outer branch of the passage vortex. As already mentioned, the analysis with (2.30) must remain of qualitative nature due to the complexity of the flow processes inside the impeller. (2.30) helps identify the driving forces generating the streamwise vorticity and thus the three-dimensional impeller flow profile.

Curvature and rotation also influence the stability of the boundary layers in the impeller passage. Figure 2.6a shows four different simple boundary layer flows to illustrate the effects of wall curvature and system rotation on the stability of the turbulent flow field. Turbulence production refers to the formation of irregular and turbulent fluctuations via the energy extraction from the mean flow by small perturbations. This is quantified by the Reynolds stress production tensor, which in cylindrical coordinates is given as

$$P = -\overline{c_i c_j}\left(\frac{\partial c}{\partial r} - \frac{c}{R}\right). \tag{2.31}$$

In (2.31), $\overline{c_i c_j}$ is the Reynolds shear stress, $\partial c/\partial r$ represents the mean shear effect, and c/R, the curvature effect (*Durbin and Pettersson Reif*, 2011, p. 173). On the convex wall from Figure 2.6a, because the velocity increases in the radial direction, it holds that $\partial c/\partial r > 0$. In this case, the two terms on the right-hand side of (2.31) have opposite sign and, generally, the mean shear production is greater than the curvature effect, leading to $P < 0$. This means that there is a decrease in turbulence energy levels or a turbulence suppression, i.e., a stabilizing effect. Contrarily, on the concave wall from Figure 2.6a, the velocity increases towards the center of curvature, thus $\partial c/\partial r < 0$. The two terms on the right-hand side of (2.31) now have the same sign, so that curvature supplements the production by the mean shear and turbulence is amplified due to $P > 0$. As for system rotation, turbulence is usually suppressed if the rotation vector and the vorticity

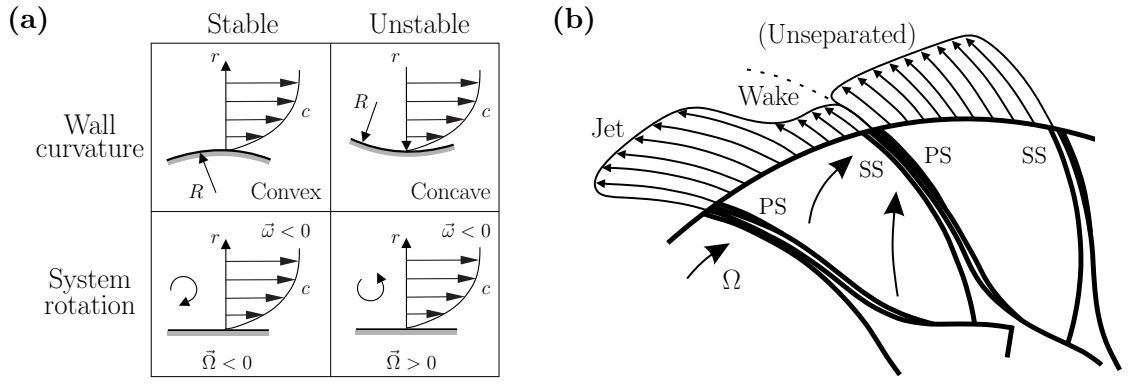

Figure 2.6: (a) Conditions for the stability of curved and rotating wall boundary layers. Based on *Johnston and Eide* (1976, p. 376, Figure 2). **(b)** Representation of the jet-wake structure at impeller outlet and comparison with an unseparated circumferential velocity distribution. Based on *Van den Braembussche* (2019, p. 94, Figure 3.39).

vector are parallel (same sign, $\Omega < 0$), and enhanced if they are antiparallel (opposite sign, $\Omega > 0$). In some cases, the stabilizing effect becomes large enough to suppress turbulence completely and the flow becomes laminar, which will easily separate under the influence of an adverse pressure gradient. Once the flow is separated, two different regions can be identified: a high energetic jet, with a high relative velocity; and a low energetic wake, i.e., the separated region (see Figure 2.6b). This *jet-wake* structure is substantially influenced by secondary flows. The three pressure gradients from (2.30) act together to determine the ultimate location of any low momentum fluid from the boundary layers feeding the wake. This wake has a much higher rate of shear than the boundary layers, and its extent in the impeller passage depends on the operating condition in the performance map.

As a conclusion, for a complex turbulent shear layer as in a radial impeller, the fluid is subject to a rate of shear not only in the close vicinity of the walls, but for the most part of the flow passage due to the close coupling between the three-dimensional boundary layers and eventually separated zones. For an adiabatic flow with no heat transfer, this shear is directly related to the entropy production in the channel by

$$T\frac{Ds}{Dt} = \frac{1}{\rho}\frac{\partial}{\partial x_j}\left(\tau_{ij}c_i\right). \tag{2.32}$$

2.3 Quasi-Three-Dimensional Flow Approximation

The computational techniques available to solve the equations of motion governing the turbulent flow through a turbomachine can be classified according to their level of sophistication. From lower to higher fidelity and accuracy, these are: (1) panel methods, (2) quasi-three-dimensional methods, and (3) solution of the exact equations. The latter include potential flow methods, Euler methods, Reynolds-averaged Navier-Stokes (RANS) methods, Large Eddy Simulations, and Direct Numerical Simulations. The required computing time increases with the level of accuracy.

The flow in radial turbomachinery is highly complex, so high-fidelity computing methods that solve the exact Navier-Stokes equations are best suited to resolving the highly involved flow phenomena that occur. These methods are referred to as Computational Fluid Dynamics (CFD) methods. Nevertheless, in preliminary design phases of turbomachinery, where faster solutions are required to iterate possible designs, lower-level tools with low computing times are necessary. For that, analytical solutions for *nearly* three-dimensional configurations are available, in the sense that one assumes that the variation of one velocity component is less important than the variations of the other two. In this way, elimination of one independent variable simplifies the equations considerably.

With this intermediate level of approximation, a Quasi-Three-Dimensional (Q3D) flow solution can be established, which consists in the description of the flow as a succession of interacting families of two-dimensional flows along intersecting surfaces—a concept originally presented by *Wu* (1952). These surfaces can be treated as *stream surfaces*,

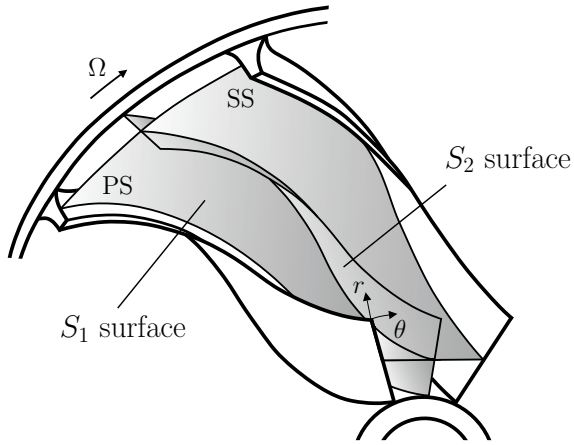

Figure 2.7: Intersecting S_1 and S_2 surfaces for the quasi-three-dimensional (Q3D) approximation of the flow in a backswept impeller. The S_1 surface is of blade-to-blade type, and the S_2, of hub-to-shroud type. Based on *Whitfield and Baines* (1990, p. 265, Figure 8.2).

which are surfaces everywhere tangent to an iteratively computed velocity vector, so that no cross-flow is allowed. This corresponds to the aforementioned step of neglecting the variation of one of the velocity components. In this case, it is the outward-pointing component to the surface.

For a rotating turbomachinery component, because the boundary walls are surfaces of revolution, it is convenient to use a relative cylindrical coordinate system (r, φ, z). Two families of surfaces are then defined for the Q3D solution (see Figure 2.7): the S_1 family, which is of blade-to-blade type, and the S_2 family, which is of hub-to-shroud type. In the case of steady flow, such a representation with two families of surfaces is equivalent to a complete three-dimensional description and no additional spatial approximations are required—for a time-dependent flow solution, three families would be necessary (*Hirsch*, 1984, p. 3). The flow solution on one family of surfaces provides the boundary conditions for the calculation on the other family of surfaces, which leads to an iterative solution procedure. The Q3D *approximation* then refers to considering a finite number of surfaces from each family—generally one single S_2 surface and several S_1 surfaces—, and keeping the three-dimensional character of the flow through the interdependence of the boundary conditions.

A simplifying assumption of the Q3D method is that the S_1 surfaces are surfaces of revolution, i.e., that the flow remains on geometrically axisymmetric surfaces as it passes through the machine. However, secondary flows are generated in a real turbomachinery flow (see Sec. 2.2). These distort the geometry of the S_1 stream surfaces with respect to the axisymmetric geometry of a surface of revolution, leading to a transfer of fluid particles and their associated mass, momentum, and energy between S_1 surfaces—especially energy and losses. Furthermore, the turbulent nature of the flow also results in random collisions between fluid particles of different S_1 stream surfaces. This process of spanwise redistribution of flow properties is called *spanwise mixing*.

2.3.1 Throughflow Solution on the Mean S2 Stream Surface

The Q3D iterative calculation, with the coupling of the solutions on the S_1 and S_2 surfaces, is recognized to be a highly unstable process (*Lakshminarayana*, 1996, p. 298). Nowadays, with the available computer resources, this calculation is generally replaced by fully 3D Navier-Stokes solvers. Still, the uncoupled solutions on each of the surfaces are extensively used in the design cycle of turbomachines. In the case of the S_2 surfaces, the flow is usually computed on the mean stream surface, S_{2m}, whose solution is called *throughflow*. This solution provides spanwise distributions of the flow quantities both at inlet and exit of the blade rows, and also inside the blades in the case of radial turbomachines, where strong curvature effects have to be taken into account. As for the S_1 surfaces, the blade-to-blade solution serves to define the blade shape in detail.

The mean S_2 stream surface (S_{2m}) is defined as an S_2 surface that has approximately the shape of the blade's mean camber surface and that generally lies halfway between the two blades. However, different representations of this surface have been established depending on the method to eliminate the partial derivative terms $\partial/\partial\theta$ in the 3D equations. These methods are: the *stream surface approach* and the *passage averaging approach*. The stream surface approach, originally proposed by *Wu* (1952), iteratively determines the shape of the stream surfaces, which means that the S_{2m} surface does not necessarily coincide with the mean camber surface. The passage averaging approach, developed by *Hirsch and Warzee* (1976, 1979), defines the representative S_2 surface as a mathematically devised surface on which the flow properties are a true circumferential average between the two blades, so that this surface can actually be highly deformed.

For the passage averaging approach, a density-weighted average of the flow equations is generally used, with the aim to account for compressibility effects. As such, the density-average of an arbitrary variable A is defined as $\tilde{A} = \overline{\rho A}/\overline{\rho}$, where the overbar $\overline{\square}$ refers to an algebraic averaging

$$\overline{\square} = \frac{1}{\theta_{SS} - \theta_{PS}} \int_{\theta_{PS}}^{\theta_{SS}} \square d\theta, \tag{2.33}$$

and $\theta_{SS} - \theta_{PS}$ denotes the integration region between the pressure and suction surfaces (see Figure 2.7 for reference). This circumferential extension can be expressed in terms of a blade blockage factor b, giving $\theta_{SS} - \theta_{PS} = \frac{2\pi}{Z}\left(1 - \frac{t}{s}\right) = \frac{2\pi b}{Z}$, where t is the blade thickness; s, the pitch; and Z, the number of blades. Finally, the density-average of the arbitrary variable $\tilde{A}$ is

$$\tilde{A} = \frac{\overline{\rho A}}{\overline{\rho}} = \frac{1}{\overline{\rho}\frac{2\pi b}{Z}} \int_{\theta_{PS}}^{\theta_{SS}} \rho A d\theta. \tag{2.34}$$

By way of example, the steady continuity equation in cylindrical coordinates is taken as

$$\frac{1}{r}\frac{\partial}{\partial r}\rho r w_r + \frac{1}{r}\frac{\partial}{\partial \varphi}\rho w_\varphi + \frac{\partial}{\partial z}\rho w_z = 0, \tag{2.35}$$

and application of the averaging from (2.34), together with neglecting $\partial/\partial\varphi$, gives

$$\frac{\partial}{\partial r}(r b \overline{\rho} \tilde{w}_r) + \frac{\partial}{\partial z}(r b \overline{\rho} \tilde{w}_z) = 0. \tag{2.36}$$

The same procedure is carried out for the radial component of the momentum equation in the relative system, yielding

$$\begin{aligned}\frac{1}{rb}\frac{\partial}{\partial r}(rb\overline{\rho w_r w_r}) + \frac{1}{b}\frac{\partial}{\partial z}(b\overline{\rho w_r w_z}) - \frac{\overline{\rho w_u w_u}}{r} - \overline{\rho}\Omega^2 r - 2\Omega\overline{\rho w_u} \\ = -\frac{\partial \overline{p}}{\partial r} - \frac{1}{b}\frac{\partial b}{\partial r}\left(\overline{p} - \frac{p_{ss}+p_{ps}}{2}\right) + F_{b,r} + \overline{F}_{f,r},\end{aligned} \tag{2.37}$$

where $F_{b,r}$ is the component of the blade force in the radial direction and $\overline{F}_{f,r}$ denotes the dissipative forces. The algebraic average of the products of density and velocities in (2.37) can be transformed by defining the relationship $A = \tilde{A} + A'$ for an arbitrary variable A. In this case, A is the sum of its density-weighted mean value $\tilde{A}$ and a fluctuating term A' with respect to this density-averaged value—similar to the decomposition of variables in turbulent flow. With that, $\overline{\rho A'} = 0$ holds, leading to, for the term $\overline{\rho w_r w_z}$, for example

$$\overline{\rho w_r w_z} = \overline{\rho}\overline{(\tilde{w}_r + w_r')(\tilde{w}_z + w_z')} = \overline{\rho}\tilde{w}_r\tilde{w}_z + \cancelto{0}{\overline{\rho\tilde{w}_r w_z'}} + \cancelto{0}{\overline{\rho w_r'\tilde{w}_z}} + \overline{\rho w_r' w_z'}, \tag{2.38}$$

and equivalently for the other terms in (2.37). The nonconservative form of (2.37) is obtained by expanding the terms with (2.38) and subtracting the continuity equation (2.36) multiplied by $\tilde{w}_r$, yielding

$$\overline{\rho}\tilde{w}_r\frac{\partial \tilde{w}_r}{\partial r} + \overline{\rho}\tilde{w}_z\frac{\partial \tilde{w}_r}{\partial z} - \frac{\overline{\rho}\tilde{w}_u\tilde{w}_u}{r} - \overline{\rho}\Omega^2 r - 2\Omega\overline{\rho}\tilde{w}_u = -\frac{\partial \overline{p}}{\partial r} + F_{b,r} + \overline{F}_{f,r} - \sum_{i=1}^{4} G_i, \tag{2.39}$$

where G_i are the fluctuation terms due to the blade-to-blade variation of flow properties and are summarized as

$$\begin{aligned} G_1 &= \frac{1}{rb}\frac{\partial}{\partial r}(rb\overline{\rho w_r' w_r'}), & G_3 &= -\frac{1}{r}\overline{\rho w_u' w_u'}, \\ G_2 &= \frac{1}{rb}\frac{\partial}{\partial z}(rb\overline{\rho w_r' w_z'}), & G_4 &= \frac{1}{b}\frac{\partial b}{\partial r}\left(\overline{p} - \frac{p_{ss}+p_{ps}}{2}\right). \end{aligned} \tag{2.40}$$

(2.39) and (2.40) show that the density-weighted passage averaging method introduces additional interaction terms, $\overline{\rho w_r' w_z'}$, which have the same structure as the turbulent Reynolds stresses but originate from the nonaxisymmetry of the flow and, therefore, describe the three-dimensional effects on the average flow. These interaction terms still have to be evaluated from the solution on the S_1 surfaces (*Lakshminarayana*, 1996, p. 297), so that the present hub-to-shroud method is actually not uncoupled from the blade-to-blade calculation.

The equations of the stream function approach are similar to the ones from the density-weighted average approach, (2.39), except for the fluctuation terms G_i (2.40). For convenience, since the passage-averaged S_2 surface is an imaginary surface that cannot be identified geometrically, most throughflow methods combine both approaches in that they perform the calculation on the geometrical S_{2m} surface and assume circum-

ferentially averaged flow. However, this is not exactly correct, mainly because of these fluctuation terms. In axial turbomachines, it is common to apply a duct flow throughflow method in which there are only calculating stations at the leading and trailing edges of the blade rows, which leads to $G_i = 0$ in (2.39) because the nonaxisymmetric blade effects are not taken into account. However, for transonic cases and radial machines, intra-blade calculating stations are needed in order to consider the Mach number and the strong curvature effects inside the blades, respectively. In this way, the nonaxisymmetric effects have to be included, thus making the thoughflow calculation, coupled with the S_1 solution, more difficult to handle.

Alternative to the explicit evaluation of the interaction terms from the S_1 calculation, an aerodynamic blockage factor can be introduced instead, which includes all the nonaxisymmetries arising from the blade and substitutes the interaction terms (2.40). This can be helpful when an uncoupled S_{2m} calculation is to be performed. The way to obtain this blockage factor in the equations is to perform a momentum averaging instead of a density-weighted one. In this case, the new aerodynamic blockage factor is additional to the geometrical tangential blockage factor b arising from the passage averaging. A momentum averaging leads to mass-averaged variables, which is also advantageous in terms of validation of throughflow results with experimental data (*Hirsch and Dring*, 1985, p. iii), because relevant flow quantities such as total pressure and temperature are generally mass-averaged in the measurements.

The momentum-averaged equations are similar to the density-averaged ones, except for additional fluctuation terms. *Hirsch and Dring* (1985) presented the momentum-averaged formulation of the governing equations—the momentum equation however in the absolute reference system for the sake of simplicity—and they defined the aerodynamic blockage factor by means of a ratio between averaged velocity components, including both density- and momentum-averaged contributions. For example, for the axial component of the absolute velocity, they established

$$\hat{c}_z = \frac{\overline{\rho c_z c_z}}{\rho \tilde{c}_z} = \frac{\overline{\rho c_z c_m}}{\tilde{\rho} \tilde{c}_m} = k^{-1} \tilde{c}_z, \tag{2.41}$$

where the operator $\hat{\square}$ stands for the momentum averaging, $\overline{\square}$ indicates an algebraic averaging, and $\tilde{\square}$ refers to the previous density-weighted averaging, which reduces to an algebraic area averaging in incompressible flow. A similar relationship to (2.41) is established for the other velocity components, with a unified aerodynamic blockage factor k. The introduction of this aerodynamic blockage factor in the continuity equation, also in the absolute reference frame, looks like

$$\frac{\partial}{\partial r}(rkb\overline{\rho}\hat{c}_r) + \frac{\partial}{\partial z}(rkb\overline{\rho}\hat{c}_z) = 0, \tag{2.42}$$

which is equivalent to the density-weighted averaged continuity equation (2.36) except for the fact that now, in (2.42), there is a global blockage factor kb accounting for both the nonaxisymmetry of the flow and the geometrical blockage from the blade.

2.3.2 Numerical Methods for the Throughflow Solution

The numerical methods available for the solution of the equations on the S_{2m} surface can be classified into two families. The first family is based on the introduction of a mean stream function ψ, derived from the continuity equation, (2.36), as

$$\begin{aligned} \frac{\partial \psi}{\partial r} &= rb\overline{\rho}\tilde{w}_z, \\ \frac{\partial \psi}{\partial z} &= -rb\overline{\rho}\tilde{w}_r. \end{aligned} \tag{2.43}$$

Insertion of (2.43) in the passage-averaged radial momentum equation, (2.39), yields a nonlinear second-order partial differential equation for the stream function with the terms $\partial^2\psi/\partial r^2$ and $\partial^2\psi/\partial z^2$ on the left-hand side of the equation. Finite differences are used to discretize this equation for the nodes (i, j) of the grid (see Figure 2.8a), resulting in a set of equations for the neighboring nodes that can be rearranged in matrix form as $[A]\{\psi\} = \{B\}$, which gives the name *matrix method* to this technique. This system of nonlinear equations is generally solved by means of iterative relaxation methods. The matrix $[A]$ generally remains fixed for a given geometry and the vector $\{B\}$ contains the nonaxisymmetric nonlinear blade terms and compressibility effects. The new solution for ψ serves to update the vector $\{B\}$ at each iteration and also to calculate the corresponding velocities from the stream function definition, (2.43). Once convergence is reached, the final distributions of fluid properties and velocities are used to build the streamlines in the flow passage. The second family of throughflow methods is based on the solution of the momentum and continuity equations for the physical variables in streamline coordinates, therefore the name *streamline curvature method*. The momentum equation is written for the meridional velocity and is solved along fixed quasi-orthogonals, which are calculating stations that are roughly normal to the streamlines (see Figure 2.8b). The meridional grid consists of these quasi-orthogonals and the streamlines of the circumferentially averaged flow, and is not fixed but changes with the iterations as the position of the streamlines also changes.

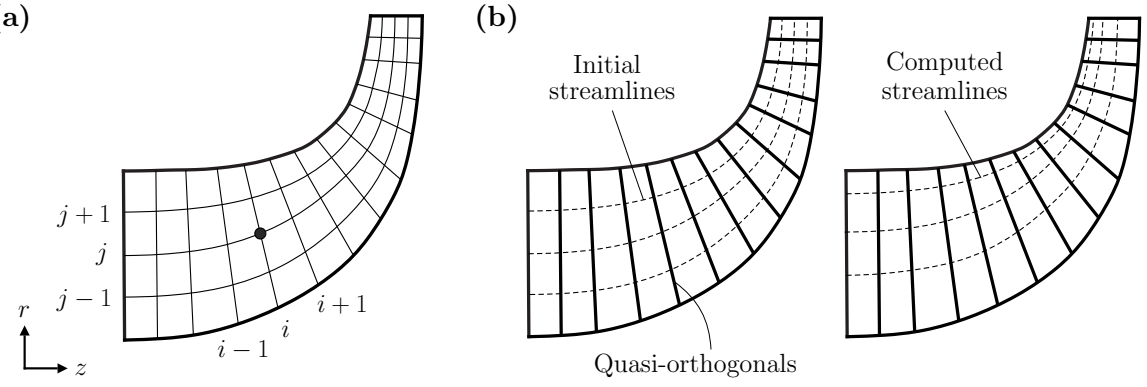

Figure 2.8: **(a)** Fixed curvilinear grid for the matrix method. **(b)** Changing curvilinear grid for the streamline curvature method: the quasi-orthogonals remain fixed, but the position of the meridional streamlines changes along the iterations. Based on *Katsanis* (1964, p. 4, Figure 3 and p. 10, Figure 7).

In principle, both matrix and streamline curvature methods solve the same equations, but the matrix method deals with a single equation, which is a coupling between the continuity and momentum equations through a stream function, while the streamline curvature method solves the two equations of continuity and momentum separately and iteratively. Generally, solving a single equation can be advantageous, but the matrix method itself encounters some difficulties in dealing with transonic and mixed flows: in this case, there exist two possible velocity distributions for each stream function value, and there is a priori no way to know which one to choose. In addition, for subsonic flow, the second-order partial differential equation is of elliptic nature, and for supersonic flow, of hyperbolic nature, meaning that different differentiation schemes need to be used. As for the streamline curvature method, the calculation with prescribed mass flow rate is not possible for choked or nearly choked flows, but these difficulties are more easily addressed than the ones from the matrix method in such flow conditions. For this reason, the streamline curvature is generally the choice for supersonic flow calculations.

The streamline curvature method solves the momentum equation for the meridional velocity. For simplicity, since $w_m = c_m$, this equation is usually written in the stationary frame of reference instead of the relative one. Recalling the rotating passage-averaged radial momentum equation, (2.39), the accelerations acting on a fluid particle are $\left(\tilde{w}_r \frac{\partial \tilde{w}_r}{\partial r} + \tilde{w}_z \frac{\partial \tilde{w}_r}{\partial z}\right)$ and $-\frac{\tilde{w}_u^2}{r}$, if the Coriolis and centrifugal accelerations are neglected due to the absolute frame of reference. These accelerations are now transformed for the meridional velocity and meridional plane shown in Figure 2.9. Since the meridional direction lies at an angle ε with respect to the axial direction, it holds that $\frac{\partial}{\partial m} = \sin\varepsilon \frac{\partial}{\partial r} + \cos\varepsilon \frac{\partial}{\partial z}$. Similarly, the relations $w_r = w_m \sin\varepsilon$ and $w_z = w_m \cos\varepsilon$ also hold. This leads to $w_m \frac{\partial}{\partial m} = w_r \frac{\partial}{\partial r} + w_z \frac{\partial}{\partial z}$, which resembles the streamwise acceleration term from (2.39), but now for the meridional velocity in the absolute reference frame it is $c_m \frac{\partial c_m}{\partial m}$. The acceleration $-\frac{\tilde{w}_u^2}{r}$ from (2.39) is now rewritten as $-\frac{c_u^2}{r}$, and because of the streamline coordinates, an additional centripetal acceleration term $\frac{c_m^2}{R_m}$ needs to be balanced. These three accelerations are illustrated in Figure 2.9. Accordingly, the momentum equation along the q-direction (quasi-orthogonal) reads

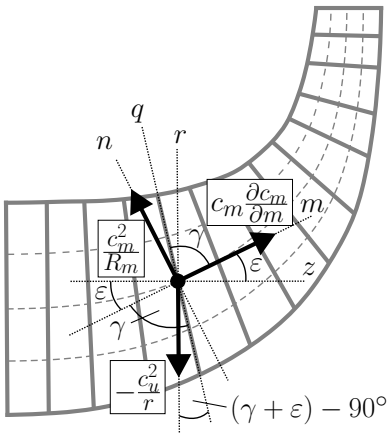

Figure 2.9: Balance of accelerations acting on a fluid particle at a particular grid point in a streamline curvature method. Based on *Casey and Robinson* (2021, p. 485, Figure 15.2) and *Cumpsty* (2004, p. 107, Figure 3.6a).

$$\frac{c_m^2}{R_m}\sin\gamma + c_m\frac{\partial c_m}{\partial m}\cos\gamma - \frac{c_u^2}{r}\sin(\gamma+\varepsilon) = -\frac{1}{\rho}\frac{dp}{dq} + F_q, \tag{2.44}$$

where

$$F_q = F_n\sin\gamma + F_m\cos\gamma = F_u\tan\gamma = \frac{c_m}{r}\frac{\partial(rc_u)}{\partial m}\tan\gamma \tag{2.45}$$

and $F_u = \frac{c_m}{r}\frac{\partial(rc_u)}{\partial m}$ is the momentum equation in the circumferential direction. The quasi-orthogonal equilibrium equation (2.44) can be solved for either the pressure gradient or for the meridional velocity gradient along the quasi-orthogonal direction. For the latter, the solution depends on the previous iteration and thus on the discretization of the grid. For the former, the previous iteration is not required but considers the current geometry of the S_{2m} surface to account for possible singularities. The equation for the meridional velocity gradient is derived from (2.44) in Appendix A.2, yielding

$$c_m\frac{dc_m}{dq} = \underbrace{\frac{dh_t}{dq} - T\frac{ds}{dq}}_{①}\underbrace{-\frac{1}{2r^2}\frac{d(r^2c_u^2)}{dq}}_{②} + \underbrace{\frac{c_m^2}{R_m}\sin\gamma}_{③} + \underbrace{c_m\frac{\partial c_m}{\partial m}\cos\gamma}_{④} - \underbrace{\frac{c_m}{r}\frac{\partial(rc_u)}{\partial m}\tan\gamma}_{⑤}, \tag{2.46}$$

where ① and ② are the quasi-orthogonal equilibrium terms, ③ is the projection of the acceleration due to streamline curvature onto the q-direction, ④ is the projection of the streamwise acceleration onto the q-direction, and ⑤ is the body force term. The computational procedure consists in going forward in the meridional direction and obtaining the distribution of meridional velocity along each quasi-orthogonal (stations i in Figure 2.8). This is achieved by solving (2.46) for each streamline position crossing the quasi-orthogonal (stations j in Figure 2.8). The solution of this differential equation comes with a constant of integration, which is then evaluated by solving the continuity equation in integral form

$$\dot{m} = 2\pi\int_{hub}^{shroud} k\rho c_m r\sin\gamma dq, \tag{2.47}$$

from hub to shroud along the q-direction. Since all the mass flow $\dot{m}$ crosses a quasi-orthogonal, it is assumed that the integration in one direction, the q-direction, is sufficient to define the total mass flow through the annulus at any given calculating station i. In (2.47), k is the aerodynamic blockage factor already presented in (2.42). The resulting distribution of meridional velocity along the quasi-orthogonals obtained from solving (2.46) and (2.47) then determines the position of the streamlines. The calculation of the streamline slopes and curvatures is critical for the convergence of the problem, because the streamline curvature κ of a parametric curve $\vec{r}(t=m) = [z(m), r(m)]$

$$\kappa(t) = \frac{\frac{dz}{dt}\frac{d^2r}{dt^2} - \frac{dr}{dt}\frac{d^2z}{dt^2}}{\left[\left(\frac{dz}{dt}\right)^2 + \left(\frac{dr}{dt}\right)^2\right]^{3/2}} \quad\rightarrow\quad \kappa(m) = \frac{dz}{dm}\frac{d^2r}{dm^2} - \frac{dr}{dm}\frac{d^2z}{dm^2} = \frac{1}{R_m} \tag{2.48}$$

depends on the first- and second-order spatial derivatives along the streamline, and any degree of displacement between the streamlines can create discrepancies in these derivatives and cause stability problems. In order to mitigate these effects and reach convergence, relaxation factors must be used, which become very small when the quasi-orthogonals are closely spaced. This is the reason why the method uses a coarse grid as pictured in Figure 2.8b.

The throughflow calculation with the streamline curvature method can be performed in either *design mode* or *analysis mode*. This refers to the way in which boundary conditions are set to aid the numerical solution of the main equation, (2.46). Boundary conditions are needed because (2.46) is a nonlinear, inhomogeneous, first-order ordinary differential equation[4], for which analytical solutions are not available. The design mode calculates an appropriate geometry for a required aerodynamic input and the analysis mode provides the aerodynamic result for a known geometry. In the analysis mode, empirical correlations are generally used to include the friction losses in the Δs in (2.46). Correlations are also used to account for the effects of the blade nonaxisymmetries on the outflow conditions—recall that (2.46) does not include the interaction terms similar to (2.40). In summary, for a radial impeller, empirical models are incorporated for the loss coefficient, the aerodynamic blockage, and the slip factor.

For the impeller friction losses, an enthalpy-based loss coefficient Δq_{12}, (2.18), is usually prescribed. This value is computed as a linear summation of different contributions, which can vary depending on the author and their definition. Examples of loss terms include skin friction, blade loading, tip clearance, etc. To build a friction force, Δq_{12} is then generally transformed into an entropy increase Δs_{12} with (2.18)–(2.24).

As for the aerodynamic blockage, it refers to the reduction in effective flow area due to local velocity defects found in boundary layers, wakes, and tip clearance vortices, and was already introduced in (2.42) and (2.47). By means of the continuity equation, $\dot{m} = \rho k A c_m$, where A is the annular cross-sectional area at a specific meridional position, it can be established that for a case without blockage, $k = 1$. Contrarily, if there is flow blockage, $k < 1$ applies, meaning that there is a reduced area available to the flow. This causes an increase in meridional velocity for the same mass flow rate, which is translated into a reduced pressure rise capability of the machine. The aerodynamic blockage factor is defined as $k = 1 - B$, where B stands for the aerodynamic blockage itself

$$B = 1 - \frac{A_{eff}}{A_{geom}}. \tag{2.49}$$

The challenge arises in the calculation of the effective area A_{eff} in (2.49). In axial turbomachinery, this area can generally be obtained via the boundary layer thickness, but for a complex turbulent shear layer as in radial impellers, this approach is not

[4]The nature of (2.46) can be analyzed by rearranging it in terms of the unknown variable c_m as $c_m \frac{dc_m}{dq} - \left[\frac{\sin\psi}{r_c}\right] c_m^2 - \left[\frac{\partial c_m}{\partial m}\cos\psi - \frac{1}{r}\frac{\partial (r c_u)}{\partial m}\tan\psi\right] c_m = \frac{dh_t}{dq} - T\frac{ds}{dq} - \frac{1}{2r^2}\frac{d(r c_u)^2}{dq}$, so that it becomes a function of a single independent variable q. This form of the equation includes the first derivative of the unknown variable c_m, so that it is a first-order ordinary differential equation (ODE). Because c_m multiplies the derivative dc_m/dq, it is also nonlinear. In addition, since the right-hand side is not equal to zero, it is also inhomogeneous.

really possible since the edge of the boundary layer is not clearly defined. In this case, an alternative is to obtain the blockage as a measure of the nonaxisymmetry of the flow, which includes all secondary flow-related effects. This approach aligns with the definition from *Hirsch and Dring* (1985) in (2.41) with the momentum-averaging of the equations, and is also supported by *Casey and Robinson* (2021, p. 157). By considering that the nonaxisymmetry causes a significant difference between circumferential mass- and area-averages at any radial position, (2.49) becomes

$$B = 1 - \frac{A_{eff}}{A_{geom}} = 1 - \frac{\overline{c}_m^{area}}{\overline{c}_m^{mass}}, \tag{2.50}$$

where $\overline{c}_m^{area}$ and $\overline{c}_m^{mass}$ are the area-averaged and mass-averaged meridional velocities, respectively. The mass-averaged velocity should therefore always be greater than the area-averaged one to ensure $B > 0$.

The nonaxisymmetry of the flow at impeller discharge and the rotation also affect the work input coefficient, (2.7), which for impellers with no inlet swirl ($c_{u1} = 0$) reads $\lambda = c_{u2}/u_2$. Generally, the flow does not leave the impeller in the same direction as the blades are pointing but, instead, there is a component of relative velocity in the opposite direction to the rotation, known as slip velocity, which reduces the attainable circumferential velocity c_{u2} at impeller outlet and, therefore, the work input. This slip phenomenon also translates into a difference in relative flow angle at impeller outlet (see Figure 2.10). This difference is analogous to the deviation angle in axial blades and is caused by both inviscid and viscous effects, although the primary cause is of inviscid nature: the force required to make the flow follow the blades comes from the blade-to-blade loading, which in the outer radial part of a radial impeller, it mainly originates from the Coriolis acceleration, so that the pressure gradient in the circumferential direction is $dp/du = -2\rho\Omega r w_r$, where du corresponds to $rd\theta$. At the trailing edge, this pressure difference must be zero to satisfy the Kutta-Joukowsky condition. This enforces a gradual reduction of the pressure difference from a point upstream of the trailing edge. With the blade force being reduced, the flow can no longer follow the blade direction and it becomes inclined backwards in the direction opposite to rotation, giving rise to the slip. The distance upstream of the trailing edge at which unloading starts is largely

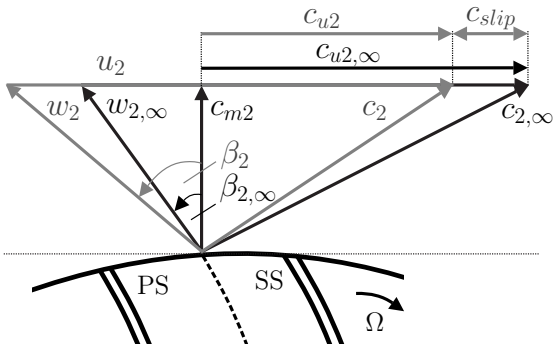

Figure 2.10: Effect of slip on the velocity triangle at the exit of a backswept impeller. The conditions for an ideal flow following the blades (∞) are depicted in black, and the actual conditions with slip are shown in dark gray.

influenced by the outlet passage width and the number of blades. There are also viscous effects which may contribute to slip, but to a lesser degree (*Senoo et al.*, 1974). The aerodynamic blockage accumulated at impeller outlet—the wake—can cause the flow to deflect further towards the pressure side, i.e., contrary to rotation (see Figure 2.10), and generate additional slip. To quantify the slip, a slip factor σ is defined as

$$\sigma = 1 - \frac{c_{slip}}{u_2} = 1 - \frac{c_{u2,\infty} - c_{u2}}{u_2} < 1, \tag{2.51}$$

where c_{slip} is the slip velocity, $c_{u2,\infty}$ is the ideal tangential velocity following the blades, and c_{u2} is the actual tangential velocity.

2.4 Metamodeling and Machine Learning

In the context of a calibration between computer analysis codes of different levels of accuracy, one of the codes is generally approximated by means of *metamodels*. Metamodels are thus models of the original computer models. In a numerical context, unlike in experimental measurements, there is no random error, so the approximation of the true data points y is written as $y = f(\mathbf{x}) + \varepsilon$, where ε is the approximation error and $f(\mathbf{x})$ is the metamodel function, which is a function of $\mathbf{x}$, the vector of *variables* or *parameters*. This approximation of a model to given data is a regression problem.

Regression problems can also be solved under the paradigm of machine learning. The difference compared with a simple curve fitting procedure is that, in machine learning, the model is trained on training data and must also perform well on new, previously unseen data (test data). Machine learning algorithms comprise a large amount of techniques (*Brunton et al.*, 2020, p. 478, Figure 1), and regression is categorized as *supervised learning*. Supervised learning means that the training data points x have labels y. Contrarily, if the data points are unlabeled, the algorithms are categorized as *unsupervised learning*. Another category is *semisupervised learning*, where either limited labeled data is available or information from the environment is used (refer, for example, to *Vignon et al.* (2023) for further information).

2.4.1 Regression as an Optimization Problem

Regression involves adjusting a smooth model function $f(\mathbf{x})$ to the given data by tuning the parameters $\mathbf{x}$ with the objective of minimizing the difference between the true points and the values predicted by the model. Therefore, it is an optimization problem where an objective function $g(\mathbf{x})$ is minimized

$$\min_{\mathbf{x}\in\mathbb{R}^n} g(\mathbf{x}) = \min_{\mathbf{x}\in\mathbb{R}^n} \sum_{i=1}^{m} \left(y_i - f(x_i)\right)^2 . \tag{2.52}$$

The nature of $g(\mathbf{x})$ against the variables can include different types of critical points relevant to the optimization problem. These are the global minimum, (multiple) local

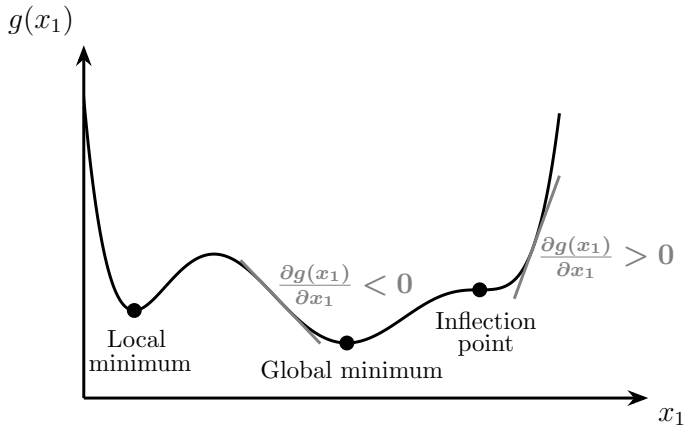

Figure 2.11: Example objective function g along a single variable x_1 to show the possible critical points, i.e., global minimum, local minima, and inflection points. The gradient of the function at two different locations is also depicted to illustrate the guided search of the global minimum by means of gradient computations. At all critical points, it holds $\partial g(x_1)/\partial x_1 = 0$. Based on *Kochenderfer and Wheeler* (2019, p. 8, Figure 1.6) and *Goodfellow et al.* (2016, p. 83, Figure 4.3).

minima, and inflection points (see Figure 2.11 for a single variable x_1 by way of example). In multiple n dimensions, the search for the global minimum can be guided with the gradient of the objective function with respect to the variables

$$\nabla g(\mathbf{x}) = \left[\frac{\partial g(\mathbf{x})}{\partial x_1}, \quad \frac{\partial g(\mathbf{x})}{\partial x_2}, \quad \ldots, \quad \frac{\partial g(\mathbf{x})}{\partial x_n}\right]^T, \tag{2.53}$$

where each component is the slope of the local tangent line (see Figure 2.11 for one dimension). These tangent lines form a local tangent hyperplane on which the vector $\nabla g(\mathbf{x})$ points in the direction of greatest increase. Second derivatives can also be used instead of the first if information about the local curvature of the function is relevant to the problem. The optimization methods that use the gradient information are referred to as gradient-based methods, and an overview is given in Figure 2.12. There are other optimization methods for continuous problems, namely gradient-free methods. Gradient-free methods are also known as zero-order methods, because they only use the function values $g(\mathbf{x})$ in the search for the optimum instead of the derivative information. Gradient-free methods can be categorized into local and global search algorithms (see Figure 2.12). Global search seeks the optimum inside an a priori defined search space or grid, and is therefore slower and more computationally demanding than local optimization. In turn, global search algorithms can be either population based or non-population based. In general, the choice of population-based algorithms comes from the need to improve the global grid search for high-dimensional grids, because the number of grid points to evaluate grows exponentially with an increasing number of arguments. What population-based methods, or *evolutionary algorithms*, do, is basically to refine the search based on biological evolution principles like mutation, recombination, and selection of the fittest, leading to a faster grid evaluation by discarding samples that do not meet the defined criteria. In principle, both gradient-based and gradient-free methods can be used in a regression problem. Gradient-based methods are more efficient in

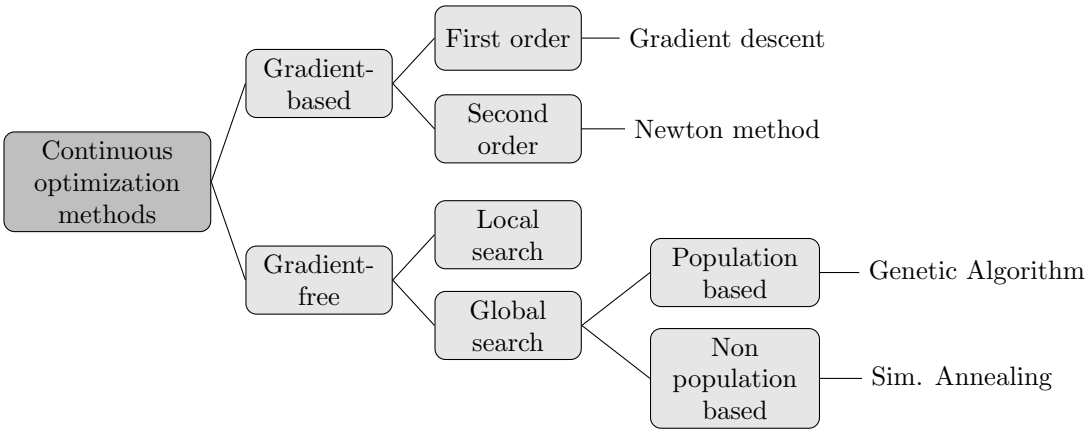

Figure 2.12: Overview of optimization methods for continuous problems, i.e., problems with formulation in terms of real variables and not discrete ones. The classification is done based on the use of gradient information for the search for the global minimum. Based on *Mendez* (2022, p. 5).

the search for the optimum, but gradient-free methods are advisable in cases where the design space is discontinuous or has multiple optima, and when the objective function is not directly known so that its derivatives cannot be computed efficiently (*Jasa*, 2021).

2.4.2 Overview of Metamodels for Regression

This section provides an overview of possible metamodels for a regression problem. The metamodels are designated hereinafter as $\hat{y}$, so that $y = \hat{y} + \varepsilon$. The simplest metamodeling technique is the use of (second-order) polynomial models—in this case known as Response Surface Methodology (RSM)—, because they are meant to be a Taylor series expansion of the unknown function

$$\hat{y} = a_0 + \sum_{i=1}^{K} a_i x_i + \sum_{i=1}^{K} a_{ii} x_i^2 + \sum\sum_{i<j=2}^{K} a_{ij} x_i x_j, \tag{2.54}$$

where K is the number of predictors. Higher polynomial orders could improve the approximation accuracy, yet with the risk of overfitting the problem and, therefore, of obtaining a poor generalization of the metamodel (*Forrester et al.*, 2008, p. 40). If increasing the order of the polynomial does not essentially improve the prediction, it may be because the function behaves differently in different parts of the range of x. The usual approach in this case consists in dividing the range into various segments and fit a function in each segment. This *piecewise polynomial fitting*, where each segment polynomial is called *spline function*, can also be extended to the case of multiple predictors. In the case of high dimensional data with more than two predictors, the regression function cannot be geometrically identified. *Additive models* are then used to represent the regression surface as a combination of a number of simple models. One additive technique that can be found in the literature is the Multivariate Adaptive Regression Splines (MARS) method by *Friedman* (1991), whose model is built with spline basis functions B_i as

$$\hat{y} = \sum_{i=1}^{K} a_i B_i(x_i), \tag{2.55}$$

where the number of basis functions and the knot locations to define the various segments are automatically determined by the data, making the algorithm an *adaptive* one. MARS models are continuous with continuous derivatives and can estimate nonlinear behavior and interactions between predictors. The final models can be rewritten in the form

$$\hat{y} = a_0 + \sum_{K=1} f_i(x_i) + \sum_{K=2} f_{ij}(x_i, x_j) + \sum_{K=3} f_{ijk}(x_i, x_j, x_k) + \ldots, \tag{2.56}$$

where the first sum accounts for all basis functions involving one predictor, the second considers the basis functions with two predictors and their interaction terms, and so on. In this way, the MARS approach is readily interpretable in a similar manner as the RSM technique, (2.54), but with a higher predictive accuracy and flexibility. Other approaches such as Kriging models can also be used as metamodels, which take an equation of the form

$$\hat{y} = f(x) + Z(x), \tag{2.57}$$

where $f(x)$ is a prescribed polynomial function, often taken as a constant, and $Z(x)$ is the correlation function. The choice of the correlation function determines the smoothness of the approximating surface, either providing an exact interpolation of the data or smoothing the data to some degree. An advantage of using a Kriging approach is that it can compute the uncertainties of the estimates and it provides a better performance than RSM (*Peter and Marcelet*, 2008). Actually, in order to use polynomials—as is the case, to some degree, of RSM, MARS, and Kriging—, the specific nature of the nonlinearity in the data must be known, because polynomials are actually an adaptation of linear models by manually adding extra terms, i.e., squared terms. In the case of inherently nonlinear models, the exact form of the nonlinearity does not need to be known explicitly or be specified prior to model training. Some inherently nonlinear models are support vector machines (SVMs), K-nearest neighbors (KNNs), tree-based models, and Artificial Neural Networks (ANNs). In the case of ANNs, they map the relationship between the inputs and the outputs by means of a set of hidden units (see Figure 2.13 for a single

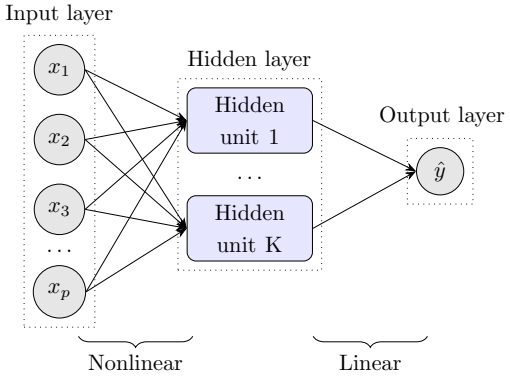

Figure 2.13: Schematic of a neural network (ANN) with a single hidden layer to explain the basic principle of the model. Based on *James et al.* (2023, p. 400, Figure 10.1).

output by way of example). These hidden units employ *activation functions*—which are nonlinear functions—to transform linear combinations of the inputs. The output results as a linear combination of the hidden units.

2.4.3 Artificial Neural Networks and Machine Learning

Neural networks that predict a response based on given inputs are called *feed-forward networks*. Such models constitute a universal approximation framework, provided that the network has enough hidden layers—single-layer neural networks can generally approximate a wide range of functions, but it is the two-layer neural networks that enable the estimation of any continuous functional mapping (*Bishop*, 1995, p. 116; *Goodfellow et al.*, 2016, p. 194). Multi-layered networks are called *multi-layer perceptrons* (MLPs), and an example architecture is depicted in Figure 2.14.

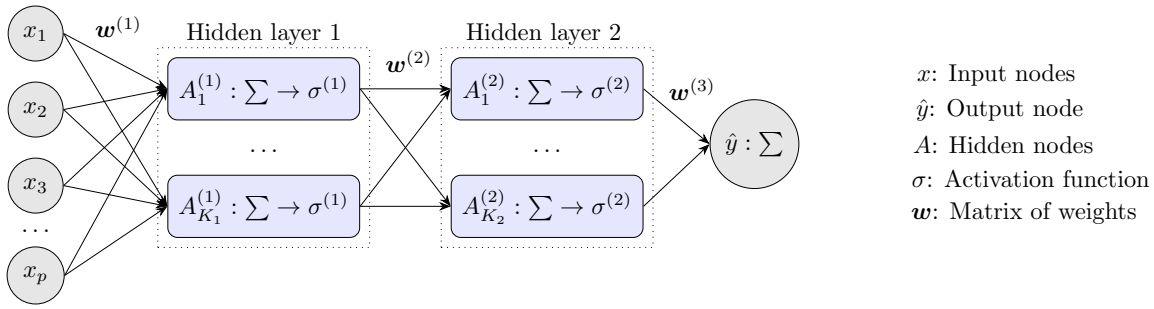

Figure 2.14: Example of a single-output feed-forward neural network with two hidden layers to derive its mathematical representation, which is given by (2.60).

To arrive at a mathematical representation $\hat{y} = f(\mathbf{x})$ of the MLP in Figure 2.14, each hidden layer takes a linear combination of the preceding layer by giving a particular weight w to each input, and then transforms this linear combination into a nonlinear response by means of an activation function $\sigma(\cdot)$ (see Figure 2.15 for the common ones). In this way, the nodes in the first hidden layer can be expressed as

$$A_j^{(1)} = h_j^{(1)}(\mathbf{x}) = \sigma^{(1)}\left(w_{j0}^{(1)} + \sum_{i=1}^{p} w_{ji}^{(1)} x_i\right), \qquad \text{for } j = 1, \ldots, K_1, \tag{2.58}$$

where $w_{j0}^{(1)} = b_j^{(1)}$ is the additional bias that is given to the linear function in order to have an affine function of the type $ax + b$; and $w_{ji}^{(1)}$ is the weight for each input x_i. The second hidden layer treats the activations $A_j^{(1)}$ as inputs and can be expressed as

$$A_k^{(2)} = h_k^{(2)}(\mathbf{x}) = \sigma^{(2)}\left(b_k^{(2)} + \sum_{j=1}^{K_1} w_{kj}^{(2)} A_j^{(1)}\right), \qquad \text{for } k = 1, \ldots, K_2. \tag{2.59}$$

Assuming no final nonlinear transformation for the output, which is common for regression problems, the response $\hat{y}$ is obtained by combining (2.58) and (2.59), yielding

$$\hat{y} = b^{(3)} + \sum_{k=1}^{K_2} w_k^{(3)} \sigma^{(2)} \left(b_k^{(2)} + \sum_{j=1}^{K_1} w_{kj}^{(2)} \sigma^{(1)} \left(b_j^{(1)} + \sum_{i=1}^{p} w_{ji}^{(1)} x_i \right) \right). \tag{2.60}$$

For given activation functions $\sigma^{(1)}$ and $\sigma^{(2)}$ (see Figure 2.15) and given number of nodes in the hidden layers—K_1 and K_2—, the parameters that can be adjusted to fit the final equation (2.60) to the data are the weights $\mathbf{w}$ and the biases $\mathbf{b}$. In the context of machine learning, these are found by means of a *learning* algorithm, which *learns* from *training data* to find the values which minimize the objective function. There are no constraints for the values of the weights and biases. The initial values are initialized randomly and then, first-order gradient-based optimization algorithms (see Figure 2.12) are used to find the optimum values—gradient-free methods do not come into consideration in this case because the grid to evaluate with the total of weights for the usually large number of hidden nodes would be far too big to allow for a computationally reasonable calculation.

What separates machine learning algorithms from traditional optimization problems is that the model is trained on *training data*, but must also perform well on new, previously unseen data (*test data*). It is possible to extend the use of the trained model to the test data via the assumption that the training and test data are generated by the same underlying probability distribution, called *data-generating distribution*. This allows to establish a mathematical relationship between the training and test errors, which basically says that the test error has to be greater than or equal to the expected training error. The training step builds the *most probable* statistical model of the process that generates the data instead of an exact representation of the training data points themselves. This is done by means of *maximum likelihood estimation*, which, in the case

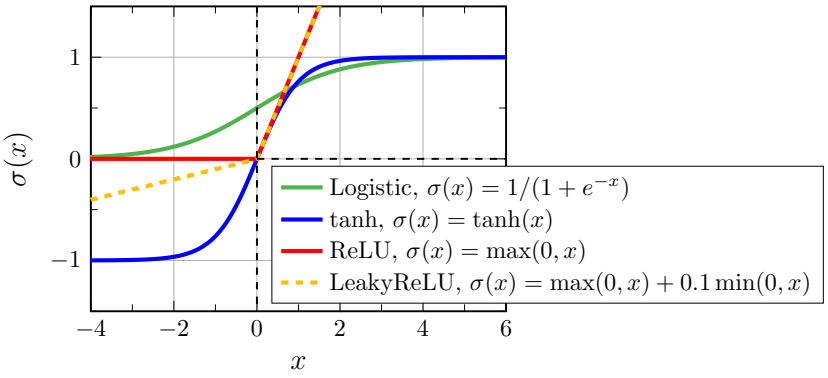

Figure 2.15: Common activation functions. The logistic function is suitable when the output takes a value between 0 and 1, i.e., for classification tasks instead of regression. Similarly, the tanh function defines the output between −1 and 1. For regression, where the output does not need to be constrained to a certain value range, a popular choice is the Rectified Linear Unit (ReLU) function. It offers the simplicity of a linear function but is still a nonlinear one. A variant, Leaky ReLU, improves convergence of the (gradient-based) optimization, as the function does not take zero values but includes a slope for $x < 0$. (*Google*, 2025; *PyTorch*, 2024b; *Mercioni and Holban*, 2020, p. 142, 143)

of an assumed normal distribution in a curve fitting approach, maximizes the following likelihood function

$$L(\mathbf{w},\mathbf{b}) = \prod_{i=1}^{m} p_{model}(\mathbf{x};\mathbf{w},\mathbf{b}) = \frac{1}{(2\pi\sigma^2)^{\frac{m}{2}}} \prod_{i=1}^{m} \Bigg\{ \exp\Big[-\frac{1}{2}\Big(\frac{y^{(i)} - \hat{y}^{(i)}(\mathbf{w},\mathbf{b})}{\sigma}\Big)^2 \Big] \Bigg\}, \quad (2.61)$$

if the probabilities are distributed as a Gaussian curve. In (2.61), σ is the standard deviation and m is the number of examples in the set (*Forrester et al.*, 2008, p. 35). To avoid rounding errors in the numerical computation, a variant of (2.61) is usually maximized instead of (2.61) itself. The natural logarithm of (2.61) is taken, leading to

$$\max_{\mathbf{w},\mathbf{b}} \sum_{i=1}^{m} -\frac{1}{2}\Big(\frac{y^{(i)} - \hat{y}^{(i)}(\mathbf{w},\mathbf{b})}{\sigma}\Big)^2 \equiv \min_{\mathbf{w},\mathbf{b}} \sum_{i=1}^{m} \big(y^{(i)} - \hat{y}^{(i)}(\mathbf{w},\mathbf{b})\big)^2, \quad (2.62)$$

which shows that maximum likelihood is obtained by minimizing the error function.

In the machine learning literature, the objective function is termed *cost function* and is represented by J. For convenience, its expression is taken to be the average of the argument in (2.62) over the number of training samples, which helps compare the results for different dataset sizes. With that, the objective of the optimization problem is $\min_{\mathbf{w},\mathbf{b}} J(\mathbf{w},\mathbf{b})$ and the cost function is

$$J(\mathbf{w},\mathbf{b}) = \frac{1}{m} \sum_{i=1}^{m} \big(y^{(i)} - \hat{y}^{(i)}(\mathbf{w},\mathbf{b})\big)^2. \quad (2.63)$$

(2.63) is a function of the adaptive parameters (weights and biases) in the network. For general networks with more than one hidden layer as the one from Figure 2.14, the J surface is typically highly nonlinear in the weights and biases' space and there exist many minima which satisfy $\nabla J = 0$ (refer to Figure 2.11). In this case, closed-form solutions for these minima are not possible and iterative search algorithms need to be used, which may not find the global minimum but a sufficiently low minimum for the problem at hand. These algorithms update the weight matrix and bias vector—simultaneously—at each iteration step $(\tau + 1)$ as

$$\mathbf{w}^{(\tau+1)} = \mathbf{w}^{(\tau)} + \Delta\mathbf{w}^{(\tau)}, \quad (2.64)$$

$$\mathbf{b}^{(\tau+1)} = \mathbf{b}^{(\tau)} + \Delta\mathbf{b}^{(\tau)}. \quad (2.65)$$

The increments $\Delta\mathbf{w}^{(\tau)}$ and $\Delta\mathbf{b}^{(\tau)}$ in (2.64) and (2.65) take different forms depending on the chosen algorithm. The most basic one is *gradient descent*, which includes a constant *learning rate* α to guide the direction of the negative gradient of the cost function, and calculates the increments as follows

$$\Delta\mathbf{w}^{(\tau)} = -\alpha \nabla J\big|_{\mathbf{w}^{(\tau)}} = -\alpha \frac{\partial J(\mathbf{w},\mathbf{b})}{\partial \mathbf{w}^{(\tau)}}, \quad (2.66)$$

$$\Delta\mathbf{b}^{(\tau)} = -\alpha \nabla J\big|_{\mathbf{b}^{(\tau)}} = -\alpha \frac{\partial J(\mathbf{w},\mathbf{b})}{\partial \mathbf{b}^{(\tau)}}. \quad (2.67)$$

However, this algorithm encounters some challenges, as a too large α will make the iterative search jump over possible minima and create an oscillatory behavior, and a too small α will increase the computation time. Several techniques have been developed to improve the performance of the gradient descent algorithm. For example, because of the stochastic nature of the cost function (2.63), which is built as the sum of subfunctions that are independent for each sample and identically distributed, the true cost function can be replaced by an estimation of (2.63) calculated from a randomly selected single subset (*minibatch*) of the training data. This variant is called *stochastic gradient descent* and accelerates convergence for high dimensional or extremely large datasets (*Goodfellow et al.*, 2016, p. 150). Another modification consists in allowing for an adaptive learning rate instead of a constant one, as its optimum value typically changes during the minimization problem (*Bishop*, 1995, p. 264). This is what the Adam (Adaptive Moment Estimation) algorithm from *Kingma and Ba* (2017) does. An example on how Adam changes (2.66) and (2.67) is given for the weights only

$$\Delta \mathbf{w}^{(\tau)} = -\alpha \frac{\hat{m}^{(\tau)}}{\sqrt{\hat{v}^{(\tau)}} + \epsilon}, \tag{2.68}$$

where $\hat{m}^{(\tau)}$ and $\hat{v}^{(\tau)}$ are the bias-corrected mean momentum and variance, respectively, and ϵ is a small positive constant used to avoid the division by zero. Substitution of the corresponding expressions for $\hat{m}^{(\tau)}$ and $\hat{v}^{(\tau)}$ in (2.68) yields

$$\begin{aligned} \Delta \mathbf{w}^{(\tau)} \approx -\alpha \frac{\hat{m}^{(\tau)}}{\sqrt{\hat{v}^{(\tau)}}} &= -\alpha \frac{\frac{m^{(\tau)}}{1-\beta_1}}{\sqrt{\frac{v^{(\tau)}}{1-\beta_2}}} = -\alpha \frac{\sqrt{1-\beta_2}}{1-\beta_1} \frac{m^{(\tau)}}{\sqrt{v^{(\tau)}}} \\ &= -\alpha \frac{\sqrt{1-\beta_2}}{1-\beta_1} \left(\frac{\beta_1 m^{(\tau-1)} + (1-\beta_1) \frac{\partial J(\mathbf{w},\mathbf{b})}{\partial \mathbf{w}^{(\tau)}}}{\sqrt{\beta_2 v^{(\tau-1)} + (1-\beta_2) \left(\frac{\partial J(\mathbf{w},\mathbf{b})}{\partial \mathbf{w}^{(\tau)}} \right)^2}} \right), \end{aligned} \tag{2.69}$$

which illustrates the evident upgrade with respect to (2.66). The same expression (2.69) applies for $\Delta \mathbf{b}^{(\tau)}$, but with $\partial J(\mathbf{w}, \mathbf{b}) / \partial \mathbf{b}^{(\tau)}$. β_1 and β_2 are fixed decay rates for the moving averages of the gradient and squared gradient, and $m^{(\tau)}$ and $v^{(\tau)}$ are initialized with zero values. Adam outperforms other stochastic optimization algorithms in terms of training time and convergence accuracy (*Kingma and Ba*, 2017). For the calculation of the gradient in (2.69), the cost function J needs to be differentiated with respect to each individual weight in the network. Because J is a function of $\hat{y}$ (see (2.63)) and, in turn, $\hat{y}$ is a function of the activation functions and the weights and biases (see (2.60)), the chain rule needs to be applied to calculate the gradients $\partial J / \partial \mathbf{w}$ and $\partial J / \partial \mathbf{b}$. This backward differentiation is called *backpropagation* and is the standard computationally efficient way to obtain the gradients of the cost function in neural networks.

For a neural network model, which usually has more than two parameters, it is generally not possible to visualize the outputs as a function of the parameters' space. Instead, a systematic way to evaluate the performance of the regression model is to look at the progression of the training and test errors over the number of training iterations (epochs).

For the total of data points, the recommendation is to build the training dataset with usually a 70-80% of the data, and the test dataset, with 30-20% (*Gholamy et al.*, 2018). If different models are to be compared to select a suitable set of hyperparameters, the training dataset is itself subdivided into an additional validation set, i.e., cross-validation (*Géron*, 2017, p. 30). In this case, the cost function J is calculated with (2.63) for the training and validation sets, giving $J_{training}$ and $J_{validation}$ for each epoch. The training accuracy is evaluated through $J_{training}$, and the ability of the trained model to generalize well to new data is determined by means of $J_{validation}$ (generalization error) and its relative position to $J_{training}$. The objective is to make not only the training error small, but also the gap between the training and generalization errors.

Depending on the nature of the training and generalization errors over the number of epochs, there exist three different situations: underfitting, overfitting, and good fit. Underfitting (see Figure 2.16a) means that the model is not capable of accurately representing the relationships in the training set. The training error curve continues to decrease by the end of the iterations, and its level is not sufficiently low. The solution in this case would be to either increase the number of iterations to allow the training curve to decrease further, or to use a bigger neural network with more hidden nodes and/or layers that is more capable of learning the training dataset. The opposite case is overfitting (see Figure 2.16b), which means that the model has learned the training set too well and is not capable of generalizing well on the validation set. The generalization error begins to increase after a number of iterations instead of further decreasing as does the training error. There is therefore a minimum in the generalization error curve. In this case, the solution would be to either stop the iterations at the point where the generalization error is at its minimum value to prevent it from increasing, or reduce the size of the network to fit a simpler model. Applying penalties to the loss function, i.e., regularization techniques, can also help improve generalization. Finally, for the case of a good fit (see Figure 2.16c), both the training and generalization errors are small and have reached a state of stability. The gap between them is also small. In this case, the model is accurate enough on the training dataset and also generalizes well on the validation dataset. Obtaining a good fit is about reaching a compromise between sufficient training accuracy and model ability to generalize well on new data. A similar case can occur where the training and generalization error curves have also reached a state of stability, but the gap between them is large. In this case, regularization techniques can

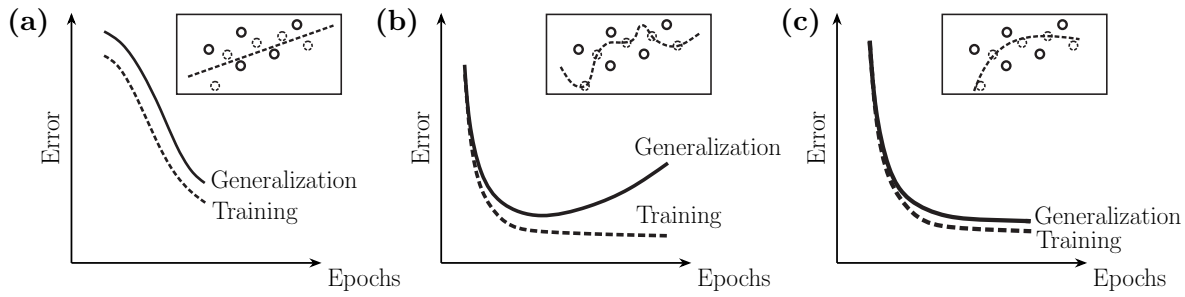

Figure 2.16: Learning curves for the training and generalization errors over the number of epochs: **(a)** underfit; **(b)** overfit; **(c)** good fit. Based on *Brownlee* (2019), *Ng* (2025), and *Goodfellow et al.* (2016, p. 113, Figure 5.3).

be applied with the aim to improve generalization but, if the gap remains significant, it might mean that the size of the training set is too small relative to the validation set size. To solve this problem of an unrepresentative training dataset, more training samples would need to be collected.

The cases of underfitting, overfitting, and good fit can also be explained by means of the statistical concepts of *bias* and *variance*. Bias corresponds to the difference between the predicted and the true values of the parameters being estimated, whereas (population) variance refers to the deviation from the true values caused by a specific sampling of the dataset. Accordingly, the case of underfitting will be characterized by a high bias, because the model has not learned the training dataset well. Contrarily, the case of overfitting will have a high variance, as the model offers too much flexibility for the particular dataset. For the case of good fit, a compromise is reached between the requirements of small bias and small variance, which is commonly known as bias-variance trade-off.

3 Literature Review, Research Approach and Objectives

In this chapter, the past work done in the field is reviewed to situate this dissertation in the broader literature and to establish the technical approach to follow. An analysis of the efforts carried out until now to extend the capabilities of throughflow calculations is presented. With that, the gaps and weaknesses that the present study will help to fulfill are described and, finally, the original contribution of this dissertation is outlined.

3.1 Literature Review

This literature review centers around three main topics: the inclusion of nonaxisymmetric effects in throughflow calculations, leading to *hybrid throughflow solutions*; the capturing of 3D flow features to derive guidelines for preliminary design analyses; and the adjustment of the empirical models by means of data-driven approaches, for both one-dimensional (1D) and 2D methods in general.

3.1.1 Hybrid Throughflow Solutions

In the literature, a *hybrid throughflow solution* is defined as the combination of an inviscid axisymmetric throughflow calculation and additional models concerning secondary flow features (*Wennerstrom*, 1991, p. 175). A practical definition of secondary flow for this purpose is that it includes all real flow features that prevent the flow from remaining inside axisymmetric concentric stream tubes[1]. These additional models can be summarized as: circumferential perturbations to the mean flow field, viscous calculations with blade force modeling, coupled boundary layer calculations, spanwise mixing models, and secondary flow models. Although the vast majority of the work on this topic has been done in the field of axial turbomachinery, the main theories and hypotheses are worth analyzing to understand their possible transfer to radial machines and assess the contributions already made.

As previously discussed in Sec. 2.3.1, the passage-averaging of the governing equations introduces fluctuation terms (see (2.40)), which are non-zero because of the nonaxisym-

[1] A stream tube is a theoretical concept used to describe a tube-shaped region rotated by the streamlines. For reference, in Figure 2.8b, there are four stream tubes, i.e., four meridional regions between consecutive streamlines in the hub-shroud direction.

metry of the flow and thus represent the 3D effects on the average flow. Several authors have pursued the quantification of the impact of these terms on axisymmetric calculations of axial compressors (*Sehra and Kerrebrock*, 1979; *Jennions and Stow*, 1985; *Dring and Joslyn*, 1986; *Baralon et al.*, 1999; *Simon et al.*, 2009). All of them concluded that these perturbations are generally small in axial compressors except in the endwall regions. For this reason, these terms are usually neglected, also because their magnitudes and distributions are difficult to determine—frequently with a coupled S_1 solution, as done by *Sehra and Kerrebrock* (1979). The latter claimed that, for their study on the MIT Blowdown Compressor with a transonic rotor, the major deviations from the inviscid axisymmetric flow arose from the streamwise variation of mean rothalpy and production of apparent entropy, and not from the circumferential perturbations. They argued that the passage-averaged rothalpy

$$\overline{I} = \overline{h} + \frac{\overline{w}^2}{2} - \frac{\overline{w'^2}}{2} - \frac{r^2\Omega^2}{2}, \tag{3.1}$$

because of the unavailability of the energy of fluctuations ($\overline{w'^2}/2$) to the mean flow, has to be rewritten as $\overline{I} = \overline{h} + \overline{w}^2/2 - r^2\Omega^2/2$, which is in this case not constant along a mean streamline—contrary to the fundamental assumption of conservation of rothalpy along a relative streamline. From this fluctuating term ($\overline{w'^2}/2$), they theorized a production of apparent entropy along the streamline

$$T\frac{D}{Dt}S_{app} = \frac{D(\overline{w'^2}/2)}{Dt} + \phi_{app}, \tag{3.2}$$

where $D(\overline{w'^2}/2)/Dt$ refers to the production of fluctuation energy along the streamline, and ϕ_{app} is the dissipation associated with the spatial transport of energy by apparent stresses. Since for an axisymmetric problem and steady mean flow it holds $\overline{D}/Dt = \overline{w}_m\partial/\partial m$, an expression for $\Delta S_{app}/\Delta m$ can be obtained from (3.2). *Sehra and Kerrebrock* finally computed the total entropy increase along a relative streamline as

$$(\Delta S)_{total} = (\Delta S)_{cascade} + (\Delta S)_{shock} + (\Delta S)_{app}, \tag{3.3}$$

where $(\Delta S)_{cascade}$ and $(\Delta S)_{shock}$ were obtained from empirical correlations, and $(\Delta S)_{app}$, from a S_1 calculation. With (3.3), *Sehra and Kerrebrock* included the 3D effects in the inviscid axisymmetric throughflow formulation via a baseline entropy increase $(\Delta S)_{baseline} = (\Delta S)_{cascade} + (\Delta S)_{shock}$ from literature correlations and then added an offset $(\Delta S)_{app}$ to obtain closure with a 3D formulation. *Dring and Joslyn* (1986) obtained closure differently: they neglected the fluctuation terms completely and introduced an aerodynamic blockage factor instead, to account for all the nonaxisymmetries arising in the blade passage. For that, they used (2.50), $B = 1 - \overline{c}_m^{area}/\overline{c}_m^{mass}$, claiming that the mass flow obtained from mass-averaged properties will not correspond to the correct mass flow, which actually needs to be an area-averaged value from hub to tip. As such, they defined the aerodynamic blockage as the ratio between these two different mass fluxes. As for the inputs of loss and deviation, they relied on well-known empirical correlations from the literature. Their throughflow results with this approach showed that both the level and the spanwise/streamwise distributions of blockage had a

significant impact of the rotor exit conditions. They recommended using a more precise formulation than (2.50), because the diffusion process in the impeller did not exactly match the measurement reference. They suggested including the effects of the radial components of the blade force and the fluctuation terms that were neglected at the beginning. Admittedly, a combination of both approaches, *Sehra and Kerrebrock*'s and *Dring and Joslyn*'s, should perhaps be pursued for a better agreement with reference results. *Dring and Oates* (1989) suggested modeling the nonaxisymmetric effects as the difference between the area-averaged and mass-averaged properties such as rothalpy, entropy, and angular momentum instead of including a factor in the continuity equation to account for the aerodynamic blockage.

Regarding the entropy production, authors such as *Horlock* (1971, p. 588) and *Bosman and Marsh* (1974, p. 25) pointed out that including a loss model in the equations for adiabatic and inviscid (reversible) flow is actually inconsistent, as the entropy should remain constant under these conditions. They claimed that, if entropy variations are to be allowed, then an additional dissipative force F_d making the adiabatic flow irreversible should be included. *Bosman and Marsh* (1974) assumed that this dissipative force opposes the relative velocity vector in direction, so that only the streamwise momentum equation contains the term $-F_d$. *Horlock* (1971), however, included this dissipative force in the radial momentum equation—which is the one of interest for a throughflow calculation—as $-F_d(w_r/w)$. His results showed that, near the design point, where radial velocities are small, the contribution of the dissipative force in the radial momentum equation was negligible. However, he expected that at off-design flow conditions, where large radial velocities may develop, the dissipative radial force may become significant. For the calculation of F_d, he arrived at the expression $F_d/\rho = T\partial s/\partial x$ from the conservation of rothalpy along the streamlines, where $\partial s/\partial x$ was obtained from empirical correlations. *Hirsch* (2007) termed this approach of modeling the effect of shear stresses by an equivalent *distributed* friction force a *distributed loss model*. Recent publications such as *Simon and Léonard* (2005) and *Pacciani et al.* (2016) also used a distributed loss model in their calculations.

Instead of this streamwise dissipative force, *Denton* (1986) and *Gallimore* (1998), for example, approximated the viscous effects in an axisymmetric throughflow code via a tangential blade force in the circumferential direction. *Denton* included the tangential blade force in the stagnation enthalpy changes along the streamlines. He modeled this force through a shear stress $\tau_w = 1/2 c_f \rho w^2$, where the skin friction coefficient c_f was adjusted empirically to obtain the correct level of loss according to experimental data for unseparated turbulent boundary layers. He approximated the blockage effect by prescribing a radial distribution of τ_w as a power law, where he adjusted the exponent—again empirically—to obtain realistic loss profiles. With this approach, his results for axial compressor and turbine blade rows matched experimental data very well, but he could only obtain qualitatively good results for a radial impeller, since the influence of the tip gap and of possibly separated boundary layers was neglected. As for *Gallimore*, he defined the total tangential blade force F_u as the result of the momentum change caused by both the pressure blade force (P_u) and the shear effects in endwall regions and within the flow field (T_u), i.e., $F_u = P_u + T_u$. He argued that this tangential force deficit, T_u, is what makes the behavior of F_u unpredictable and difficult to correlate,

and that for this reason, coupled integral boundary layer methods did not progress further because they required an assumed distribution of T_u as input[2]. With that, he approximated the problem as $F_u = P_u + T_u = P_u K$, where K summed up all the corrections applied to a baseline P_u from an axisymmetric throughflow calculation. The first correction consisted in applying a limiting loading coefficient at each spanwise location—specifically near the endwalls to represent the effect of the boundary layers—, which was defined from the diffusion on the suction surface of the blade. The second adjustment of P_u focused on correcting its radial gradient between the streamlines in the endwall regions. From the final distributions of F_u, he adjusted the spanwise profiles of loss and deviation as well. The results matched experimental data except for the case of multistage axial compressors with large hub separation. Nevertheless, he claimed that the level of accuracy achieved was sufficient for preliminary design purposes.

So far in the publications discussed, the spanwise profiles of the models were defined somewhat arbitrarily with mathematical expressions, or by prescribing percentages of spanwise height where the endwall boundary layers were expected to concentrate. As already mentioned in Sec. 2.3, throughflow calculation methods neglect the spanwise transport of fluid properties. With the aim to develop models to overcome this deficiency, two different physical mechanisms were recognized in the literature to play a role in this spanwise mixing process, originally for multistage axial compressors: convective transport through secondary flows (*Adkins and Smith*, 1982) and diffusive transport through turbulence (*Gallimore and Cumpsty*, 1986; *Gallimore*, 1986; *Howard and Gallimore*, 1993). The method from *Adkins and Smith* was based on the inviscid convection of fluid properties by the secondary flow field. They emphasized that frictional effects were not included directly in the analysis but, instead, the secondary flow resulting from annulus wall and blade boundary layers represented these effects in an approximate way. From the secondary flow velocities obtained, they arrived at computing the streamwise gradient of flow properties (total temperature, total pressure, and angular momentum) via a diffusion-type equation, $\partial \overline{P}/\partial z = \varepsilon\, \partial^2 \overline{P}/\partial y^2$, where ε was the mixing coefficient, which they adjusted empirically at each radial position to account for the interactions with the endwalls. Contrary to this approach, *Gallimore* (1986, p. 10) claimed, based on own experiments (*Gallimore and Cumpsty*, 1986), that it is the turbulent diffusion caused by the random fluctuations in the radial direction that gives rise to the radial transport of the flow properties rather than the convection by secondary flows. They reformulated the energy and momentum equations in each direction as a function of the eddy viscosity, μ_t, to calculate the streamwise changes of total enthalpy, entropy, and angular momentum. Results for low speed multistage axial compressors near the design point were similar with both approaches—convection and diffusion—and matched experimental data very well in comparison with the unmixed case. To close this debate on which mechanism causes spanwise mixing—a rather academic one, as indicated by *Wennerstrom* (1991, p. 177), because results were nearly the same—, experimental and CFD

[2]Throughflow methods with coupled boundary calculations did not develop further than the work of *De Ruyck and Hirsch* (1981) (*Gallimore*, 1998, p. 3). It was recognized that conventional boundary layer theory was not appropriate to represent the strong 3D flow phenomena that take place in the endwall regions (*Horlock and Denton*, 2005, p. 8). In view of the emerging fully 3D calculation methods in the late 1980s (*Denton and Dawes*, 1998, p. 107), the degree of complexity of upgrading to coupled 3D boundary layer calculations would not have been justified.

results from *Wisler et al.* (1987) and *Leylek and Wisler* (1990) led to the conclusion that it is a combination of both secondary flow convection and turbulent diffusion that results in spanwise mixing, and that their contribution depends on the location inside the compressor and on the aerodynamic loading level (*Wennerstrom*, 1991, p. 177). *Smith* (1987) added that, certainly, secondary flows emerge from phenomena that agitate the flow and cause turbulent mixing (*Wennerstrom*, 1991, p. 177). Extension of spanwise mixing modeling to turbines by *Kirtley et al.* (1990) showed that diffusion models alone underpredicted results near the endwalls, so that, in these regions, secondary flow models should be given preference (*Wennerstrom*, 1991, p. 177). As for other low-aspect ratio blades like radial impellers, *Casey and Robinson* (2010, p. 4) recognized the difficulty in separating the flow regions to apply diffusion and convective schemes independently, and pointed out that a successful approximation nowadays consists in specifying a meanline value of the loss coefficient at each streamline position, thus assuming a complete mixing across the span. Nevertheless, *Casey and Robinson* (2010, 2021) still tried to include a spanwise mixing algorithm for radial impellers, derived as a combination of convective and diffusion formulations from multistage axial compressors. This mixing scheme was shown to be able to closely reproduce the CFD simulation results of the impeller analyzed (*Casey and Robinson*, 2010, p. 6).

A different approach to predicting the correct spanwise outlet profiles in radial impellers is the introduction of a model for the impeller jet-wake flow structure (see Sec. 2.2.2) in a streamline curvature method. *Howard and Osborne* (1977, p. 141) argued that the inviscid calculation with loss adjustment serves to match circumferentially averaged reference values but that, in reality, the circumferential variation in relative total pressure needs to be modeled to represent the real flow processes within the impeller passage. The historical jet-wake modeling made clear assumptions about the nature of the flow: (1) the impeller core flow is isentropic and the wake is nonisentropic, containing all the losses; (2) the wake is formed once the passage boundary layers separate, typically within 40% meridional distance, and it contains approximately 20% of the through flow; (3) the jet and wake are separated by the Coriolis force and do not mix in the impeller passage, but after leaving the wheel; and (4) it is the jet that deviates or *slips*, while the wake follows the blade angle at impeller exit (*Japikse*, 1985, p. 4). *Howard and Osborne* (1977) treated the wake as additional blockage and defined the distribution of the width of the wake along the passage as quadratic—in accordance with their experimental data. *Howard et al.* (1994, p. 2) later recognized that the accuracy of this procedure did not match that of a fully 3D viscous flow analysis and that the method was relatively inconvenient for rapid manipulation. Under these premises, *Japikse* (1985) developed a new scheme which he called *two-zone impeller modeling*. In contrast to earlier jet-wake modeling, it did not require any detailed assumptions about the structure of the second zone—only that it is nonisentropic. This method was developed for one-dimensional meanline calculations where the governing equations were applied separately to each of the zones, and not specifically for throughflow calculations. Traditional single-zone calculations assume that the fluid conditions are uniform over certain cross-sections in the flow passage and the internal losses are determined by means of correlations for various loss mechanisms. Contrarily, two-zone modeling separates the impeller flow into an isentropic jet and a nonisentropic wake zone, and requires fewer empirical correlations

than single-zone modeling in that the internal losses are accounted for directly by the specification of the unloaded tip condition ($p_{2,wake} = p_{2,jet}$). However, empiricism is still present by means of the impeller effectiveness parameters η_a and η_b and the wake mass flow fraction. Authors such as *Oh et al.* (1997) and *Britton and Gauthier* (2008) found for their two-zone calculations of well-known impellers from the open literature that, although the two-zone approach built a more detailed picture of the impeller flow, it tended to underpredict performance, and that more accurate values of the empirical parameters η_a and η_b should help improve the results. Thus, both single- and two-zone approaches do involve an amount of empiricism. A recent publication from *Stuart et al.* (2019) even considered three zones, also for a meanline method: aside from the jet-wake division in circumferential direction, they divided the flow in spanwise direction into an active flow region and a recirculation region—the latter being responsible for the aerodynamic blockage in modern automotive turbocharger compressors. They correlated the wake mass flow fraction and wake area fraction using CFD simulation data. With these new correlations and the three-zone modeling equations, they achieved an improved prediction of the slip factor over the compressor map compared to initial results obtained using correlations from the literature. This highlighted the importance of accurately specifying the values of the empirical parameters, regardless of the modeling approach chosen.

3.1.2 Capturing 3D Features for Preliminary Design

Section 3.1.1 was concerned with different approaches to make streamline curvature methods more realistic. Despite the efforts, the complexity of such hybrid throughflow solutions and their limited degree of accuracy in comparison with full Navier-Stokes solutions—in particular for radial machines—makes them difficult to develop further and, instead, other approaches may come into consideration. In this section, the literature review covers some publications that have focused on turning knowledge about 3D flow into guidelines for assessing the aerodynamic behavior in preliminary design.

In the field of radial impellers, authors such as *Howard and Lennemann* (1971), *Johnson* (1978), *Johnson and Moore* (1983), *Hirsch et al.* (1996), and *Kang and Hirsch* (2001) focused on characterizing the development of the wake inside the impeller passage. They all agreed that an appropriate way of studying the viscous effects was to follow the rate of increase of the streamwise vorticity, so that the formation and position of the wake could be predicted by the convection of low rotary stagnation pressure ($p^* = p + \frac{1}{2}\rho w^2 - \frac{1}{2}\rho u^2$) by secondary flows inside the impeller. The basis of all of their studies was the equation for the streamwise vorticity production along a relative streamline, (2.30), which is recalled here again for completeness

$$\frac{\partial}{\partial s}\left(\frac{\omega_s}{w}\right) = \frac{2}{\rho w^2}\left[\frac{1}{R_m}\frac{\partial p^*}{\partial b} + \frac{1}{R_b}\frac{\partial p^*}{\partial n} + \frac{\Omega}{w}\frac{\partial p^*}{\partial z}\right]. \tag{3.4}$$

Despite starting from the same equation, the aforementioned authors followed different approaches to quantify the effects generating this vorticity and thus to predict the position of the wake. *Howard and Lennemann* calculated the streamwise vorticity only

along the mid-passage streamline, and therefore assumed that the impeller passage consisted of a single stream tube and that the vorticity was uniform across the passage. Despite this simplified approach, they achieved a fair agreement between measurement data and prediction results of vorticity, which would be sufficient for analyses in the preliminary design phase. As for *Johnson* and *Johnson and Moore*, they proceeded by analyzing the gradients of rotary stagnation pressure alone at various cross-sections in the impeller passage. With that, they could quantify the position of the wake based solely on the convection of low stagnation pressure fluid by secondary flows. With regard to the publications of *Hirsch et al.* and *Kang and Hirsch*, they modeled the three terms from (3.4), i.e., $\frac{1}{R_m}\frac{\partial p^*}{\partial b}$, $\frac{1}{R_b}\frac{\partial p^*}{\partial n}$, and $\frac{\Omega}{w}\frac{\partial p^*}{\partial z}$, and obtained a ratio between them to quantify the relative effects of the passage vortices and blade surface vortices on the formation of the wake. Due to the complex nature of radial impeller flow, the aforementioned efforts focused on a rather qualitatively assessment of the position of the wake, i.e., the high-loss region, without extensively analyzing the causes of this distinctive flow phenomenon inside impellers.

As with the spanwise mixing models from Sec. 3.1.1, apart from these *convective* approaches with secondary flows, authors such as *Balje* (1978, 1981) developed a model for the characterization of the jet-wake structure based on turbulence considerations, i.e., a *diffusive* approach. He followed *Johnston and Eide* (1976)'s description of curvature and rotation effects on the stability of the boundary layer in radial impeller blades by means of the gradient Richardson number (Ri), and proposed two diffusion factors, one for the pressure to suction direction (DF_{SP}), and one for the hub to shroud direction (DF_{SH}). These factors were considered as similarity parameters in radial bladed impellers without backsweep ($\beta_2 = 0°$ in Figure 2.1b) and were built as $DF_{SP} = Ri_{SP} \cdot f(\text{deceleration})$ and $DF_{SH} = Ri_{SH} \cdot f(\text{deceleration})$. *Rodgers* (1978, p. 593) supported such an approach with two different diffusion factors instead of a global one, arguing that the impeller diffusion needs to be analyzed separately in each direction and that individual design limitations need to be specified for each one. He pointed out, however, that due to limited experimental data at that moment, preliminary design analyses continued to apply simplified diffusion criteria as overall performance measures instead of separated diffusion factors. *Balje* (1978) also quantified the slip differences in the jet and wake regions at impeller outlet by means of the Richardson numbers Ri_{SP} and Ri_{SH}, which he applied as scaling factors in the calculation of the actual circumferential velocity c_{u2}. *Coppage et al.* (1956), in turn, had already included the global impeller diffusion w_1/w_2 as a correction factor in the slip factor calculation, also to account for the effect of boundary layer growth on the streamline pattern at impeller exit. As such, both *Balje* and *Coppage et al.* recognized the need to account for viscous effects in an often considered inviscid phenomenon such as the slip.

To summarize, the 3D features in radial impellers were generally described in terms of loading parameters by means of either pressure differences in the flow passage or by diffusion factors. *Casey and Robinson* (2021, p. 188, 190) argued, however, that in modern backswept impellers, the strength of the wake has been reduced in comparison with past radial bladed impellers. Nevertheless, the wake is still present at off-design operation and becomes stronger towards surge. It is still customary to characterize the impeller performance in the preliminary design based on wake-related considerations.

3.1.3 Data-Driven Performance Modeling

Instead of building a hybrid throughflow solution with the approaches discussed in Sec. 3.1.1, a more straightforward and common way to include the three-dimensional (3D) effects in inviscid throughflow methods is via empirical correlations: meanline correlations are commonly applied and a spanwise distribution of the quantities is then prescribed. For impellers, empirical models for the slip factor, boundary layer blockage, and losses can be specified. The question is whether these models can make the throughflow solver reach the accuracy from 3D calculation methods. Regarding the slip factor, relevant models in the literature were obtained in the past for the design point of low-speed compressors with generally radial bladed impellers, and were dependent mainly on geometry parameters. Therefore, according to this class of models, the slip factor remained constant with varying flow condition (*Van den Braembussche*, 2007, p. 97; *Harrison*, 2020, p. 38). However, for modern impellers with backswept blades and at off-design operation, it has been recognized that the slip factor actually varies with flow condition (*Dean*, 1967, p. 567; *Traupel*, 1962, as cited in *Van den Braembussche*, 2007, p. 99; *Qiu et al.*, 2011, p. 5). As for the boundary layer blockage, the model development for radial compressors has been much more limited than for axial compressors, with a correlation from *Aungier* (1995, 2000). For the loss models, several attempts have been made at providing a sound combination of different loss mechanisms, which relied on a linear summation of the contributions—see *Oh et al.* (1997) for an overview. This approach with the addition of loss terms originated in the axial turbine loss modeling field and has also been established for radial compressors (*Japikse*, 2009, p. 11). The problem with such an approach is the lack of coupling and of nonlinearity of the physical processes involved, which is necessary in radial machines (*Japikse*, 2009, p. 7, 11).

In an attempt to match reference data with historical correlations better, data-driven approaches have been developed in the literature. For axial and radial turbomachinery, the majority of publications concerned with the calibration of correlations with optimization algorithms have employed gradient-free/global search methods (see Figure 2.12 for the classification of optimization methods). Most of them have pursued the extension of their predictive capabilities, mainly with 1D meanline solvers, to calculate off-design performance. For example, *Hansen and Kappis* (2001), for their axial compressors under study, assumed known loss and deviation curves for the design point and defined polynomials that would shift the initial polars based on the effects of incidence, Mach number, and blade thickness. They found the values of the coefficients of these polynomials via a Simulated Annealing optimization method. Another global search optimization technique was used by *Benini and Cenzon* (2009), in this case an Evolutionary Algorithm, for their calibration of pump global correlations of efficiency and slip factor, also based on newly defined polynomials as correction factors. *Lawerenz et al.* (2014) also used a population-based optimization algorithm, specifically a Genetic Algorithm, to calibrate their impeller correlations of loss coefficient, slip factor, and aerodynamic blockage. A further example of the adoption of a population-based optimization method is found in *Geller et al.* (2017), who included scaling factors before the loss correlations from *Aungier* (2000), and calibrated them with an evolutionary algorithm that minimized the gap in the prediction of the surge limit from a 1D meanline and a CFD code.

So far, the approaches discussed focused on finding the coefficients of a given regression equation, usually of second-degree polynomial form. As described in Chapter 2, Sec. 2.4, metamodeling techniques serve to bridge between computer codes of different accuracy. *Bonaiuti et al.* (2006) used the Response Surface Methodology (RSM) metamodels in the context of the design optimization of a transonic radial impeller. Because this method is based on second-order polynomials, they discussed that the main advantages of such a technique are its interpretability and robustness, but that it becomes less reliable when dealing with more than ten variables. In the context of calibrating a throughflow solver to CFD data, in *Labat Casajust et al.* (2023) an RSM technique with second-order polynomials was also employed. Despite achieving significant improvements in the prediction of performance with respect to a baseline throughflow calculation with literature correlations, there were still offsets in the isentropic efficiency prediction that could have been further improved. Alternative methods such as MARS modeling have, however, not been used in the context of turbomachinery. Instead, Kriging models have found wide acceptance, mainly for the design optimization of compressors (*Wang et al.*, 2006; *Bellary et al.*, 2016; *Aissa and Verstraete*, 2019).

Regarding inherently nonlinear metamodels such as neural networks, they have been used for both design optimization (*Rubechini et al.*, 2011; *Agnolucci et al.*, 2021, 2023) and preliminary design (*Japikse and Oliphant*, 2005; *Pelton et al.*, 2005; *Japikse et al.*, 2005; *Dubitsky and Japikse*, 2005; *Schmitz et al.*, 2011, 2012; *Schnoes and Nicke*, 2017; *Ren et al.*, 2023; *Lottini et al.*, 2024). As part of a four paper series (*Japikse and Oliphant*, 2005; *Pelton et al.*, 2005; *Japikse et al.*, 2005; *Dubitsky and Japikse*, 2005), Japikse and his colleagues focused on modeling the impeller performance by means of their own two-zone approach from 1985 (*Japikse*, 1985). They used neural networks to build relationships from scratch that would relate their dependent parameters η_a and η_b (impeller effectiveness parameters in the two-zone model) to independent parameters that follow similitude principles such as Reynolds number, Mach number, rotation number, Rossby number, Richardson number, geometric parameters, etc. They argued that, nowadays, the use of mathematical algorithms to relate physically coherent variables to known physical processes according to principles of fluid dynamics and thermodynamics is of great importance for scientific development. However, this process of model development is challenging when building equations from scratch, because the final models must make physical sense (*Pelton et al.*, 2005, p. 8)—this degree of complexity in checking for singularities and asymptotes of the new equations might not be strictly necessary in the context of a mere calibration of reference equations; the approach followed by Japikse was to build equations from scratch with full flexibility for the form of the equation. For axial compressors, *Schmitz et al.* (2011, 2012) and *Schnoes and Nicke* (2017) also used neural networks to build relationships between geometrical/flow parameters and airfoil performance data from a large randomly created database, and integrated the new models of loss and deviation in a 2D throughflow calculation program. As for 1D meanline calculations, *Ren et al.* (2023) calibrated a meanline code to a CFD database with neural networks surrogates for the improved map prediction of radial turbines. A different approach was followed by *Lottini et al.* (2024), who corrected the end results of pressure ratio and efficiency of expander-compressors by means of neural networks instead of the intermediate performance models as the previously discussed publications.

3.2 Research Approach

This dissertation aims to contribute to the improvement of the predictive accuracy of two-dimensional streamline curvature methods for radial impellers at design and off-design operating conditions. As discussed in the literature review (see Sec. 3.1), three research lines have directed the development of throughflow methods until the present day: the inclusion of nonaxisymmetric effects yielding hybrid throughflow solutions; the extraction of 3D flow features as parameters to guide the preliminary design analysis; and the calibration of empirical models to match reference data.

In summary, efforts in the literature focused on including viscosity through entropy gradients and aerodynamic blockage factors. The spanwise redistribution across stream tubes was modeled via flow convection through secondary flows and turbulent mixing. A certain degree of empiricism was still present in the reviewed studies, and the resulting level of accuracy was not able to match reference 3D results completely—merely qualitatively in the case of radial impellers. By reflecting on how the authors approached the problem, it can be recognized that, in general, the losses were included as a baseline contribution from well-known empirical correlations and then, an offset was added to account for the nonaxisymmetric viscous effects and close the gap with 3D results; see *Sehra and Kerrebrock* (1979). A similar approach was pursued in terms of the aerodynamic blockage; see *Dring and Joslyn* (1986). In this case, the authors recognized that the baseline blockage definition (2.50) needed to be adapted to match both the level and distribution from experimental data near the impeller exit. In this sense, it seems conceivable that, in the present dissertation, a baseline aerodynamic blockage and loss are implemented, and then, an offset is added to amount to 3D reference results. The same applies for the slip, as done by *Coppage et al.* (1956) and *Balje* (1978), who included a factor representing the viscous effects affecting the slip. In line with these approaches, in the present dissertation, a baseline throughflow calculation with well-known empirical correlations for the metrics of slip factor, loss coefficient, and outlet aerodynamic blockage will be established.

Then, instead of calibrating the coefficients of the empirical correlations, I propose to multiply additional correction models to the baseline equations. These models will be expressed as offsets between the baseline metrics and 3D benchmark values and will be defined as functions of aerodynamic loading parameters. These parameters will be intended to capture the effects of 3D flow, particularly of the boundary layer fluid accumulation near the impeller exit, across the operating map. In the radial compressor literature, diffusion and blade loading concepts are grouped together to describe the boundary layer growth and separation, as well as secondary flows; see *Coppage et al.* (1956, p. 6). The accumulation of low-momentum fluid at the suction side shroud corner near impeller exit, i.e., the wake, driven by secondary flows in the impeller passage, was studied qualitatively by different authors; see, for example, *Johnson and Moore* (1983) and *Hirsch et al.* (1996). They included the frictional effects in an approximate way by following the rate of increase of the streamwise vorticity. This was in line with the research from *Adkins and Smith* (1982), who approximated the viscous effects by convection of inviscid secondary flow in axial machines, claiming that, although inviscid, the secondary flow results from the annulus wall and blade boundary layers. A different

approach was followed by *Balje* (1978, 1981), who identified similarity parameters characterizing the nature of the wake in the impeller passage and applied them to represent the diffusion taking place in each direction. Conforming to these research lines, the aerodynamic loading parameters in this dissertation will be selected to describe the 3D viscous diffusion in the impeller qualitatively. To represent the coupling and nonlinearity of the flow processes involved, the correction models will be built by means of artificial neural networks (ANNs), in line with the state of the art in the field.

The proposed research approach for the present dissertation is depicted in Figure 3.1 and will be applied to two unshrouded impellers of similar nominal characteristics. The initial baseline throughflow calculations with literature correlations will be discussed in Chapter 5 and compared with benchmark 3D Computational Fluid Dynamics (CFD) results. The results of the proposed calibration will be presented in Chapter 6. Performance data from both test cases will be combined in a unified training database for the calibration with the neural network regression model. New results for the metrics of slip factor (σ_{calib}), loss coefficient $(\Delta s/R)_{calib}$, and outlet aerodynamic blockage ($B_{2,calib}$) will be obtained. Subsequently, throughflow calculations with the calibrated metrics will be performed, which will provide the final results for the total-total pressure ratio ($\pi^{tt}_{Imp.,calib}$) and isentropic efficiency ($\eta^{tt}_{s,Imp.,calib}$) at each operating point in the performance map of the corresponding impeller geometry.

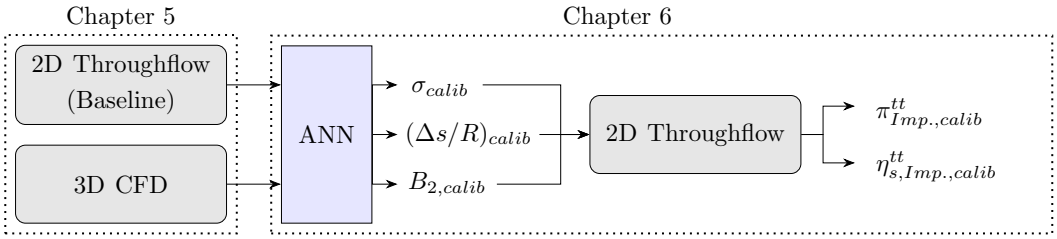

Figure 3.1: Schematic showing the approach followed in this dissertation.

3.3 Research Objectives

To fulfill the aim of improving the predictive accuracy of throughflow methods for radial impellers across the operating map, the following four research objectives have been defined:

1. Development of a proposal for a suitable combination of empirical correlations for the metrics of slip factor, impeller loss coefficient, and outlet aerodynamic blockage that apply to two different impeller geometries of similar nominal characteristics without individual adjustment. The aim is to build a standard initial 2D throughflow calculation of these two impellers.

2. Quantification of the predictive accuracy achieved with the initial 2D throughflow calculation with respect to benchmark CFD simulations of the same impeller geometries at across the operating map. For each test case, three different speed lines will be considered, ranging from near choke to near surge operation.

3. Development of a proposal for a calibration methodology of the initial 2D throughflow calculations to the benchmark CFD results of the two impeller geometries across the operating map by means of machine learning methods such as artificial neural networks.

4. Quantification of the predictive accuracy achieved with the proposed machine learning-enhanced 2D throughflow method with respect to the benchmark CFD results for the whole range of operating conditions considered. The aim is to assess whether the devised methodology, despite being limited to two test cases, exhibits the potential to be considered a viable alternative to traditional CFD methods for the preliminary design of radial impellers.

4 Methodology

In this chapter, the methods and methodology used to follow the proposed research approach in Sec. 3.2 are described. A baseline two-dimensional (2D) throughflow calculation workflow was built with the aim to provide an initial performance estimation of modern impellers. Reference three-dimensional (3D) Computational Fluid Dynamics (CFD) simulations were performed as well, with a uniform numerical setup for the chosen test cases. Finally, a calibration methodology was designed by means of an artificial neural network (ANN) regression algorithm, and was incorporated into the baseline throughflow workflow to provide the calibrated throughflow results. Over this chapter, emphasis is placed on how the different workflows for the *baseline* and *calibrated* throughflow solutions were set up.

4.1 Test Cases

The test cases used for the methodology in this dissertation are two radial compressors with an unshrouded impeller and a vaneless diffuser. Both of them belong to the Institute of Jet Propulsion and Turbomachinery of the RWTH Aachen University, and they were investigated experimentally and numerically in previous dissertations (*Ziegler*, 2003; *Hehn*, 2018; *Enneking*, 2020). The first one is the RADIVER compressor, from which the vaneless configuration was chosen, and the second one is the transonic compressor Design603, which incorporates splitter blades and is the result of a free-form geometry optimization from *Hehn* (2018). The control volume considered in both cases was comprised between compressor inlet and diffuser outlet. Design603 also has a volute (see Figure 2.1a for reference), but due to proprietary reasons, its geometry and data were not available for this work. Both test cases have similar nominal characteristics (see Table 4.1). The relevant geometry parameters of the impellers, which are the components of interest in this dissertation, are also given in Table 4.1.

Table 4.1: Relevant data of the impellers from the test cases RADIVER Vaneless (*Ziegler*, 2003, p. 22) and Design603 (*Enneking*, 2020, p. 60, 63).

Parameter	RADIVER Vaneless	Design603
Z [-]	15	$13 + 13$
D_2 [mm]	270	356
b_2 [mm]	11.1	16.1
n_{nom} [1/min]	35,200	31,461

4.2 CFD Calculations

In this dissertation, CFD is taken to mean 3D Reynolds-averaged Navier-Stokes (RANS) simulations. Because CFD results will be used as the reference for calibration, it is essential to evaluate the suitability of the CFD simulations in order to rely on them as the reference. As numerical methods always produce approximate solutions to the governing equations, in the following sections the various types of error found in CFD calculations are analyzed, which are *iteration*, *discretization*, and *modeling* errors.

4.2.1 Numerical Setup and Iteration Error

To begin with, the *iteration error* is defined as the difference between the exact and the iterative solutions of the discretized equations. An iterative solution is usually chosen against the direct one to avoid higher computational costs, and as such, a convergence criterion needs to be defined to decide when to stop the iteration process and be able to assume a sufficiently converged solution. For the CFD simulations in this work, the RANS solver TRACE (Turbomachinery Research Aerodynamic Computational Environment), v9.4, was used, which is jointly developed by the German Aerospace Center (DLR) and MTU Aero Engines AG (*DLR*, 2023). TRACE offers, amongst others, a nonlinear module in the time domain and solves the compressible 3D Navier-Stokes equations in the rotating frame of reference[1]. For the sake of exemplification, these equations in differential form can be summarized as

$$\frac{\partial \hat{\mathbf{Q}}}{\partial t} + \frac{\partial \hat{\mathbf{F}}}{\partial \xi} + \frac{\partial \hat{\mathbf{G}}}{\partial \eta} + \frac{\partial \hat{\mathbf{H}}}{\partial \zeta} = \left[\frac{\partial \hat{\mathbf{F}}_v}{\partial \xi} + \frac{\partial \hat{\mathbf{G}}_v}{\partial \eta} + \frac{\partial \hat{\mathbf{H}}_v}{\partial \zeta} \right] + \hat{\mathbf{S}}, \tag{4.1}$$

where (ξ, η, ζ) represents the body-fitted coordinate system; $\hat{\mathbf{Q}} = (1/J)[\rho, \rho u, \rho v, \rho w, \rho E]^T$ is the solution state vector; $J = \partial(\xi, \eta, \zeta, t)/\partial(x, y, z, t)$ is the transformation Jacobian from a cartesian to a body-fitted grid; $\hat{\mathbf{S}}$ denotes the source term; $\hat{\mathbf{F}}$, $\hat{\mathbf{G}}$, and $\hat{\mathbf{H}}$ are the inviscid/convective fluxes; and $\hat{\mathbf{F}}_v$, $\hat{\mathbf{G}}_v$, and $\hat{\mathbf{H}}_v$ are the viscous ones. TRACE uses a cell-centered finite volume method which discretizes the viscous fluxes by means of central differences. Contrarily, for the spatial discretization of the convective fluxes, the upwind scheme is used, which aims to avoid instabilities by considering the direction of flux propagation. For first order accurate schemes, the flow variables within a cell are averaged and have a constant value, which leads to discontinuities in flow values on the lateral surfaces of neighboring cells. This issue is addressed by means of the shock-tube problem, also known as the *Riemann problem*. The Roe scheme provides a framework for computing a unique flux over the cell face. This is achieved by first applying a linearized homogeneous approximate Riemann solver and then using flux difference splitting to obtain the unique flux. Shock-like problems do not necessarily involve shock waves, but simply regions of complex solution structure with large gradients and curvatures (*Roache*, 1997, p. 142). In this sense, the convective fluxes are a function of the left and right cell values, i.e., $\hat{\mathbf{F}}, \hat{\mathbf{G}}, \hat{\mathbf{H}} = f(Q_L, Q_R)$. The order of accuracy

[1] See, for example, *Engel* (1997) and *Nürnberger* (2004) for implementation and verification details.

of the flow solution is then determined by the method to calculate Q_L and Q_R. For schemes higher than first order, an extrapolation with higher-order polynomials with the MUSCL (Monotonic Upstream Scheme for Conservation Laws) scheme is performed (*Benetschik*, 2023, p. 180), for which $Q_L, Q_R = f(\kappa, L_i)$. For the CFD calculations in this work, $\kappa = 0$ was chosen, which meant a second-order Fromm scheme, and L_i was taken to be the Van Albada limiter. According to the TRACE documentation (*DLR*, 2023), this combination of κ and L_i offers the best compromise between stability and accuracy. Regarding the time discretization of (4.1), all the terms that do not contain the time derivative can be summarized as a residual $\hat{\mathbf{R}}(\hat{\mathbf{Q}})$ yielding

$$\frac{\partial \hat{\mathbf{Q}}}{\partial t} + \hat{\mathbf{R}}(\hat{\mathbf{Q}}) = 0, \tag{4.2}$$

for which $\hat{\mathbf{R}}(\hat{\mathbf{Q}}) = 0$ gives a steady-state solution. To realize a time-hyperbolic approach independent of the flow Mach number, TRACE treats the actual steady problem as an unsteady one and integrates in time until a steady solution is obtained. Between an explicit or implicit scheme to calculate the flow variables at the new time step $(\tau + 1)$, an explicit time discretization scheme was chosen, as recommended in the TRACE documentation for faster convergence, which also needs the prescription of a CFL condition to control the instabilities in the solving process. The selected Predictor Corrector method includes an Euler-backward scheme with a second-order accuracy. In an iterative calculation, the residual will never reach zero, but the aim is to obtain a sufficiently small value to stop the calculation and assume a nearly steady-state solution. A representative residual for all the cells or *global residual* can be obtained by means of the L_1, L_2, or L_∞ norms of the residual vector containing all the cell residuals. The global iteration error ($\varepsilon^\tau = u - u^\tau$, where u is a scalar quantity in place of $\hat{\mathbf{Q}}$) will thus be proportional to this global residual. According to *Ferziger et al.* (2020, p. 149), the sum of absolute residuals (L_1 norm) with equal weighting to all residual components can be used instead of the r.m.s norm (L_2), and the estimation of iteration error can be done within a single calculation. TRACE uses nondimensional quantities for the calculation of the L_1 norm

$$L_1 = \frac{1}{n_{\text{cells}}} \sum_{j}^{n_{\text{cells}}} \sum_{i}^{n_{\text{equations}}} \left| \frac{\Delta t_j}{V_j c} R_i^j \right|, \tag{4.3}$$

where R_i^j represents each the residual component; i stands for each one of the five governing equations for each cell j of the domain; V_j is the cell volume; Δt_j is the local pseudo-time step size; and c is the CFL number.

Block-structured grids of the test cases RADIVER Vaneless and Design603 were created with the meshing program AutoGrid5™. An O-block was chosen to wrap around the impeller blade, while the rest of the blocks were of H-type. The cell width at the walls was chosen so that, globally, the meshes had y^+ values close to one. Subsequently, the preprocessor interface GMC from the TRACE package served to build the numerical model by defining the rows *rotor*—rotating including the impeller blade—and *stator*—stationary containing the vaneless diffuser. A mixing plane approach was adopted between the rotor and stator—at a radial position further inside the vaneless diffuser

passage—to enable steady-stage, single-passage simulations through the blade rows in relative motion. Turbulence was modeled using the k-ω model from *Wilcox* (1988) with additional turbomachinery-specific curvature extensions. An initial 2D throughflow solution from a proprietary code from MTU Aero Engines AG (see Sec. 4.3) was used to set the boundary and initial conditions for the 3D CFD simulations. The inlet conditions for this 2D calculation were extracted from experimental data.

With this numerical setup, reference CFD calculations near the design point of each compressor yielded global L_1-residual values, (4.3), in the order of 10^{-5}. The total reduction in L_1-residual over the iteration process was of approximately four orders of magnitude, which can be translated into a 0.01% iteration error, approximately. Convergence per se was also assessed by means of the global imbalance of the mass flow rate from compressor inlet to outlet, which was approximately zero at the end of the iterations for all the simulations considered.

4.2.2 Grid Independence and Discretization Error

To quantify the *discretization error*, which is defined as the difference between the exact solutions of the governing and the discretized equations, a systematic grid independence study following the Grid Convergence Index (GCI) from the *Journal of Fluids Engineering* (2008) was carried out. This GCI serves as a measure of the discretization error, and the method is a revised and generalized procedure for turbulent flows of the original GCI introduced by *Roache* (1997). The original CGI is based on a Richardson extrapolation and requires a smooth, monotonic dependence on grid resolution, which is difficult to achieve in turbulent flows (*Ferziger et al.*, 2020, p. 63). Therefore, in this study, the revised GCI subject to the Journal of Fluids Engineering was used.

The grid independence study was carried out with three different grids for each compressor. A reference mesh density (*medium*) was defined, and then a *fine* and a *coarse* mesh were created additionally. In this refinement/coarsening process, the grid topology was unchanged. The grid cell size (h) in three-dimensions is defined as

$$h = \left[\frac{1}{N} \sum_{i=1}^{N} (\Delta V_i) \right]^{1/3}, \tag{4.4}$$

where ΔV_i is the cell volume and N is the total number of cells. Setting h_1 (fine) $< h_2$ (medium) $< h_3$ (coarse), the scaling factors between consecutive grid densities were obtained as

$$r_{21} = \frac{h_2}{h_1} = \left[\frac{N_1}{N_2} \right]^{1/3} \quad \text{and} \quad r_{32} = \frac{h_3}{h_2} = \left[\frac{N_2}{N_3} \right]^{1/3}, \tag{4.5}$$

for the same total discretization volume. The factors r_{21} and r_{32} from (4.5) were set to be around approximately 1.3, as recommended in the *Journal of Fluids Engineering* (2008, p. 1). For each of these grids, CFD simulations at the same operating point were carried out. Because in this dissertation the CFD calculations were used to calibrate the throughflow results for the impeller flow alone, the focus here was on the uncertainty

of the impeller results, and the GCI was computed for the impeller total-static pressure ratio, $\pi^{ts}_{Imp.}$, and total-static isentropic efficiency, $\eta^{ts}_{s,Imp.}$. The GCI was obtained, for both the fine and medium meshes, as

$$\mathrm{GCI}^{21}_{\mathrm{fine}} = \frac{1.25 e^{21}_a}{r^p_{21} - 1} \qquad \text{and} \qquad \mathrm{GCI}^{32}_{\mathrm{medium}} = \frac{1.25 e^{32}_a}{r^p_{32} - 1}, \tag{4.6}$$

where $e^{21}_a = |(\varphi_1 - \varphi_2)/\varphi_1|$ and $e^{32}_a = |(\varphi_2 - \varphi_3)/\varphi_2|$ are the approximate relative errors; φ denotes the variable in question—in this case, either $\pi^{ts}_{Imp.}$ or $\eta^{ts}_{s,Imp.}$; and p is the apparent order, which was calculated from the following implicit equation

$$p = \frac{1}{\ln(r_{21})} \left| \ln|\varepsilon_{32}/\varepsilon_{21}| + \ln\left(\frac{r^p_{21} - 1 \cdot \mathrm{sgn}(\varepsilon_{32}/\varepsilon_{21})}{r^p_{32} - 1 \cdot \mathrm{sgn}(\varepsilon_{32}/\varepsilon_{21})} \right) \right|. \tag{4.7}$$

In (4.7), $\varepsilon_{21} = \varphi_2 - \varphi_1$ and $\varepsilon_{32} = \varphi_3 - \varphi_2$ are the differences in the solution of consecutive mesh densities.

As expected for turbulent cases, the calculated apparent order (4.7) was not in agreement with the formal order of the discretization scheme (which is 2; see Sec. 4.2.1) for any of the cases. The results for the GCI are given in Table 4.2 for the two test cases RADIVER Vaneless and Design603. According to *Martin et al.* (2024, p. 5), the solution can be considered as independent on the grid if the GCI is equal to or less than the level of experimental uncertainty. In the case of Design603, the measurements from *Enneking* (2020) at the simulated operating point in this study provided an uncertainty of 0.68% for $\pi^{ts}_{Imp.}$ and a 1.29% uncertainty for $\eta^{ts}_{s,Imp.}$. From Table 4.2, $\mathrm{GCI}^{21}_{\mathrm{fine}}$ is in both cases lower than these experimental values, but the required computing time for the fine mesh in a calibration context with a simulation database would be nonviable. A compromise can be obtained with the medium grid, for which $\mathrm{GCI}^{32}_{\mathrm{medium}}$ for the pressure ratio is slightly over the experimental uncertainty, but for the isentropic efficiency it certainly lies within the experimental range. As for RADIVER Vaneless, which presented an oscillatory convergence ($\varepsilon_{32}/\varepsilon_{21} < 0$), the $\mathrm{GCI}^{32}_{\mathrm{medium}}$ for the pressure ratio and efficiency is about the same order of magnitude as for Design603. For the case of the fine mesh with $\mathrm{GCI}^{21}_{\mathrm{fine}} = 0.001\%$ for $\pi^{ts}_{Imp.}$, the discretization error would be smaller than the iteration error—which was approximated to 0.01% in Sec. 4.2.1—, and this should ideally not be the case (*Ferziger et al.*, 2020, p. 453). Accordingly, for RADIVER Vaneless, the medium mesh was also chosen, with the aim to define a unified procedure for both test cases.

Table 4.2: Results from the grid independence study. The GCI level of uncertainty, i.e., discretization error, is given for the impeller performance figures $\pi^{ts}_{Imp.}$ and $\eta^{ts}_{s,Imp.}$ on both the fine and medium meshes of the test cases.

	RADIVER Vaneless (*with oscillatory convergence*)		Design603 (*with monotonic convergence*)	
Parameter	$\varphi = \pi^{ts}_{Imp.}$	$\varphi = \eta^{ts}_{s,Imp.}$	$\varphi = \pi^{ts}_{Imp.}$	$\varphi = \eta^{ts}_{s,Imp.}$
$\mathrm{GCI}^{21}_{\mathrm{fine}}$	0.001%	0.11%	0.02%	0.01%
$\mathrm{GCI}^{32}_{\mathrm{medium}}$	0.04%	0.25%	0.76%	0.50%

4.2.3 Modeling Error

Now that the iteration and discretization errors have been shown to be small enough and that a grid-independent solution lies for both test cases, the *modeling error* with respect to experimental data is evaluated. The level of detail of the measurement data which is required for this purpose was only available for Design603. *Ziegler* (2003) provided the compressor map data for RADIVER Vaneless but argued (*Ziegler*, 2003, p. 37) that the upstream effect of the discharge collector on the impeller—which could not be quantified but affected the symmetry of the flow—hinders the use of the data for validation purposes. Also, at impeller outlet, kinematic quantities were measured for a single operating point. Contrarily, for Design603, *Enneking* (2020) provided detailed measurements at both impeller and compressor outlet, together with the corresponding measurement uncertainty values at each point. Therefore, in this section, the modeling error of the unified numerical setup will be quantified using Design603 data exclusively.

As with the discretization error, the focus here was on validating the CFD results for the impeller alone by means of $\pi^{ts}_{Imp.}$ and $\eta^{ts}_{s,Imp.}$. The comparison of experimental and CFD results for Design603 is given in Figure 4.1. For the selected operating point in red on the lowest rotational speed line in Figure 4.1a ($\pi^{ts}_{Imp.}$), the relative error of CFD with respect to experiment is of 0.21%, which is definetely inside the relative measurement uncertainty of 0.32% for this specific operating point. Overall, the agreement between the experimental and numerical results for this speed line is very high, with the exception of a few points in the vicinity of choke. In turn, for the selected operating point on the mid speed line—for which the discretization error was quantified; see Table 4.2—, the relative error of the CFD total-static impeller pressure ratio amounts to 1.00%, which is

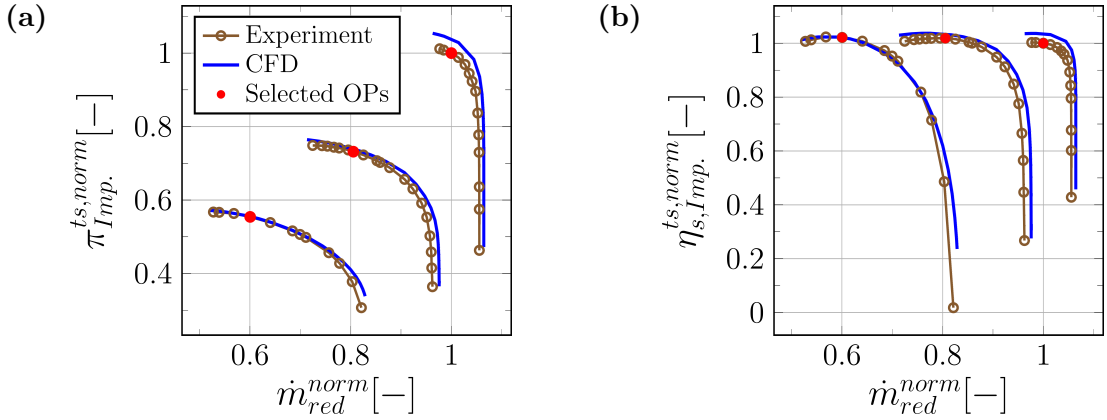

Figure 4.1: Comparison of CFD results and experimental data for Design603 for the purpose of analyzing the modeling error. Here the comparison is done for: **(a)** the total-static pressure ratio of the impeller, $\pi^{ts}_{Imp.}$; and **(b)** the total-static isentropic efficiency of the impeller, $\eta^{ts}_{s,Imp.}$. The selected operating points (OPs) in red on each speed line are chosen to analyze the relative error of CFD with respect to experiment—the measurement data are taken from *Enneking* (2020). The selected OP on the mid speed line corresponds to the point where the discretization error was quantified in Sec. 4.2.2. With that, the total numerical error in $\pi^{ts}_{Imp.}$ from the three error sources at this operating point adds up to 1.77%, and in $\eta^{ts}_{s,Imp.}$, to 1.98%.

over the relative uncertainty bound of 0.68%. This trend remains and becomes greater with increasing rotational speed: for the selected operating point on the highest speed line, which is also the design point of the compressor, the relative error adds up to 3.87%, which is clearly outside the measurement relative uncertainty range of 1.26% for this point.

The same behavior can be observed for the total-static isentropic efficiency, $\eta^{ts}_{s,Imp.}$ (see Figure 4.1b). While the relative error for the lowest rotational speed lies inside the measurement uncertainty range, for the highest rotational speed it becomes 2.01%, evidently outside the relative uncertainty bound of 1.42% in this case. This trend was also observed by *Enneking* (2020) with his RANS simulations of this same compressor, despite using a different turbulence model and a different CFD solver. He then argued (*Enneking*, 2020, p. 186) that the volute installed in the test rig, which corresponds to a volute casing for a marine turbocharger application, is too large for the rest of the compressor and causes a mismatch with the other components of approximately 67% at the design point (marked in red on the highest rotational speed in Figure 4.1b). This too large cross-sectional area for the incoming mass flow from the diffuser makes the flow decelerate and the static pressure increase, leading to a circumferentially inhomogeneous pressure field at diffuser outlet. This in turn results in a back-pressure of unsteady nature at impeller outlet (*Enneking*, 2020, p. 186; *Reymond et al.*, 2023, p. 3). In order to quantify this effect, *Enneking* (2020) carried out unsteady RANS (URANS) simulations of the entire circumferential section, still up until diffuser outlet but this time with experimentally determined inhomogeneous pressure profiles at diffuser outlet. He could identify a drop in stage efficiency of -1.1% from using unsteady simulations instead of steady ones. Similarly, *Reymond et al.* (2023) performed URANS simulations of the test rig with the same volute but with a different impeller, and they could also obtain a lower efficiency value than with RANS simulations. It is thus clear that for Design603, URANS simulations would be necessary to match experimental data better. However, this type of simulations are still too time consuming for routine design and for the purpose of this dissertation to build a database of CFD results, it would definitely be impractical. With the given conditions for this work, RANS simulations still have proven to be suitable to match the impeller experimental data reasonably well for the most points on the low to mid rotational speed lines.

4.3 Baseline Throughflow Calculations

In this section, the throughflow meshes for the impellers under consideration are presented and the algorithm for the baseline throughflow calculations is outlined.

4.3.1 Throughflow Setup and Basic Algorithm

For the throughflow calculations, a proprietary code from MTU Aero Engines AG was used, which is based on the streamline curvature method. The code can deal with arbitrary annulus geometries and curved calculating stations. Figure 4.2 shows the

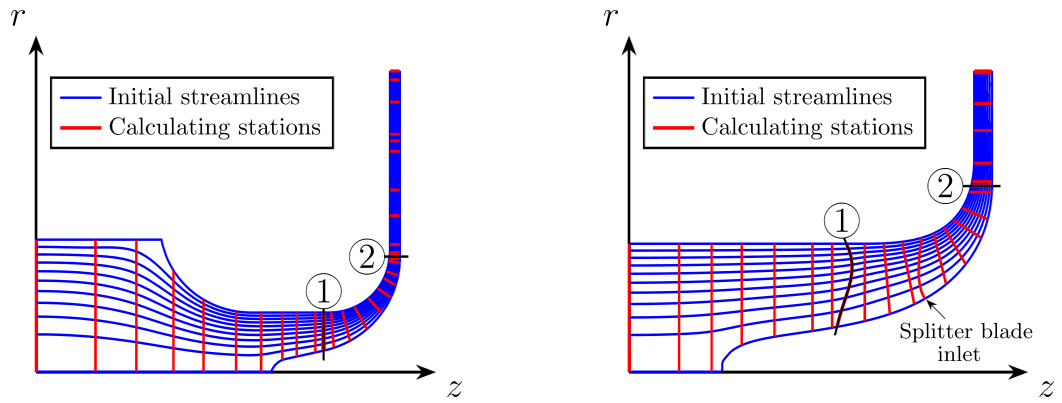

(a) RADIVER Vaneless **(b)** Design603

Figure 4.2: Initial throughflow meshes for: **(a)** RADIVER Vaneless, and **(b)** Design603. The index ① stands for impeller inlet, and the index ②, for impeller outlet.

2D meshes consisting of quasi-orthogonal calculating stations—depicted in red, which remain fixed during the calculation—and quasi streamlines—in blue, which change along the iteration process except for the hub and shroud streamlines.

Because the focus of this dissertation lies in calculating the performance of validated geometries, the analysis mode (refer to Sec. 2.3.2) is the appropriate solution approach in this case. Figure 4.3 shows the throughflow program structure to calculate the performance of a given geometry at a given operating point. This algorithm was taken as given by MTU Aero Engines AG and used as a black box in this dissertation. The baseline and calibrated throughflow workflows (see Sec. 4.3.2 and Sec. 4.4.1, respectively) were built around this basic algorithm from Figure 4.3.

The throughflow algorithm from Figure 4.3 works as follows. First of all, the solver needs the definition of the hub and shroud contours, as well as the quasi-orthogonal calculating stations (see Figure 4.2). Other necessary inputs include the entry flow conditions, such as total pressure, total temperature, swirl, mass flow rate, and rotational speed. Once the input file is read, the streamlines are initialized. This can be achieved by means of an equal-area distribution between the hub and shroud contours from Figure 4.2, divided by the total number of streamlines defined—in Figure 4.2, for example, eleven streamlines are depicted, including the hub and shroud streamlines. A previous flow solution can also be taken to initialize the position of the streamlines. After this step, the algorithm enters the core of the throughflow program. First, there is the choice whether to use prescribed values for the row losses, flow angles, and boundary layer blockage from the input file, or to use internal correlations to calculate them. Then, an internal loop is run to obtain the mass flow rate at the mean streamline of each calculating station. For that, the solver first sets constant total enthalpy for stator passages or constant rothalpy for rotors along a streamline—thus the value from the previous calculating station is taken, because the solver marches from inlet to outlet. Then, the target mass flow rate at each station is set through the Laval number and the conservation of energy at the mean streamline. The actual mass flow rate at each station is obtained by solving the radial equilibrium equation and subsequently integrating the continuity equation. The target and actual values of mass flow rate are compared and the iteration loop is repeated

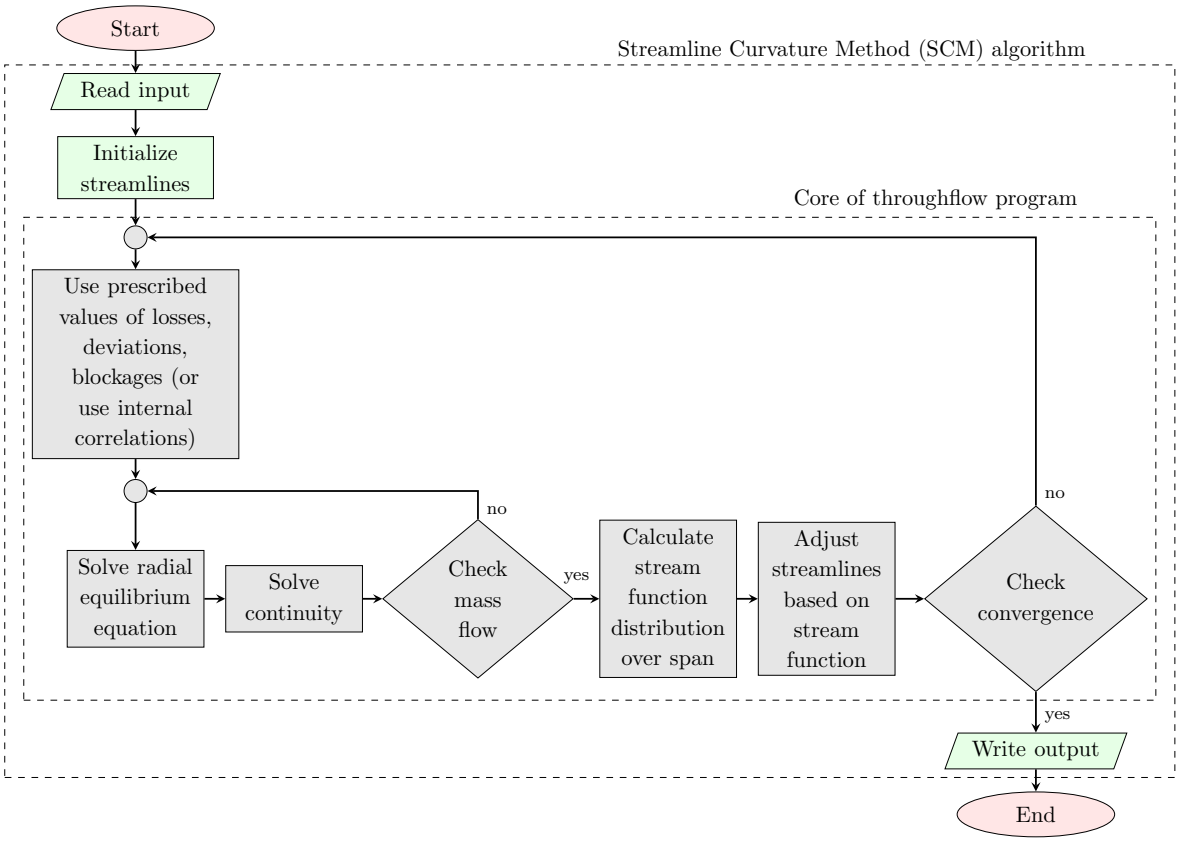

Figure 4.3: Basic throughflow calculation algorithm in the analysis mode to obtain the performance of a given geometry at a given operating point.

until a specified tolerance is reached. Once the final value of the mass flow rate is found, the solver proceeds to computing a distribution of the stream function values along the spanwise direction. Now, these values at each streamline position of the corresponding calculating station are compared with the target stream function distribution of 0.0, 0.1, 0.2, ..., 0.9, 1.0 for the predefined eleven streamlines. Underrelaxation is used to bring the calculated stream function values to the target ones. The streamlines are obtained by fitting a spline curve through the points with the required values of the stream function. With the second derivative of this curve, the streamline curvature radius can be calculated; see (2.48). The shift between the old and the new streamline positions is critical to the solver convergence, because significant shifts can boost instabilities of the overall algorithm. A tolerance is specified for the maximum change in streamline position. Until convergence is reached, the iteration loop is repeated with the current solution of the streamlines for the initialization. In the end, an output file is written with the aerodynamic results for each calculating station (average values and spanwise distributions), and also for each row defined and the whole domain from inlet to outlet.

The algorithm from Figure 4.3 was taken as given by MTU Aero Engines AG and used as a black box in this dissertation. The project's constraints forced the utilization of the algorithm in an external manner, precluding access to the source code of the core of the throughflow program highlighted in Figure 4.3. For this reason, to operate with the algorithm, external Python routines were developed which calculated the values of

the row losses, angles, and blockage, and then prescribed these values in the input file to Figure 4.3. This corresponds to the implementation of models for the impeller loss coefficient, the slip factor—which was then used to obtain the actual flow angles—, and the aerodynamic blockage in the impeller. This external operation loop for the throughflow solver is designated as *baseline throughflow algorithm* in this dissertation. A detailed description of this algorithm can be found in Sec. 4.3.2.

4.3.2 Baseline Throughflow Algorithm

As mentioned in Sec. 4.3.1, the basic throughflow algorithm from Figure 4.3 was used as a black box. The baseline workflow was built around it to calculate the performance of the impeller geometries according to specific empirical correlations for the slip factor, loss coefficient, and outlet aerodynamic blockage.

Figure 4.4 shows the implemented baseline calculation algorithm, which was designed for an automatic calculation of a set of predefined operating points, i.e., for the whole performance map of each geometry. Some of the empirical correlations depend on the impeller's outflow conditions. Therefore, to start the baseline calculation, an initial aerodynamic solution is required. For this, the algorithm first reads the predefined input file containing the geometry, inflow conditions, and initial prescription of values for row losses, angles, and aerodynamic blockage. It then enters the black box SCM algorithm (refer to Figure 4.3) to solve for the position of the streamlines and the corresponding aerodynamic solution. This constitutes the first block in the baseline workflow algorithm, as highlighted in Figure 4.4. With the initial flow solution, the baseline workflow from Figure 4.4 calls a set of new Python scripts—written in Python 3.6—to calculate the baseline values of the slip factor σ_{base}, the loss coefficient $(\Delta s/R)_{base}$, and the outlet aerodynamic blockage $B_{2,base}$ by means of empirical correlations from the literature—the specific correlations implemented are discussed in Chapter 5, Sec. 5.2, and chosen based on reference CFD results. The results for these three performance metrics (loss coefficient, slip factor, aerodynamic blockage) are calculated for the mean streamline.

As explained in Sec. 4.3.1, the core of the throughflow solver takes solely the mean streamline to evaluate the resulting mass flow rate at each calculating station. Accordingly, it made sense to implement literature correlations for the mean streamline and later define the spanwise distribution of the resulting flow quantities. This was also advantageous because, for radial compressors, there are no established two-dimensional correlations, but one-dimensional ones. In this case, as already mentioned in the literature review (see Sec. 3.1.1), for a one-dimensional calculation there are mainly two approaches: *single-zone* and *two-zone* modeling. As discussed in Sec. 3.1.1, the two-zone approach initially appears to offer a better representation of the impeller flow picture compared to the single-zone method. However, both single- and two-zone approaches do involve a certain degree of empiricism, and the two-zone solution algorithm was not easily compatible with the throughflow algorithm solving the radial equilibrium and continuity equations. For these reasons, a single-zone calculation was implemented in this case.

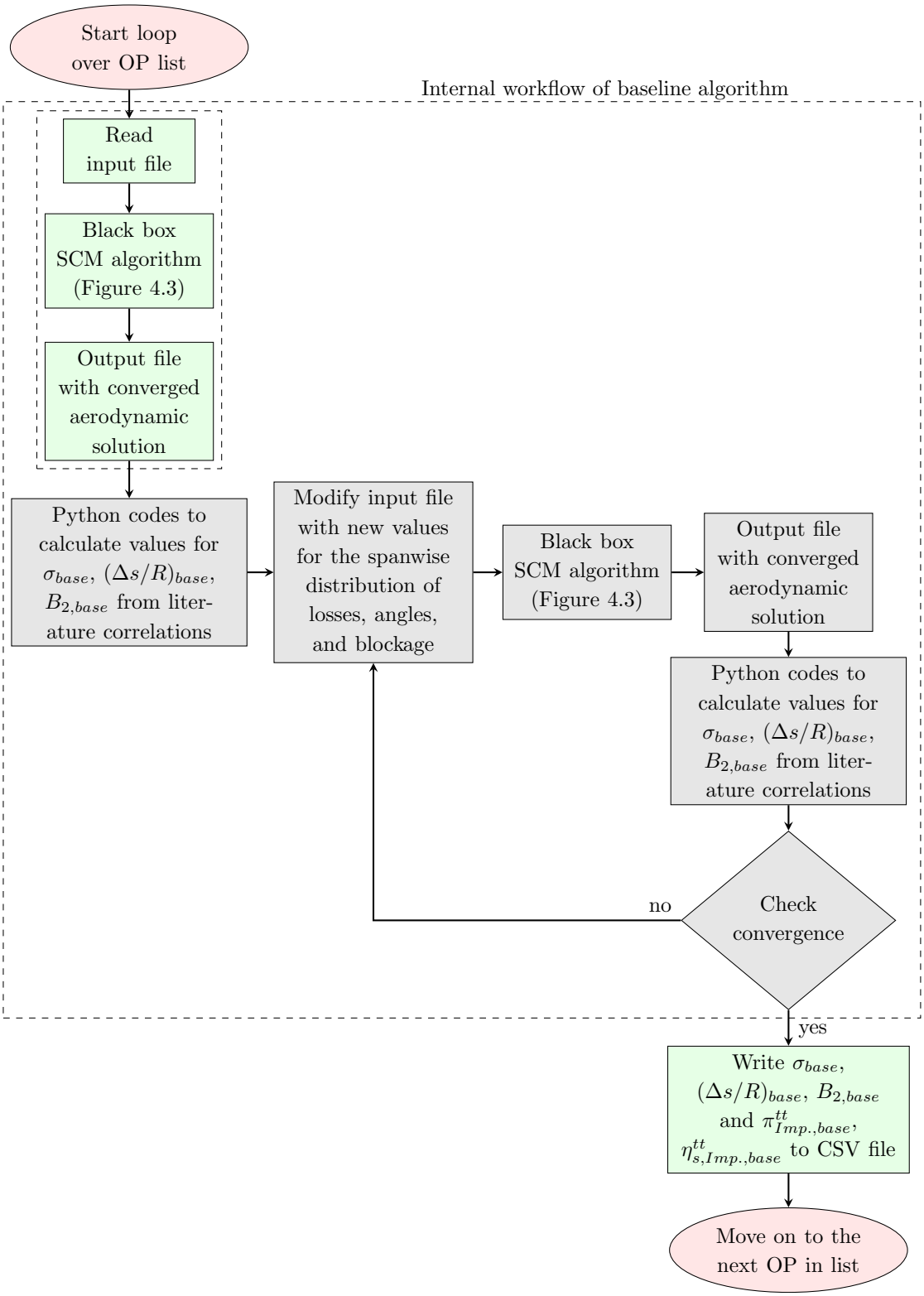

Figure 4.4: Flow chart describing the baseline throughflow calculation. The workflow is built for an automatic map calculation over all predefined operating points (OPs).

With the meanline results from the correlations, spanwise distributions were defined afterwards. The same meanline value was prescribed for each streamline position (see Sec. 5.2.2 for further details). From the uniform slip factor distribution and the given blade angle values at each spanwise location, the corresponding relative outflow angle distribution was calculated. The spanwise distributions of relative outflow angle, oulet loss coefficient, and outlet aerodynamic blockage were introduced in the initial input file. With the modified input file, the black box SCM algorithm was run again to obtain the corresponding aerodynamic solution. Because this aerodynamic solution is the result of the calculation with the prescribed values from the correlations, which in turn used an initial aerodynamic solution with values initialized from the design point, the current output cannot be taken as the correct one. Instead, the calculation of the values for the metrics of slip factor, loss coefficient, and aerodynamic blockage with the empirical correlations needs to be iterated until these values do not change more than a specified tolerance with respect to the previous iteration. Because this loop can take very long, as it always waits for the internal convergence of the position of the streamlines, it may also be replaced by a specific number of iterations instead, such as ten, which was found to be satisfactory for most of the operating conditions under study. Finally, once convergence is reached—or the prescribed number of iterations is finished—, the algorithm writes the output with the final results for the empirical metrics and the corresponding total-total impeller pressure ratio and isentropic efficiency results. After that, the algorithm proceeds on to the next operating point on the list and starts the calculation workflow again. The results for the subsequent operating points are appended to the existing results file to provide a unique list of performance map results.

4.4 Machine Learning-Enhanced Throughflow Calculations

In this section, the implemented algorithm for the machine learning-enhanced throughflow calculations (*calibrated*) is described. An overview of the proposed sampling method to collect the training data for the neural network regression is also given.

4.4.1 Calibrated Throughflow Algorithm

Figure 4.5 shows the calibrated throughflow algorithm, which was also built for an automatic map calculation as the baseline workflow. The algorithm here starts by calling the baseline calculation from Figure 4.4 to obtain a converged baseline solution, which will be the starting point for the calibration. The basic idea of the calibration algorithm is that any user-defined operating point in the performance map of the two test cases from Sec. 4.1 can be calculated with the 2D throughflow solver. Each calculation accesses a predefined *solution surface* that maps scaling factors $\hat{F}$ to be multiplied to the baseline slip factor, loss coefficient, and aerodynamic blockage in order to match reference 3D CFD results

$$\sigma_{calib} = \hat{F}_{\sigma}\sigma_{base}, \tag{4.8}$$

$$(\Delta s/R)_{calib} = \hat{F}_{\Delta s/R}(\Delta s/R)_{base}, \tag{4.9}$$

$$B_{2,calib} = \hat{F}_{B_2}B_{2,base}. \tag{4.10}$$

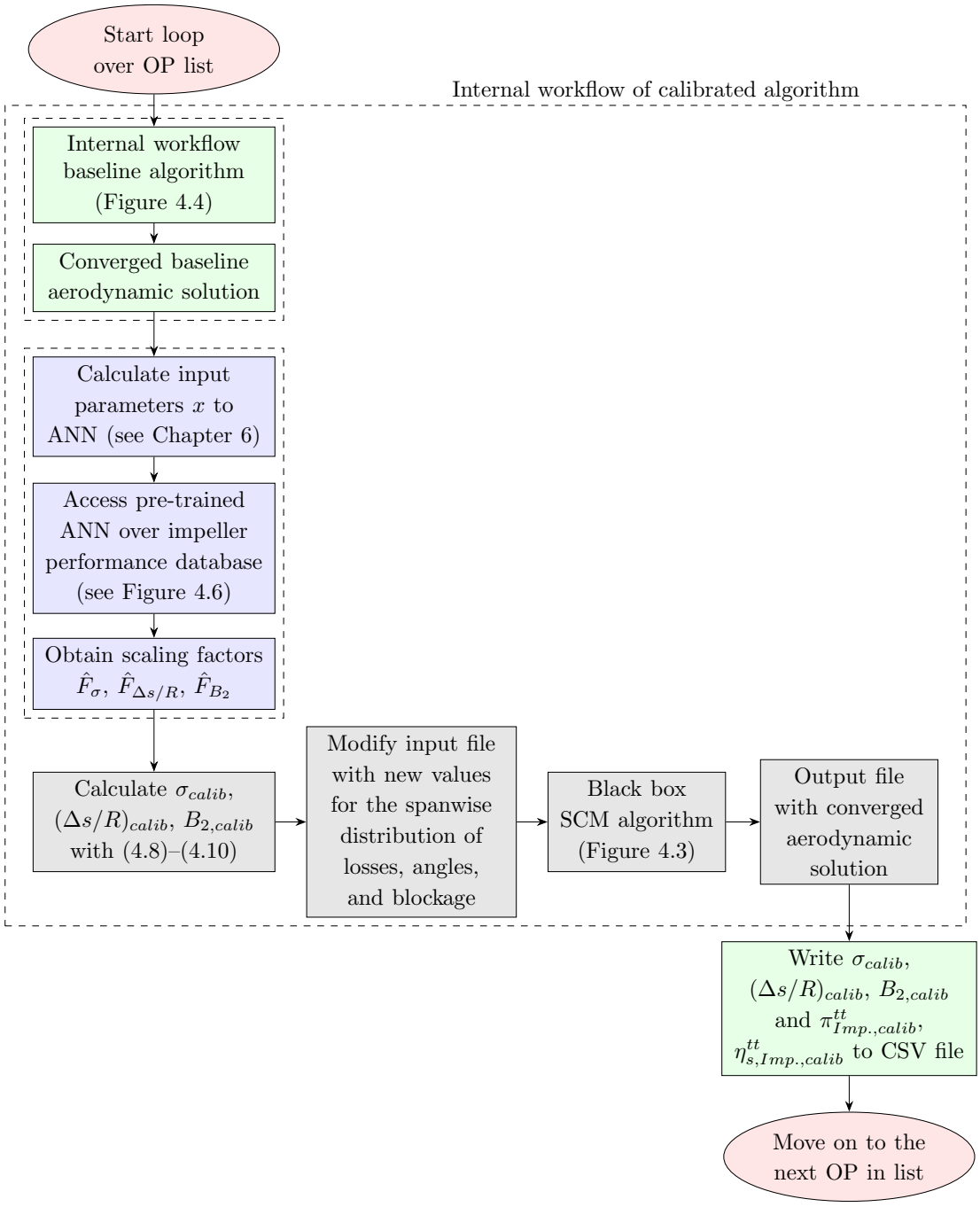

Figure 4.5: Flow chart describing the calibrated throughflow calculation.

This mapping is carried out prior to the calibrated throughflow workflow by means of an artificial neural network (see Figure 4.6), which is trained offline on a predefined database of CFD and baseline throughflow results (see Sec. 4.4.2). In the calibrated throughflow algorithm from Figure 4.5, after obtaining the converged baseline solution, the workflow calculates the current input SCM parameter values to enter the ANN pre-trained model. With these parameters $\mathbf{x}$ (see Sec. 6.1 for details), the workflow accesses the available ANN surface and interpolates on it to find the corresponding output values for the scaling factors $\hat{F}_\sigma$, $\hat{F}_{\Delta s/R}$, $\hat{F}_{B_2}$. The true values for these factors are set in the ANN training as

$$F_\sigma = \frac{\sigma_{CFD}}{\sigma_{base}}, \qquad F_{\Delta s/R} = \frac{(\Delta s/R)_{CFD}}{(\Delta s/R)_{base}}, \qquad F_{B_2} = \frac{B_{2,CFD}}{B_{2,base}}, \tag{4.11}$$

at identical operating points for CFD and baseline. What the ANN regression does is to approximate these true responses (4.11) as nonlinear functions $\hat{F} = f(\mathbf{x})$ of the given input parameters $\mathbf{x} = (x_1, x_2, \ldots, x_p)$, so that $F = \hat{F} + \varepsilon$ holds, where ε is the error of approximation.

To account for the coupling between the flow processes in the impeller, which altogether determine not only the losses, but also the slip and the aerodynamic blockage at impeller outlet, a three-input/three-output neural network was built (see Figure 4.6), instead of three separate ones for each output. In such multi-task learning, multiple responses ($\hat{F}_\sigma$, $\hat{F}_{\Delta s/R}$, $\hat{F}_{B_2}$) are predicted simultaneously, and they all contribute towards the formation of the hidden layers (*James et al.*, 2023, p. 403). This helps improve generalization, as soft constraints are intrinsically imposed on the parameters, in order for them to match the multiple output targets at the same time (*Goodfellow et al.*, 2016, p. 241). The network, outlined in Figure 4.6, was chosen to have two hidden layers, as this is the minimum number that allows a neural network model to provide a universal approximation framework (*Goodfellow et al.*, 2016, p. 194). For the activation functions,

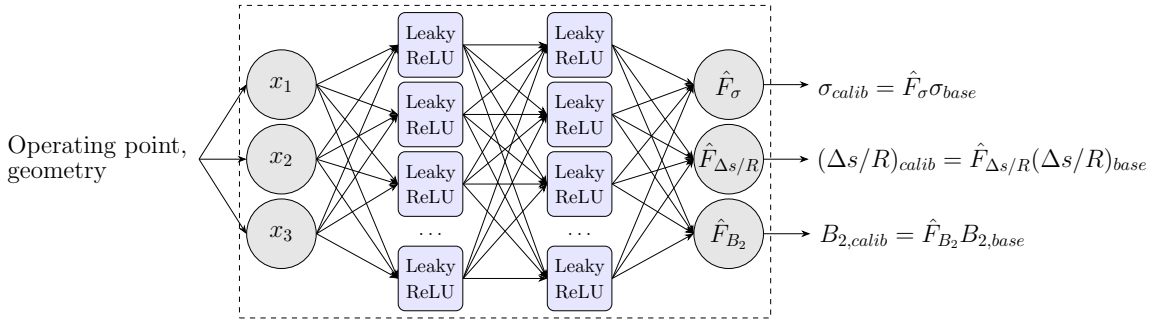

Figure 4.6: Chosen neural network architecture. It consists of three input nodes (x_1, x_2, x_3), three output nodes ($\hat{F}_\sigma$, $\hat{F}_{\Delta s/R}$, $\hat{F}_{B_2}$), and two hidden layers of nodes with the LeakyReLU activation function (refer to Figure 2.15). The specific input parameters x_1, x_2, x_3 and the number of nodes in the hidden layers were chosen as part of the results section in Chapter 6. The final values for the calibrated slip factor, loss coefficient, and aerodynamic blockage are obtained by multiplying the output network values by the baseline throughflow results.

the LeakyReLU function was chosen due to its improved performance for regression problems, as discussed in Figure 2.15. The specific input parameters and the number of nodes in the hidden layers were chosen as part of the results section in Chapter 6.

To train and evaluate the performance of the ANN regression model, a PyTorch algorithm was implemented. The library PyTorch written in the Python programming language was chosen because it is the most predominant deep learning library for research purposes. It provides more flexibility to build your own project compared to other more commercial tools such as TensorFlow (*AnalytixLabs*, 2024). The Python-like coding was also advantageous for the incorporation of the regression algorithm into the calibrated throughflow calculation workflow from Figure 4.5, which was also written in Python. The high-level flowchart algorithm is depicted in Figure 4.7 to visually show the broad steps and the logic of the ANN training.

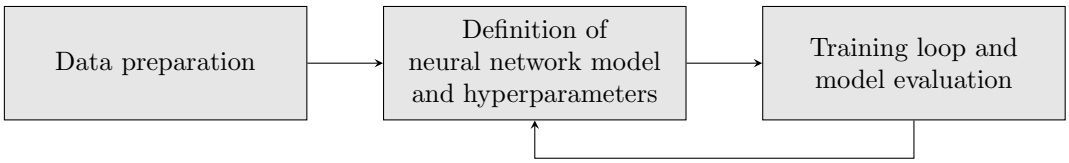

Figure 4.7: Broad steps of the regression workflow with neural networks.

The flowchart in Figure 4.7 consists of three steps: data preparation, neural network model definition, and training loop and evaluation. Broadly, in the data preparation, the training and test data sets are defined and standardized (see *scikit-learn* (2025)). Subsequently, in the second step, the neural network model is defined as a sequential stack of layers—each layer is a combination of a linear function of the inputs and an additional activation function. The hyperparameters that are defined here are: number of inputs and outputs to the neural network, number of hidden layers, number of nodes per hidden layer, activation function for each hidden layer, learning rate for the Adam algorithm (see Sec. 2.4.3), batch size, and number of epochs (iterations). The last step is the training of the model and performance evaluation. This is an iterative process that loops over the number of epochs, batches, and training/validation datasets with the equations (2.63)–(2.69) from Sec. 2.4.3. If the performance of the current model is not the desired one, hyperparameters are changed and the model is trained again.

The final model was then used to obtain the corresponding scaling factors $\hat{F}$ for each user-defined operating point and geometry. These factors were then used to calculate the calibrated values for the slip factor, loss coefficient, and aerodynamic blockage with (4.8)–(4.10). With these new *meanline* results, the spanwise distributions were defined in the same way as with the baseline algorithm (see Sec. 4.3.2) and incorporated into the input file for the throughflow solver. With the modified input file, the black box SCM algorithm was run again to obtain the corresponding aerodynamic solution with the final values for the the total-total pressure ratio and isentropic efficiency, $\pi^{tt}_{Imp.,calib}$ and $\eta^{tt}_{s,Imp.,calib}$. The calibrated algorithm from Figure 4.5 writes these results to the map CSV file and proceeds on to calculating the next operating point on the list.

4.4.2 Training Data Collection

For the regression with the artificial neural network, the dataset must be separated into training and test data, in order to assess the performance of the machine learning model on unseen data. For the relatively low number of test cases in this dissertation, the compressor map data was certainly insufficient to carry out successful training and test procedures. In the machine learning community, a usual technique to increase the amount of training data is to modify some features of the current samples, thus to fabricate new data as a means of data augmentation (*Goodfellow et al.*, 2016, p. 236). Accordingly, in this study, additional samples were created by means of scaling and similarity concepts to the speed lines in the compressor maps. In this way, the reference compressors RADIVER Vaneless and Design603 were still preserved, but additional operating conditions could be included in the database.

First of all, for the *geometric scaling*, not all compressor dimensions were scaled by a reference length, but the clearance gap alone. The clearance gap changes with operating condition under the influence of structural and thermal loads. A suggested parameter in the literature (*Senoo and Ishida*, 1987; *Diehl et al.*, 2020) for this scaling is the *tip clearance ratio*, which for the impeller exit is given by $CR_2 = \varepsilon_2/b_2$. In the present case, b_2 was left constant and ε_2 was varied. The second scaling was done by means of the Reynolds number, which is known to greatly influence the performance of radial compressors (*Wiesner*, 1979; *Simon and Bülskämper*, 1984; *Casey*, 1985). The variation of Reynolds number constitutes a *fluid dynamic scaling*, and the definition adopted in this dissertation is the generally accepted one for impellers with narrow channels (*Casey*, 1985), which reads

$$Re = \frac{u_2 b_2}{\nu_1} = \frac{\rho_{t1} u_2 b_2}{\mu_{t1}} = \frac{p_{t1} u_2 b_2}{R T_{t1} \mu_{t1}}. \tag{4.12}$$

The approach from *Simon and Bülskämper* (1984) was followed, who also adopted (4.12) and carried out variations of Reynolds number (in their case, experimental) basically by altering the inlet pressure. This means that the quantities u_2 and T_{t1} in (4.12) were assumed to be constant, which corresponds to having a *thermodynamic similarity*. In radial compressors, thermodynamic similarity is characterized by the tip-speed Mach number $M_{u2} = u_2/\sqrt{\kappa R T_{t1}}$. With that, the parameter for the Reynolds number variations in the present work was $p_{t1}/p_{t1,ref}$, where ref refers to the speed line in question.

To determine the spatial arrangement of the computer samples within the design space, the technique *Latin hypercube sampling* (LHS) was chosen, which is basically a multi-dimensional stratification or uniform distribution of the parameters within the design space. This technique splits the range of each variable, $p_{t1}/p_{t1,ref}$ and CR_2, into a predefined number of equal sized bins (hypercubes)—in the present case, ten—and generates a random sample for each of these bins. The range of the parameter CR_2 was chosen so that it fitted both test cases, which was about ±20% the reference value in each case. As for parameter $p_{t1}/p_{t1,ref}$, its range was selected based on the model from *Casey* (1985) for Reynolds-dependent losses depicted in Figure 4.8a. The model shows that, as the Reynolds number increases, the efficiency tends towards an asymptotic behavior, where the flow becomes hydraulically rough and does not allow for a change in performance

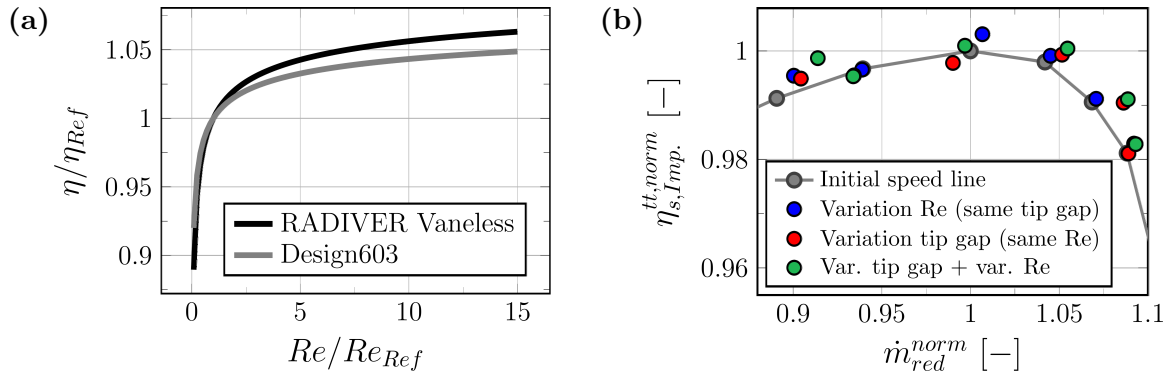

Figure 4.8: **(a)** Dependency of the efficiency with Reynolds number for a single operating point of each compressor, in order to identify the range to sample in the LHS. Here, the model from *Casey* (1985) was used, $\eta - \eta_{Ref} = -k(\lambda - \lambda_{Ref})$, where Ref corresponds to the CFD values at the selected operating point, k is a function of b_2/D_2 and c_{u2}/u_2, and $\lambda = f(Re)$ is the friction factor of the equivalent pipe flow—here for fully turbulent flow and hydraulically smooth surfaces, with the Colebrook-White formula. **(b)** Zoom on a Design603 speed line to illustrate the application of the sampling concept. This was done for a total of ten points on each of the three speed lines of each compressor, and the combination of $(p_{t1}/p_{t1,ref}, CR_2)$ values was the same for each speed line.

with Reynolds number anymore (*Casey and Robinson*, 2011, p. 866). The present study focused on the region where the flow is still hydraulically smooth, which is where there are significant changes in performance with Reynolds number. A representative section of the curves in Figure 4.8a where the changes are evident for both compressors was selected. Sampling simulations were carried out for values of Re/Re_{ref} up until approximately 3, which corresponds to $p_{t1}/p_{t1,ref} \approx 3$. A similar approach with this section of the efficiency curve was also followed by *Diehl et al.* (2020).

This sampling concept was first presented in *Labat Casajust et al.* (2023). Confirmation of the suitability of such an approach was found in *Lottini et al.* (2024), who also built a database of radial compressor performance results by means of p_{t1} variations. *Lottini et al.* also sampled T_{t1} and $\dot{m}$ values. In the present dissertation and in *Labat Casajust et al.* (2023), T_{t1} was left unchanged—thus assuming thermodynamic similarity—, and the operating point variations were also included in the way that the sampling was applied to each speed line. The resulting values from the LHS were applied in a systematic way to ten given operating points on each speed line of both CFD and baseline throughflow calculations. The combinations, depicted in Figure 4.8b, were: variation of Reynolds number, variation of tip gap, and variation of tip gap plus variation of Reynolds number. These sampling results were used as training data, and the operating points on the initial speed lines were taken as test data (approx. 70-30% distribution).

5 Baseline Results and Discussion

In this chapter, a comprehensive analysis of possible literature correlations that apply to both test cases under study is carried out, with the aim to define a unified methodology for the baseline throughflow calculation. The choice of correlations is done primarily according to reference Computational Fluid Dynamics (CFD) results with the numerical setup from Sec. 4.2. In the end, a robust set of correlations is recommended, which provides an accurate initial performance map prediction of modern impeller geometries. The yet present shortcomings of such an empirical methodology are also analyzed, and the potential for improvement with the calibration is outlined.

5.1 Definition of Reference Curves

To begin with, the modeling error of the throughflow solver with respect to CFD is quantified, with the aim to address possible differences between them. Only then can the reference curves be established, based on which the quality of the modeling in this chapter will be assessed.

5.1.1 Throughflow Results with CFD Values of Models

In order to validate the baseline calculation workflow from Sec. 4.3.2, the CFD values of slip factor, loss coefficient, and aerodynamic blockage were first prescribed in the throughflow solver. Then, the results of pressure ratio and isentropic efficiency were compared between the two solution methods. Here, the assessment was done based on the impeller total-total quantities $\pi^{tt}_{Imp.}$ and $\eta^{tt}_{s,Imp.}$ and not on the total-static ones as in Sec. 4.2 (CFD vs. experiment), because the total quantities are a direct measure of the component performance losses to be modeled in this dissertation. For the slip factor (σ), the American definition was used

$$\sigma = 1 - \frac{c_{\text{slip}}}{u_2} = 1 - \frac{c_{u2,\infty} - c_{u2}}{u_2}, \tag{5.1}$$

which is the common one in the literature, also among European authors such as *Hildebrandt and Genrup* (2006) and *Stuart et al.* (2017), for example. The European definition ($\sigma' = c_{u2}/c_{u2,\infty}$) quantifies the work reduction instead of the slip velocity. For the test cases in this work—RADIVER Vaneless and Design603—, which are both backswept impellers, the velocity triangle at the outlet is built with a relative velocity vector pointing in the opposite direction to the wheel rotation. As such, in accordance with the liter-

ature convention (*Whitfield and Baines*, 1990, p. 89; *Casey and Robinson*, 2022, p. 1), the blade angle is considered to be negative. From the velocity triangles in Figure 2.1b, it holds that

$$\begin{cases} \tan\beta_2 = \dfrac{c_{u2} - u_2}{c_{m2}} \rightarrow c_{u2} = u_2 + c_{m2}\tan\beta_2, & (5.2) \\ \tan\beta_{2b} = \dfrac{c_{u2,\infty} - u_2}{c_{m2}} \rightarrow c_{u2} = \sigma u_2 + c_{m2}\tan\beta_{2b}. & (5.3) \end{cases}$$

In (5.3), the slip factor definition (5.1) has been introduced. Equating (5.2) and (5.3) yields

$$\sigma = 1 + \varphi_2(\tan\beta_2 - \tan\beta_{2b}), \tag{5.4}$$

where $\varphi_2 = c_{m2}/u_2 > 0$ is the flow coefficient at impeller outlet. The reference CFD slip factor was obtained with (5.4) using mass-averaged properties at impeller outlet. For the CFD impeller loss coefficient

$$\left.\frac{\Delta s}{R}\right|_{Imp.} = \frac{\kappa}{\kappa - 1}\ln\left(\frac{T_{t2,rel}}{T_{t1,rel}}\right) - \ln\left(\frac{p_{t2,rel}}{p_{t1,rel}}\right), \tag{5.5}$$

also mass-averaged properties were taken. Finally, for the aerodynamic blockage at impeller outlet (B_2), the definition (2.50) was used, which involves both mass- and area-averaged quantities

$$B_2 = 1 - \frac{A_{2,\text{eff}}}{A_2} = 1 - \frac{\overline{c}_{m2}^{area}}{\overline{c}_{m2}^{mass}}. \tag{5.6}$$

The evaluating planes ① (impeller inlet) and ② (impeller outlet) are outlined in Figure 4.2 and were taken to be exactly the same in CFD and in throughflow.

When prescribing these CFD values (5.4)–(5.6) in the throughflow calculation workflow from Figure 4.4, significant differences in total-total pressure ratio and isentropic efficiency were obtained between CFD and throughflow. In an attempt to match the results from both modeling approaches, the throughflow solver setup was adjusted to CFD at the peak efficiency (PE) point on the mid speed line of each compressor: the blockage from CFD needed to be scaled in the throughflow code with a constant factor for each compressor to reach the same meridional velocity at impeller outlet, and this correction factor was then maintained for the other speed lines under study. The results for this adjustment are given in Figure 5.1, where throughflow is hereinafter referred to as "SCM" for Streamline Curvature Method.

For RADIVER Vaneless (see Figure 5.1a), the blockage adjustment yielded, at the peak efficiency point, a relative error in outlet meridional velocity of -0.79% from SCM with respect to CFD, while in isentropic efficiency the error corresponds to -0.15%, and in pressure ratio, it is of -2.55%. This significant offset in $\pi_{Imp.}^{tt}$ prediction occurred despite matching the meridional velocity. By observing the other speed lines, it can be recognized that this prediction offset increases with rotational speed and towards lower mass flow rates: for the lowest mass flow rate at the lowest rotational speed, the relative error in $\pi_{Imp.}^{tt}$ from SCM with respect to CFD is of -2.84%; for the mid speed line, it becomes -4.25%; and for the highest rotational speed, it reaches a value of -5.36%.

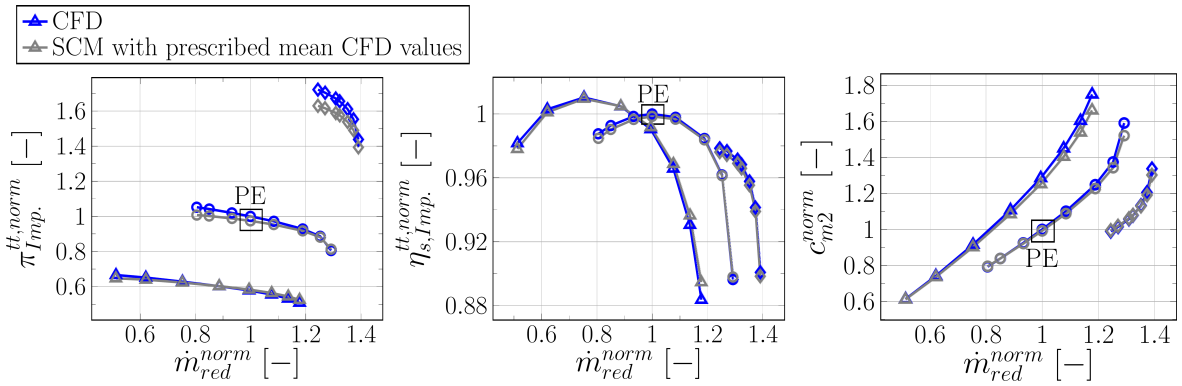

(a) RADIVER Vaneless

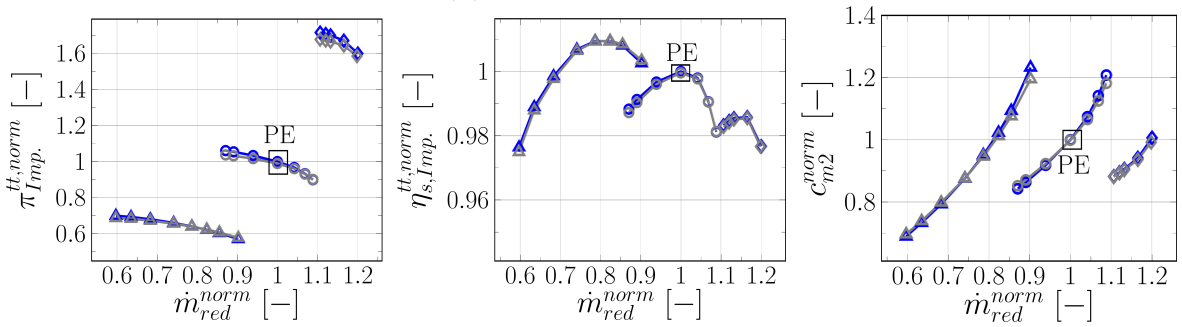

(b) Design603

Figure 5.1: Comparison of throughflow (SCM) and CFD results for the purpose of quantifying the throughflow modeling error. SCM was calculated with prescribed CFD mean values and uniform spanwise distributions of σ (5.4), $(\Delta s/R)_{Imp.}$ (5.5), and kB_2 (5.6), with $k < 1$ required to match the reference CFD curves. This blockage adjustment was done for the peak efficiency (PE) point on the mid speed line of each compressor and the scaling factor was maintained for the rest of the speed lines. The SCM results were calculated up until impeller outlet and not until compressor outlet with the aim to focus the calibration in this thesis on the impeller as a standalone component and avoid diffuser effects which are not modeled.

The relative error in isentropic efficiency prediction at these points is nearly negligible, with all values under -0.4%. A similar trend in throughflow pressure ratio prediction was obtained for Design603 (see Figure 5.1b), where in this case the relative error in pressure ratio at the lowest mass flow rates increases from -1.78% to -2.25% with rotational speed.

To investigate this difference in pressure ratio results between SCM and CFD, the prediction of work input with identical losses is compared in Figure 5.2. For both RADIVER Vaneless (see Figure 5.2a) and Design603 (see Figure 5.2b), the blade work coefficient $\lambda_b = c_{u2}/u_2$ matches towards lower mass flow rates, but there is an increasing offset in total work input coefficient $\lambda = \Delta h_{t,12}/u_2^2$ between CFD and SCM. This points to a difference in total enthalpy results at impeller outlet between the two solvers. With that, a check on the conservation of rothalpy ($I = h_t - uc_u$) gives $\Delta I_{12,CFD} \neq 0$ and $\Delta I_{12,SCM} = 0$ at each operating point in the performance map. Therefore, the rothalpy is conserved in SCM—which conforms to the common approach in throughflow methods

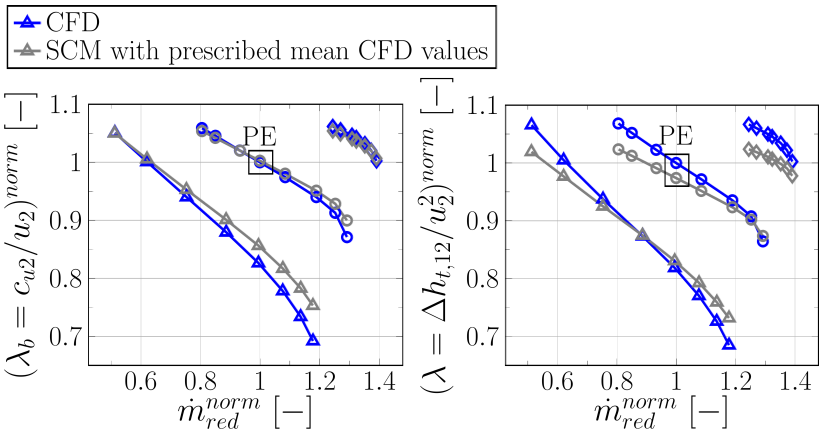

(a) RADIVER Vaneless

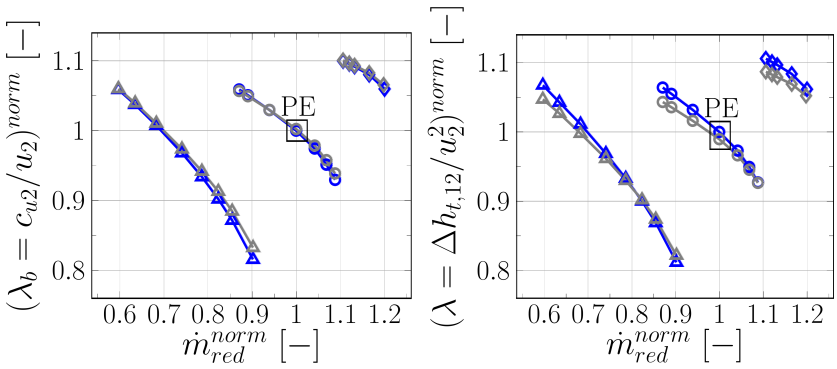

(b) Design603

Figure 5.2: Comparison of throughflow (SCM) and CFD results for the purpose of identifying the cause for the mismatch in pressure ratio prediction between SCM and CFD when the same model values are prescribed (see Figure 5.1). Here, the comparison is done for the blade work coefficient ($\lambda_b = c_{u2}/u_2$) and the total work coefficient ($\lambda = \Delta h_{t,12}/u_2^2$). The peak efficiency (PE) point is also highlighted in each figure.

to assume constant rothalpy, because it helps simplify the calculation along the streamlines (refer to Sec. 4.3.1)—, but not in CFD. Several authors have already addressed the nonconservation of rothalpy in radial impellers (*Moore et al.*, 1984, p. 478; *Lyman*, 1992, p. 4, 5; *Casey and Robinson*, 2021, p. 71, 72). *Lyman* (1992, p. 2) pointed out that, for convenience, viscosity is usually neglected in the derivation of the Euler's turbine equation, but that it is actually a relevant contribution to the rothalpy transport. This was also confirmed by *Casey and Robinson* (2021, p. 71, 72), who claimed that for open impellers with a tip clearance gap, the viscous fluid on the walls of the stationary shroud extracts shear work from the impeller control volume in the rotating frame of reference. The shaft must supply this extra work, which leads to an increase in rothalpy. *Moore et al.* (1984, p. 478) found for their CFD calculations of an open impeller that the shear work at the impeller shroud accounted for 1.17% of the total work input. *Bosman and Jadayel* (1996, p. 411), however, indicated that this viscosity near the tip region can be influenced by the chosen numerical scheme and its inherent numerical errors, especially with RANS simulations.

5.1.2 CFD Results Correction for Throughflow Comparison

Given the constraints imposed by the project (see Sec. 4.3.1), it was not possible to modify the core algorithm of the throughflow solver. Consequently, the assumption of conservation of rothalpy in the throughflow calculation could not be modified. To ensure a valid comparison with CFD, it is essential that the results from CFD and SCM are calculated at the same total enthalpy level at impeller outlet. The compression process that takes place in CFD and in "SCM with prescribed mean CFD values" is depicted in Figure 5.3 (blue and gray, respectively). The losses that were prescribed in Figure 5.1 and Figure 5.2 correspond to Δs_{total} in Figure 5.3, because this is the compression process $1 \rightarrow 2$ from CFD. However, as discussed in the previous section, these losses contain not only the internal flow contribution but an external loss from the viscosity in the near tip region. This external or parasitic loss absorbs work and increases the total temperature, but does not contribute to the total pressure rise across the impeller (p_{t2} is the same). Based on Figure 5.3, because in Sec. 5.1.1 the Δs_{total} was prescribed and the rothalpy is set constant in SCM, the outflow conditions had to remain at the $\Delta h_{t,Euler}$ level. This caused an offset in the total pressure isobar, leading to $p'_{t2} < p_{t2}$, and thus to $\pi^{tt}_{Imp.,SCM} < \pi^{tt}_{Imp.,CFD}$ in Figure 5.1.

Because the throughflow solver had to be used externally (refer to Sec. 4.3.1), only the impeller losses, flow angles, and aerodynamic blockage could be prescribed in the input file. The values of $\Delta s/R$ in the input file corresponded exclusively to the internal losses, which diminish the total pressure. Nevertheless, in an attempt to include the effect of the external losses in a post-processing step after the baseline throughflow calculation

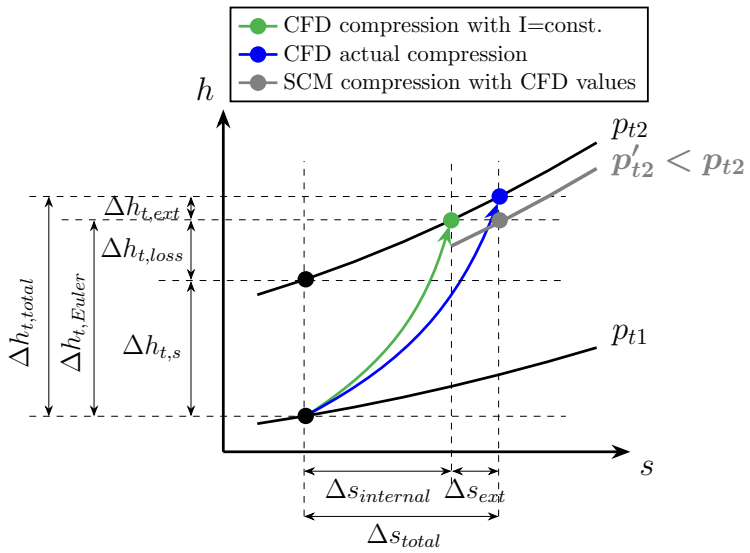

Figure 5.3: Representation of the compression process in CFD and in "SCM with prescribed mean CFD values". The actual compression process in CFD includes the external losses Δs_{ext} which increase the total temperature at outlet without a corresponding increase in total pressure. If Δs_{total} is prescribed in SCM, because of the conservation of rothalpy, the compression process remains at the $\Delta h_{t,Euler}$ level, resulting in a smaller total pressure at impeller outlet p'_{t2}.

loop from Figure 4.4, additional literature correlations for disk friction and recirculation effects were implemented. However, the SCM results still did not completely match the CFD reference curves. This introduced an additional degree of uncertainty in the modeling procedure. Consequently, the focus was shifted to modeling only the internal losses in an attempt to first ensure a correct modeling approach in line with the project's constraints. Extending the methodology to include external losses was considered a future line of research. Accordingly, the CFD loss values were corrected to only account for the internal contribution (Δs_{int}). The new outflow conditions for the CFD results correspond to the green point in Figure 5.3 and were obtained by setting the rothalpy constant, $I_1 = I_2$, i.e., $h_{t1} - u_1 c_{u1} = h_{t2,new} - u_2 c_{u2}$. From this expression, the new outlet total temperature was calculated as $T_{t2,abs,new} = T_{t1} + (u_2 c_{u2} - u_1 c_{u1})/c_p$, which was then used to obtain the internal loss coefficient to be prescribed in SCM as

$$\left.\frac{\Delta s}{R}\right|_{Imp.}^{int.} = \frac{\kappa}{\kappa - 1} \ln\left(\frac{T_{t2,abs,new}}{T_{t1,abs}}\right) - \ln\left(\frac{p_{t2,abs}}{p_{t1,abs}}\right). \tag{5.7}$$

The slip factor and the aerodynamic blockage do not have to be changed, as they already describe the useful work input of the blade. The new performance map results for total-total pressure ratio and isentropic efficiency are given in Figure 5.4. For both test cases,

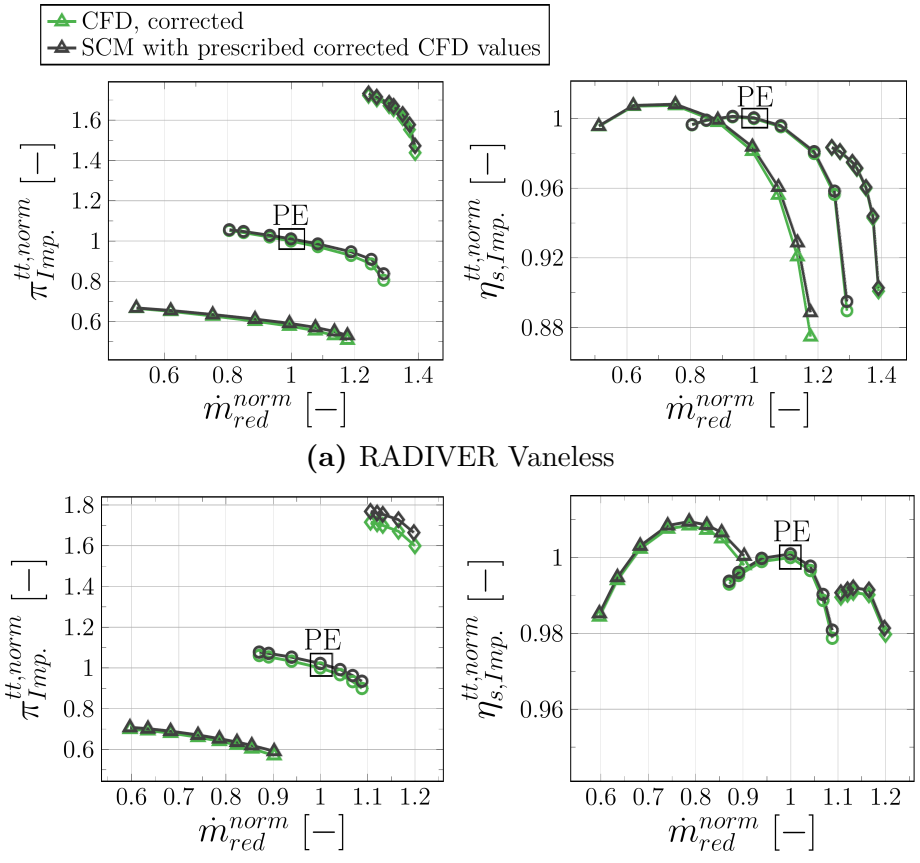

(a) RADIVER Vaneless

(b) Design603

Figure 5.4: Comparison of impeller total-total pressure ratio and total-total isentropic efficiency for CFD and throughflow (SCM) when constant rothalpy is set.

the modification of the CFD loss coefficient with (5.7) allows the prediction with SCM to match the CFD results towards low mass flow rates, and generally over the whole speed lines. There are still some minor differences between them, mostly for Design603 at the highest rotational speed (see Figure 5.4b), where the SCM prediction yields higher values of $\pi^{tt}_{Imp.}$ and $\eta^{tt}_{s,Imp.}$ than CFD. However, these offsets now remain approximately constant over the speed line as opposed to Figure 5.1—the mean offset in $\pi^{tt}_{Imp.}$ is about 3.37% and in $\eta^{tt}_{s,Imp.}$, of 0.13%. This means that the losses are in this case lower than they should be, which based on Figure 5.3 causes a higher outlet total pressure for the same Euler work input. These small discrepancies could have been caused by the true spanwise profiles at impeller outlet from CFD and the employed averaging method. Contrarily, in SCM, a uniform spanwise profile was prescribed, in accordance with the suggestion from (*Casey and Robinson*, 2010, p. 4)—refer also to Sec. 3.1.1.

To sum up, parasitic losses which increase towards lower mass flow rates and with increasing speed have been detected near the trailing edge in the CFD simulations. These were found in the literature to be typical in open impellers. However, the amount to which they occur should be further analyzed, because there are various mechanisms that can increase their contribution. For example, an insufficiently accurate mesh resolution in the tip region could amplify the losses between the stationary shroud and the rotating blade. Also, a partly recirculating flow at trailing edge, which can be found for highly diffusing impellers, could also increase the work at outlet without a corresponding increase in pressure ratio. Other turbulence models could be tested to discard a possible extra viscosity production in this region. However, these investigations would lie beyond the scope of this work. For the purpose of this dissertation to build a methodology to improve the capabilities of throughflow calculation methods and approximate their prediction to reference 3D results, the corrected curves obtained by setting constant rothalpy in CFD (see Figure 5.4) already serve this objective. Accordingly, the reference curves of work input, total-total pressure ratio, and total-total isentropic efficiency will be "SCM with prescribed corrected CFD values" from Figure 5.4, because these are the curves that can be obtained in SCM when the reference values of slip factor, internal loss coefficient, and aerodynamic blockage are prescribed.

5.2 Choice of Baseline Models for Internal Flow

In this section, the implementation of literature correlations for the slip factor, the impeller internal loss coefficient, and the outlet aerodynamic blockage in the baseline throughflow calculation workflow from Figure 4.4 is described. The throughflow results with various correlations are discussed and compared with the reference results ("SCM with prescribed corrected CFD values" from Figure 5.4). In an attempt to build a general methodology that applies to different types of impellers, the choice of the models is done according to their suitability for both test cases RADIVER Vaneless and Design603 together. The analysis of the models for the slip factor, the loss coefficient, and the blockage is carried out separately to avoid interaction effects between them. The effects of combining the selected models are discussed in Sec. 5.3.

5.2.1 Slip Factor

The results for the slip factor versus the reduced mass flow rate are given in Figure 5.5a for RADIVER Vaneless and in Figure 5.5b for Design603. The CFD reference values of slip factor are depicted in dark gray and were obtained as described in Sec. 5.1 with (5.4). For both test cases, the CFD slip factor increases with mass flow rate and has a maximum value approaching choke on each speed line. This behavior of the slip factor was also observed by *Eckardt* (1980), as cited in *Qiu et al.* (2011, p. 5), with the experimental results of his backswept impeller[1]. *Eckardt* attributed this upward trend to the S-shaped blade design of the impeller (*Qiu et al.*, 2011, p. 5), i.e., the

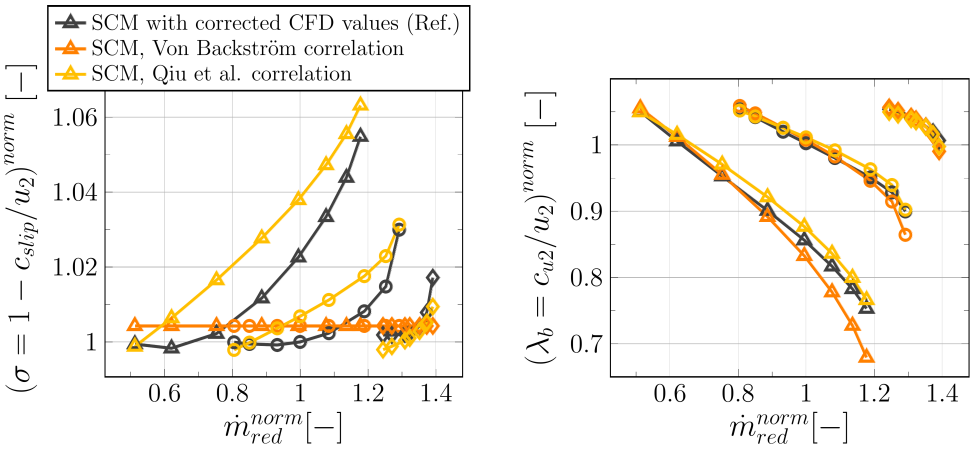

(a) RADIVER Vaneless

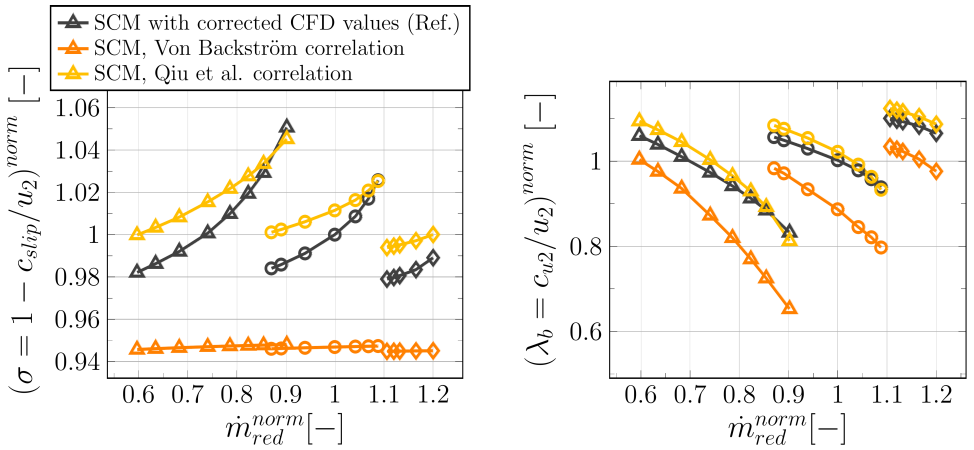

(b) Design603

Figure 5.5: Comparison of the predicted slip factor (σ) in throughflow (SCM) by means of the *Von Backström* (2005) correlation and the *Qiu et al.* (2011) correlation, with respect to the reference slip factor values from CFD. From these slip factor predictions, the resulting blade work coefficient (λ_b) over the mass flow rate is also assessed—here the reference curves are "SCM with corrected CFD values", as discussed in Sec. 5.1.

[1] Although *Eckardt* (1980) used the European definition of slip factor ($\sigma' = c_{u2}/c_{u2,\infty}$), the upward trend of the American slip factor ($\sigma = 1 - (c_{u2,\infty} - c_{u2})/u_2$) also applies, because of the proportionality between them, i.e., $\sigma = 1 + c_{u2,\infty}(\sigma' - 1)/u_2$.

backsweep. RADIVER Vaneless and Design603 also present such a blade design, with backsweep angles in the same order of magnitude as the Eckardt impeller. Prediction of this upward trend with literature correlations still remains a challenge, mainly because of two reasons: (1) the models generally only account for geometry parameters and not for flow coefficient dependency—this dependency is shown in Figure 5.5 with the CFD results and is also confirmed in *Qiu et al.* (2011); and (2) the geometry parameters included in the correlations are mostly just the exit blade angle, the number of blades, and the inlet-to-exit radius ratio, so that the effect of the backsweep on the slip factor behavior is not included. Under these conditions, the slip factor from literature models generally remains constant for the whole operating map—for radial ended impellers with no backsweep, for which the historical correlations were developed, the work input is actually independent of flow rate for a given rotational speed.

To choose the slip factor correlation for the baseline throughflow calculation, the results from two different correlations with respect to the CFD reference from Figure 5.5 are compared: the first one is the expression from *Von Backström* (2005), which unifies the historical correlations (Busemann, Stodola, Stanitz, Wiesner, Eck, and Csanady) in one single equation; and the second one is the expression from *Qiu et al.* (2011), which includes the effects of flow coefficient and blade curvature on the slip factor calculation. The results for RADIVER Vaneless are presented in Figure 5.5a, and for Design603, in Figure 5.5b. The *Von Backström* (2005) correlation focuses on the blade solidity (c/s_e) to determine the strength of the relative-eddy-induced slip and reads

$$\sigma = 1 - \frac{c_{\text{slip}}}{u_2} = 1 - \frac{1}{1 + F_0(c/s_e)(\cos\beta_{2b})^{0.5}}, \quad \text{with} \quad c/s_e = \frac{(1 - r_1/r_2)Z_{eff}}{2\pi\cos\beta_{2b}}. \tag{5.8}$$

In (5.8), β_{2b} is negative according to the angle convention in the present study (see Figure 2.1b); $F_0 = 5$ is a constant given by *Von Backström* that was calibrated by considering backswept impellers as well; Z_{eff} is the effective number of blades[2]; and r_1/r_2 is the radius ratio, which must be greater or equal to 0.5. For RADIVER Vaneless (see Figure 5.5a), the throughflow calculation with this Von Backström correlation (5.8) certainly gives a constant slip factor value with flow coefficient, but the prediction is capable of matching the mean value of the CFD curves. The relative error between SCM and CFD at the highest mass flow rates, which goes from -4.79% to -1.27% with increasing rotational speed, translates into discrepancies in work input prediction going from -9.80% to -1.63% at these same points. For Design603 (see Figure 5.5b), the Von Backström correlation (5.8) also provides nearly constant values of slip factor throughout the entire operating map[3], but underpredicts the reference CFD values and

[2] *Aungier* (2000, p. 57) suggests using an effective number of blades in the literature slip correlations for the case of an impeller with splitter blades—such as Design603. The expression reads $Z_{eff} = Z_{FB} + Z_{SB}(L_{SB}/L_{FB})$, where FB and SB stand for full blades and splitter blades, respectively. The lengths L_{FB} and L_{SB} are known for the given geometries. For RADIVER Vaneless, $Z_{eff} = Z_{FB}$.

[3] The slight differences in slip factor prediction between operating points with the Von Backström correlation in Figure 5.5b are due to the changing radius ratio r_1/r_2 with flow condition. In a throughflow program, the position of the streamlines changes along iterations for the specific flow solution. Because the mean streamline was taken as the reference one to solve the correlations (see throughflow solver algorithm from Figure 4.3), the radial position of this streamline may slightly deviate for different mass flow rates.

thus the work input is also largely underpredicted—in this case, not only towards choke, but for the whole speed lines. For example, the relative slip factor offset between SCM and CFD at the largest mass flow rate for the lowest rotational speed is of −9.77%, which at this point translates into a −21.59% relative error in work input.

The reason for the large underprediction in slip factor for Design603 with the Von Backström correlation cannot be attributed to the correlation being derived for radial ended impellers and not being suitable for backswept ones, because RADIVER Vaneless is also a backswept impeller and its results match the reference better. The main difference in geometry design between the two test cases is that RADIVER Vaneless has a ruled-surface impeller, while Design603 is a free-form one—the free-form design methodology was part of the optimization carried out by *Hehn* (2018) for this transonic compressor. The blade angle distribution in streamwise direction for both impellers RADIVER and Design603 is outlined in Figure 5.6, with spanwise locations 0% (hub), 50% (mid span), and 100% (tip). For RADIVER Vaneless (see Figure 5.6a), the blade angle distribution follows a similar trend along the meridional direction for each span position, while for Design603 (see Figure 5.6b), the distributions at each span location are different. The blade loading, which is a direct measure of the strength of the slip velocity, can be related to the blade angle distribution by means of the momentum equation in the circumferential direction (*Casey and Robinson*, 2021, p. 147, 367): the blade-to-blade pressure gradient is $-\partial p/\partial\theta = \rho r F_u$, which for an assumed linear distribution and substituting the tangential force by $F_u = (c_m/r)\partial(rc_u)/\partial m$ (see (2.45)), yields $(p_{ps} - p_{ss}) \approx \rho c_m \Delta\theta \partial(rc_u)/\partial m$. Assuming incompressible flow, this pressure difference can be rewritten in terms of the relative velocity as

$$(w_{ss} - w_{ps}) \approx \frac{(p_{ps} - p_{ss})}{\rho w} = \Delta\theta \frac{c_m}{w} \frac{\partial(rc_u)}{\partial m} = \Delta\theta \cos\beta \frac{\partial(rc_u)}{\partial m}, \tag{5.9}$$

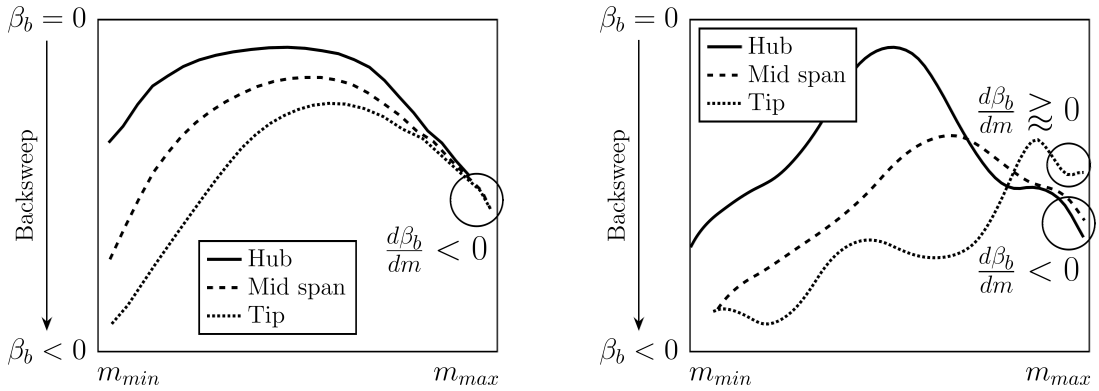

(a) RADIVER Vaneless **(b)** Design603

Figure 5.6: Blade angle distribution along the streamwise direction for the two impellers RADIVER and Design603 at span locations 0% (hub), 50% (mid span), and 100% (tip). RADIVER, as a ruled-surface impeller, presents a similar blade angle distribution for each span position along the meridional direction. Design603, by contrast, shows a dissimilar distribution as it is a free-form impeller. The raw geometry data for Figure 5.6a were taken from *Ziegler* (2003), and for Figure 5.6b, from *Enneking* (2020).

where $\cos\beta = c_m/w$ holds from the velocity triangle convention from Figure 2.1b. From (5.9), it follows that $(w_{ss} - w_{ps}) \propto \cos\beta_b$, if just the blade-turning force is considered and not the Coriolis and centrifugal forces, thus leaving the swirl increase $\Delta(rc_u) > 0$ aside for this analysis. Because the blade angle is negative to indicate the backsweep opposite to the wheel rotation, $\cos\beta_b$ follows the exact same trend as Figure 5.6 and, therefore, the blade loading can be said to have this same distribution, approximately. For the mid span and tip of both RADIVER and Design603 blades, it can be recognized from Figure 5.6 that the loading increases from inlet to outlet, thus they have a rear loading at these span locations. However, this rear loading has different magnitude and course at mid span and at the tip for Design603. At the tip, the loading is reduced further upstream of the trailing edge, and not immediately before, as it is the case of the mid span distribution. This reduction in loading then maintains its level until reaching the trailing edge, with a blade-turning rate $(d\beta_b/dm)$ of approximately zero. The fact that the tip of the Design603 impeller is unloaded before reaching the trailing edge contributes to reducing the slip velocity in this case, according to $c_{\text{slip}} = (w_{ss} - w_{ps})/4$ (*Qiu et al.*, 2011, p. 2), which translates into an increase in slip factor $(\sigma = 1 - c_{\text{slip}}/u_2)$ compared to a conventional loading profile near the trailing edge as the one from mid span and hub. Design603 has therefore higher slip factor values than RADIVER because of the loading distribution from mid span towards the tip, despite both being backswept impellers. The Von Backström correlation (5.8) just includes the blade solidity $c/s_e = (1 - r_1/r_2)Z_{eff}/(2\pi\cos\beta_{2b})$ to characterize the blade geometry[4], so it does not account for these blade-turning profiles of free-form impellers, and it is therefore not capable of reaching the higher reference CFD values of slip factor for Design603 in Figure 5.5b.

One correlation that does include the blade turning influence on the slip factor is the model from *Qiu et al.* (2011). The authors recognize that the slip velocity is a direct consequence of the blade loading and derive a geometrical expression for $(w_{ss} - w_{ps})$ which includes the blade-turning rate. The slip factor is then given as[5]

$$\sigma = 1 - \frac{c_{\text{slip}}}{u_2} = 1 - \Delta\sigma_{\text{radial}} - \Delta\sigma_{\text{turn}} = 1 - \frac{F\pi\cos\beta_{2b}}{Z_{eff}} - \frac{Fs_2\varphi_2}{4\cos\beta_{2b}}\left(\frac{d\beta_b}{dm}\right)_2, \qquad (5.10)$$

where $s_2 = (2\pi r_2)/Z_2$ is the pitch at impeller exit; $(d\beta_b/dm)_2$ is the blade-turning rate close to discharge (see Figure 5.6); and F is a shape factor which relates the loading at the last meridional position where the flow is still guided by the blades and the loading at impeller discharge[6], and reads

[4] *Von Backström* (2005, p. 9) suggests that the value of the constant $F_0 = 5$ may be modified for different impeller families. In the case of Design603, a greater value $F_0 > 5$ would be necessary to increase the slip factor prediction values.

[5] In their derivation, *Qiu et al.* (2011) include an additional term $\Delta\sigma_{\text{passage}}$ which accounts for the passage width variation near the impeller outlet, $(d\rho b/dm)_2$. They argue, however, that this term is very small compared to $\Delta\sigma_{\text{radial}}$ and $\Delta\sigma_{\text{turn}}$, and they set $\Delta\sigma_{\text{passage}} = 0$ in all their calculations.

[6] *Qiu et al.* (2011) do not include the case of impellers with splitter blades in their derivation. However, as suggested by *Aungier* (2000, p. 57) and as already done for the calculation with the Von Backström correlation (5.8), in (5.10) and (5.11) the effective number of blades Z_{eff} was used instead of Z_2. Because the loading calculation that *Qiu et al.* (2011) carried out to obtain (5.11) considers the whole impeller passage from inlet to exit, the effect of the splitter blades on the loading must be considered in the equation, and therefore the use of Z_{eff} appears to be justified.

$$F = 1 - \sin\left(\frac{\pi}{Z_{eff}}\right)\sin\left(\frac{\pi}{Z_{eff}} + \beta_{2b}\right)\cos\beta_{2b} - \frac{t_2}{s_2\cos\beta_{2b}}, \tag{5.11}$$

where t_2 is the blade thickness at impeller exit. F must be greater than the radius ratio r_1/r_2 and smaller than 1. This Qiu et al. correlation (5.10) also includes the flow coefficient at impeller outlet, φ_2, with the aim to control the slip factor behavior at off-design operating conditions.

The throughflow (SCM) results with the Qiu et al. correlation (5.10) are also given in Figure 5.5a for RADIVER Vaneless, and in Figure 5.5b for Design603. For both test cases, (5.10) is capable of reproducing the upward trend of the slip factor from CFD. This comes from the dependency of the slip factor with flow coefficient φ_2 and the negative blade-turning rate near impeller discharge—for both test cases, the $(d\beta_b/dm)_2$ value was calculated at mid span (see Figure 5.6), because the mean streamline was taken to solve the correlations. Despite matching the off-design trend, this correlation generally overpredicts the reference slip factor for both RADIVER Vaneless and Design603. For RADIVER Vaneless at the lowest and mid speed lines (see Figure 5.5a), the prediction generally matches the end points of the curves, but fails to reproduce the parabola trend of the reference CFD values and remains approximately linear. For the highest rotational speed, the behavior is opposite in that the prediction is capable of matching the mid operating points but fails to match the end points of the speed line. This translates into an overprediction of the work coefficient with respect to CFD for the low and mid speed lines, while, for the highest rotational speed, it matches the reference work coefficient values. For Design603 (see Figure 5.5b), the Qiu et al. correlation (5.10) also overpredicts the reference slip factor values and matches solely the points near choke for the low and mid speed lines. This also results in an overprediction of the work coefficient. Nevertheless, these prediction results lie far better than the ones from the Von Backström correlation (5.8) with respect to the CFD reference for this test case. Choosing the blade-turning rate at mid span has also proven satisfactory in this case, because the value at the tip is slightly positive (see Figure 5.6b) and this would have changed the orientation of the curve, from upward to downward based on (5.10). The correlation is still capable of reaching the high reference CFD values that the historical-based Von Backström one cannot. To summarize, the Qiu et al. correlation has proven the dependency of the slip factor with flow condition and blade turning ($\Delta\sigma_{\text{turn}}$) apart from the relative-eddy effect from impeller rotation ($\Delta\sigma_{\text{radial}}$). It has also provided a more accurate prediction of the slip factor with respect to the CFD reference. For these reasons, the Qiu et al. correlation (5.10) was chosen over the Von Backström one (5.8) for the baseline throughflow calculations in this dissertation.

5.2.2 Loss Coefficient

The discussion of the results in this section is concerned with: (1) the behavior of the individual loss correlations for the test cases RADIVER Vaneless and Design603, and (2) the final comparison of the $(\Delta s/R)_{Imp.}$ from throughflow (SCM) and CFD. Similar to the evaluation of slip factor correlations in the previous section, here the effect of the losses is also isolated in that the mean CFD values of slip factor and blockage were

prescribed as described in Sec. 5.1. The throughflow solver required the losses to be defined in terms of the entropy, $\Delta s/R$, which is convenient for the comparison with CFD results, but the literature correlations give the loss coefficient in terms of the stagnation enthalpy as

$$\Delta q = \frac{h_{t2,rel} - h_{t2,s,rel}}{u_2^2} = \frac{\Delta h_{t,loss}}{u_2^2}. \tag{5.12}$$

In (5.12), $\Delta h_{t,loss}$ represents the difference between actual end state of the compression and the one from the equivalent isentropic process, as explained in Sec. 2.1. For a given Δq from the correlations, the $\Delta h_{t,loss}$ was calculated from (5.12), and then introduced into (2.19)–(2.24) to obtain the corresponding $(\Delta s/R)_{Imp.}$.

As mentioned in the literature review from Sec. 3.1.3, the established procedure in the radial compressor field is to obtain the loss coefficient as the summation of different loss contributions, each of them representing a loss mechanism. Despite recognizing the limitations of this approach due to the inherent interdependence among loss-producing factors, such a methodology was still employed for the baseline throughflow calculations in this work. However, for the calibration process in Chapter 6, the resulting $(\Delta s/R)_{Imp.}$ was the value adjusted to CFD rather than the parameters of the individual loss correlations. This adjustment was so conceived to compensate for the fundamental oversimplification of the linear summation methodology.

The Δq in (5.12) was built as the combination of the following loss contributions

$$\Delta q = \Delta q_{sf} + \Delta q_{bl} + \Delta q_{cl} + \Delta q_{inc}, \tag{5.13}$$

where Δq_{sf} is the skin friction loss, which models the loss caused by the bounding surfaces of the impeller that generate shear forces on the fluid; Δq_{bl} is the blade loading loss, which is the momentum loss from the boundary-layer build-up on the blade surfaces; Δq_{cl} denotes the tip clearance loss for open impellers, which is determined by the pressure difference across the gap from the leaking flow; and Δq_{inc} stands for the incidence loss from the alignment of the flow to the blade at inlet. Some authors also included a choking loss in one-dimensional codes (*Aungier*, 2000, p. 83). However, because a throughflow program with given mass flow cannot calculate choked operating points in any machine (*Denton*, 1978, p. 214; *Casey and Robinson*, 2021, p. 487, 488), I decided not to include this loss, which caused convergence problems in the calculation workflow. The addition of a supercritical Mach number loss correlation, for example the one from *Aungier* (1995), also did not contribute significantly to the results near choke at the highest rotational speeds.

Despite calculating the loss coefficient as a meanline value with (5.13), the throughflow code from the baseline calculation workflow in Figure 4.4 requires a two-dimensional distribution of the loss coefficient to proceed on to subsequent iterations. There are no generally accepted methods to define the two-dimensional profiles in radial compressors. However, as *Casey and Robinson* (2021, p. 509, 513) argued, for the narrow channels at impeller outlet, it is sensible to assume a complete mixing of the losses across the

span, and thus to prescribe the same meanline value for each streamline[7]. With this assumption of fully developed flow, the impellers in this work were modeled according to the pipe flow analogy. *Casey and Robinson* (2011, p. 867, 868) argued, however, that the pipe flow analogy should only be applied in the case of narrow channels with $b_2/D_2 < 0.03$, where the boundary layers are certainly fully merged as in a pipe (*Casey*, 1985, p. 543), and suggested using a flat plate analogy otherwise. For the two test cases in the present dissertation, $b_2/D_2 \approx 0.04$ applies (see Table 4.1). Nevertheless, the pipe flow approach was chosen to maintain consistency with the loss correlations implemented, which are based on this pipe analogy. Further approximations for this approach are given in *Casey* (1985, p. 543), who showed that the hydraulic diameter can be expressed as $D_h \approx 2b_2$, and the mean relative flow velocity, as $\overline{w} \approx u_2/2$. With that, the Reynolds number was defined as

$$Re = \frac{\overline{w} D_h}{\nu_1} \approx \frac{u_2 b_2}{\nu_1} = \frac{p_{t1,abs} u_2 b_2}{R T_{t1,abs} \mu_{t1}} \tag{5.14}$$

to have the same definition in CFD (see (4.12)) and in throughflow for the intended comparison purposes in this dissertation.

To analyze the behavior of the correlations implemented for Δq in (5.13), the results for each loss contribution are given in Figure 5.7a for RADIVER Vaneless and, in Figure 5.7b, for Design603. First and foremost, for the skin friction loss coefficient, Δq_{sf}, both RADIVER Vaneless and Design603 show the same trend: the skin friction loss coefficient increases towards higher mass flow rates and decreases with rotational speed.

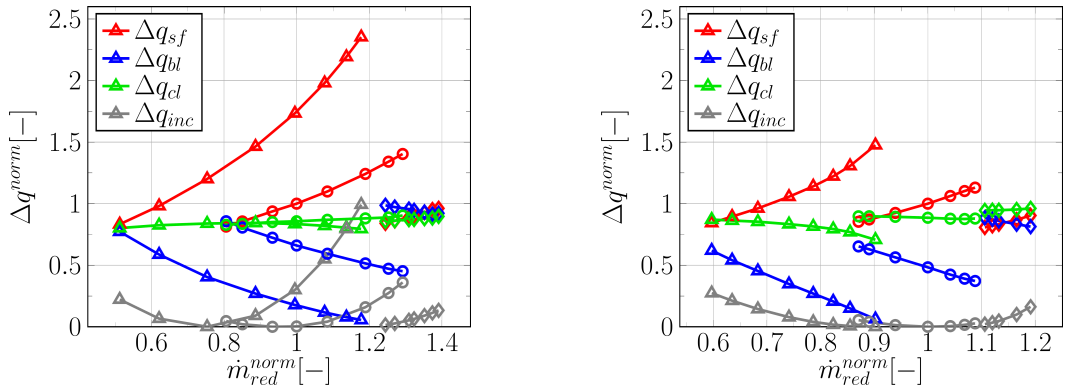

(a) RADIVER Vaneless **(b)** Design603

Figure 5.7: Throughflow results with the baseline calculation workflow (see Figure 4.4) for the various loss coefficient contributions Δq listed in (5.13) over the impeller map of the two test cases RADIVER Vaneless and Design603. The skin friction loss Δq_{sf} was calculated with (5.15); the blade loading loss Δq_{bl}, with (5.17); the tip clearance loss Δq_{cl}, with (5.19); and the incidence loss Δq_{inc}, with (5.20).

[7] I did not prescribe the same $(\Delta s/R)_{Imp.}$ for each streamline, but $\Delta h_{t,loss}$, because the enthalpy loss is the actual empirical model from the literature. Then, for each streamline, I transformed the mean $\Delta h_{t,loss}$ value to $(\Delta s/R)_{Imp.}$ separately with (2.19)–(2.24), which yielded slightly different values of $(\Delta s/R)_{Imp.}$ across the span. In the chordwise direction from inlet to outlet, a linear distribution of the resulting $(\Delta s/R)_{Imp.}$ value at each streamline was applied.

This behavior is directly recognizable from the *Jansen* (1967, p. 140) correlation implemented

$$\Delta q_{sf} = 2c_f \frac{L}{D_h} \left(\frac{\overline{w}}{u_2} \right)^2, \tag{5.15}$$

where the only quantities that vary—significantly—with changing operating conditions are the mean relative velocity $\overline{w} = (w_1 + w_2)/2$ (*Whitfield and Baines*, 1990, p. 201) and the tip speed u_2. The tip speed remains constant along a speed line, so that the quadratic behavior of Δq_{sf} is due to the mean velocity $\overline{w}$. For radial impellers with parallel wall vaneless diffusers, towards choke, the relative velocity at impeller outlet w_2 generally increases up to the point where there is no diffusion of the relative velocity, so that the ratio of impeller relative velocities at choke becomes, according to *Rodgers* (1978, p. 599), about $w_{1,rms}/w_2 \approx 0.9$. Accordingly, for each speed line, i.e., each u_2, the operating point at the highest mass flow rate represents a borderline case with the highest w_2 values and, therefore, with the highest skin friction losses. (5.15) results from writing the Bernoulli equation between two points in an equivalent pipe of circular cross section with diameter D_h and equivalent length[8] L. Viscosity is taken into account by a difference in head from inlet to outlet, ΔH, which is then nondimensionalized by the square of the tip speed, u_2, to give Δq. The expression for this ΔH is approximated by means of the Darcy-Weisbach equation. For the skin friction coefficient c_f in (5.15), numerous approaches can be found in the literature. In line with the CFD modeling in this study, where fully turbulent flow was assumed (see Sec. 4.2), here I also chose a friction coefficient which applied to pipe turbulent flow and smooth walls—roughness effects were not considered. Several authors provide such an expression, based on historic pipe friction diagrams. The implicit equation from *Aungier* (2000, p. 74)

$$\frac{1}{\sqrt{4c_f}} = -2 \log_{10} \left[\frac{2.51}{Re\sqrt{4c_f}} \right] \tag{5.16}$$

was finally chosen, which provided the same c_f results as the expression from *Casey* (1985, p. 543) if zero roughness was assumed[9].

The blade loading loss coefficient, Δq_{bl}, is given in blue in Figure 5.7. For both RADIVER Vaneless (see Figure 5.7a) and Design603 (see Figure 5.7b), the trend is opposite to the skin friction loss coefficient: the blade loading loss increases towards lower mass flow rates and with rotational speed. From the implemented correlation from *Coppage et al.* (1956), as given by *Whitfield and Baines* (1990, p. 201)

$$\Delta q_{bl} = 0.05 DF^2, \tag{5.17}$$

[8] In this case, although not specified by the original author (*Jansen*, 1967), I used an effective length to account for the increased flow surface in an impeller with splitter blades, in line with the approach followed with the number of blades for the slip factor correlations. The mean value of full and splitter blades length, $L = (L_{FB} + L_{SB})/2$, proved to be suitable. For RADIVER Vaneless, $L = L_{FB}$.

[9] A correction for this skin friction coefficient as suggested by *Musgrave* (1979, p. 186) and *Jansen* (1967, p. 140) proved to not be necessary to reach adequate levels of skin friction loss. The correction $c_f' = c_f[Re(D_h/(2r_c))^2]^{0.05}$ provided too high of a skin friction value, which resulted in a too high loss coefficient ($\Delta s/R$) from SCM with respect to the CFD reference for both compressors. Such a comparison would actually require the CFD being performed including a rough wall treatment.

$$DF = 1 - \frac{w_2}{w_{1,shr}} + \frac{0.75(u_2 c_{u2} - u_1 c_{u1})/u_2^2}{\frac{w_{1,shr}}{w_2}\left(\frac{Z_{eff}}{\pi}\left(1 - \frac{D_{1,shr}}{D_2}\right) + 2\frac{D_{1,shr}}{D_2}\right)}, \tag{5.18}$$

it can be seen that the ratio of relative velocities, w_1/w_2, is also present. The borderline case of highest mass flow rate at the lowest speed is confirmed here with the blade loading loss being nearly zero, typical of near-choke operating points. On the other end of the speed line towards stall, greater deceleration takes place, usually around $(w_{1,rms}/w_2)_{stall} \approx 1.4 - 1.7$, as given by *Rodgers* (1978, p. 599) for radial impellers with vaneless diffusers. This leads to an increased boundary layer thickness and accumulation on the suction side near the tip, which is what is meant by *blade loading* in the literature. *Coppage et al.* (1956) correlated this effect by means of a diffusion factor DF, (5.18), which includes the flow deceleration, but also an estimation of the loading distribution on the blades—uniform in this case. As discussed in Sec. 5.2.1 with the blade loading distributions from Figure 5.6, neither RADIVER Vaneless nor Design603 present a uniform loading profile. RADIVER Vaneless shows an enhanced front loading with enhanced aft loading, while Design603 has an unloaded inducer with less aft loading. Also, the blade loading distribution of Design603 is different at each span location. This suggests that the implemented correlation (5.17) might have left room for improvement in the loss prediction for Design603 with respect to CFD. *Rodgers* (1978, p. 593) already acknowledged the inadequacy of such diffusion factor correlations with simplified loading distributions in the case of impellers with splitter blades. Similarly, *Galvas* (1973, p. 49) suggested changing the 0.75 in (5.18) for 0.6 for impellers with splitter blades. However, for Design603, this change did not represent a significant difference in prediction. As such, the correlation from *Coppage et al.* (1956) was implemented in its original form as given by (5.18).

The tip clearance loss coefficient, Δq_{cl}, is outlined in green in Figure 5.7. For RADIVER Vaneless (see Figure 5.7a), Δq_{cl} remains nearly constant with throttling and rotational speed, except for the last operating points near choke on the lowest speed line. For Design603 (see Figure 5.7b), a more distinctive trend can be recognized, i.e., that the tip clearance loss coefficient increases towards lower mass flow rates and with rotational speed, although just slightly. The implemented model from *Jansen* (1967, p. 141) is

$$\Delta q_{cl} = 0.6\frac{\varepsilon_{cl}}{b_2}\frac{c_{u2}}{u_2}\sqrt{\frac{4\pi}{b_2 Z_{eff}}\left[\frac{r_{1,shr}^2 - r_{1,hub}^2}{(r_2 - r_{1,shr})(1 + \rho_2/\rho_1)}\right]\frac{c_{u2}}{u_2}\frac{c_{m1}}{u_2}}, \tag{5.19}$$

where ε_{cl} is the average height of the clearance gap from impeller inlet to outlet. (5.19) was devised by means of a sudden expansion analysis of the flow across the gap. Near the edge of a loaded blade, the pressure difference across the blade is less than the value without clearance, and this defect in pressure difference is related to the contraction of the leakage flow through the clearance gap (*Senoo and Ishida*, 1987, p. 56). (5.19) is also a function of the work input coefficient $\lambda = c_{u2}/u_2$ for impellers without prewhirl.

As for the incidence loss coefficient, Δq_{inc}, for most of the operating points in the impeller map of RADIVER Vaneless (see Figure 5.7a) and Design603 (see Figure 5.7b), its value is considerably lower than the other loss contributions, with the exception of the points near choke on the lowest speed line of RADIVER Vaneless—for this speed line, the

steepness of the skin friction loss is quite pronounced with respect to the other speed lines in RADIVER's performance map. The implemented model is taken from *Whitfield and Baines* (1990, p. 195–198), which is based on the adjustment of the relative velocity vector to the optimum direction at blade inlet. According to the model, the change in relative tangential velocity results in kinetic energy being transformed into internal energy, which appears as an increase in entropy. The optimum direction is therefore not the blade direction itself, but the one at which there is no change in swirl, rc_u. With that, the incidence loss is given as

$$\Delta q_{inc} = \frac{1}{2} \frac{w_{1,shr}^2}{u_2^2} \sin^2 \left(|\beta_{1,shr} - \beta_{1,shr,opt}| \right), \tag{5.20}$$

where $\beta_{1,shr,opt}$ is the optimum relative flow angle and $\beta_{1,shr}$ is the actual relative flow angle at the shroud. For the calculation of $\beta_{1,shr,opt}$, there exist various approaches in the literature, e.g., *Galvas* (1973), but here the approach from *Whitfield and Baines* (1990) was followed as well. The model considers an imaginary duct of small finite length in the direction of the flow, which includes the regions immediately upstream and downstream of the blade leading edge. Assuming incompressible flow, *Whitfield and Baines* wrote the continuity equation between these two regions, $c_{m,1^-} A_{1^-} = c_{m,1} A_1$, where the subscript 1^- corresponds to the immediately upstream location. From this continuity equation and with the velocity triangles, they gave an expression to obtain the optimum angle as

$$\beta_{1,shr,opt} = \arctan \left[\frac{A_{1^-}}{A_1} \tan(\beta_{1b,shr}) \right]. \tag{5.21}$$

Here, in (5.21), A_{1^-} was approximated as the area at the immediately upstream calculating station from Figure 4.2, and $\beta_{1b,shr}$ corresponds to the blade angle at inlet at the shroud. Effects due to metal blockage and boundary layer blockage were not considered.

The models (5.15)–(5.20) were added to give the final Δq results according to (5.13). This Δq was then transformed into $(\Delta s/R)_{Imp.}$ as explained at the beginning of this section. The loss coefficient in terms of entropy is the one compared in Figure 5.8 with the CFD reference values obtained with (5.7). For both test cases, RADIVER Vaneless in Figure 5.8a and Design603 in Figure 5.8b, the chosen combination of loss correlations and their implementation in the throughflow calculation workflow have provided a rather satifactory prediction for all the speed lines. The levels of loss coefficient are nearly met for the design speeds (highest rotational speeds) away from choke, while for the off-design speeds, the SCM prediction consistently matches the reference at the extremes, mainly near surge. For both test cases, the prediction at off-design conditions generally fails to reproduce the more pronounced trend from CFD, and appear, to a certain extent, fairly uniform over the range of mass flow rate values. Recalling the Δq_i results from Figure 5.7, it can be recognized that the distributions of skin friction and blade loading loss are approximately linear from choke to surge, and that the tip clearance loss remains nearly constant over the operating points. As mentioned before, the correlation for the blade loading loss, (5.17)–(5.18), assumed a uniform loading on the blades, which is not true for neither of the compressors investigated. RADIVER, with its enhanced front loading (see Figure 5.6a), might create more diffusive losses near choke

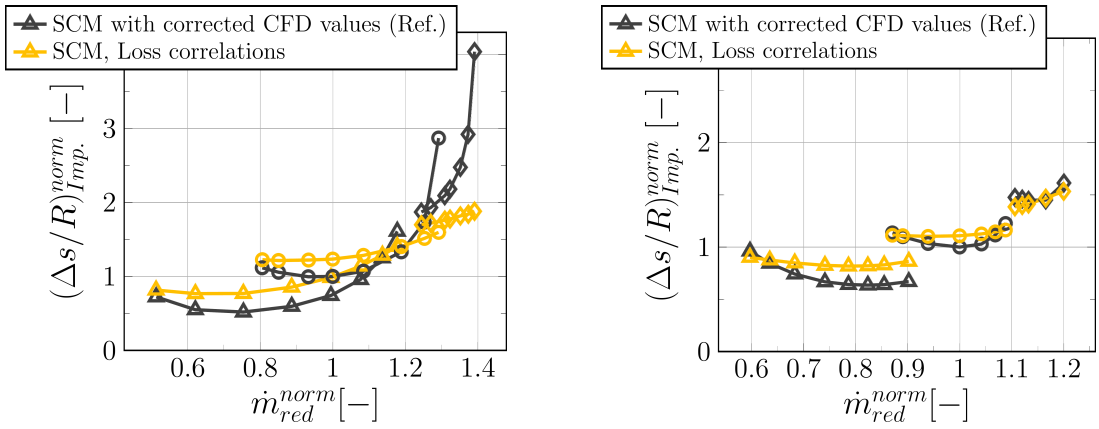

(a) RADIVER Vaneless **(b)** Design603

Figure 5.8: Resulting loss coefficient $(\Delta s/R)_{Imp.}$ from throughflow (SCM) with loss correlations (5.15)–(5.20) versus the reference loss coefficient from CFD, (5.7), over the impeller map of the two test cases RADIVER Vaneless and Design603.

than the ones predicted with the correlation, (5.17)–(5.18). An enhanced front loading prematurely amplifies diffusion along the pressure sides of the blades. This might explain the increased CFD reference loss values for the mid and highest speed lines of RADIVER towards choke (see Figure 5.8a). Contrarily, the transonic impeller Design603 has an unloaded inducer (see Figure 5.6b), which helps delay the transition to choking at higher flow rates. In Figure 5.8b, there is no indication suggesting enhanced diffusion losses from CFD in the vicinity of choke. In general, in both Figure 5.8a and Figure 5.6b, the loss prediction levels remain similar over the different rotational speeds for each compressor. Accordingly, there is an overprediction of the loss coefficient for the off-design speed lines, since the loss level has been better approximated for the highest speed. It is thus recognized from the results in Figure 5.8 that the selected literature correlations can predict performance losses relatively well for the design speeds away from choke, but they would require additional adjustment to be able to reproduce the loss levels and curve form from CFD at off-design speeds.

5.2.3 Aerodynamic Blockage

To quantify the blockage resulting from the boundary layer development in the impeller channel and its accumulation near the tip at impeller discharge, authors such as *Rodgers* (1978) and *Aungier* (1995, 2000) devised correlations which recognize the blockage producing factors to be: the impeller geometry, the diffusion ratio w_1/w_2, the inducer incidence—and resulting boundary layer growth near choke and surge—, and the tip clearance effects in the case of open impellers. Blockage is thus a direct measure of the boundary layer build up with increasing diffusion in the impeller passage—same as the blade loading loss described in Sec. 5.2.2. For this reason, increasing blockage values towards lower mass flow rates are generally expected, and also near choke since the flow detaches at the blades' pressure sides. The results from CFD are shown in Figure 5.9, where the trend of increasing blockage towards lower mass flow rates can be recognized

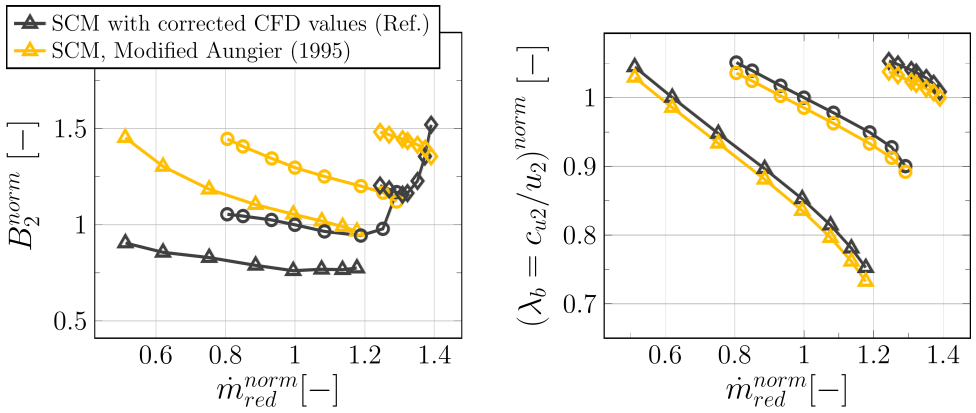

(a) RADIVER Vaneless

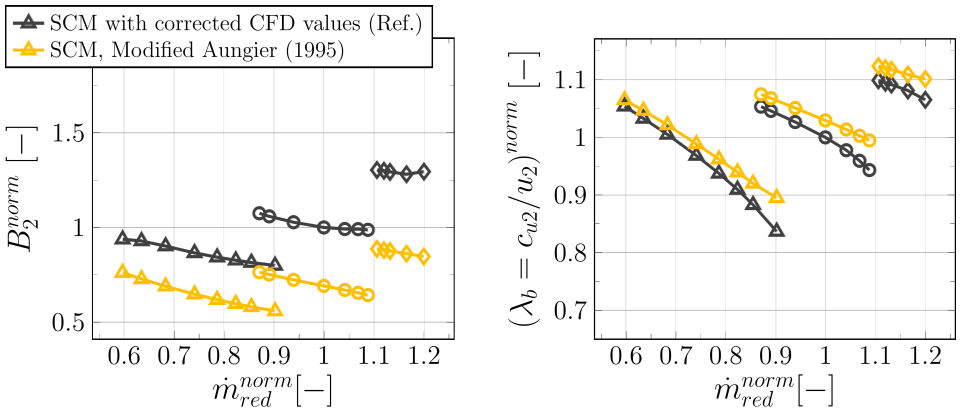

(b) Design603

Figure 5.9: Impeller outlet aerodynamic blockage from CFD (kB_2, with (5.6) and $k < 1$) versus throughflow (in amber, with (5.23), and modified by a unified scaling factor smaller than one). The blade work coefficient λ_b is also depicted, which was calculated by prescribing the slip factor values from CFD and only modeling the blockage.

for both impellers. For RADIVER Vaneless (see Figure 5.9a), however, the CFD blockage near choke on the mid and highest speed lines exhibits an abrupt increase in value. This corresponds to the enhanced front loading profile of the RADIVER impeller (see Figure 5.6a), which, as discussed in Sec. 5.2.2, amplifies diffusion along the pressure sides of the blades and promotes an earlier transition to choking. The sudden increases in blockage depicted in Figure 5.9a align with the steep loss curves from Figure 5.8a in the vicinity of choke. This behavior of the boundary layer growth towards negative incidence was also observed by *Whitfield* (1974, p. 420) in his experimental investigation of an impeller plus a vaneless diffuser. As in Figure 5.9a, *Whitfield* also observed a progressive blockage growth towards stall and a sudden and larger growth near choke. However, this trend of the CFD blockage is not observed for Design603 (see Figure 5.9b). In this case, as mentioned in Sec. 5.2.2, Design603 has an unloaded inducer (see Figure 5.6b), which delays the transition to choking. Design603 also includes a forward swept leading edge and a concave suction side at the tip of the inlet, contributing to a reduction in shock strength—features which are the result of a design optimization carried out by *Hehn* (2018). *Ziegler* (2003, p. 85) confirmed that, for the test case RADIVER Vaneless, the choked behavior results, at all speeds, from the impeller.

The levels of CFD blockage from Figure 5.9 were difficult to achieve with correlations from the literature. For example, *Aungier* (2000) derived an empirical equation for the tip blockage, B_2, which was obtained as the offset between experimental work input curves and predicted work input curves with the *correct* slip factor values. It reads

$$B_2 = 2c_f \left(1 + \frac{w_2^2}{w_1^2}\right) \frac{L}{D_h} \left(\frac{p_{t1} - p_1}{p_{t2} - p_2}\right) \sqrt{\frac{w_1 D_h}{w_2 b_2}} + \left(0.3 + \frac{b_2^2}{L^2}\right) \frac{A_R^2 \rho_2 b_2}{\rho_1 L} + \frac{\varepsilon_{cl}}{2b_2}, \tag{5.22}$$

where A_R is the area ratio of the impeller. In (5.22), Aungier used the inlet relative velocity w_1 for the nondimensionalization of the velocity term, which provided blockage results with SCM in the opposite direction as expected, as $B_2 \propto w_2/w_1$, which is the inverse of the diffusion ratio. As for his older correlation (*Aungier*, 1995), he used w_2 for the nondimensionalization instead, yielding

$$B_2 = c_f \left(1 + \frac{w_1^2}{w_2^2}\right) \frac{L}{D_h} + \left(0.3 + \frac{b_2^2}{L^2}\right) \frac{A_R^2 \rho_2 b_2}{\rho_1 L} + \frac{\varepsilon_{cl}}{2b_2}. \tag{5.23}$$

(5.23) is a slightly modified version of the original correlation from *Aungier* (1995). The original expression contains an additional hub-shroud loss term. However, because this loss contribution was not considered in Sec. 5.2.2 and the blockage levels with (5.23) were already higher than the ones from CFD, I did not include the hub-shroud loss in (5.23). The most recent correlation from Aungier, (5.22), which is taken to be an actualized version of (5.23), does not include such a loss contribution. As such, this approach of excluding the hub-shroud loss seemed justified. For the present dissertation, (5.23) provided the correct blockage trend—increasing towards stall—, but overpredicted the blockage results for both impellers. By comparing both correlations, the factor $\left(2\left(\frac{p_{t1}-p_1}{p_{t2}-p_2}\right)\sqrt{\frac{w_1 D_h}{w_2 b_2}}\right)$ in (5.22) appears to represent a scaling to the blockage levels given by (5.23). The blockage levels obtained with (5.22)—although in the opposite direction—were consistent for RADIVER, but largely underpredicted for Design603. To obtain a blockage prediction in SCM in the correct direction and with appropriate prediction levels, (5.23) was finally chosen and an additional scaling factor was included, which was smaller than one and the same for both test cases, as the objective was to build a standardized methodology for different geometries. This additional unified factor allowed to obtain similar offsets between CFD and SCM for both impellers, which was considered adequate for the subsequent calibration of the ratio between CFD and SCM values in Chapter 6. The results with this modification are the ones given in Figure 5.9. For RADIVER Vaneless (see Figure 5.9a), the modified correlation overpredicts the blockage, and for Design603 (see Figure 5.9b), it underpredicts the reference CFD values of aerodynamic blockage. This might be due to different levels of stratification of the flow field for the two impellers, with RADIVER having an enhanced unloading in the aft region, while Design603 showing less aft unloading (see Figure 5.6).

The relationship between aerodynamic blockage and blade work coefficient λ_b is also evident from Figure 5.9, where for RADIVER Vaneless, the overprediction of blockage means a reduction in work coefficient, and conversely, the blockage underprediction for Design603 provides higher work coefficient values than the reference curves—this direct relationship is obtained by prescribing the reference slip factor values in SCM, so that

the slip model is *correct*. This can also be identified from expressing the definition of blade work coefficient in terms of the velocity triangles from Figure 2.1b

$$\lambda_b = \frac{c_{u2}}{u_2} = \frac{\sigma u_2 + c_{m2} \tan \beta_{2b}}{u_2} = \sigma + \left(\frac{c_{m2}}{u_2}\right) \tan \beta_{2b} = \sigma - \text{const.} \left(\frac{c_{m2}}{u_2}\right), \qquad (5.24)$$

where c_{u2} has been substituted by (5.3), for which the blade angle is negative and so is its tangent. Therefore, by means of (5.24), if the slip factor values are the reference ones, an increase in aerodynamic blockage—which means an increase in meridional velocity, according to $\dot{m} = \rho_2 k c_{m2} A_2 = \rho_2 (1 - B_2) c_{m2} A_2$—will imply a reduction in work coefficient λ_b, and vice versa.

5.3 Final Baseline Results with Combined Models

In Sec. 5.2, the models for slip factor, loss coefficient, and outlet aerodynamic blockage were analyzed separately to make a reasoned choice on the models without considering possible interaction effects between them. In the present section, the chosen models are combined, with the aim to examine the influence between them and on the final baseline results for work coefficient, total-total pressure ratio, and isentropic efficiency.

5.3.1 Slip Factor, Loss Coefficient, and Aerodynamic Blockage

The results for the combined baseline models for each test case are given in Figure 5.10 in red, together with the results with the isolated models from Sec. 5.2, which are given in amber. Only the slip factor, loss coefficient, and blockage were modeled, but the resulting work coefficient λ_b is also depicted in order to show the cumulative effect between slip factor and blockage, and outline how the errors in both models can be compensated to give appropriate work input results.

In Figure 5.10, the loss coefficient results remain fairly similar between the isolated and combined models. Contrarily, for the slip factor and the blockage, there are visible differences, although minimal, for both RADIVER Vaneless (see Figure 5.10a) and Design603 (see Figure 5.10b). The chosen slip factor model, (5.10), is a function of the outlet flow coefficient, $\varphi_2 = c_{m2}/u_2$, i.e., $\sigma = 1 - \text{const.}(c_{m2}/u_2)$. By means of c_{m2}, the slip factor is therefore a function of the aerodynamic blockage B_2. Accordingly, the slight increase in blockage from *isolated* to *combined* models for both test cases generally translates into a corresponding decrease in slip factor. This is recognized for all speed lines of Design603, but for just the highest rotational speed line of RADIVER Vaneless. This relationship between blockage and slip factor may have also been influenced by the fact that the blockage itself, (5.23), is a function of the diffusion ratio, w_1/w_2, where the outflow relative velocity w_2 is determined by the slip factor values. The combination of the present offsets in slip factor and blockage prediction has led to the work coefficient results from Figure 5.10. In the isolated analysis from Sec. 5.2, the overpredicted slip factor for RADIVER Vaneless gave an overpredicted work coefficient (see Figure 5.5a),

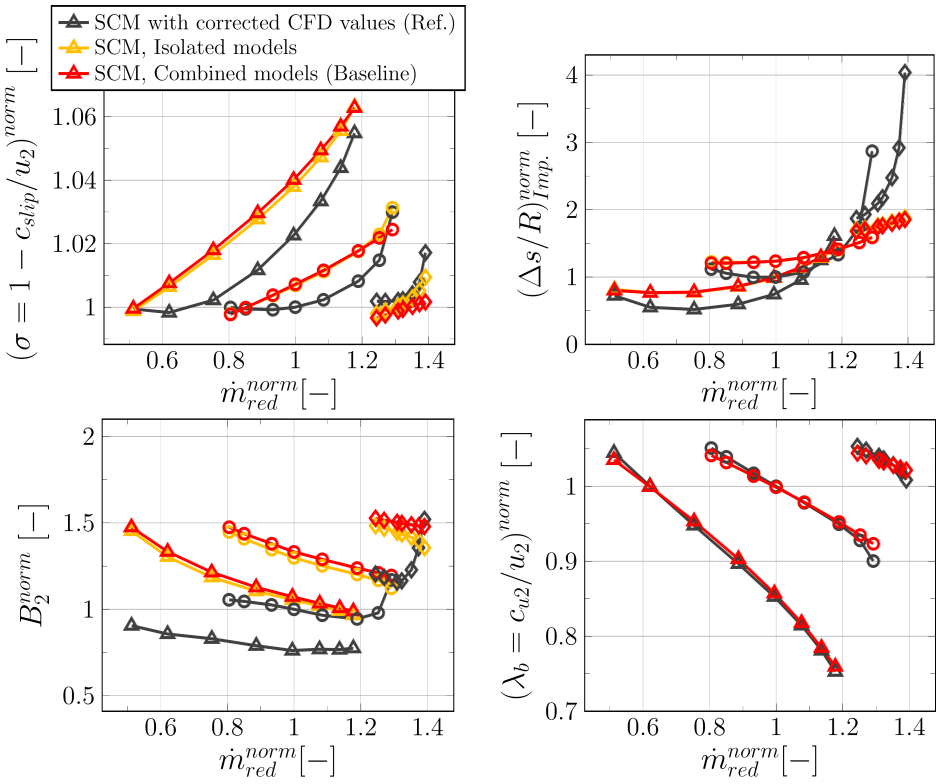

(a) RADIVER Vaneless

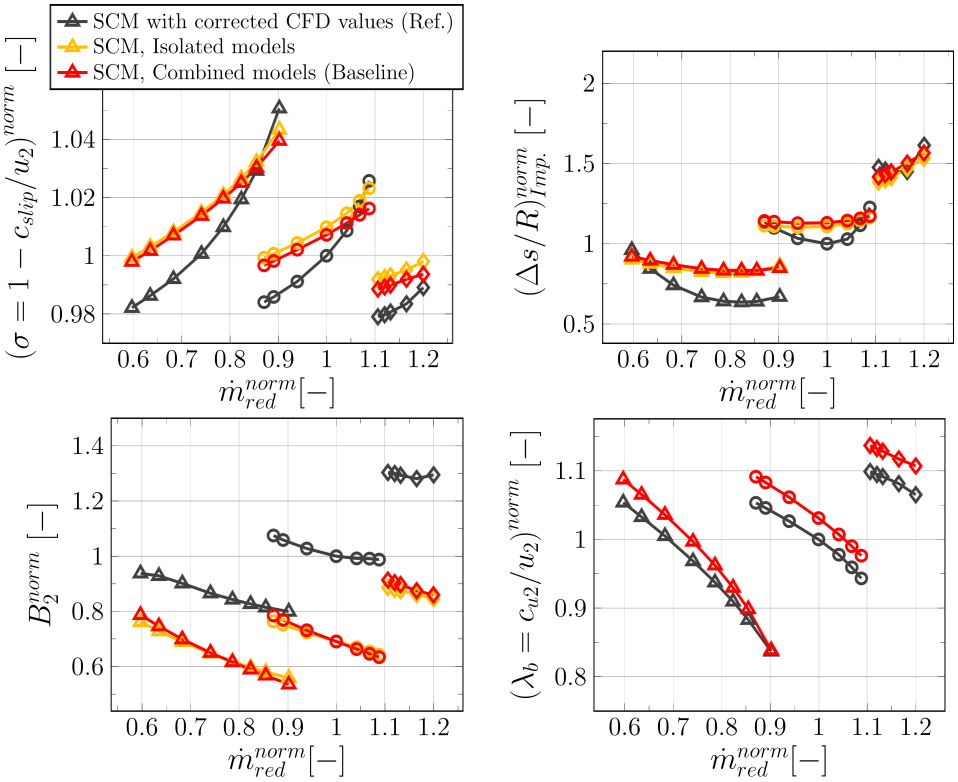

(b) Design603

Figure 5.10: Final results for the combined baseline models of slip factor, loss coefficient, and outlet aerodynamic blockage versus the CFD reference and the isolated results. The resulting work input coefficient for each test case is also depicted.

because $\lambda_b = \sigma - \text{const.}(c_{m2}/u_2)$, and the c_{m2} was the *correct* value from the prescribed CFD blockage values. Also, for this test case, the overpredicted aerodynamic blockage in the isolated analysis (see Figure 5.9a) gave an underpredicted work coefficient. Through the combination of these two models in this section, the offsets have nearly canceled out and the baseline prediction of work coefficient matches the reference curves for RADIVER Vaneless (see Figure 5.10a). This situation is different for Design603 (see Figure 5.10b), where for the combination of models there is still an overprediction of the work coefficient with respect to the reference. In this case, the baseline slip factor is overpredicted, but the blockage is underpredicted. This means that both models have contributed to an increase in work coefficient, and have added up to give the results from Figure 5.10b. A specific adjustment of these levels to match the reference work coefficient values of Design603 was not the objective in this case; instead, a unified modeling methodology for both RADIVER Vaneless and Design603 was pursued.

5.3.2 Total-total Pressure Ratio and Isentropic Efficiency

Baseline throughflow calculations with the empirical models from Sec. 5.3.1 have yielded the impeller total-total pressure ratio and isentropic efficiency results from Figure 5.11. As with the work coefficient from Figure 5.10, the pressure ratio here is nearly matched

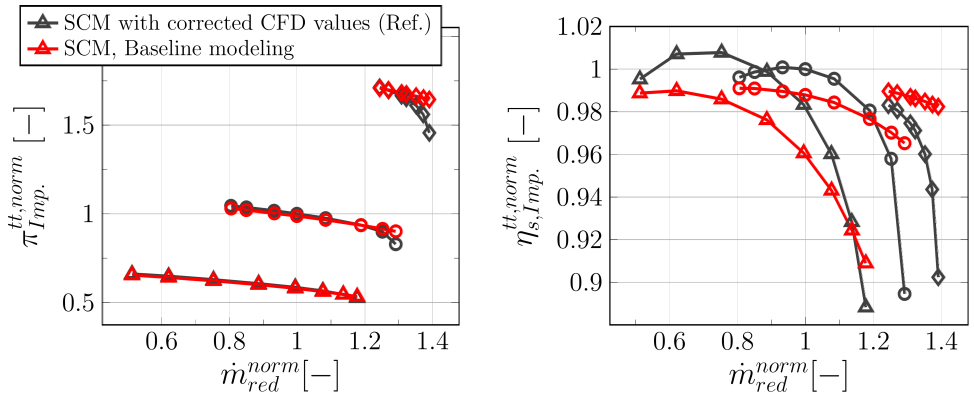

(a) RADIVER Vaneless

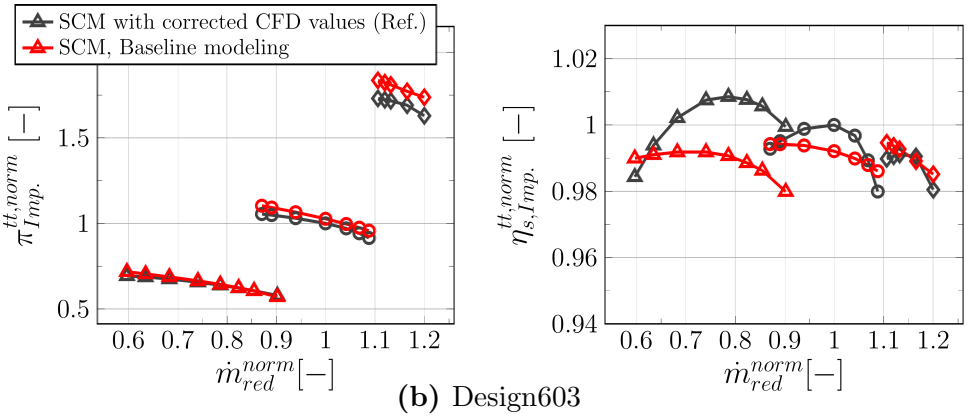

(b) Design603

Figure 5.11: Final baseline results for the impeller total-total pressure ratio and total-total isentropic efficiency for the two test cases RADIVER Vaneless and Design603.

for RADIVER Vaneless and overpredicted for Design603. Overall, the combination of chosen models in Sec. 5.2 has yielded a fairly accurate total-total pressure ratio prediction for both test cases, except for the highest rotational speed of Design603—this is due to the high blockage level of this test case at full speed, which is underpredicted by conventional correlations. Regarding the isentropic efficiency levels of both test cases (see Figure 5.11), they are nearly matched for the highest speeds when approaching surge, but underpredicted for the other two off-design rotational speeds. The offsets in isentropic efficiency prediction with respect to the reference curves are the highest at the lowest rotational speed of both test cases. Nevertheless, the use of a linear summation of the different loss factors (see (5.13)) has given a fairly accurate efficiency prediction for the design speeds, and has shown the potential for improvement at off-design speeds.

The employed literature correlations are empirical expressions, which represent relationships between relevant geometry and flow parameters, but most of them include empirical constants which make the expressions not dimensionally homogeneous. From a mathematical point of view, the addition of non-dimensionally homogenous expressions is valid. However, they cannot provide additional physical information beyond the initial expressions (*Spurk*, 1992, p. 5, 6). It is therefore difficult to determine whether some of these particular individual models should be extended to include additional terms regarding other relevant flow processes in the impeller. In this sense, for the subsequent calibration in Chapter 6 of the baseline throughflow results to CFD, this linear summation of individual contributions is left behind and what is calibrated is the resulting loss coefficient as a whole.

6 Calibration Results and Discussion

The present chapter is concerned with the calibration to correct the throughflow (SCM) prediction by means of a regression with an artificial neural network (ANN) with respect to reference data from Computational Fluid Dynamics (CFD) simulations. The calibration algorithm is depicted again in Figure 6.1 to highlight the steps to be described in this chapter. To begin with, in Sec. 6.1, the input parameters for the ANN (x_1, x_2, x_3) are defined based on theoretical considerations about the impeller flow. Their suitability for the two selected test cases is assessed based on baseline throughflow and reference results from Chapter 5. Subsequently, the training and test datasets are prepared for the defined input parameters (see Sec. 6.2). A thorough analysis on the appropriate number

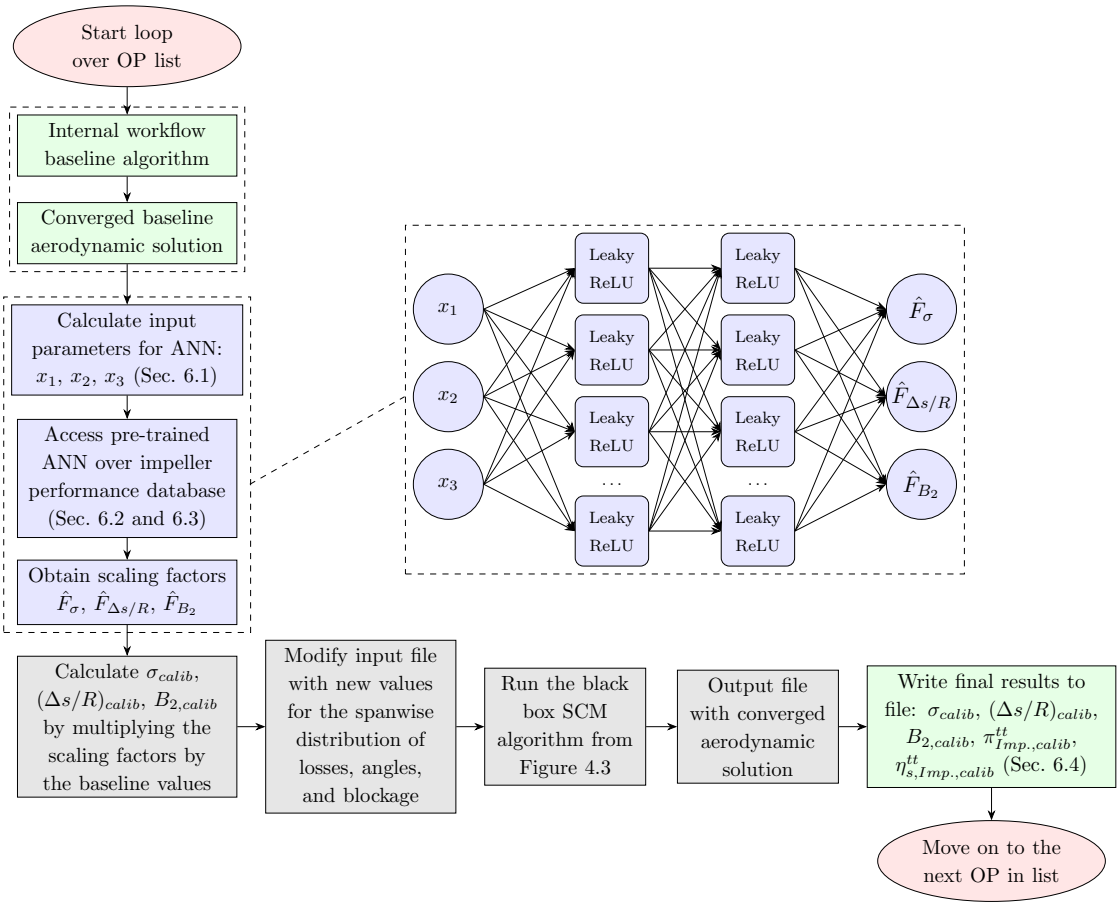

Figure 6.1: Calibrated throughflow algorithm to highlight the steps to be described in this chapter: calculation of input parameters for the ANN (Sec. 6.1), ANN training and choice of hyperparameters (Sec. 6.2 and 6.3), and evaluation of final throughflow results (Sec. 6.4).

of nodes in each hidden layer of the neural network model is carried out in Sec. 6.3, and additional regularization techniques are tested with the aim to improve generalization. The reduction in the prediction gap between baseline throughflow and the reference is quantified based on the results for impeller total-total pressure ratio and isentropic efficiency in Sec. 6.4. In the end, the suitability of the proposed methodology is discussed to determine if it would be a realistic alternative to conventional CFD simulations in the preliminary design of radial impellers.

6.1 Feature Engineering Results

In the field of machine learning, feature engineering is defined as the process of applying domain knowledge to extract analytical representations from raw data and build suitable features for training the model. In this section, input features x_1, x_2, and x_3 for the ANN model are proposed, and their suitability is discussed based on results for the test cases RADIVER Vaneless and Design603.

6.1.1 Proposed Similarity Parameters

Given the highly specific nature of the problem addressed in this dissertation (refer to Sec. 3.2), it is appropriate to design the input features based on prior physical knowledge such as conservation laws (*Jakeman et al.*, 2025, p. 7). The approach with the model parameters in this study is inspired by the work from *Balje* (1978, 1981), who identified the gradient Richardson numbers in the momentum equations along the blade-to-blade and normal directions in radial bladed impellers ($\beta_2 = 0°$) and used them as similarity parameters to characterize the wake-related behavior in the channel. The gradient Richardson number is a nondimensional parameter defined as the ratio between buoyant or body forces and flow shear (*Bradshaw*, 1973, p. 25, 31). As discussed in Chapter 5, the test cases in this dissertation are backswept impellers. As such, the momentum equations are slightly different from the ones derived by *Balje* (1978, 1981).

For backswept impellers, *Bräunling* (2009, p. 759–772), *Hehn* (2018, p. 15–17), and *Enneking* (2020, p. 11–14) derived the inviscid momentum equation in the relative frame of reference along the curvilinear metric dimensions (b, s, n) depicted in Figure 6.2. The system of equations reads

$$-\frac{1}{\rho}\begin{pmatrix}\frac{\partial p}{\partial b}\\ \frac{\partial p}{\partial s}\\ \frac{\partial p}{\partial n}\end{pmatrix} = \begin{pmatrix}-\frac{w^2}{R_b}\\ w\frac{\partial w}{\partial s}\\ -\frac{w^2}{R_n}\end{pmatrix} - 2\Omega w\begin{pmatrix}-\sin\varepsilon\\ 0\\ \cos\varepsilon\sin\beta\end{pmatrix} - \Omega^2 r\begin{pmatrix}-\sin\varepsilon\sin\beta\\ \sin\varepsilon\cos\beta\\ \cos\varepsilon\end{pmatrix}, \tag{6.1}$$

for the angle convention from the meridional direction in this work (see Figure 2.1b). In (6.1), ε is the inclination angle of the streamline to the axial direction (between m and z, see Figure 6.2), and β is the relative flow angle, which is negative because of backsweep pointing against rotation. An inviscid analysis is carried out, in line with the impeller modeling studies in the literature (see Sec. 3.1.2).

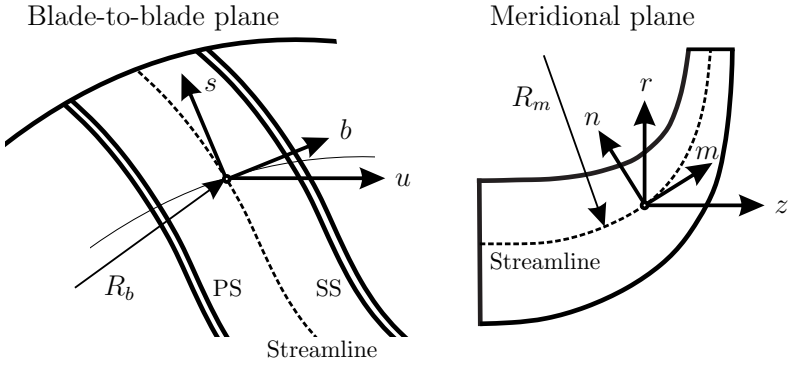

Figure 6.2: Curvilinear metric dimensions (b, s, n) along which the similarity parameters are defined in this section. This figure was already shown in Chapter 2 but is recalled here again for better elucidation of the methodology discussed.

The aim here is to obtain, for the mean streamline, a similarity parameter for each of the flow directions (b, s, n) by means of (6.1). First of all, for the blade-to-blade direction (b), the velocity-related terms in (6.1) are separated from the radius-related terms, leading to

$$\begin{aligned}\frac{1}{\rho}\frac{dp}{db} &= \frac{w^2}{R_b} - 2\Omega w \sin\varepsilon - \Omega^2 r \sin\varepsilon \sin\beta \\ &= \frac{w^2}{s_{SP}}\Big[\underbrace{\frac{s_{SP}}{R_b}}_{Ri_{c,b}} - \underbrace{\frac{2\Omega s_{SP}}{w}}_{Ri_{\Omega,b}} \sin\varepsilon\Big] - \Omega^2 r \sin\varepsilon \sin\beta, \end{aligned} \tag{6.2}$$

where two Richardson numbers can be identified, one for the curvature, $Ri_{c,b}$, and one for rotation, $Ri_{\Omega,b}$ (recall from Sec. 2.2.2, Figure 2.6a that curvature and rotation are the two effects that determine the nature of the wake). These two Richardson numbers are built by respectively dividing the relative and Coriolis accelerations by the shear as

$$Ri_{c,b} = \frac{w^2/R_b}{w(dw/dy)} \approx \frac{w^2/R_b}{w(w/s_{SP})} = \frac{s_{SP}}{R_b}, \tag{6.3}$$

$$Ri_{\Omega,b} = \frac{2\Omega w}{w(dw/dy)} \approx \frac{2\Omega w}{w(w/s_{SP})} = \frac{2\Omega s_{SP}}{w}, \tag{6.4}$$

where the gradient (dw/dy) has been approximated to w/s_{SP}, as done in *Balje* (1978), with s_{SP} being the pitch between the pressure and suction side. R_b is known for the given geometries. Accordingly, the global Richardson number for the pressure to suction side direction (Ri_{SP}) should include these two effects of curvature and rotation, projected to the b direction. This corresponds to the term inside the brackets in (6.2)

$$Ri_{SP} = \frac{s_{SP}}{R_b} - \frac{2\Omega s_{SP}}{c_m} \sin\varepsilon, \tag{6.5}$$

where w has been changed, for the mean streamline, to $w_m = c_m$. This was done so by *Balje* (1978), as he identified the Ri_{SP} with the relative velocity gradient $\Delta w/w_m$. For convenience in this dissertation with the equations for the streamline curvature method, the absolute meridional velocity c_m is used instead.

A similar procedure can be followed to obtain the global Richardson number for the hub to shroud direction (Ri_{SH}). For the normal (n) direction in (6.1), the velocity-related terms are again separated from the radius-related terms, leading to

$$\begin{aligned}\frac{1}{\rho}\frac{dp}{dn} &= \frac{w^2}{R_n} + 2\Omega w\cos\varepsilon\sin\beta + \Omega^2 r\cos\varepsilon \\ &= \frac{w^2}{b_{SH}}\Big[\underbrace{\frac{b_{SH}}{R_n}}_{Ri_{c,n}} + \underbrace{\frac{2\Omega b_{SH}}{w}}_{Ri_{\Omega,n}}\cos\varepsilon\sin\beta\Big] + \Omega^2 r\cos\varepsilon,\end{aligned} \tag{6.6}$$

where two Richardson numbers can be extracted in the same way as (6.3) and (6.4), but here the gradient (dw/dy) is approximated to (w/b_{SH}), where b_{SH} is the channel height from hub to shroud in the meridional plane. The global Richardson number then reads

$$Ri_{SH} = \frac{b_{SH}}{R_n} + \frac{2\Omega b_{SH}}{c_m}\cos\varepsilon\sin\beta, \tag{6.7}$$

where R_n is calculated from the known $R_m = \partial m/\partial\varepsilon$ (see Figure 6.2) with the expression given in *Bräunling* (2009, p. 768), but with β defined from the meridional direction. Finally, for the momentum equation in the streamwise (s) direction from (6.1)

$$\frac{1}{\rho}\frac{\partial p}{\partial s} = -w\frac{\partial w}{\partial s} + \Omega^2 r\sin\varepsilon\cos\beta, \tag{6.8}$$

the only contribution of w-related terms is from the relative acceleration. In this case, the velocity gradient ($\partial w/\partial s$) can be better substituted by a more standardized parameter as the de Haller number

$$DH = \frac{w_2}{w_{1,shr}}, \tag{6.9}$$

which is a similarity parameter that characterizes the diffusion in the impeller. According to (6.5) and (6.7), Ri_{SP} and Ri_{SH} can certainly be obtained at each position in the impeller. For consistency with DH, (6.9), which is the ratio between outlet and inlet conditions, for the Richardson numbers I also considered the whole impeller passage. As such, I defined the input parameters in the b and n directions as the ratios between the outlet and inlet Richardson numbers. This appeared to be advantageous because, at inlet, $\varepsilon = 0°$, and at outlet, $\varepsilon = 90°$, which simplified expressions (6.5) and (6.7) to some extent. The proposed similarity parameters for the (b, s, n) directions then become

$$x_1 = \frac{Ri_{SP,2}}{Ri_{SP,1}} = \frac{\frac{s_{SP,2}}{R_{b,2}} - \frac{2\Omega s_{SP,2}}{c_{m,2}}}{\frac{s_{SP,1}}{R_{b,1}}}, \tag{6.10}$$

$$x_2 = DH = \frac{w_2}{w_{1,shr}}, \tag{6.11}$$

$$x_3 = \frac{Ri_{SH,2}}{Ri_{SH,1}} = \frac{\frac{b_{SH,2}}{R_{n,2}}}{\frac{b_{SH,1}}{R_{n,1}} + \frac{2\Omega b_{SH,1}}{c_{m,1}}\sin\beta_1}, \tag{6.12}$$

which are a contribution from this dissertation's work.

6.1.2 Analysis of Suitability of Proposed Parameters

In this section, the suitability of the proposed features (6.10)–(6.12) for the present modeling problem is analyzed based on the raw data from baseline throughflow (SCM) and reference CFD simulations. To begin with, the results for the slip factor (σ) versus the first parameter, x_1, (6.10), are depicted in Figure 6.3 for the two test cases RADIVER Vaneless and Design603. The inputs x_1 are obtained from SCM to allow for the calculation of new operating points with the intended calibrated workflow. Each dataset (RADIVER SCM, RADIVER CFD, Design603 SCM, Design603 CFD) corresponds to the operating points on their respective speed lines analyzed in Chapter 5—each dataset is a whole performance map.

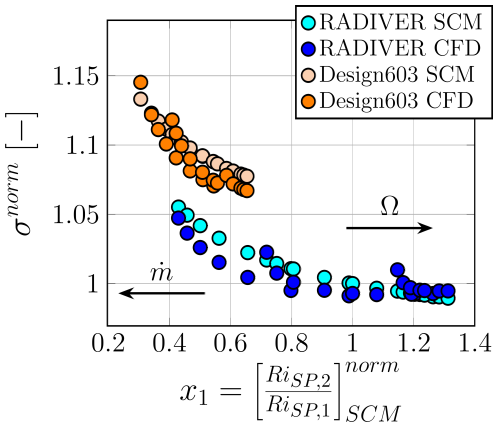

Figure 6.3: Dependency of slip factor σ from CFD (5.4) and SCM baseline (5.10) with the parameter x_1 (6.10) from SCM baseline. Each dataset contains the results for the three speed lines of each compressor considered in Chapter 5. Comparison of this figure with Figure 5.5 (σ vs. $\dot{m}$) helps establish that x_1 increases with rotational speed and decreases with mass flow rate. The distinctive and similar trend in the present figure would allow, for both test cases, to fit the whole performance map with a single curve.

From Figure 6.3, it can be recognized that the trend of the slip factor results versus the first parameter, x_1, is the same for both test cases. Higher slip factor values are found for lower x_1 values, and the curves show a parabolic behavior. The SCM datasets show a rather steady parabola trend, while the CFD datasets present some differences in slope between speed lines. Nevertheless, the points in each dataset could still be successfully fitted with a polynomial. The fact that a distinctive and similar trend is achieved for both geometries confirms the suitability of x_1 (6.10) as an input parameter to the regression model. Despite these similarities, the x_1 values for RADIVER Vaneless and Design603 in Figure 6.3 lie in different ranges, which, for the purpose of correlating both test cases together, could reduce the predictive accuracy of the regression model towards lower x_1 values. To bring the data points from RADIVER Vaneless and Design603 from Figure 6.3 to similar x-ranges, I included a scaling factor $1/\tan(2\pi/Z_{eff}) = \cot(2\pi/Z_{eff})$ to adjust x_1 with the influence of the effective number blades in each case (see Sec. 5.2.1 for the calculation of Z_{eff}). The idea of including this factor came by observing that the x_1 values of Design603 in Figure 6.3

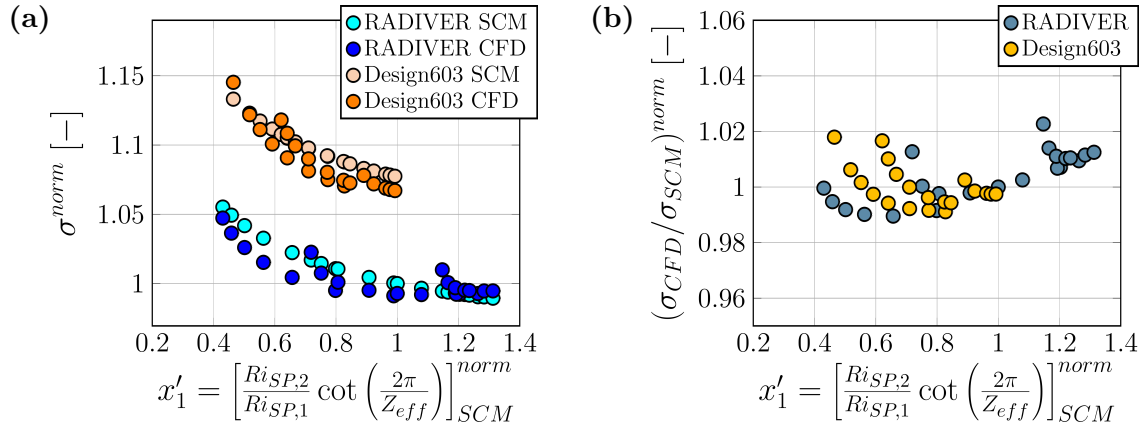

Figure 6.4: **(a)** Adjustment of the parameter x_1 (6.10) with the factor $\cot(2\pi/Z_{eff})$ to bring the data from both compressors to similar abscissa coordinates, for the purpose of increasing the predictive accuracy of the regression model. **(b)** Ratio of slip factor values from CFD (5.4) and SCM baseline (5.10) versus x_1'; these are the x and y values that entered the regression with the artificial neural network.

are smaller than the ones for RADIVER, and by recalling that Design603 has a larger number of blades than RADIVER because of the splitter blades. As such, it holds that $[\tan(2\pi/Z_{eff})]_{Design603} < [\tan(2\pi/Z_{eff})]_{RADIVER}$, which should make the Design603 x_1 values higher when included in the denominator. The results of this adjustment are depicted in Figure 6.4a, where it can be seen that the x_1 values of RADIVER Vaneless and Design603 are certainly brought together and now lie in the same range. These are however still not the data that entered the regression. As described in the calibration algorithm in Sec. 4.4.1, the idea is that the throughflow solver can be run at any operating point and can access the corresponding scaling factor $\hat{F}_\sigma$ to be multiplied by the current σ_{base}. Therefore, the mapping for the ANN regression was done based on true $F_\sigma = \sigma_{CFD}/\sigma_{base}$ values. These F_σ results are given in Figure 6.4b versus the adjusted parameter x_1'. A trend can now be recognized in the data for both compressors together, although of complex form. Because neural networks are known to be universal approximators of arbitrary nonlinear functional mappings (*Bishop*, 1995, p. 116), they are the appropriate regression method for the calibration in this dissertation.

As for the other input parameters x_2, (6.11), and x_3, (6.12), a similar analysis of the data was carried out and the results are depicted in Figure 6.5. In Figure 6.5a, the de Haller number has already proven to yield results for both compressors in the same range of abscissa values, so that no further adjustment with the number of blades is needed. As the de Haller number is the inverse of the diffusion factor used in the baseline modeling in Chapter 5, the highest values of x_2 in Figure 6.5a can be identified with the highest mass flow rates, or with the lowest diffusion. Both compressors follow a similar trend for each three speed lines. Regarding Figure 6.5b with the parameter x_3', in this case the correction factor with $\cot(2\pi/Z_{eff})$ was necessary to bring the data of both compressors together again. Nevertheless, the trends in the data are different for each test case. The cause of these discrepancies may be related to the blade profile at the inlet, because $Ri_{SH,2}/Ri_{SH,1} = f(u_1/c_{m1}, \beta_1)$; see (6.12). From the blade metal angle distribution along the streamwise direction of each test case in Figure 5.6, it is clear that, at the

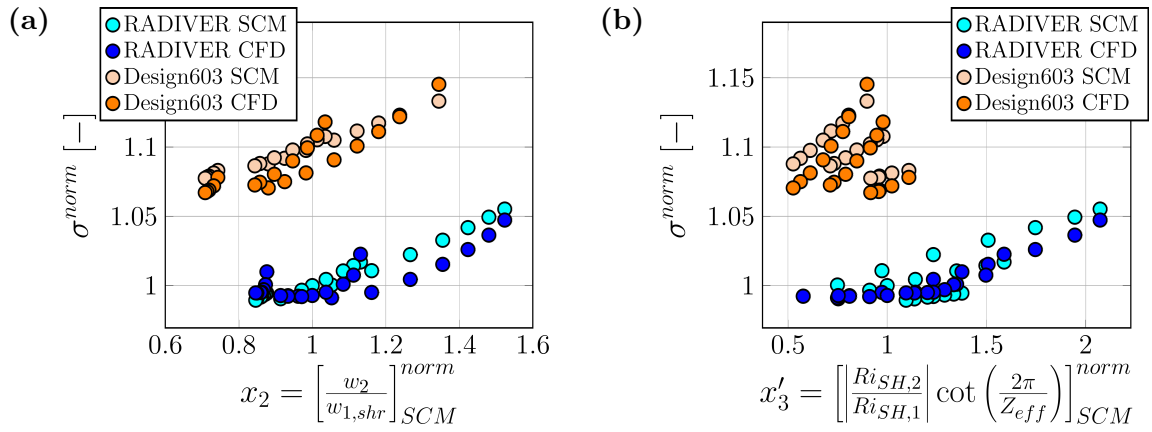

Figure 6.5: **(a)** Dependency of slip factor from CFD (5.4) and SCM baseline (5.10) with the input parameter x_2 (6.11) from SCM baseline. **(b)** Results for the slip factor from CFD (5.4) and SCM baseline (5.10) versus the adjusted input parameter x'_3 from SCM baseline. The purpose of these figures is to show the dependency of the slip factor with the chosen parameters to check the physical consistency of the modeling approach.

inlet, the inclination of the β_b profile is different for each test case. This difference in inclination is also evident in Figure 6.5b. Despite this mismatch between test cases, the actual y values that entered the regression are the respective ratios between CFD and SCM, so that a unification of the data was still possible. The parameter x'_3 is nevertheless an appropriate choice because it includes a measure of the incidence effects on the boundary layer development in the impeller. For the sake of convenience in the machine learning regression, the absolute value of $(Ri_{SH,2}/Ri_{SH,1})$ in x'_3 is taken. With that, the final set of input parameters reads

$$x'_1 = \frac{Ri_{SP,2}}{Ri_{SP,1}} \cot\left(\frac{2\pi}{Z_{eff}}\right) = \frac{\frac{s_{SP,2}}{R_{b,2}} - \frac{2\Omega s_{SP,2}}{c_{m,2}}}{\frac{s_{SP,1}}{R_{b,1}}} \cot\left(\frac{2\pi}{Z_{eff}}\right), \tag{6.13}$$

$$x'_2 = x_2 = DH = \frac{w_2}{w_{1,shr}}, \tag{6.14}$$

$$x'_3 = \left|\frac{Ri_{SH,2}}{Ri_{SH,1}}\right| \cot\left(\frac{2\pi}{Z_{eff}}\right) = \left|\frac{\frac{b_{SH,2}}{R_{n,2}}}{\frac{b_{SH,1}}{R_{n,1}} + \frac{2\Omega b_{SH,1}}{c_{m,1}} \sin\beta_1}\right| \cot\left(\frac{2\pi}{Z_{eff}}\right). \tag{6.15}$$

These three input parameters (6.13)–(6.15) were used to correct the baseline models regarding not only the slip factor, but also the loss coefficient and the aerodynamic blockage. One might argue that there are other important parameters aside from (6.13)–(6.15) that influence impeller performance, such as the Reynolds number, Mach number, main impeller dimensions, etc. These are already included in the literature correlations for the baseline modeling which is always the basis of the throughflow calculation in the present work. For this reason, the aim was to seek additional parameters that would include the effects of rotation and curvature on the three-dimensional impeller flow, as a means of bringing throughflow methods closer to 3D formulations for a broad range of operating conditions.

6.2 Training and Test Dataset Results

The training and test datasets were built for the input parameters (6.13)–(6.15). The sampling results from Sec. 4.4.2 were used for the training dataset, and the operating points on the initial speed lines were employed to build the test dataset. By way of example, the train and test results are shown in Figure 6.6a for the ratio of impeller outlet blockage versus the parameter x_3'—outliers have been removed, and points for which the CFD calculations did not converge have not been included. The sampling results for both compressors are depicted in different gray tones and the initial speed line points are shown in orange (RADIVER Vaneless) and in red (Design603).

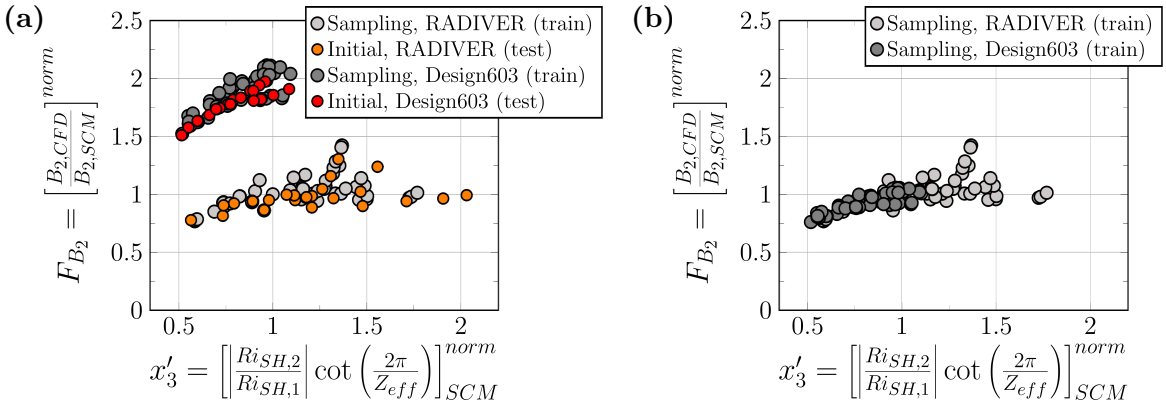

Figure 6.6: **(a)** Sampling results for each test case (RADIVER in light gray and Design603 in dark gray) for the ratio of outlet aerodynamic blockage (CFD/SCM) versus the input parameter x_3'. These sampling results form the training dataset. The test sets from the initial speed line points are also included in the figure to show that both train and test sets follow a similar distribution and represent the overall trends in the data of each compressor. **(b)** For the training of the machine learning model, the ordinate values of Design603 are halved in order to bring the data from both compressors together. This is an intermediate step and the true values were recovered for the test evaluation.

From Figure 6.6a, it can be recognized that each set—train and test—follows a similar trend for each compressor. Therefore, both train and test sets represent the overall distribution of the data points, which is important for the evaluation of the generalization performance of the model. Nevertheless, the ordinate levels for RADIVER and Design603 are clearly different. This was already discussed in the baseline modeling (see Sec. 5.2.3), where the chosen correlation gave an overprediction of the blockage from SCM with respect to CFD for RADIVER Vaneless, and an underprediction of the SCM blockage for Design603—this was done so in Chapter 5 as a means of building a standard baseline modeling for different kinds of impellers without adjusting each test case separately. However, in this chapter, to calibrate both impellers together, the ordinate values were brought together in an intermediate step for the training by halving the y values of Design603 (see Figure 6.6b). After the training, the true ordinate values of Design603 were restored. This adjustment of y values was only necessary for the blockage—the slip factor and loss coefficient did not need further adjustment.

The final grid of features and responses is given in Figure 6.7. Here, the training and test datasets contain the data from both RADIVER Vaneless and Design603, since the aim was to build a general database and demonstrate the capability of the proposed methodology to calibrate different geometries together for the whole performance map. Although there are pairs of variables that show a distinctive trend, there are others with more of a complex nature. The regions with steep curves correspond mainly to the CFD data from RADIVER Vaneless, which already showed quite a pronounced and differentiated behavior towards higher mass flow rates due to its front loading profile (see Figures 5.8a and 5.9a for reference). In this case of data with arbitrary forms from Figure 6.7, neural networks appear to be the appropriate choice of regression method. To avoid convergence issues in the multi-output neural network model due to the different orders of magnitude in Figure 6.7, both features and responses were scaled prior to training and converted to their respective units afterwards.

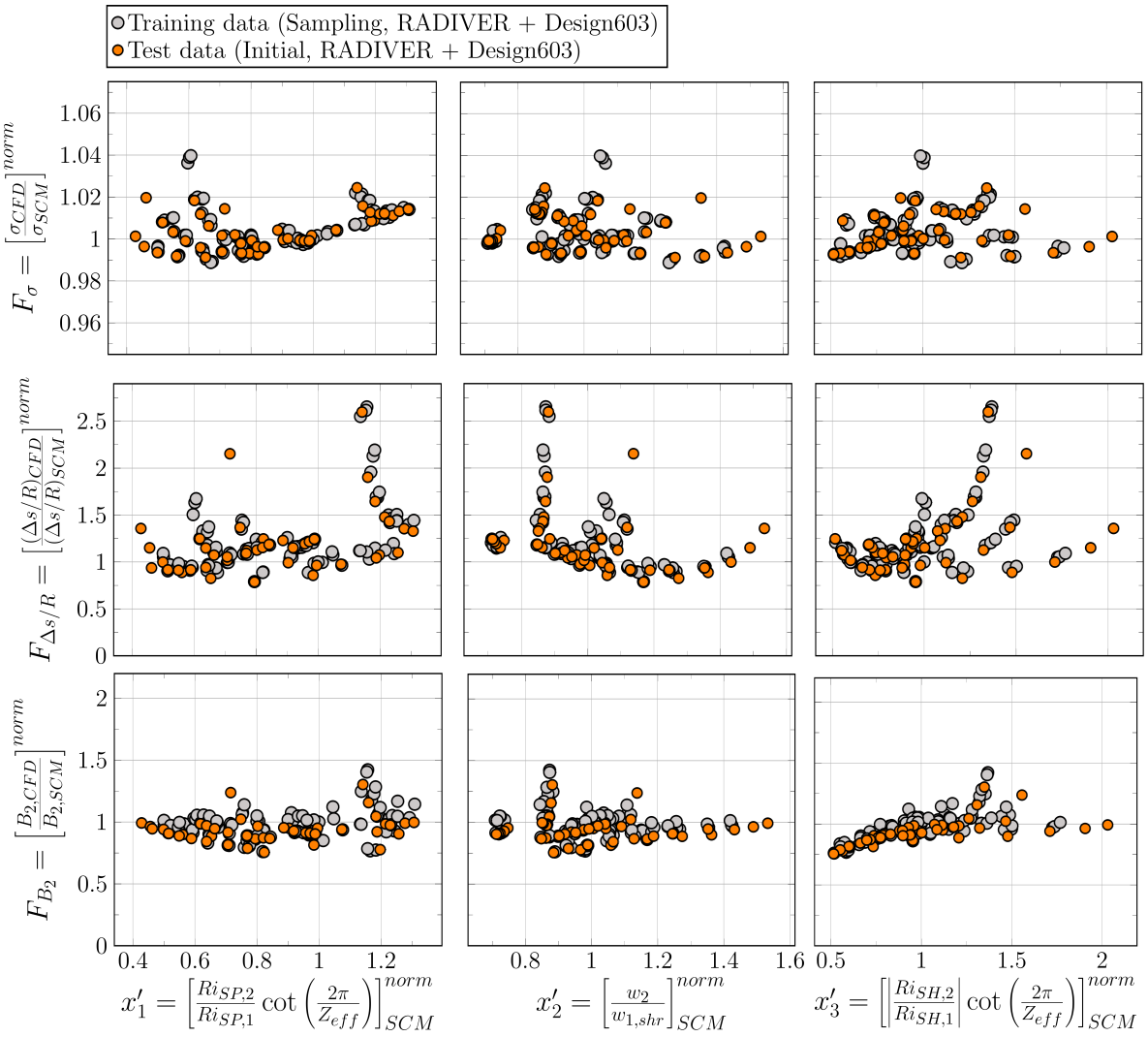

Figure 6.7: Final grid of training and test datasets containing data of both RADIVER Vaneless and Design603. The datasets include operating points for the whole performance map of each test case (three speed lines each).

6.3 Choice of Neural Network Hyperparameters

In this section, the hyperparameters for the neural network model are defined. Different choices of number of nodes per hidden layer, learning rate for the Adam optimization algorithm, and batch size are analyzed in this section. A solution is proposed based on the model's capability to generalize well to new data.

The representational capacity of the network was found to be sufficient with two hidden layers, without the need for more. The chosen activation function for each hidden node is the LeakyReLU with a slope of 0.1, as described in Figure 2.15, due to its improved performance with respect to the original ReLU function. The optimization algorithm is Adam (see Sec. 2.4.3) and the learning rate was reduced from the default $\alpha = 1e{-}3$ to $\alpha = 1e{-}4$ to ensure a smooth convergence of the training and generalization errors without oscillations (see Figure 6.8). A batch size of 40 also contributed to reducing oscillatory behavior of the curves with respect to lower batch sizes. To select the number of nodes in each hidden layer, a comparison of the model performance for different numbers of nodes was carried out and the results are depicted in Figure 6.8 in the logarithmic scale to better distinguish the curves of each setup. The same number of nodes has been set for each of the two hidden layers. For all cases outlined in Figure 6.8 except for $K = 8$, the training error (dashed lines) progresses towards a minimum while the generalization error (solid lines) stabilizes at a comparable ordinate value in all setups—as expected, the generalization error is greater than the training error (refer to Sec. 2.4.3). The fact that only the training error changes is because the number of hidden nodes affects the representational capacity of the network, i.e., its ability to fit the relationships in the training data. As such, lower training errors are found for higher numbers of hidden nodes, while fewer units cause the training

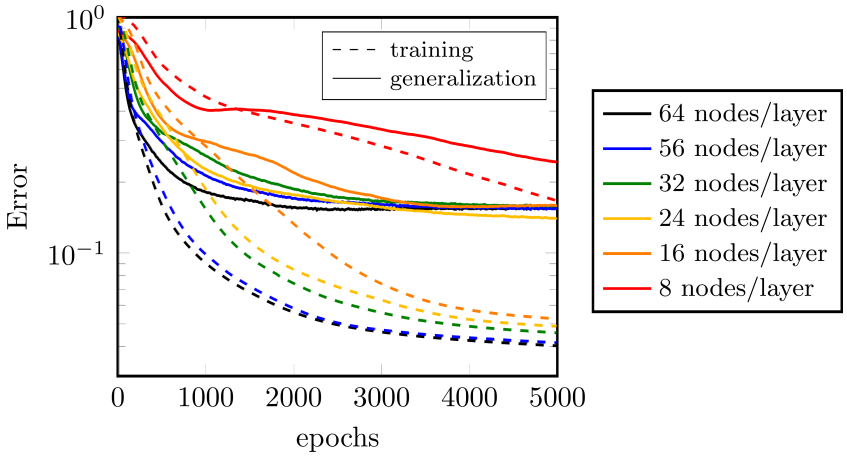

Figure 6.8: Progression of training and generalization errors over the number of epochs for different numbers of nodes in the hidden layers of the neural network model from Figure 6.1. The hyperparameter setup included: LeakyReLU activation function with slope of 0.1 in each hidden layer (see Figure 2.15); Adam optimization algorithm with learning rate $\alpha = 1e{-}4$; and batch size of 40. No regularization has been applied here yet. The objective with this figure was to choose an adequate number of nodes in the hidden layers.

error to increase because of decreased accuracy—the limit case is given for $K = 8$, where the curves do not follow the expected trend as the other cases with the specified numerical setup. For K between 64 and 16, the generalization gap—between training and generalization curves—is considerably large and of similar order of magnitude in all cases. A large gap usually means that the model is overfitting the data, i.e., that the learned model does not generalize well enough for new data because it is highly sensitive to the small fluctuations between points in the training set. This gap can usually be reduced by applying regularization techniques for a given number of hidden nodes. Based on Figure 6.8, the number of hidden nodes is chosen to be $K = 32$ as a compromise between training accuracy and generalization gap, and regularization is applied next. The calculations in Figure 6.8 were performed locally in a CPU computer platform of 8 cores and the run time was of approximately 20 seconds in each case.

To choose the form of regularization that best suits the particular task of the present investigation, several tests were carried out and the results are depicted in Figure 6.9. With the same hyperparameter setup from Figure 6.8 and 32 nodes in each hidden layer, the techniques tested were *weight decay* and *dropout*. Weight decay, or L^2-regularization, consists in including an L^2-norm penalty to the weights—the biases remain untouched—in the cost function (2.63), leading to

$$\tilde{J}(\mathbf{w}, \mathbf{b}) = \frac{1}{m} \sum_{i=1}^{m} \left(F^{(i)} - \hat{F}^{(i)}(\mathbf{w}, \mathbf{b}) \right)^2 + \frac{\lambda}{2} \|\mathbf{w}\|_2^2 , \tag{6.16}$$

where λ controls the strength of the penalty—the higher the λ, the higher the regularization (*Goodfellow et al.*, 2016, p. 118, Figure 5.5). (6.16) constraints the model by

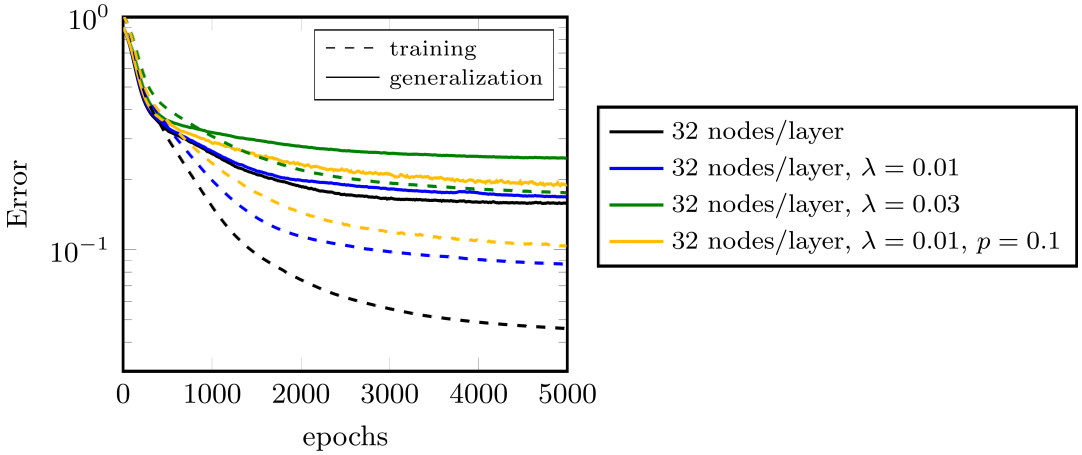

Figure 6.9: Progression of training and generalization errors over the number of epochs for the neural network model from Figure 6.1. The hyperparameter setup included: 32 nodes/hidden layer (based on Figure 6.8); LeakyReLU activation function with slope of 0.1 in each hidden layer (see Figure 2.15); Adam optimization algorithm with learning rate $\alpha = 1\text{e}{-4}$; and batch size of 40. In order to reduce the generalization gap from the initial setup (in black), regularization techniques have been applied here, such as weight decay (controlled by λ, see (6.16)) and dropout of nodes (controlled by the probability p to be multiplied by zero).

penalizing large weights in favor of smaller and more stable weights, which ultimately lead to a better generalization behavior. In Figure 6.9, adding a penalty of $\lambda = 0.01$ has significantly reduced the gap between the training and generalization errors, but at the expense of predictive accuracy, because the training error has actually increased. Further increasing λ up to 0.03 (in green) contributes to an even smaller gap, but the high error levels achieved by both training and generalization curves are considered inappropriate based on the reference case with no regularization (in black). Another possibility to lower the generalization gap is the dropout method, which basically consists in omitting some of the nodes in the hidden layers by multiplying their output value by zero to obtain a simpler model. This is controlled by a probability p of a hidden node to be zeroed (*PyTorch*, 2024a). In Figure 6.9, an additional $p = 0.1$ to the case with weight decay $\lambda = 0.01$ has certainly reduced the gap (blue to amber), actually by leaving the generalization error nearly unchanged and increasing the training error level. In order to reach a compromise between training accuracy and generalization gap, the chosen regularization is weight decay with $\lambda = 0.01$ with no dropout (blue in Figure 6.9)—recall that the plots are on a logarithmic scale, so that the true errors are actually closer.

The final true error curves in a linear scale are depicted in Figure 6.10. In summary, a reasonable compromise between training accuracy and generalization gap has been reached for $\lambda = 0.01$ without dropout. Still, a possibility to further improve the model's performance would be to increase the number of training samples, as suggested by *Bishop* (1995, p. 337) and *Brownlee* (2019). This would allow to use more complex models, which would learn the training data better while also providing additional constraints to the model. This, in turn, would serve to reduce the generalization gap further. Additional samples could be collected by extending the sampling procedure from Sec. 4.4.2 through the simulation of new operating points as a means of data augmentation. Nevertheless, the solution reached here is already regarded as satisfactory, and this would represent a future line of research.

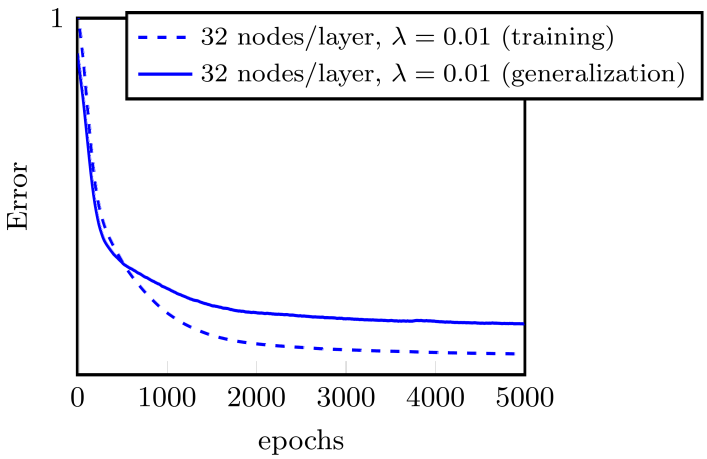

Figure 6.10: Final curves of the training and generalization errors over the number of epochs for the chosen neural network model in this work. The hyperparameter setup includes: 32 nodes/hidden layer (based on Figure 6.8); LeakyReLU activation function with slope of 0.1 in each hidden layer (see Figure 2.15); Adam optimization algorithm with learning rate $\alpha = 1\text{e}{-4}$; batch size of 40; and weight decay with $\lambda = 0.01$.

6.4 Final Calibrated Throughflow Results

In this section, an analysis of the calibrated slip factor, loss coefficient, and aerodynamic blockage at the initial operating points (test data) is conducted. The neural network model from Sec. 6.3 was incorporated into the calibrated workflow from Figure 6.1 to obtain the resulting total-total pressure ratio and isentropic efficiency of the impellers. The suitability of the calibration method developed in this dissertation is evaluated based on the improvement in the total-total pressure ratio and efficiency prediction.

6.4.1 Slip Factor, Loss Coefficient, and Aerodynamic Blockage

The results for the calibrated metrics of slip factor (σ_{calib}), loss coefficient ($(\Delta s/R)_{calib}$), and impeller outlet aerodynamic blockage ($B_{2,calib}$) are shown in green in Figure 6.11 as "SCM, Calibrated" for both RADIVER Vaneless and Design603. For the purpose of comparison, the baseline and reference results from Chapter 5 are also depicted. In general, the calibration has yielded substantial enhancements in the calculation of the throughflow performance metrics relative to the reference values (in black), as compared to the initial baseline modeling results (in red).

For the slip factor, the regression with the neural network model has been capable of matching the majority of the points on the three speed lines of each test case. For RADIVER Vaneless (see Figure 6.11a), solely the points at near-choke condition are generally underpredicted. This steepness of the reference slip factor curves near choke has also been difficult for the regression to match the Design603 values (see Figure 6.11b). Otherwise, the calibration method certainly allows for the parabola trend of the reference slip factor curves, increasing towards higher mass flow rates. As for the loss coefficient of both test cases, the calibration method has improved the prediction for the majority of the points on especially the lowest and highest rotational speeds. Visible discrepancies between "SCM, Calibrated" and "SCM with corrected CFD values (Ref.)" are found for the mid speed lines of both RADIVER Vaneless and Design603. For RADIVER Vaneless at this speed line, the calibration overpredicts the loss coefficient towards lower mass flow rates and underpredicts the peak reference value near choke. The opposite happens for the mid speed line of Design603, where the calibration overpredicts the loss coefficient value towards higher mass flow rates. Despite these differences, the new method still provides an improvement with respect to the initial baseline modeling. Lastly, for the outlet aerodynamic blockage, the calibration has been capable of reducing the baseline offsets to a large extent for both test cases. For RADIVER Vaneless, the calibration still overpredicts the reference blockage values at all speed lines; however, the mean relative error with respect to the reference at the lowest mass flow condition has been improved by 59.1%, 40.2%, and 22.2% with increasing rotational speed, respectively. Significant is also the reduction in the blockage prediction offset for Design603. In this case, the calibration brings the baseline results from an underprediction to a slight overprediction with respect to the reference values. The improvement in relative error compared to "baseline" ranges, for the lowest mass flow rate, from -20.1% to -25.3% and -30.8% with increasing speed.

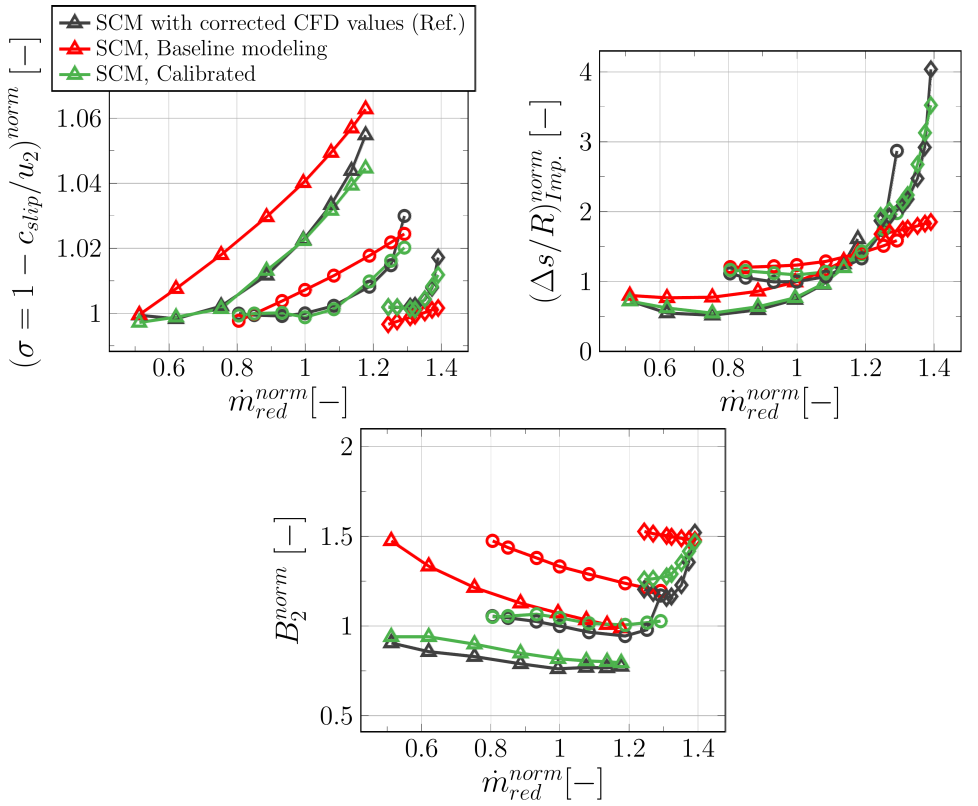

(a) RADIVER Vaneless

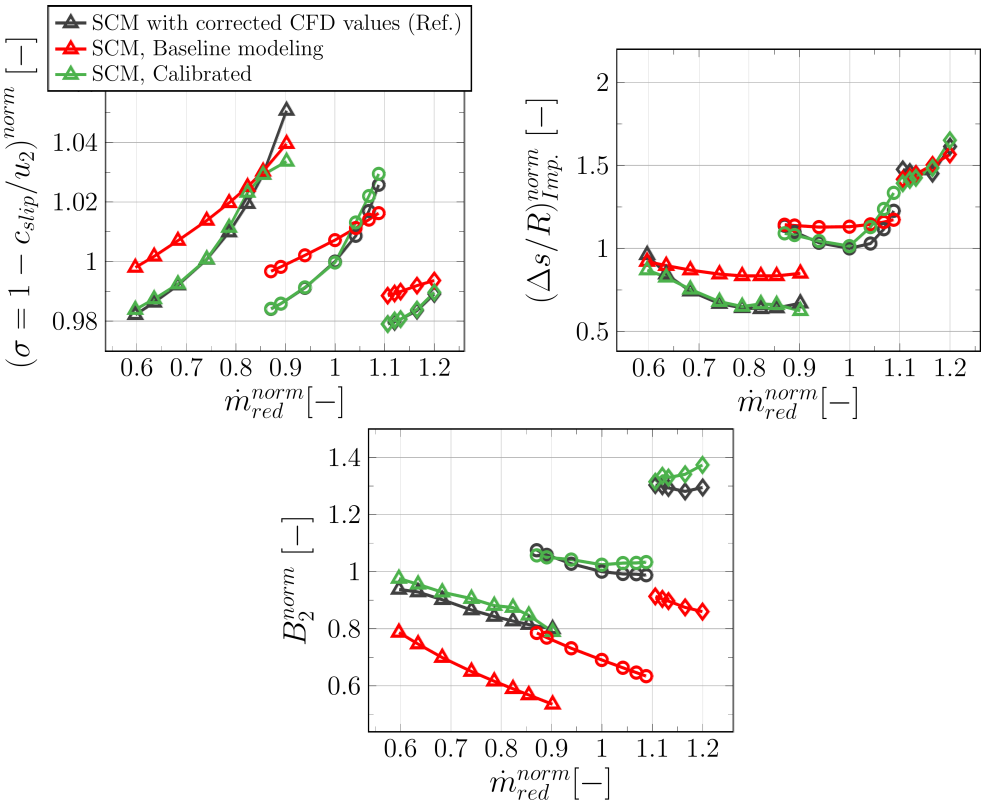

(b) Design603

Figure 6.11: Calibrated results for the slip factor, loss coefficient, and outlet aerodynamic blockage. The reference and baseline results are also included to assess the relative improvement achieved by the calibration with respect to the baseline calculation.

In summary, the calibration has effectively enhanced the calculation of the slip factor, loss coefficient, and aerodynamic blockage metrics. The neural network architecture, including three inputs that represent the loading in each flow direction and three outputs to represent the coupling effects between slip, losses, and blockage, has proven suitable. The reference curves have been successfully reached for all the speed lines of two test cases of different geometry, but similar nominal characteristics, concurrently.

6.4.2 Total-total Pressure Ratio and Isentropic Efficiency

Throughflow calculations with the calibrated values of slip factor, loss coefficient, and aerodynamic blockage from Figure 6.11 resulted in the total-total pressure ratio and isentropic efficiency curves from Figure 6.12. These results are depicted in green ("SCM, Calibrated"). For the purpose of comparison, the baseline results ("SCM, Baseline modeling") and the reference curves ("SCM with corrected CFD values (Ref.)") are also displayed.

For RADIVER Vaneless (see Figure 6.12a), the baseline results for the total-total pressure ratio were already close to the reference because of the overprediction of both the slip factor and aerodynamic blockage, which resulted in the right level of work coefficient (see Figure 5.10a). However, this combination of models was still not optimal, as the models themselves deviated significantly from the reference. The calibration with the neural network has demonstrated to produce models for the slip factor and aerodynamic blockage that correspond to the reference curves along the speed lines (see Figure 6.11a). Consequently, the total-total pressure ratio is now of the right level, again, but with the correct models as well. The largest difference between the calibration and the baseline results in this case is observed at the highest rotational speed, where the total-total pressure ratio now aligns with the reference curve towards choke. Significant is certainly the improvement in isentropic efficiency prediction with the calibration, which now follows the reference curves for all three speed lines. The calibration has successfully corrected the baseline overprediction for the design speed line—the highest rotational speed in Figure 6.11a. For the off-design speeds, i.e., the lowest and mid-speed lines, the calibration has aided in increasing the prediction levels up to the reference curves for the majority of the operating points along these speed lines. However, minor discrepancies with regard to the reference remain evident. At the lowest rotational speed, the maximum relative error with respect to the reference, excluding the near choke operating point, is -0.58%. At the mid-speed line, the maximum relative error is -0.63%, and at the highest speed line, it is -0.82%.

For Design603 (see Figure 6.12b), the calibration is also capable of accurately reproducing the reference curves of total-total pressure ratio. In this case, the improvement compared to the baseline modeling is more significant than for RADIVER Vaneless, as evidenced in Figure 6.12a. The improvement in relative error achieved by the calibration compared to baseline, with respect to reference ranges, for the lowest mass flow rate points, from -2.2% on the lowest speed line, to -5.0% for the highest one. These correct levels of total-total pressure ratio result from the accurate prediction of slip factor and outlet aerodynamic blockage from Figure 6.11b. The order of magnitude of the

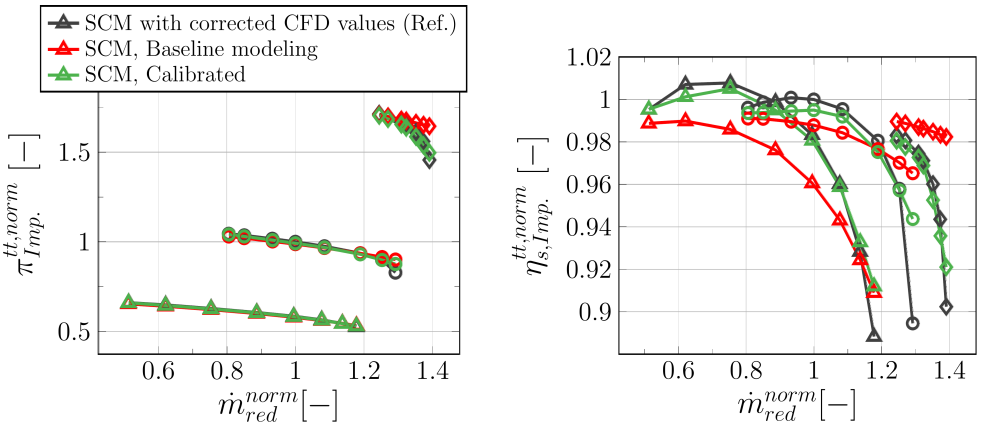

(a) RADIVER Vaneless

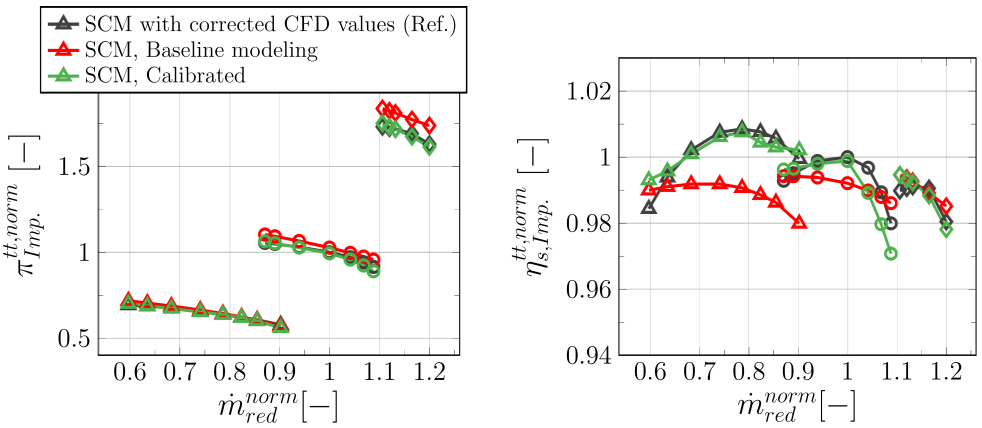

(b) Design603

Figure 6.12: Calibrated results for the total-total pressure ratio and the isentropic efficiency of the impellers of RADIVER Vaneless and Design603. The reference and baseline results are also included to assess the relative improvement achieved by the calibration with respect to the initial baseline calculation.

slight overprediction in B_2 in Figure 6.11b does not translate into a major discrepancy in the prediction of pressure ratio. With respect to the isentropic efficiency, the calibration methodology also brings the off-design speed lines (lowest and mid speeds) to the right levels. Nevertheless, at the lowest speed line, there are a few data points that do not align with the expected parabola trend. This deviation is attributable to the regression with the neural network, which builds arbitrary and complex functions based on the given data. Furthermore, at the mid speed line, the choke condition seems to be reached prematurely and the curve falls under the reference from the mid operating point towards choke. The design speed line, representing the highest rotational speed, remains close to the baseline prediction, with the exception of the choke region. In this area, the calibration permits the efficiency to align with the reference curve.

Despite the satisfactory results achieved with the calibration, there is an inherent uncertainty associated with the use of a neural network model for the regression, i.e., from the specific model selected. As previously discussed in Sec. 6.3, there are various hyperparameters in a neural network model that can be chosen for a specific problem. These

include, but are not limited to, the number of hidden layers and their dimension, the optimization algorithm and its learning rate, the activation functions, and other relevant parameters. A thorough examination of the impact of varying these parameters has been previously conducted in Sec. 6.3. The yet present potential for improvement could be addressed in the future by exploring the influence of varying sizes of training data, with the objective of optimizing the training process and the network weight prediction. This would still be far from a standardized Uncertainty Quantification (UQ) method. The quantification of uncertainty in neural networks can be achieved through the implementation of a Bayesian neural network (BNN) model (*He et al.*, 2025). A BNN represents an extension of a traditional neural network model—such as the one in this dissertation—, but with the distinction that it uses probability distributions instead of single values for prediction. However, this line of research would lie beyond the scope of this dissertation and is intended as a suggestion for future research.

7 Summary and Outlook

This dissertation has focused on the improvement of the predictive accuracy of two-dimensional (2D) streamline curvature throughflow methods with respect to three-dimensional (3D) Computational Fluid Dynamics (CFD) simulations for radial impellers across the operating map. To ensure that the throughflow method accurately matched the results of benchmark CFD simulations, a calibration methodology based on an artificial neural network (ANN) regression was developed, which provided new values for the metrics of slip factor, loss coefficient, and aerodynamic blockage required in a throughflow calculation. The results for the impeller total-total pressure ratio and isentropic efficiency were then determined by using these three calibrated metrics in a throughflow calculation. A summary of the main results of this dissertation is given here, together with a discussion of the degree of achievement of the originally defined objectives.

In Chapter 5, a comprehensive analysis of the suitability of established literature correlations for the metrics of slip factor, loss coefficient, and aerodynamic blockage was performed. The goal was to recommend a robust set of correlations that would fit two different backswept impellers. The test cases analyzed were RADIVER Vaneless and Design603. For the slip factor, the reference CFD curves showed an upward trend towards choke, which is typical for backswept impellers. For the prediction with the throughflow solver, the historical empirical correlations for the slip factor proved to give constant values instead. In order to reproduce the reference upward trend that varies with flow condition, it was found necessary to implement a correlation that took into account the influence of the blade turning rate and the flow coefficient. However, with the improved correlation from *Qiu et al.* (2011), a general overprediction of the reference values was obtained for the two impellers, showing that there was still a need for calibration in this case. For the loss coefficient, the linear summation of individual loss correlations for the skin friction, blade loading, tip clearance, and incidence was found to be suitable to match the CFD reference loss level for the design speed line of both test cases. For the off-design speed lines, it was found that additional adjustment was required to reproduce the CFD loss levels, proving that the correlations available in the literature were actually devised for design conditions. Nevertheless, the two different impeller geometries of RADIVER Vaneless and Design603 could be modeled with a unified combination of empirical loss models. Finally, for the outlet aerodynamic blockage, the CFD reference values were difficult to achieve with literature models. In particular, the aerodynamic blockage of Design603 was too high compared to RADIVER Vaneless, probably due to the different levels of stratification of the flow field for the two impellers: RADIVER demonstrated an enhanced unloading in the aft region, while Design603 exhibited less aft unloading. The correlations from the literature, however, were devised for uniform loading profiles. Despite this limitation, the combination of the selected models resulted

in a fairly accurate prediction of the total-total pressure ratio for both test cases overall, with the exception of the highest rotational speed of Design603 due to the large underprediction of the blockage. Regarding the isentropic efficiency, only those points at full speed were adequately estimated, while large discrepancies were obtained at off-design operation. In general, the analysis conducted in Chapter 5 yielded satisfactory results. The objective was to develop a general methodology that could be applied to two test cases of different design philosophies without including specific adjustments to each one. A satisfactory initial performance prediction at design conditions was attained, and the necessity for calibration at off-design operation was confirmed through the results of total-total pressure ratio and isentropic efficiency.

In Chapter 6, the results with the new calibration methodology using artificial neural networks (ANNs) were analyzed and discussed with the aim of quantifying the reduction of the prediction offsets from Chapter 5. For the ANN regression model, the idea behind the choice of input parameters was to include the effects of rotation and curvature on the accumulation of boundary layer fluid near the impeller exit (wake), especially at off-design operation. This was seen as a means of resembling a 3D calculation approach. Similarity parameters were extracted from the momentum equation in each flow direction, which allowed unified trends in the data from both test cases. The representational capacity of the neural network, i.e., its ability to fit the relationships in the training data, was found to be sufficient with two hidden layers of 32 nodes each, as a compromise between training accuracy and generalization gap. Reducing this gap was possible by applying weight decay with $\lambda = 0.01$ to favor smaller and more stable weights in the neural network model. Higher weight decay rates further reduced the gap but increased the training error levels, which was considered inappropriate in this case. Additional regularization techniques such as dropout with $p = 0.1$ were also found to reduce the generalization gap, but reduced the training accuracy as well.

With the final ANN model, the prediction results in Chapter 6 were significantly better than those from the baseline throughflow calculation in Chapter 5. For the slip factor and loss coefficient metrics, the calibration was able to match most of the points on the three reference speed lines of each test case, with the largest discrepancies at the limits of the operating range, i.e., in the vicinity of choke and near surge. With respect to the outlet aerodynamic blockage, a slight overprediction relative to the CFD reference was found for all the points on the three speed lines of both impellers. The new impeller total-total pressure ratio and isentropic efficiency results were obtained as a result of new throughflow calculations with these calibrated models. For both test cases, the calibration brought all the pressure ratio speed lines to the correct levels. Between the near-choke and near-surge operating points, the relative errors in pressure ratio remained within -2.01% and 0.46% with respect to the reference curves for all the speed lines considered. The accuracy of the isentropic efficiency results was also found to be satisfactory, with relative errors ranged between -0.98% and 0.48%. For the baseline calculation, the relative errors in pressure ratio at the same points were between maximum values of -1.45% and 5.90%, and in isentropic efficiency, between -2.31% and 4.22%. This shows the clear improvement in predictive accuracy brought about by the calibration. Overall, the reduction in the maximum pressure ratio prediction gap relative to the baseline is of -5.44%, and in isentropic efficiency, of -3.74%, for the

full set of speed lines analyzed. With these numbers, it is concluded that the goal of this dissertation to reduce the prediction gap relative to the baseline to match CFD reference levels across the operating map has been successfully achieved.

The high degree of accuracy achieved for pressure ratio and efficiency prediction with the calibration supports the hypothesis that the proposed machine learning-enhanced throughflow method is a realistic alternative to conventional 3D CFD simulations in the preliminary design of radial impellers. The presented methodology is capable of correcting all operating points in the performance map of two distinct impellers concurrently, at a comparable degree of accuracy to 3D methods, yet in a shorter amount of time. Despite the relatively limited number of test cases examined, the research conducted in this dissertation shows promise for the analysis of additional geometries in the future. A larger number of test cases would certainly contribute to the enhancement of the method's current predictive accuracy across a more extensive range of operating conditions.

Suggestions for future research include the continued study of the performance of the neural network model. In order to further reduce the current generalization gap of the ANN model, the collection of additional training samples could perhaps be extended to include other relevant regions of the scaling parameters in the proposed sampling method. Furthermore, exploring alternative sampling techniques beyond the scope of the current Latin Hypercube Sampling method could be a reasonable line of investigation. The objective would be to determine whether more optimal distributions of the sampling parameters can be achieved and to determine whether they provide more distinctive trends in some regions of the datasets. Additionally, the calibrated throughflow workflow algorithm could be adapted to include an online training procedure, as opposed to the current offline one, together with an adaptive sampling design. This would facilitate the continuous search for optimal values of the scaling parameters, thereby enhancing the clarity of the trends observed in the datasets. Another line of future research could be the examination of other neural network models. Traditional neural network architectures such as the one in this dissertation have an inherent uncertainty associated with the presence of user-defined, and often non-optimized, hyperparameters for the specific problem under consideration. This uncertainty could be quantified through the implementation of a Bayesian neural network model, which uses probability distributions instead of single values for the model training process.

Additionally, alternative approaches to the current strategy for calibration could be evaluated. The methodology employed has been, to a certain extent, a consequence of the project's constraints, which have restricted the adoption of a more automated approach. Rather than utilizing the additional offset equations to calibrate the baseline slip factor, loss coefficient, and aerodynamic blockage results, it would be worthwhile to explore the calibration of the individual coefficients of the empirical models. In the present study, calibrating the coefficients would have resulted in a substantial number of input parameters for the artificial neural network model. Due to the limited amount of simulation data that was viable to obtain manually in the TRACE CFD environment without resorting to automated generation or parametrization platforms, this calibration strategy might have led to overfitting of the data directly, and thus to suboptimal

performance of the machine learning model—the optimal number of parameters depends on the complexity of the problem and the size of the dataset. Such an approach would have been feasible if larger amounts of training data would have been available. Consequently, this method is regarded as a potential approach for subsequent investigations, provided that the systems are automated.

Nomenclature

Roman letters

a	(1) Acceleration
	(2) Regression coefficients in (2.54)–(2.56)
A	(1) Area
	(2) Arbitrary variable in Sec. 2.3.1
	(3) Left-hand side matrix in the matrix method
	(4) Hidden nodes in a neural network model
A_R	Area ratio of the impeller
b, s, n	Curvilinear metric dimensions in the directions of a body-fitted curvilinear coordinate system
b	(1) Blade blockage factor
	(2) Biases in a neural network model
	(3) Channel height
B	(1) Aerodynamic blockage
	(2) Right-hand side vector in the matrix method equation
	(3) Spline basis functions in the MARS method
c	(1) Absolute velocity
	(2) CFL number
c_r, c_u, c_z	Absolute velocity components in cylindrical coordinates
c_m	Absolute meridional velocity component
c_{slip}	Slip velocity
c_f	Friction coefficient
c_p	Specific heat capacity at constant pressure
c_v	Specific heat capacity at constant volume
D	Diameter
D_h	Hydraulic diameter
DF	Diffusion factor
DH	De Haller number
Δq	Loss coefficient based on stagnation enthalpy
$\Delta s/R$	Entropy-based loss coefficient
e	(1) Specific energy

	(2) Relative error
E_t	Total energy of the system
f	Approximating function
F	(1) Force
	(2) Ratio between CFD and baseline throughflow metrics
	(3) Shape factor in the *Qiu et al.* (2011) slip factor correlation
$\hat{F}$	Approximated F values with the neural network regression
F_u	Tangential force component
F_d	Dissipative force
F_0	Constant in the Von Backström slip factor correlation
$\hat{\mathbf{F}}$, $\hat{\mathbf{G}}$, $\hat{\mathbf{H}}$	Inviscid/convective fluxes in the compressible 3D Navier-Stokes equations in differential form in the rotating frame
$\hat{\mathbf{F}}_v$, $\hat{\mathbf{G}}_v$, $\hat{\mathbf{H}}_v$	Viscous fluxes in the compressible 3D Navier-Stokes equations in differential form in the rotating frame
g	Objective function
G	Fluctuation term in the passage-averaged throughflow equation
h	(1) Specific enthalpy
	(2) Auxiliary function in (2.58) and (2.59)
	(3) Grid cell size
H	Head
h_t	Specific total enthalpy
I	Specific rothalpy
J	(1) Cost function
	(2) Jacobian
k	(1) Aerodynamic blockage factor
	(2) Turbulent kinetic energy
K	(1) Number of predictors in (2.54)–(2.56)
	(2) Number of nodes per hidden layer of a neural network model
L	(1) Likelihood function
	(2) Blade meridional length
L_i	Limiter in the MUSCL scheme
L_1	L1 or Manhattan distance norm
L_2	L2 or Euclidean norm
L_∞	L-infinity norm
m	(1) Mass
	(2) Distance along the meridional direction
	(3) Number of samples
	(4) Momentum in the Adam algorithm

M	Mach number
$\dot{m}$	Mass flow rate
$\hat{m}$	Bias-corrected momentum in the Adam algorithm
n	(1) Normal vector to a surface
	(2) Distance in the normal direction
	(3) Rotational speed
	(4) Number
N	Total number of cells
ν	Molecular/Kinematic viscosity
p	(1) Static pressure
	(2) Number of inputs to a neural network model
	(3) Probability
	(4) Apparent order of numerical scheme
p_t	Total pressure
p^*	Rotary stagnation pressure
P	(1) Reynolds stress production tensor
	(2) Arbitrary variable in a diffusion-type equation
P_u	Pressure blade force
q	Quasi-orthogonal direction
Q	Heat input
$\hat{\mathbf{Q}}$	Solution state vector to the compressible 3D Navier-Stokes equations in differential form in the rotating frame
Q_L, Q_R	Left and right states of a cell
r, φ, z	Coordinates in a cylindrical coordinate system
r	(1) Radius
	(2) Grid scaling factor
r_c	Radius of curvature of the streamline
R	(1) Specific gas constant
	(2) Radius of curvature of the streamline
$\hat{\mathbf{R}}$	Residual
Ri	Richardson number
Re	Reynolds number
s	(1) Specific entropy
	(2) Distance along a streamline, in the streamwise direction
	(3) Blade pitch
S	Entropy
$\hat{\mathbf{S}}$	Source term in the compressible 3D Navier-Stokes equations in differential form in the rotating frame

S_1	Blade-to-blade stream surface
S_2	Hub-to-shroud stream surface
S_{2m}	Mean S_2 stream surface
t	(1) Time
	(2) Blade thickness
	(3) Independent variable that controls the position of a point on a curve
T	(1) Torque
	(2) Temperature
T_t	Total temperature
T_u	Tangential force deficit
u	Blade speed
v	(1) Specific volume
	(2) Variance in the Adam algorithm
$\hat{v}$	Bias-corrected variance in the Adam algorithm
V	Cell volume
w	(1) Relative velocity
	(2) Specific work input
	(3) Weights in a neural network model
W	Work input
$\dot{W}$	Rate of work, i.e., power
x	Variables or parameters, inputs
x_1, x_2, x_3	Input parameters for the ANN model
x'_1, x'_2, x'_3	Adjusted parameters for the ANN with the effective number of blades
y	True responses
$\hat{y}$	Predictions
y^+	Nondimensional wall distance
z	Axial coordinate/direction in cylindrical coordinates
Z	(1) Number of impeller blades
	(2) Correlation function in the Kriging method

Greek letters

α	(1) Flow angle in the absolute system, from meridional direction
	(2) Learning rate
β	Flow angle in the relative system, from meridional direction
β_b	Blade metal angle, from meridional direction
β_1, β_2	Decay rates in the Adam algorithm
δ	Boundary layer width
η	Efficiency

η_a, η_b	Impeller effectiveness parameters in the two-zone modeling method
ϵ	Small positive constant to avoid division by zero
γ	Angle between the meridional and quasi-orthogonal directions
Γ	Circulation
κ	(1) Ratio of specific heats
	(2) Curvature
	(3) Constant in the MUSCL extrapolation for a second-order Fromm scheme
λ	(1) Work coefficient
	(2) Penalty in the L2-regularization technique
μ	Dynamic viscosity
μ_t	Eddy viscosity
ω	(1) Absolute vorticity
	(2) Specific rate of dissipation
Ω	Angular speed
π	Pressure ratio
ψ	Mean stream function
ρ	Density
σ	(1) Slip factor, American definition
	(2) Standard deviation
	(3) Activation function in a neural network model
σ'	Work reduction factor
τ	(1) Shear stress
	(2) Iteration step
θ	Angular distance
ε	(1) Inclination angle of the streamline to the axial direction
	(2) Mixing coefficient in a diffusion-type equation
	(3) Iteration error
	(4) Approximation error in regression
	(5) Tip clearance gap
φ	Local flow coefficient
ξ, η, ζ	Body-fitted coordinate system

Subscripts

0	At compressor inlet
1	At impeller inlet
2	At impeller outlet
12	From impeller inlet to impeller outlet
app	Apparent, from the energy fluctuations

abs	In the absolute system
b	(1) Blade
	(2) Along the b direction
base	Baseline
bl	Blade loading
calib	Calibrated
cl	Clearance
c	Relative to the curvature
eff	Effective
ext	External
f	Friction
geom	Geometrical
hub	Hub
i	Row index
Imp.	Relative to the impeller
inc	Incidence
∞	Perfect flow guidance condition at impeller outlet
j	Column index
loss	Loss between the real and the isentropic compression process
m	Meridional
n	Normal, spanwise
new	Relative to the corrected outflow conditions at impeller outlet
nom	Nominal
opt	Optimum
Ω	Relative to rotation
q	Along the quasi-orthogonal direction
r	Radial
rel	In the relative system
rev	Reversible
red	Reduced, used for the mass flow as $\dot{m}_{red} = \dot{m}\sqrt{T_{t0}}/p_{t0}$
ref	Reference
s	(1) Isentropic
	(2) Streamwise
sf	Skin friction
shr	Shroud
u	Tangential
z	Axial

Superscripts

area	Area-averaged
int	Internal
mass	Mass-averaged
norm	Normalized
ts	Total-static
tt	Total-total
$\bar{}$	Average, algebraic average
$\hat{}$	Momentum average
$\tilde{}$	Density average
’	Fluctuation magnitude
$\vec{}$	Vectorial quantity

Abbreviations

1D	One-dimensional
2D	Two-dimensional
3D	Three-dimensional
ANN	Artificial Neural Network
Adam	Adaptive Moment Estimation
BNN	Bayesian Neural Network
CO_2	Carbon dioxide
CFD	Computational Fluid Dynamics
CFL	Courant-Friedrichs-Lewy (number)
CR	Clearance Ratio
CPU	Central Processing Unit
DLR	Deutsches Zentrum für Luft- und Raumfahrt
FB	Full blades
SB	Splitter blades
GMC	General Mesh Connector
GCI	Grid Convergence Index
KNN	K-nearest Neighbors
LHS	Latin Hypercube Sampling
MARS	Multivariate Adaptive Regression Splines
MLP	Multi-layer Perceptron
MIT	Massachusetts Institute of Technology
MUSCL	Monotonic Upstream Scheme for Conservation Laws
OP	Operating Point
ODE	Ordinary Differential Equation

PE	Peak Efficiency
PS	Pressure side
SS	Suction side
SP	From pressure to suction side
SH	From hub to shroud
Q3D	Quasi-Three-Dimensional
RANS	Reynolds-averaged Navier-Stokes
RSM	Response Surface Methodology
ReLU	Rectified Linear Unit
SVM	Support Vector Machines
SCM	Streamline Curvature Method
TRACE	Turbomachinery Research Aerodynamic Computational Environment
UQ	Uncertainty Quantification
URANS	Unsteady Reynolds-averaged Navier-Stokes

Mathematical operators

δ	Limiting value
∂	Partial derivative
d	Regular derivative
D	Material derivative
Δ	Delta operator
∇	Nabla operator
$\cdot$	Vector dot product
$\times$	Vector cross product
$\mathbf{F}$	Vectorial or matrix quantity
$\square^T$	Transpose

References

Adkins, G. G., J. and Smith, L. H., J. (1982). Spanwise Mixing in Axial-Flow Turbomachines. *Journal of Engineering for Power*, 104(1):97–110. https://doi.org/10.1115/1.3227271.

Agnolucci, A., Marconcini, M., Arnone, A., Toni, L., Grimaldi, A., and Giachi, M. (2021). Centrifugal Compressor Stage Efficiency and Rotor Stiffness Augmentation via Artificial Neural Networks. *Proceedings of the ASME Turbo Expo 2021: Turbomachinery Technical Conference and Exposition. Volume 2D: Turbomachinery – Multidisciplinary Design Approaches, Optimization, and Uncertainty Quantification; Radial Turbomachinery Aerodynamics; Unsteady Flows in Turbomachinery.* Virtual, Online. June 7-11, 2021. V02DT37A014. ASME. https://doi.org/10.1115/GT2021-59998.

Agnolucci, A., Marconcini, M., Biliotti, D., Toni, L., Baroni, A., Romani, L., and Arnone, A. (2023). Robust Design of a Vaned Diffuser in a Centrifugal Compressor Stage With a High Load Impeller. *Proceedings of the ASME Turbo Expo 2023: Turbomachinery Technical Conference and Exposition. Volume 13D: Turbomachinery – Multidisciplinary Design Approaches, Optimization, and Uncertainty Quantification; Radial Turbomachinery Aerodynamics; Unsteady Flows in Turbomachinery.* Boston, Massachusetts, USA. June 26-30, 2023. V13DT35A022. ASME. https://doi.org/10.1115/GT2023-103585.

Aissa, M. H. and Verstraete, T. (2019). Metamodel-Assisted Multidisciplinary Design Optimization of a Radial Compressor. *International Journal of Turbomachinery, Propulsion and Power*, 4(4):35. https://doi.org/10.3390/ijtpp4040035.

AnalytixLabs (2024). *Pytorch vs. TensorFlow*. Medium. Retrieved March 25, 2025, from https://medium.com/@byanalytixlabs/pytorch-vs-tensorflow-which-framework-to-choose-ed649d9e7a35.

Aungier, R. H. (1995). Mean Streamline Aerodynamic Performance Analysis of Centrifugal Compressors. *Journal of Turbomachinery*, 117(3):360–366. https://doi.org/10.1115/1.2835669.

Aungier, R. H. (2000). *Centrifugal Compressors: A Strategy for Aerodynamic Design and Analysis.* ASME Press. https://doi.org/10.1115/1.800938.

Balje, O. E. (1978). A Flow Model for Centrifugal Compressor Rotors. *Journal of Engineering for Power*, 100(1):148–158. https://doi.org/10.1115/1.3446308.

Balje, O. E. (1981). *Turbomachines: A Guide to Design Selection and Theory.* John Wiley & Sons.

Baralon, S., Eriksson, L.-E., and Håll, U. (1999). Evaluation of Higher-Order Terms in the Throughflow Approximation Using 3D Navier-Stokes Computations of a Transonic Compressor Rotor. *Proceedings of the ASME 1999 International Gas Turbine and Aeroengine Congress and Exhibition. Volume 1: Aircraft Engine; Marine; Turbomachinery; Microturbines and Small Turbomachinery.* Indianapolis, Indiana, USA. June 7-10, 1999. V001T03A013. ASME. https://doi.org/10.1115/99-GT-074.

Bellary, S. A. I., Samad, A., Couckuyt, I., and Dhaene, T. (2016). A Comparative Study of Kriging Variants for the Optimization of a Turbomachinery System. *Engineering with Computers*, 32(1):49–59. https://doi.org/10.1007/s00366-015-0398-x.

Benetschik, H. (2023). *Numerische Integrationsverfahren für Strömungen in Turboarbeitsmaschinen und Strahlantrieben I* [Lecture]. RWTH Aachen University, Institut für Strahlantriebe und Turbomaschinen, WS 2023/2024.

Benini, E. and Cenzon, M. (2009). Calibration of a Meanline Centrifugal Pump Model Using Evolutionary Algorithms. *Proceedings of the Institution of Mechanical Engineers, Part A: Journal of Power and Energy*, 223(7):835–847. https://doi.org/10.1243/09576509JPE742.

Bishop, C. M. (1995). *Neural Networks for Pattern Recognition*. Oxford University Press.

Bonaiuti, D., Arnone, A., Ermini, M., and Baldassarre, L. (2006). Analysis and Optimization of Transonic Centrifugal Compressor Impellers Using the Design of Experiments Technique. *Journal of Turbomachinery*, 128(4):786–797. https://doi.org/10.1115/1.1579507.

Bosman, C. and Jadayel, O. (1996). A Quantified Study of Rothalpy Conservation in Turbomachines. *International Journal of Heat and Fluid Flow*, 17(4):410–417. https://doi.org/10.1016/0142-727X(96)00030-6.

Bosman, C. and Marsh, H. (1974). An Improved Method for Calculating the flow in Turbo-Machines, Including a Consistent loss Model. *Journal of Mechanical Engineering Science*, 16(1):25–31. https://doi.org/10.1243/JMES_JOUR_1974_016_006_02.

Bradshaw, P. (1973). Effects of Streamline Curvature on Turbulent Flow. *Advisory Group for Aerospace Research and Development, AGARDograph No.169*. AGARD-AG-169. https://apps.dtic.mil/sti/trecms/pdf/AD0768316.pdf.

Bräunling, W. J. G. (2009). *Flugzeugtriebwerke: Grundlagen, Aero-Thermodynamik, ideale und reale Kreisprozesse, Thermische Turbomaschinen, Komponenten, Emissionen und Systeme*. Springer Vieweg Berlin, Heidelberg. https://doi.org/10.1007/978-3-642-34539-5.

Britton, I. and Gauthier, J. E. D. (2008). Performance Prediction of Centrifugal Impellers Using a Two-Zone Model. *Proceedings of the ASME Turbo Expo 2008: Power for Land, Sea, and Air. Volume 6: Turbomachinery, Parts A, B, and C*. Berlin, Germany. June 9-13, 2008. pp. 1695–1704. ASME. https://doi.org/10.1115/GT2008-51530.

Brownlee, J. (2019). *How to use Learning Curves to Diagnose Machine Learning Model Performance*. Machine Learning Mastery. Retrieved April 3, 2025, from https://machinelearningmastery.com/learning-curves-for-diagnosing-machine-learning-model-performance/.

Brunton, S. L., Noack, B. R., and Koumoutsakos, P. (2020). Machine Learning for Fluid Mechanics. *Annual Review of Fluid Mechanics*, 52:477–508. https://doi.org/10.1146/annurev-fluid-010719-060214.

Casey, M. and Robinson, C. (2010). A New Streamline Curvature Throughflow Method for Radial Turbomachinery. *Journal of Turbomachinery*, 132(3):031021. https://doi.org/10.1115/1.3151601.

Casey, M. and Robinson, C. (2021). *Radial Flow Turbocompressors: Design, Analysis, and Applications*. Cambridge University Press. https://doi.org/10.1017/9781108241663.

Casey, M. and Robinson, C. (2022). Some Properties of the Exit Velocity Triangle of a Radial Compressor Impeller. *Journal of Turbomachinery*, 145(5):051007. https://doi.org/10.1115/1.4056088.

Casey, M. V. (1985). The Effects of Reynolds Number on the Efficiency of Centrifugal Compressor Stages. *Journal of Engineering for Gas Turbines and Power*, 107(2):541–548. https://doi.org/10.1115/1.3239767.

Casey, M. V. and Robinson, C. J. (2011). A Unified Correction Method for Reynolds Number, Size, and Roughness Effects on the Performance of Compressors. *Proceedings of the Institution of Mechanical Engineers, Part A: Journal of Power and Energy*, 225(7):864–876. https://doi.org/10.1177/0957650911410161.

Coppage, J. E., Dallenbach, F., Eichenberger, H. P., Hlavaka, G. E., Knoernschild, E. M., and Van Le, N. (1956). *Study of Supersonic Radial Compressors for Refrigeration and Pressurization Systems*. WADC TR 55-257. AiResearch Manufacturing Company. https://digital2.library.iit.edu/files//original/24c8c16d925ecd4ab4a1e167b2eaaf7d7ec938e5.pdf.

Cumpsty, N. A. (2004). *Compressor Aerodynamics*. Krieger Publishing Company.

De Ruyck, J. and Hirsch, C. (1981). Investigations of an Axial Compressor End-Wall Boundary Layer Prediction Method. *Journal of Engineering for Power*, 103(1):20–33. https://doi.org/10.1115/1.3230699.

Dean, R. C., J. (1967). Discussion: "A Review of Slip Factors for Centrifugal Impellers" (Wiesner, F. J., 1967, ASME J. Eng. Power, 89, pp. 558-566). *Journal of Engineering for Power*, 89(4):567–568. https://doi.org/10.1115/1.3616735.

Denton, J. D. (1978). Throughflow Calculations for Transonic Axial Flow Turbines. *Journal of Engineering for Power*, 100(2):212–218. https://doi.org/10.1115/1.3446336.

Denton, J. D. (1986). The Use of a Distributed Body Force to Simulate Viscous Effects in 3D Flow Calculations. *Proceedings of the ASME 1986 International Gas Turbine Conference and Exhibit. Volume 1: Turbomachinery*. Düsseldorf, West Germany. June 8-12, 1986. V001T01A058. ASME. https://doi.org/10.1115/86-GT-144.

Denton, J. D. and Dawes, W. N. (1998). Computational Fluid Dynamics for Turbomachinery Design. *Proceedings of the Institution of Mechanical Engineers, Part C: Journal of Mechanical Engineering Science*, 213(2):107–124. https://doi.org/10.1243/0954406991522211.

Diehl, M., Schreiber, C., and Schiffmann, J. (2020). The Role of Reynolds Number Effect and Tip Leakage in Compressor Geometry Scaling at Low Turbulent Reynolds Numbers. *Journal of Turbomachinery*, 142(3):031003. https://doi.org/10.1115/1.4045465.

DLR (2023). *TRACE User Guide: Theory*. TRACE User Guide. Retrieved May 3, 2024, from https://www.trace-portal.de/userguide/trace/page_theory.html.

Dring, R. P. and Joslyn, H. D. (1986). Through-Flow Modeling of Axial Turbomachinery. *Journal of Engineering for Gas Turbines and Power*, 108(2):246–253. https://doi.org/10.1115/1.3239895.

Dring, R. P. and Oates, G. C. (1989). Through Flow Theory for Nonaxisymmetric Turbomachinery Flow: Part I – Formulation. *Proceedings of the ASME 1989 International Gas Turbine and Aeroengine Congress and Exposition. Volume 1: Turbomachinery*. Toronto, Ontario, Canada. June 4-8, 1989. V001T01A106. ASME. https://doi.org/10.1115/89-GT-304.

Dubitsky, O. and Japikse, D. (2005). Vaneless Diffuser Advanced Model (2005D). *Proceedings of the ASME Turbo Expo 2005: Power for Land, Sea, and Air. Volume 6: Turbo Expo 2005, Parts A and B*. Reno, Nevada, USA. June 6-9, 2005. pp. 823-834. ASME. https://doi.org/10.1115/GT2005-68130.

Durbin, P. A. and Pettersson Reif, B. A. (2011). *Statistical Theory and Modeling for Turbulent Flows*. John Wiley & Sons. https://doi.org/10.1002/9780470972076.

Eckardt, D. (1980). Flow Field Analysis of Radial and Backswept Centrifugal Compressor Impellers: Part I – Flow Measurements Using a Laser Velocimeter. *Proceedings of the Twenty-fifth Annual International Gas Turbine Conference and Exhibit and Twenty-second Annual Fluids Engineering Conference. Volume: Performance Prediction of Centrifugal Pumps and Compressors*. New Orleans, La., March 9-13, 1980. pp. 77-86. ASME.

Engel, K. (1997). *Numerische Simulation der instationären Strömung in Turbomaschinenkomponenten* (Report No. 97-19). Deutsches Zentrum für Luft- und Raumfahrt. https://elib.dlr.de/38473.

Enneking, M. (2020). *Experimentelle Validierung einer numerischen Optimierungsmethode zur Wirkungsgradsteigerung eines transsonischen Radialverdichters.* [Doctoral dissertation, RWTH Aachen University]. RWTH Publications. https://publications.rwth-aachen.de/record/801985.

Ferziger, J. H., Perić, M., and Street, R. L. (2020). *Computational Methods for Fluid Dynamics.* Springer Cham. https://doi.org/10.1007/978-3-319-99693-6.

Forrester, A. I. J., Sobester, A., and Keane, A. J. (2008). *Engineering Design via Surrogate Modelling: A Practical Guide.* John Wiley & Sons. https://doi.org/10.1002/9780470770801.

Friedman, J. H. (1991). Multivariate Adaptive Regression Splines. *The Annals of Statistics*, 19(1):1–67. https://doi.org/10.1214/aos/1176347963.

Gallimore, S. J. (1986). Spanwise Mixing in Multistage Axial Flow Compressors: Part II – Throughflow Calculations Including Mixing. *Journal of Turbomachinery*, 108(1):10–16. https://doi.org/10.1115/1.3262009.

Gallimore, S. J. (1998). Viscous Throughflow Modeling of Axial Compressor Bladerows Using a Tangential Blade Force Hypothesis. *Journal of Turbomachinery*, 120(4):662–670. https://doi.org/10.1115/1.2841775.

Gallimore, S. J. and Cumpsty, N. A. (1986). Spanwise Mixing in Multistage Axial Flow Compressors: Part I – Experimental Investigation. *Journal of Turbomachinery*, 108(1):2–9. https://doi.org/10.1115/1.3262019.

Galvas, M. R. (1973). *Fortran Program for Predicting Off-Design Performance of Centrifugal Compressors* (Report No. NASA-TN-D-7487). National Aeronautics and Space Administration. https://ntrs.nasa.gov/api/citations/19740001912/downloads/19740001912.pdf.

Geller, M., Schemmann, C., and Kluck, N. (2017). Identification of Loss Model Parameters for Highly Loaded Centrifugal Impellers. *Proceedings of the 15th International Probabilistic Workshop & 10th Dresdner Probabilistic Workshop.* Dresden, Germany, September 27-29, 2017.

Géron, A. (2017). *Hands-On Machine Learning with Scikit-Learn and TensorFlow.* O' Reilly Media.

Gholamy, A., Kreinovich, V., and Kosheleva, O. (2018). *Why 70/30 or 80/20 Relation between Training and Testing Sets: A Pedagogical Explanation* (Report No. UTEP-CS-18-09). University of Texas at El Paso. https://scholarworks.utep.edu/cs_techrep/1209.

Goodfellow, I., Bengio, Y., and Courville, A. (2016). *Deep Learning.* MIT Press. http://www.deeplearningbook.org.

Google (2025). *Neural Networks: Activation Functions.* Machine Learning, Google for Developers. Retrieved March 25, 2025, from https://developers.google.com/machine-learning/crash-course/neural-networks/activation-functions.

Greitzer, E. M., Tan, C. S., and Graf, M. B. (2004). *Internal Flow: Concepts and Applications.* Cambridge University Press. https://doi.org/10.1017/CBO9780511616709.

Hansen, A. and Kappis, W. (2001). Automised Calibration of Empirical Loss- and Deviation Models for Compressor Blade Rows. *Proceedings of the ASME Turbo Expo 2001: Power for Land, Sea, and Air. Volume 1: Aircraft Engine; Marine; Turbomachinery; Microturbines and Small Turbomachinery.* New Orleans, Louisiana, USA. June 4-7, 2001. V001T03A042. ASME. https://doi.org/10.1115/2001-GT-0346.

Harrison, H. M. (2020). *Development and Validation of a New Method to Model Slip and Work Input for Centrifugal Compressors.* [Doctoral dissertation, Purdue University]. Purdue University Graduate School Research Repository. https://doi.org/10.25394/PGS.11905593.v1.

Hawthorne, W. R. (1951). Secondary Circulation in Fluid Flow. *Proceedings of the Royal Society of London. Series A, Mathematical and Physical Sciences*, 206(1086):374–387. http://www.jstor.org/stable/98575.

He, W., Jiang, Z., Xiao, T., Xu, Z., and Li, Y. (2025). A Survey on Uncertainty Quantification Methods for Deep Learning. arXiv preprint arXiv:2302.13425. https://arxiv.org/abs/2302.13425.

Hehn, A. P. (2018). *Aerodynamische Analyse eines numerisch optimierten transsonischen Radialverdichters mit Freiformflächenbeschaufelung.* [Doctoral dissertation, RWTH Aachen University]. RWTH Publications. https://publications.rwth-aachen.de/record/728359.

Hildebrandt, A. and Genrup, M. (2006). Numerical Investigation of the Effect of Different Back Sweep Angle and Exducer Width on the Impeller Outlet Flow Pattern of a Centrifugal Compressor With Vaneless Diffuser. *Journal of Turbomachinery*, 129(2):421–433. https://doi.org/10.1115/1.2447873.

Hirsch, C. (1984). *Computational Models for Turbomachinery Flows* (Report No. NPS67-84-022). Naval Postgraduate School. https://apps.dtic.mil/sti/pdfs/ADA573595.pdf.

Hirsch, C. (2007). *Numerical Computation of Internal and External Flows: The Fundamentals of Computational Fluid Dynamics.* Elsevier. https://doi.org/10.1016/B978-0-7506-6594-0.X5037-1.

Hirsch, C. and Dring, R. P. (1985). *Through-Flow Models for Mass and Momentum Averaged Variables* (Report No. NPS67-85-012CR). Naval Postgraduate School. https://apps.dtic.mil/sti/pdfs/ADA173887.pdf.

Hirsch, C., Kang, S., and Pointel, G. (1996). A Numerically Supported Investigation of the 3D Flow in Centrifugal Impellers: Part II – Secondary Flow Structure. *Proceedings of the ASME 1996 International Gas Turbine and Aeroengine Congress and Exhibition. Volume 1: Turbomachinery.* Birmingham, UK. June 10-13, 1996. V001T01A049. ASME. https://doi.org/10.1115/96-GT-152.

Hirsch, C. and Warzee, G. (1976). A Finite-Element Method for Through Flow Calculations in Turbomachines. *Journal of Fluids Engineering*, 98(3):403–414. https://doi.org/10.1115/1.3448341.

Hirsch, C. and Warzee, G. (1979). An Integrated Quasi-3D Finite Element Calculation Program for Turbomachinery Flows. *Journal of Engineering for Power*, 101(1):141–148. https://doi.org/10.1115/1.3446435.

Horlock, J. H. (1971). On Entropy Production in Adiabatic Flow in Turbomachines. *Journal of Basic Engineering*, 93(4):587–593. https://doi.org/10.1115/1.3425313.

Horlock, J. H. and Denton, J. D. (2005). A Review of Some Early Design Practice Using Computational Fluid Dynamics and a Current Perspective. *Journal of Turbomachinery*, 127(1):5–13. https://doi.org/10.1115/1.1650379.

Howard, J. H. G. and Lennemann, E. (1971). Measured and Predicted Secondary Flows in a Centrifugal Impeller. *Journal of Engineering for Power*, 93(1):126–131. https://doi.org/10.1115/1.3445380.

Howard, J. H. G. and Osborne, C. (1977). A Centrifugal Compressor Flow Analysis Employing a Jet-Wake Passage Flow Model. *Journal of Fluids Engineering*, 99(1):141–147. https://doi.org/10.1115/1.3448515.

Howard, J. H. G., Osborne, C., and Japikse, D. (1994). A Rapid Aerodynamic Loading Procedure for Centrifugal Impeller Design. *Proceedings of the ASME 1994 International Gas Turbine and Aeroengine Congress and Exposition. Volume 1: Turbomachinery.* The Hague, Netherlands. June 13-16, 1994. V001T01A058. ASME. https://doi.org/10.1115/94-GT-148.

Howard, M. A. and Gallimore, S. J. (1993). Viscous Throughflow Modeling for Multistage Compressor Design. *Journal of Turbomachinery*, 115(2):296–304. https://doi.org/10.1115/1.2929235.

Jakeman, J. D., Barba, L. A., Martins, J. R. R. A., and O'Leary-Roseberry, T. (2025). Verification and Validation for Trustworthy Scientific Machine Learning. arXiv preprint arXiv:2502.15496. https://arxiv.org/abs/2502.15496.

James, G., Witten, D., Hastie, T., Tibshirani, R., and Taylor, J. (2023). *An Introduction to Statistical Learning: With Applications in Python*. Springer Cham. https://doi.org/10.1007/978-3-031-38747-0.

Jansen, W. (1967). A Method for Calculating the Flow in a Centrifugal Impeller when Entropy Gradients are Present. *Proceedings of the Institution of Mechanical Engineers, Internal Aerodynamics (Turbomachinery)*. Cambridge, England, UK. July 19-21, 1967. pp. 133–146.

Japikse, D. (1985). Assessment of Single- and Two-Zone Modeling of Centrifugal Compressors, Studies in Component Performance: Part 3. *Proceedings of the ASME 1985 International Gas Turbine Conference and Exhibit. Volume 1: Aircraft Engine; Marine; Turbomachinery; Microturbines and Small Turbomachinery*. Houston, Texas, USA. March 18-21, 1985. V001T03A023. ASME. https://doi.org/10.1115/85-GT-73.

Japikse, D. (2009). Turbomachinery Performance Modeling. *2008 Cliff Garrett Turbomachinery and Applications Engineering Award, SAE 2009 World Congress*. Detroit, Michigan, USA. April 20, 2009. 2009-01-0307. SAE International. https://doi.org/10.4271/2009-01-0307.

Japikse, D., Dubitsky, O., Oliphant, K. N., Pelton, R. J., Maynes, D., and Bitter, J. (2005). Multi-Variable, High Order, Performance Models (2005C). *Proceedings of the ASME 2005 International Mechanical Engineering Congress and Exposition. Fluids Engineering*. Orlando, Florida, USA. November 5-11, 2005. pp. 513–521. ASME. https://doi.org/10.1115/IMECE2005-79416.

Japikse, D. and Oliphant, K. N. (2005). Turbomachinery Modeling: Explicit and Implicit Knowledge Capturing (2005A). *Proceedings of the ASME Turbo Expo 2005: Power for Land, Sea, and Air. Volume 6: Turbo Expo 2005, Parts A and B*. Reno, Nevada, USA. June 6-9, 2005. pp. 15–24. ASME. https://doi.org/10.1115/GT2005-68099.

Jasa, J. (2021). *When to Use Gradient-Free Optimizers*. Practical MDO. Retrieved March 15, 2024, from https://openmdao.github.io/PracticalMDO/Notebooks/Optimization/when_to_use_gradient_free_methods.html.

Jennions, I. K. and Stow, P. (1985). A Quasi-Three-Dimensional Turbomachinery Blade Design System: Part II – Computerized System. *Journal of Engineering for Gas Turbines and Power*, 107(2):308–314. https://doi.org/10.1115/1.3239716.

Johnson, M. W. (1978). Secondary Flow in Rotating Bends. *Journal of Engineering for Power*, 100(4):553–560. https://doi.org/10.1115/1.3446393.

Johnson, M. W. and Moore, J. (1983). The Influence of Flow Rate on the Wake in a Centrifugal Impeller. *Journal of Engineering for Power*, 105(1):33–39. https://doi.org/10.1115/1.3227395.

Johnston, J. P. (1974). The Effects of Rotation on Boundary Layers in Turbomachine Rotors. *Symposium held at the Pennsylvania State University: Fluid Mechanics, Acoustics, and Design of Turbomachinery, Part I* (NASA SP-304). University Park, Pennsylvania, USA. August 31-September 3, 1970. pp. 207–249. National Aeronautics and Space Administration. https://ntrs.nasa.gov/citations/19750003111.

Johnston, J. P. and Eide, S. A. (1976). Turbulent Boundary Layers on Centrifugal Compressor Blades: Prediction of the Effects of Surface Curvature and Rotation. *Journal of Fluids Engineering*, 98(3):374–381. https://doi.org/10.1115/1.3448327.

Journal of Fluids Engineering (2008). Procedure for Estimation and Reporting of Uncertainty Due to Discretization in CFD Applications. *Journal of Fluids Engineering*, 130(7):078001. https://doi.org/10.1115/1.2960953.

Kang, S. and Hirsch, C. (2001). Numerical Simulation and Theoretical Analysis of the 3D Viscous Flow in Centrifugal Impellers. *Task Quarterly*, 5(4):433–458. https://journal.mostwiedzy.pl/TASKQuarterly/article/view/2273.

Katsanis, T. (1964). *Use of Arbitrary Quasi-Orthogonals for Calculating Flow Distribution in the Meridional Plane of a Turbomachine* (Report No. NASA-TN-D-2546). National Aeronautics and Space Administration. https://ntrs.nasa.gov/citations/19650002705.

Kingma, D. P. and Ba, J. (2017). Adam: A Method for Stochastic Optimization. arXiv preprint arXiv:1412.6980. https://arxiv.org/abs/1412.6980.

Kirtley, K., Beach, T., and Adamczyk, J. (1990). Numerical Analysis of Secondary Flow in a Two-Stage Turbine. *Proceedings of the AIAA/SAE/ASME/ASEE 26th Joint Propulsion Conference*. Orlando, Florida, USA. July 16-18, 1990. AIAA-90-2356. https://doi.org/10.2514/6.1990-2356.

Kochenderfer, M. J. and Wheeler, T. A. (2019). *Algorithms for Optimization*. MIT Press. https://algorithmsbook.com/optimization/files/optimization-1e.pdf.

Labat Casajust, S., Möller, D., and Jeschke, P. (2023). A CFD-Assisted Throughflow Approach for the Map Calculation of Centrifugal Compressors. *Proceedings of the ASME Turbo Expo 2023: Turbomachinery Technical Conference and Exposition. Volume 13D: Turbomachinery – Multidisciplinary Design Approaches, Optimization, and Uncertainty Quantification; Radial Turbomachinery Aerodynamics; Unsteady Flows in Turbomachinery*. Boston, Massachusetts, USA. June 26-30, 2023. V13DT35A006. ASME. https://doi.org/10.1115/GT2023-101906.

Lakshminarayana, B. (1996). *Fluid Dynamics and Heat Transfer of Turbomachinery*. John Wiley & Sons. https://doi.org/10.1002/9780470172629.

Lawerenz, M., Teich, M., Willburger, A., and Ganse, J. (2014). *Modellentwicklung zur aerodynamischen Simulation der Turbomaschinenkomponenten in Mikrogasturbinen für die energetische Biomassenutzung* (Abschlussbericht LA1299/3-1). kassel university press GmbH. https://doi.org/10.17170/kobra-202311219051.

Leylek, J. H. and Wisler, D. C. (1990). Mixing in Axial-Flow Compressors: Conclusions Drawn From 3-D Navier-Stokes Analyses and Experiments. *Proceedings of the ASME 1990 International Gas Turbine and Aeroengine Congress and Exposition. Volume 1: Turbomachinery*. Brussels, Belgium. June 11-14, 1990. V001T01A101. ASME. https://doi.org/10.1115/90-GT-352.

Lottini, F., Bicchi, M., Agnolucci, A., Marconcini, M., and Arnone, A. (2024). Artificial Intelligence-Based Performance Maps for Expander-Compressor Analysis in Energy Transition Applications. *Proceedings of the ASME Turbo Expo 2024: Turbomachinery Technical Conference and Exposition. Volume 12D: Turbomachinery – Multidisciplinary Design Approaches, Optimization, and Uncertainty Quantification; Radial Turbomachinery Aerodynamics; Unsteady Flows in Turbomachinery*. London, United Kingdom. June 24-28, 2024. V12DT35A026. ASME. https://doi.org/10.1115/GT2024-128901.

Lyman, F. A. (1992). On the Conservation of Rothalpy in Turbomachines. *Proceedings of the ASME 1992 International Gas Turbine and Aeroengine Congress and Exposition. Volume 1: Turbomachinery*. Cologne, Germany. June 1-4, 1992. V001T01A078. ASME. https://doi.org/10.1115/92-GT-217.

Martin, P., Spence, S., Stuart, C., Leonard, T., Starke, A., and Geron, M. (2024). Investigating the Suitability of Multi-Scroll Volutes for Improving Spanwise Incidence of Mixed Flow Turbine Rotors With Varying Blade Cone Angles in Automotive Turbocharging Applications. *Journal of Turbomachinery*, 146(6):061009. https://doi.org/10.1115/1.4064339.

Massey, B. and Ward-Smith, J. (2006). *Mechanics of Fluids*. Taylor & Francis.

Mendez, M. A. (2022). *Lecture 6: Bio-Inspired Optimization. Genetic Algorithms and Particle Swarms* [Lecture]. VKI Lecture Series: Hands on Machine Learning for Fluid Dynamics, Online, February 7-11, 2022.

Mercioni, M. A. and Holban, S. (2020). The Most Used Activation Functions: Classic Versus Current. *2020 International Conference on Development and Application Systems (DAS)*. Suceava, Romania. May 21-23, 2020. pp. 141-145. https://doi.org/10.1109/DAS49615.2020.9108942.

Moore, J., Moore, J. G., and Timmis, P. H. (1984). Performance Evaluation of Centrifugal Compressor Impellers Using Three-Dimensional Viscous Flow Calculations. *Journal of Engineering for Gas Turbines and Power*, 106(2):475–481. https://doi.org/10.1115/1.3239590.

Musgrave, D. S. (1979). The Prediction of Design and Off-design Efficiency for Centrifugal Compressor Impellers. *The 25th Annual International Gas Turbine Conference and Exhibit and the 22nd Annual Fluids Engineering Conference. Performance Prediction of Centrifugal Pumps and Compressors*, New Orleans, Louisiana, USA. March 9-13, 1980. pp. 185-189.

Ng, A. (2025). *Advanced Learning Algorithms: Diagnosing Bias and Variance* [Lecture]. DeepLearning.AI & Stanford University on Coursera. https://www.coursera.org/learn/advanced-learning-algorithms/lecture/L6SHx/diagnosing-bias-and-variance.

Nürnberger, D. (2004). *Implizite Zeitintegration für die Simulation von Turbomaschinenströmungen* (Report No. 2004-27). Deutsches Zentrum für Luft- und Raumfahrt. https://elib.dlr.de/49328.

Oh, H. W., Yoon, E. S., and Chung, M. K. (1997). An Optimum Set of Loss Models for Performance Prediction of Centrifugal Compressors. *Proceedings of the Institution of Mechanical Engineers, Part A: Journal of Power and Energy*, 211(4):331–338. https://doi.org/10.1243/0957650971537231.

Pacciani, R., Rubechini, F., Marconcini, M., Arnone, A., Cecchi, S., and Daccà, F. (2016). A CFD-based throughflow method with an explicit body force model and an adaptive formulation for the S2 streamsurface. *Proceedings of the Institution of Mechanical Engineers, Part A: Journal of Power and Energy*, 230(1):16–28. https://doi.org/10.1177/0957650915607091.

Pelton, R. J., Japikse, D., Maynes, D., and Oliphant, K. N. (2005). Turbomachinery Performance Models (2005B). *Proceedings of the ASME 2005 International Mechanical Engineering Congress and Exposition. Fluids Engineering.* Orlando, Florida, USA. November 5-11, 2005. pp. 501-511. ASME. https://doi.org/10.1115/IMECE2005-79414.

Peter, J. and Marcelet, M. (2008). Comparison of Surrogate Models for Turbomachinery Design. *WSEAS Transactions on Fluid Mechanics*, 3(1):10–17. https://www.wseas.us/e-library/transactions/fluid/2008/25-252.pdf.

PyTorch (2024a). *PyTorch documentation: Dropout*. PyTorch. Retrieved April 8, 2025, from https://pytorch.org/docs/stable/generated/torch.nn.Dropout.html.

PyTorch (2024b). *PyTorch documentation: LeakyReLU*. PyTorch. Retrieved March 25, 2025, from https://pytorch.org/docs/stable/generated/torch.nn.LeakyReLU.html.

Qiu, X., Japikse, D., Zhao, J., and Anderson, M. R. (2011). Analysis and Validation of a Unified Slip Factor Model for Impellers at Design and Off-Design Conditions. *ASME Journal of Turbomachinery*, 133(4):041018. https://doi.org/10.1115/1.4003022.

Ren, P., Stuart, C., Spence, S., Inomata, R., Kobayashi, T., and Morita, I. (2023). Using Machine Learning for Loss Prediction in a Hybrid Meanline Modeling Method to Deliver Improved Radial Turbine Performance Prediction. *Journal of Turbomachinery*, 145(7):071013. https://doi.org/10.1115/1.4056777.

Reymond, L. M., Geilich, M., Stemmermann, J., and Jeschke, P. (2023). Investigation of the Aerodynamic Losses Caused by the Impeller/Volute Interaction in a Transonic Centrifugal Compressor. *Proceedings of the ASME Turbo Expo 2023: Turbomachinery Technical Conference and Exposition. Volume 13D: Turbomachinery – Multidisciplinary Design Approaches, Optimization, and Uncertainty Quantification; Radial Turbomachinery Aerodynamics; Unsteady Flows in Turbomachinery.* Boston, Massachusetts, USA. June 26-30, 2023. V13DT36A010. ASME. https://doi.org/10.1115/GT2023-102145.

Roache, P. J. (1997). Quantification of Uncertainty in Computational Fluid Dynamics. *Annual Review of Fluid Mechanics*, 29:123–160. https://doi.org/10.1146/annurev.fluid.29.1.123.

Rodgers, C. (1978). A Diffusion Factor Correlation for Centrifugal Impeller Stalling. *Journal of Engineering for Power*, 100(4):592–601. https://doi.org/10.1115/1.3446403.

Rubechini, F., Schneider, A., Arnone, A., Cecchi, S., and Malavasi, F. (2011). A Redesign Strategy to Improve the Efficiency of a 17-Stage Steam Turbine. *Journal of Turbomachinery*, 134(3):031021. https://doi.org/10.1115/1.4003082.

Schmitz, A., Aulich, M., and Nicke, E. (2011). Novel Approach for Loss and Flow-Turning Prediction Using Optimized Surrogate Models in Two-Dimensional Compressor Design. *Proceedings of the ASME 2011 Turbo Expo: Turbine Technical Conference and Exposition. Volume 7: Turbomachinery, Parts A, B, and C.* Vancouver, British Columbia, Canada. June 6-10, 2011. pp. 1103-1114. ASME. https://doi.org/10.1115/GT2011-45086.

Schmitz, A., Aulich, M., Schönweitz, D., and Nicke, E. (2012). Novel Performance Prediction of a Transonic 4.5 Stage Compressor. In *Proceedings of the ASME Turbo Expo 2012: Turbine Technical Conference and Exposition. Volume 8: Turbomachinery, Parts A, B, and C*, pages 2123–2134, Copenhagen, Denmark. June 11-15, 2012. https://doi.org/10.1115/GT2012-69003.

Schnoes, M. and Nicke, E. (2017). A Database of Optimal Airfoils for Axial Compressor Throughflow Design. *Journal of Turbomachinery*, 139(5):051008. https://doi.org/10.1115/1.4035075.

scikit-learn (2025). *scikit-learn API Reference: StandardScaler*. scikit-learn, Machine Learning in Python. Retrieved March 26, 2025, from https://scikit-learn.org/stable/modules/generated/sklearn.preprocessing.StandardScaler.html#sklearn.preprocessing.StandardScaler.

Sehra, A. and Kerrebrock, J. (1979). The Effect of Blade-to-blade Flow Variations on the Mean Flow-Field of a Transonic Compressor. *AIAA 12th Fluid and Plasma Dynamics Conference.* Williamsburg, Virginia, USA. July 23-25, 1979. 79-1515. https://doi.org/10.2514/6.1979-1515.

Senoo, Y. and Ishida, M. (1987). Deterioration of Compressor Performance Due to Tip Clearance of Centrifugal Impellers. *Journal of Turbomachinery*, 109(1):55–61. https://doi.org/10.1115/1.3262070.

Senoo, Y., Maruyama, S., Koizumi, T., and Nakase, Y. (1974). Viscous Effects on Slip Factor of Centrifugal Blowers. *Journal of Engineering for Power*, 96(1):59–65. https://doi.org/10.1115/1.3445749.

Simon, H. and Bülskämper, A. (1984). On the Evaluation of Reynolds Number and Relative Surface Roughness Effects on Centrifugal Compressor Performance Based on Systematic Experimental Investigations. *Journal of Engineering for Gas Turbines and Power*, 106(2):489–498. https://doi.org/10.1115/1.3239592.

Simon, J.-F. and Léonard, O. (2005). A Throughflow Analysis Tool Based on the Navier-Stokes Equations. *Proceedings of the 6th European Turbomachinery Conference.* Lille, France. https://citeseerx.ist.psu.edu/document?repid=rep1&type=pdf&doi=b9ae3b5c5794a3ace0d0944a9e0e6b4da5ceb8e4.

Simon, J.-F., Thomas, J. P., and Léonard, O. (2009). On the Role of the Deterministic and Circumferential Stresses in Throughflow Calculations. *Journal of Turbomachinery*, 131(3):031019. https://doi.org/10.1115/1.2992514.

Smith, A. G. (1957). On the Generation of the Streamwise Component of Vorticity for Flows in Rotating Passages. *Aeronautical Quarterly*, 8(4):369–383. https://doi.org/10.1017/S0001925900010635.

Smith, L. H., J. (1987). Discussion: "Secondary Flow, Turbulent Diffusion, and Mixing in Axial-Flow Compressors" (Wisler, D. C., Bauer, R. C., and Okiishi, T. H., 1987, ASME J. Turbomach., 109, pp. 455-469). *Journal of Turbomachinery*, 109(4):471–471. https://doi.org/10.1115/1.3262129.

Spurk, J. H. (1992). *Dimensionsanalyse in der Strömungslehre*. Springer Berlin, Heidelberg. https://doi.org/10.1007/978-3-662-01581-0.

Stuart, C., Spence, S., Filsinger, D., Starke, A., and Kim, S. I. (2017). Characterizing the Influence of Impeller Exit Recirculation on Centrifugal Compressor Work Input. *Journal of Turbomachinery*, 140(1):011005. https://doi.org/10.1115/1.4038120.

Stuart, C., Spence, S., Filsinger, D., Starke, A., and Kim, S. I. (2019). A Three-Zone Modeling Approach for Centrifugal Compressor Slip Factor Prediction. *Journal of Turbomachinery*, 141(3):031008. https://doi.org/10.1115/1.4042248.

Traupel, W. (1962). *Die Theorie der Strömung durch Radialmaschinen*. G. Braun.

Van den Braembussche, R. (2019). *Design and Analysis of Centrifugal Compressors*. John Wiley & Sons. https://doi.org/10.1002/9781119424086.

Van den Braembussche, R. A. (2007). *Centrifugal Compressors Analysis and Design* [Lecture]. Course Note 192, Von Karman Institute for Fluid Dynamics.

Vignon, C., Rabault, J., and Vinuesa, R. (2023). Recent advances in applying deep reinforcement learning for flow control: Perspectives and future directions. *Physics of Fluids*, 35(3):031301. https://doi.org/10.1063/5.0143913.

Von Backström, T. W. (2005). A Unified Correlation for Slip Factor in Centrifugal Impellers. *ASME Journal of Turbomachinery*, 128(1):1–10. https://doi.org/10.1115/1.2101853.

Wang, X.-F., Xi, G., and Wang, Z.-H. (2006). Aerodynamic Optimization Design of Centrifugal Compressor's Impeller with Kriging Model. *Proceedings of the Institution of Mechanical Engineers, Part A: Journal of Power and Energy*, 220(6):589–597. https://doi.org/10.1243/09576509JPE201.

Wennerstrom, A. J. (1991). A Review of Predictive Efforts for Transport Phenomena in Axial Flow Compressors. *Journal of Turbomachinery*, 113(2):175–179. https://doi.org/10.1115/1.2929080.

Whitfield, A. (1974). Slip Factor of a Centrifugal Compressor and Its Variation with Flow Rate. *Proceedings of the Institution of Mechanical Engineers*, 188(1):415–421. https://doi.org/10.1243/PIME_PROC_1974_188_047_02.

Whitfield, A. and Baines, N. C. (1990). *Design of Radial Turbomachines*. Longman Scientific & Technical.

Wiesner, F. J. (1979). A New Appraisal of Reynolds Number Effects on Centrifugal Compressor Performance. *Journal of Engineering for Power*, 101(3):384–392. https://doi.org/10.1115/1.3446586.

Wilcox, D. C. (1988). Reassessment of the Scale-determining Equation for Advanced Turbulence Models. *AIAA Journal*, 26(11):1299–1310. https://doi.org/10.2514/3.10041.

Wisler, D. C., Bauer, R. C., and Okiishi, T. H. (1987). Secondary Flow, Turbulent Diffusion, and Mixing in Axial-Flow Compressors. *Journal of Turbomachinery*, 109(4):455–469. https://doi.org/10.1115/1.3262127.

Wu, C.-H. (1952). *A General Theory of Three-dimensional Flow in Subsonic and Supersonic Turbomachines of Axial-, Radial, and Mixed-flow Types* (Report No. NACA-TN-2604). National Advisory Committee for Aeronautics. https://apps.dtic.mil/sti/pdfs/ADA380493.pdf.

Ziegler, K. U. (2003). *Experimentelle Untersuchung der Laufrad-Diffusor-Interaktion in einem Radialverdichter variabler Geometrie*. [Doctoral dissertation, RWTH Aachen University]. RWTH Publications. http://publications.rwth-aachen.de/record/58848.

A Derivations

A.1 Streamwise Vorticity Equation for Rotating Systems

In this Appendix, the equation for the *absolute* streamwise vorticity generation along a *relative* streamline is derived. This equation was first presented by *Smith* (1957) for general rotating systems.

To account for the effects of rotation on the generation of streamwise vorticity, the analysis is carried out in the relative frame. If $\vec{c}$ is the absolute velocity and $\vec{w}$ the relative one, the relationship between the absolute and relative vorticities $\vec{\omega} = \vec{\omega}_{rel} + 2\vec{\Omega}$ can be rewritten with the curl of the respective velocities as

$$\nabla \times \vec{c} = \nabla \times \vec{w} + 2\vec{\Omega} \quad \rightarrow \quad \nabla \times \vec{u} = 2\vec{\Omega}, \tag{A.1}$$

where $\vec{c} = \vec{u} + \vec{w}$ has been applied. The absolute acceleration of a fluid particle in the rotating frame of reference is

$$\vec{a} = \frac{D\vec{c}}{Dt} = \frac{\partial \vec{w}}{\partial t} + (\vec{w} \cdot \nabla)\,\vec{w} + \vec{\Omega} \times (\vec{\Omega} \times \vec{r}) + 2(\vec{\Omega} \times \vec{w}), \tag{A.2}$$

where the terms $\vec{\Omega} \times (\vec{\Omega} \times \vec{r})$ and $2(\vec{\Omega} \times \vec{w})$ are the centrifugal and Coriolis accelerations, respectively, which are the kinematic consequences of decomposing the acceleration in terms of relative quantities. For steady relative flow, it holds that $\partial \vec{w}/\partial t = 0$. The convective acceleration of the fluid $(\vec{w} \cdot \nabla)\,\vec{w}$ is due to the velocity changes along the streamline. Neglecting the gravity and blade forces, and assuming inviscid fluid, the momentum equation $m\vec{a} = \vec{F}$, with the acceleration from (A.2), takes the form

$$(\vec{w} \cdot \nabla)\,\vec{w} + \vec{\Omega} \times (\vec{\Omega} \times \vec{r}) + 2(\vec{\Omega} \times \vec{w}) = -\frac{\nabla p}{\rho}. \tag{A.3}$$

(A.3) can be rewritten in the Crocco form, which involves the vorticity $\vec{\omega} = \nabla \times \vec{c}$ and relates the kinematic and thermodynamic properties in an inviscid fluid. For that, the first term on the left-hand side of (A.3) is manipulated by means of vector identity relations as

$$\begin{aligned}(\vec{w} \cdot \nabla)\,\vec{w} &= \frac{1}{2}\nabla w^2 - \vec{w} \times (\nabla \times \vec{w}) = \frac{1}{2}\nabla w^2 - \vec{w} \times (\nabla \times (\vec{c} - \vec{u})) \\ &= \frac{1}{2}\nabla w^2 - \vec{w} \times \vec{\omega} + \vec{w} \times (\nabla \times \vec{u}).\end{aligned} \tag{A.4}$$

The second term on the left-hand side of (A.3) is in turn rewritten as

$$\vec{\Omega} \times (\vec{\Omega} \times \vec{r}) = -\nabla \left(\Omega^2 \left(\frac{r^2}{2} \right) \right) = -\frac{1}{2} \nabla u^2, \tag{A.5}$$

and the third one can be expressed, by means of (A.1), as

$$2(\vec{\Omega} \times \vec{w}) = (\nabla \times \vec{u}) \times \vec{w} = -\vec{w} \times (\nabla \times \vec{u}). \tag{A.6}$$

Incorporation of (A.4)–(A.6) into (A.3) yields

$$\vec{w} \times \vec{\omega} = \frac{\nabla p}{\rho} + \frac{1}{2} \nabla w^2 - \frac{1}{2} \nabla u^2. \tag{A.7}$$

The Gibbs equation can be used in the form $\nabla h = T \nabla s + \nabla p / \rho$ to substitute the pressure term in (A.7), giving

$$\vec{w} \times \vec{\omega} = \nabla \underbrace{\left(h + \frac{1}{2} w^2 \right)}_{h_{t,rel}} - T \nabla s - \frac{1}{2} \nabla u^2. \tag{A.8}$$

Identification of the Gibbs equation in (A.8) again, but now in the relative reference frame, allows to write

$$\vec{w} \times \vec{\omega} = \frac{1}{\rho} \nabla p_{t,rel} - \frac{1}{2} \nabla u^2 \quad \rightarrow \quad \rho (\vec{w} \times \vec{\omega}) = \nabla \underbrace{\left(p_{t,rel} - \frac{1}{2} \rho u^2 \right)}_{p_{t,red}}. \tag{A.9}$$

From (A.9), a reduced stagnation pressure $p_{t,red}$ can be defined as

$$p_{t,red} = p_{t,rel} - \frac{1}{2} \rho u^2 = p + \frac{1}{2} \rho w^2 - \frac{1}{2} \rho u^2, \tag{A.10}$$

which is consistent with the rothalpy conserved along a streamline and is also referred to as *rotary stagnation pressure*, p^*. In an inviscid flow, (A.10) is conserved along a relative streamline. With the introduction of (A.10), (A.9) becomes

$$\vec{w} \times \vec{\omega} = \frac{\nabla p^*}{\rho}, \tag{A.11}$$

which implies, by the definition of the vector cross product, that the vortex lines in the stationary frame of reference and the streamlines in the relative frame are contained in surfaces of constant p^*. This helps decompose the absolute vorticity vector into two components

$$\vec{\omega} = \vec{\omega}_{||,\vec{w}} + \vec{\omega}_{\perp,\vec{w}}, \tag{A.12}$$

one along the relative velocity vector ($\vec{\omega}_{||,\vec{w}}$), and the other one normal to it and at the same time tangential to the surface of constant rotary stagnation pressure ($\vec{\omega}_{\perp,\vec{w}}$).

To obtain an expression for each of the terms in (A.12), it is recalled that the general expression for the tangential component of a vector to a surface is

$$\vec{v}_{tang} = -\hat{n} \times (\hat{n} \times \vec{v}), \tag{A.13}$$

with $\vec{v}$ being the vector in question and $\hat{n}$ the unit vector perpendicular to the surface. Accordingly, the tangential component of the absolute vorticity vector to the surface ($\vec{\omega}_{\perp,\vec{w}}$) in (A.12) can be written, with unit vector $\hat{w}$, as

$$\vec{\omega}_{\perp,\vec{w}} = (\hat{w} \times \vec{\omega}) \times \hat{w} = \left(\frac{\vec{w}}{\sqrt{\vec{w} \cdot \vec{w}}} \times \vec{\omega} \right) \times \frac{\vec{w}}{\sqrt{\vec{w} \cdot \vec{w}}} = \frac{(\vec{w} \times \vec{\omega}) \times \vec{w}}{\vec{w} \cdot \vec{w}}. \tag{A.14}$$

As for the streamwise component $\vec{\omega}_{||,\vec{w}}$ in (A.12), its expression is obtained by combining (A.12) and (A.13), leading to

$$\begin{aligned} \vec{\omega}_{||,\vec{w}} &= \vec{\omega} - \vec{\omega}_{\perp,\vec{w}} = \vec{\omega} - (\hat{w} \times \vec{\omega}) \times \hat{w} = \vec{\omega} + \hat{w} \times (\hat{w} \times \vec{\omega}) \\ &= \vec{\omega} + (\hat{w} \cdot \vec{\omega})\hat{w} - \underbrace{(\hat{w} \cdot \hat{w})}_{=1}\vec{\omega} = (\hat{w} \cdot \vec{\omega})\hat{w}, \end{aligned} \tag{A.15}$$

which can be further developed with the definition of the unit vector

$$\vec{\omega}_{||,\vec{w}} = (\vec{\omega} \cdot \hat{w})\hat{w} = \left(\vec{\omega} \cdot \frac{\vec{w}}{\sqrt{\vec{w} \cdot \vec{w}}} \right) \frac{\vec{w}}{\sqrt{\vec{w} \cdot \vec{w}}} = \left(\frac{\vec{\omega} \cdot \vec{w}}{\vec{w} \cdot \vec{w}} \right) \vec{w} = \frac{(\vec{\omega} \cdot \vec{w})\vec{w}}{w^2} = \frac{\omega_s}{w}\vec{w}, \tag{A.16}$$

where the scalar value of the streamwise vorticity, ω_s, has been defined as

$$\omega_s = \frac{\omega \cdot \vec{w}}{w}. \tag{A.17}$$

With (A.14) and (A.16), the vorticity is expressed as

$$\vec{\omega} = \frac{\omega_s}{w}\vec{w} + \frac{(\vec{w} \times \vec{\omega}) \times \vec{w}}{\vec{w} \cdot \vec{w}}. \tag{A.18}$$

From (A.18), an equation can be set up by taking the divergence of vorticity field, because the vorticity is solenoidal—meaning that it has no sources or sinks—and its divergence is thus equal to zero

$$\nabla \cdot \vec{\omega} = \nabla \cdot \left(\frac{\omega_s}{w}\vec{w} \right) + \nabla \cdot \left(\frac{(\vec{w} \times \vec{\omega}) \times \vec{w}}{\vec{w} \cdot \vec{w}} \right) = 0. \tag{A.19}$$

(A.19) can be further manipulated by taking into account that it contains the divergence of the product of scalars (ω_s/w and $1/\vec{w}\cdot\vec{w}$) by vectors. Therefore, the identity $\nabla\cdot(\psi\vec{v}) = \psi\nabla\cdot\vec{v} + (\nabla\psi)\cdot\vec{v}$ applies, leading to

$$\underbrace{\frac{\omega_s}{w}\nabla \cdot \vec{w}}_{①} + \underbrace{\vec{w} \cdot \nabla \left(\frac{\omega_s}{w} \right)}_{②} + \underbrace{\frac{1}{\vec{w} \cdot \vec{w}}\nabla \cdot [(\vec{w} \times \vec{\omega}) \times \vec{w}]}_{③} + \underbrace{[(\vec{w} \times \vec{\omega}) \times \vec{w}] \cdot \nabla \left(\frac{1}{\vec{w} \cdot \vec{w}} \right)}_{④} = 0\,. \tag{A.20}$$

Since by continuity, $\nabla \cdot \vec{w} = 0$, term ① in (A.20) cancels. As for term ②, it represents the growth of streamwise vorticity. Term ③ can be developed by means of the vector identity $\nabla \cdot (a \times b) = (\nabla \times a) \cdot b - (\nabla \times b) \cdot a$, with $a \equiv (\vec{w} \times \vec{\omega})$ and $b \equiv \vec{w}$, giving

$$\begin{aligned}
③ &\equiv \frac{1}{w^2}\nabla \cdot [(\vec{w} \times \vec{\omega}) \times \vec{w}] = \frac{1}{w^2}[\nabla \times \underbrace{(\vec{w} \times \vec{\omega})}_{\text{(A.11)}} \cdot \vec{w} - (\nabla \times \vec{w}) \cdot (\vec{w} \times \vec{\omega})] \\
&= \frac{1}{w^2}\underbrace{\left(\nabla \times \frac{\nabla p^*}{\rho}\right)}_{=0} \cdot \vec{w} - \frac{1}{w^2}(\nabla \times (\vec{c} - \vec{u})) \cdot (\vec{w} \times \vec{\omega}) \\
&= \frac{1}{w^2}[(-\underbrace{\nabla \times \vec{c}}_{=\vec{\omega}} + \underbrace{\nabla \times \vec{u}}_{=2\vec{\Omega}}) \cdot (\vec{w} \times \vec{\omega})] \\
&= \frac{1}{w^2}[\underbrace{-\vec{\omega} \cdot (\vec{w} \times \vec{\omega})}_{=-\vec{w}\cdot(\vec{\omega}\times\vec{\omega})=0} + 2\vec{\Omega} \cdot (\vec{w} \times \vec{\omega})] = \frac{2\vec{\Omega} \cdot (\vec{w} \times \vec{\omega})}{w^2}.
\end{aligned} \tag{A.21}$$

Regarding term ④ in (A.20), it applies that the gradient of an inverse function is $\nabla\left(\frac{1}{v}\right) = -\frac{1}{v^2}\nabla(v)$, thus it takes the form

$$④ \equiv [(\vec{w} \times \vec{\omega}) \times \vec{w}] \cdot \nabla\left(\frac{1}{\vec{w} \cdot \vec{w}}\right) = -\frac{[(\vec{w} \times \vec{\omega}) \times \vec{w}]\nabla(\vec{w} \cdot \vec{w})}{w^4}. \tag{A.22}$$

The term $\nabla(\vec{w} \cdot \vec{w})$ in (A.22) can be substituted by the vector identity

$$\nabla(\vec{w} \cdot \vec{w}) = 2(\vec{w} \cdot \nabla)\vec{w} + 2\vec{w} \times (\nabla \times \vec{w}), \tag{A.23}$$

where

$$\begin{aligned}
\vec{w} \times (\nabla \times \vec{w}) &= \vec{w} \times (\nabla \times (\vec{c} - \vec{u})) \\
&= \vec{w} \times (\nabla \times \vec{c} - \nabla \times \vec{u}) = \vec{w} \times (\vec{\omega} - 2\vec{\Omega}) = \vec{w} \times \vec{\omega} - 2\vec{w} \times \vec{\Omega},
\end{aligned} \tag{A.24}$$

leading to

$$\begin{aligned}
④ &\equiv -\frac{2[(\vec{w} \times \vec{\omega}) \times \vec{w}][(\vec{w} \cdot \nabla)\vec{w} + \vec{w} \times \vec{\omega} - 2\vec{w} \times \vec{\Omega}]}{w^4} = \\
&= -\frac{2[(\vec{w} \times \vec{\omega}) \times \vec{w}](\vec{w} \cdot \nabla)\vec{w}}{w^4} - \frac{2[(\vec{w} \times \vec{\omega}) \times \vec{w}] \cdot (\vec{w} \times \vec{\omega})}{w^4} + \frac{4[(\vec{w} \times \vec{\omega}) \times \vec{w}] \cdot (\vec{w} \times \vec{\Omega})}{w^4}.
\end{aligned} \tag{A.25}$$

The second term of (A.25) is equal to zero due to the self cross product of $(\vec{w} \times \vec{\omega})$

$$-\frac{2[(\vec{w} \times \vec{\omega}) \times \vec{w}] \cdot (\vec{w} \times \vec{\omega})}{w^4} = -\frac{2}{w^4}\left[\vec{w} \cdot [(\vec{w} \times \vec{\omega}) \times (\vec{w} \times \vec{\omega})]\right] = 0, \tag{A.26}$$

and the third term in (A.25) can be expressed, by means of the vector relation $(a \times b) \cdot (c \times d) = (a \cdot c)(b \cdot d) - (a \cdot d)(b \cdot c)$, as

$$\begin{aligned}\frac{4[(\vec{w} \times \vec{\omega}) \times \vec{w}] \cdot (\vec{w} \times \vec{\Omega})}{w^4} &= \frac{4}{w^4}[\underbrace{((\vec{w} \times \vec{\omega}) \cdot \vec{w})}_{=0}(\vec{w} \cdot \vec{\Omega}) - ((\vec{w} \times \vec{\omega}) \cdot \vec{\Omega})\underbrace{(\vec{w} \cdot \vec{w})}_{=w^2}] \\ &= -\frac{4\vec{\Omega} \cdot (\vec{w} \times \vec{\omega})}{w^2}, \end{aligned} \tag{A.27}$$

yielding the final expression for term ④ in (A.20)

$$④ \equiv -\frac{2[(\vec{w} \times \vec{\omega}) \times \vec{w}](\vec{w} \cdot \nabla)\vec{w}}{w^4} - \frac{4\vec{\Omega} \cdot (\vec{w} \times \vec{\omega})}{w^2}. \tag{A.28}$$

With the previous transformations, the vector equation for the growth of streamwise vorticity in the relative frame, (A.20), finally reads

$$\begin{aligned}\vec{w} \cdot \nabla\left(\frac{\omega_s}{w}\right) &= -\frac{2\vec{\Omega} \cdot (\vec{w} \times \vec{\omega})}{w^2} + \frac{2[(\vec{w} \times \vec{\omega}) \times \vec{w}](\vec{w} \cdot \nabla)\vec{w}}{w^4} + \frac{4\vec{\Omega} \cdot (\vec{w} \times \vec{\omega})}{w^2} \\ &= \frac{2[(\vec{w} \times \vec{\omega}) \times \vec{w}](\vec{w} \cdot \nabla)\vec{w}}{w^4} + \frac{2\vec{\Omega} \cdot (\vec{w} \times \vec{\omega})}{w^2}. \end{aligned} \tag{A.29}$$

The Crocco equation (A.11) can be substituted in (A.29), yielding

$$\vec{w} \cdot \nabla\left(\frac{\omega_s}{w}\right) = \frac{2}{\rho w^4}[\nabla p^* \times \vec{w}] \cdot (\vec{w} \cdot \nabla)\vec{w} + \frac{2\vec{\Omega}}{\rho w^2} \cdot \nabla p^*. \tag{A.30}$$

Because the aim is to analyze the generation of the streamwise vorticity *along* a relative streamline, the streamwise direction s is the one of interest (see Figure 2.5). Accordingly, (A.30) becomes, in scalar form

$$w\frac{\partial}{\partial s}\left(\frac{\omega_s}{w}\right) = \frac{2}{\rho w^4}[\nabla p^* \times \vec{w}] \cdot (\vec{w} \cdot \nabla)\vec{w} + \frac{2\Omega}{\rho w^2} \cdot \nabla p^*. \tag{A.31}$$

The term $(\vec{w} \cdot \nabla)\vec{w}$ in (A.31) is the fluid acceleration at a point on the relative streamline, and can be resolved into a component along the streamline and a normal component. Because this acceleration term is in scalar product with $[\nabla p^* \times \vec{w}]$ in (A.31), only the normal component of the acceleration remains, as the scalar product of two orthogonal vectors is zero. The acceleration term is thus written as w^2/R, where R is the principal radius of curvature of the relative streamline. With that, (A.31) becomes

$$\frac{\partial}{\partial s}\left(\frac{\omega_s}{w}\right) = \frac{2}{\rho w^2}\Big[\underbrace{\frac{1}{R}\nabla p^*}_{\text{curvature}} + \underbrace{\frac{\Omega}{w}\nabla p^*}_{\text{rotation}}\Big]. \tag{A.32}$$

A.2 Meridional Velocity Gradient Equation

In Sec. 2.3.2, the momentum equation was balanced in streamline coordinates for its use in the streamline curvature method. The equation is recalled here again for completeness

$$\frac{c_m^2}{R_m}\sin\gamma + c_m\frac{\partial c_m}{\partial m}\cos\gamma - \frac{c_u^2}{r}\sin(\gamma+\varepsilon) = -\frac{1}{\rho}\frac{dp}{dq} + F_q, \tag{A.33}$$

where q is the quasi-orthogonal direction (see Figure 2.9) and the force term is expressed as

$$F_q = F_n\sin\gamma + F_m\cos\gamma = F_u\tan\gamma = \frac{c_m}{r}\frac{\partial(rc_u)}{\partial m}\tan\gamma \tag{A.34}$$

with $F_u = \frac{c_m}{r}\frac{\partial(rc_u)}{\partial m}$ being the momentum equation in the circumferential direction.

In this Appendix, the objective is to rewrite (A.33) in terms of the meridional velocity gradient along the quasi-orthogonal direction, dc_m/dq. To achieve this, the pressure gradient along the q-direction needs to be rewritten in such a way that it contains the meridional velocity gradient. This is done by means of the Gibbs equation

$$Tds = dh - \frac{1}{\rho}dp \tag{A.35}$$

through the substitution of the dh term. The static enthalpy can be expressed by means of $h_t = h + \frac{1}{2}c^2$ and $c^2 = c_m^2 + c_u^2$ as

$$h = h_t - \frac{1}{2}c^2 = h_t - \frac{1}{2}c_m^2 - \frac{1}{2}c_u^2, \tag{A.36}$$

and its derivative then reads

$$dh = dh_t - c_m dc_m - c_u dc_u. \tag{A.37}$$

(A.37) is substituted in (A.35), yielding

$$\frac{1}{\rho}dp = dh_t - Tds - c_m dc_m - c_u dc_u. \tag{A.38}$$

With (A.38), the pressure gradient along the q-direction is

$$\frac{1}{\rho}\frac{dp}{dq} = \frac{dh_t}{dq} - T\frac{ds}{dq} - c_m\frac{dc_m}{dq} - c_u\frac{dc_u}{dq}. \tag{A.39}$$

(A.39) is then included in (A.33), giving

$$\begin{aligned} c_m\frac{dc_m}{dq} = {} & \frac{dh_t}{dq} - T\frac{ds}{dq} \\ & - c_u\frac{dc_u}{dq} - \frac{c_u^2}{r}\sin(\gamma+\varepsilon) + \frac{c_m^2}{R_m}\sin\gamma + c_m\frac{\partial c_m}{\partial m}\cos\gamma - \frac{c_m}{r}\frac{\partial(rc_u)}{\partial m}\tan\gamma. \end{aligned} \tag{A.40}$$

The term $-\left(c_u \frac{dc_u}{dq} + \frac{c_u^2}{r}\sin(\gamma+\varepsilon)\right)$ in (A.40) can be rewritten, considering from Figure 2.9 that $\sin(\gamma+\varepsilon) = dr/dq$, as

$$\begin{aligned} -\left(c_u\frac{dc_u}{dq} + \frac{c_u^2}{r}\frac{dr}{dq}\right) &= -\left(\frac{1}{2}\frac{dc_u^2}{dq} + \frac{c_u^2}{r}\frac{dr}{dq}\right) = -\frac{1}{2r^2}\left(r^2\frac{dc_u^2}{dq} + c_u^2 2r\frac{dr}{dq}\right) \\ &= -\frac{1}{2r^2}\left(r^2\frac{dc_u^2}{dq} + c_u^2\frac{dr^2}{dq}\right) = -\frac{1}{2r^2}\frac{d(r^2c_u^2)}{dq}. \end{aligned} \tag{A.41}$$

With that, the final form of the velocity gradient equation for the streamline curvature method is

$$\begin{aligned} c_m\frac{dc_m}{dq} = \\ \frac{dh_t}{dq} - T\frac{ds}{dq} - \frac{1}{2r^2}\frac{d(r^2c_u^2)}{dq} + \frac{c_m^2}{R_m}\sin\gamma + c_m\frac{\partial c_m}{\partial m}\cos\gamma - \frac{c_m}{r}\frac{\partial(rc_u)}{\partial m}\tan\gamma. \end{aligned} \tag{A.42}$$